Collective effects in muscle contraction and cellular adhesion

Hudson Borja da Rocha

université PARIS-SACLAY

ESPCI PARIS
EDUCATION SCIENCE INNOVATION

ÉCOLE POLYTECHNIQUE
UNIVERSITÉ PARIS-SACLAY

NNT: 2018SACLX072

Thèse de doctorat

Collective effects in muscle contraction and cellular adhesion

Thèse de doctorat de l'Université Paris-Saclay
préparée à l'École Polytechnique

École doctorale n°579: Sciences mécaniques et énergétiques, matériaux et géosciences (SMEMAG)

Spécialité de doctorat: Mécanique des solides

Thèse présentée et soutenue a Paris, le 27 septembre 2018, par

Hudson Borja da Rocha

Composition du jury:

Basile Audoly Research Director CNRS – Ecole Polytechnique	Examinateur
Matthieu Caruel Maître de conférences – Univérsité Paris-Est Créteil	Examinateur
Hans Jürgen Herrmann Full Professor – ETH Zürich	Rapporteur
Pascal Martin Research Director CNRS – Institut Curie	Examinateur
Jacques Prost Research Director CNRS – Institut Curie	Président
Stéphane Roux Research Director CNRS –ENS Paris Saclay	Examinateur
Lev Truskinovsky Research Director CNRS – ESPCI	Directeur de Thèse
Claude Verdier Research Director CNRS – Université Grenoble Alpes	Rapporteur

"'Exactly!" said Deep Thought. "So once you do know what the question actually is, you'll know what the answer means."

Douglas Adams, The Hitchhiker's Guide to the Galaxy

Thèse de doctorat de l'École Polytechnique

Abstract

Department of Mechanics
Laboratoire de Mécanique des Solides (LMS) et Physique et Mécanique des Milieux Hétérogènes (PMMH)

Doctor of Philosophy

Collective effects in muscle contraction and biological adhesion

by Hudson BORJA DA ROCHA

Two biological systems, a half-sarcomere of a skeletal muscle and an adhesive cluster of a crawling keratocyte, are considered in parallel because of the deep similarity in their structure and functionality. Their passive response can be modeled by a large number of multi-stable units coupled through long-range interactions, frustrated by quenched disorder and exposed to thermal noise. In such systems, long-range interactions lead to synchronization, defying temporal and spatial fluctuations. We use a mean-field description to obtain analytic results and elucidate the remarkable ensemble-dependence of the mechanical behavior of such systems in the thermodynamic limit. Despite important structural differences between muscle cross-bridges and adhesive binders, one can identify a common underlying spin glass structure, which we fully exploit in this work. Our study suggests that the muscle machinery is fine-tuned to operate near criticality, and we argue that in this respect the quenched disorder, reflecting here steric incommensuration, may be functional. We use the analogy between cell detachment and thermal fracture of disordered solids to study the statistics of fluctuations during cellular adhesion. We relate the obtained results to recent observations of intermittent behavior involved in cell debonding, also suggesting near-criticality. In addition to the study of the equilibrium properties of adhesive clusters, we also present the first results on their kinetic behavior in the presence of time-dependent loading.

Résumé

La nature fournit une abondance d'exemples de systèmes qui, bien que constitués de composants fondamentaux très simples, présentent un comportement global extrêmement complexe. Cette complexité est due aux interactions entre les composants, qui génèrent des effets collectifs. Les phénomènes émergents (''le tout est plus que la somme de ses parties'') sont fréquents dans les systèmes biologiques et des efforts considérables ont été récemment déployés pour les interpréter en tant que systèmes physiques. Le principal outil utilisé dans ces études est la mécanique statistique, qui établit un pont entre les lois microscopiques et les phénomènes macroscopiques. Le grand nombre et la distribution spatiale des éléments impliqués dans le fonctionnement de ces systèmes suggère également que la mécanique des milieux continus peut être un langage pertinent pour capturer une telle complexité.

Les systèmes biologiques consomment en permanence de l'énergie issue du métabolisme et fonctionnent loin de l'équilibre thermodynamique. Ceci rend les méthodes classiques de la mécanique statistique de l'équilibre et la théorie de Onsager hors équilibre peu applicables. Le comportement passif des systèmes biologiques fait cependant figure d'exception. Tout en restant assez complexe, ce régime peut souvent être analysé avec les méthodes de la théorie classique. Dans ce travail, nous considérons deux exemples représentatifs de comportement passif: le détachement des sites d'adhésion et la réponse passive des muscles squelettiques.

Ces deux systèmes biomoléculaires partagent une architecture commune, à la fois générique et pertinente pour de nombreux autres systèmes biologiques. Ils peuvent être décrits grossièrement comme un grand nombre d'unités multistables couplées par des interactions à longue portée. Cet arrangement est généralement frustré par du désordre spatial fixé et fonctionne dans un environnement brownien, ce qui signifie qu'il est exposé à un bruit thermique qui ne peut pas être traité comme une petite perturbation.

Nous présentons dans une première partie une description mécanique minimaliste de l'adhésion cellulaire, que nous modélisons comme un problème de fracture thermalisée dans des systèmes discrets désordonnés. Un site d'adhésion cellulaire est décrit comme une collection d'unités cassables en parallèle. Notre modèle est une extension du modèle de faisceau de fibres (FBM), qui a déjà été utilisé comme outil pour l'analyse de la rupture fragile dans les systèmes à seuils de défaillance aléatoires. Le FBM démocratique (qui suppose une répartition égale de la charge entre les fibres intactes) n'a été étudié jusqu'à présent que dans un contexte de chargement par force imposée et le comportement décrit a toujours été fragile. Pour capturer un comportement quasi-fragile (ductile) dans le même cadre prototype, nous avons augmenté le FBM en ajoutant des ressorts internes (en série par rapport aux fibres) et externes (en série par rapport au faisceau) et avons étudié ce système soumis à des déplacements imposés. En modifiant la rigidité des ressorts en série, nous sommes en mesure d'identifier le passage d'une réponse fragile à une réponse ductile. Alors que le premier cas est caractérisé par une distribution intermittente des avalanches près du seuil de défaillance global, le second cas possède des statistiques principalement gaussiennes. Près du point de transition fragile à ductile, la longueur de corrélation diverge et la transition devient du second ordre (point critique). Nous calculons les exposants critiques de champ moyen de manière analytique pour les processus de décohésion minimisant l'énergie (limite de température zéro du système en équilibre thermique) et en stabilité marginale (non équilibré, limite de viscosité zéro d'une dynamique suramortie). Nous étudions également la réponse mécanique à l'équilibre de notre modèle à température finie. Bien que, à des

températures physiologiques, l'établissement de l'équilibre thermique puisse prendre un temps excessivement long, il est intéressant de voir dans quelle mesure le désordre spatial fixé et la température sont interchangeables et à quel point chacune de ces sources d'inhomogénéité suppriment le détachement collectif.

Dans la second partie, nous étudions les particularités de la mécanique de la génération de force passive dans les muscles squelettiques. Sous une perturbation mécanique abrupte, une fibre musculaire tétanisée répond d'abord de manière élastique, puis montre une récupération de tension (contre-intuitive) à l'échelle de la milliseconde. Cette récupération de force rapide est essentiellement indépendante de la présence d'ATP, et les expériences montrent qu'elle est due au changement de conformation collectif des têtes de myosine liant les filaments d'actine. Nous étudions un modèle minimaliste purement mécanique d'un demi-sarcomère, l'unité de base de la contraction. Nous montrons que l'analogie directe entre notre modèle et le Modèle d'Ising à Champ Aléatoire (Random Field Ising Model) permet de calculer les propriétés thermodynamiques du système musculaire désordonné en utilisant des techniques classiques (Replica Trick). Le nouveau résultat est la démonstration que la frustration géométrique, causée par le manque de cohérence entre les périodicités des têtes de myosine extrudées et les sites de liaison à l'actine, est le facteur garant du fonctionnement optimal du système. L'optimalité est comprise ici comme la proximité d'un point critique, et nous montrons que la machinerie musculaire fonctionne au voisinage de deux points critiques adjacents, mais distincts, correspondant aux ensembles à élongation contrôlée et à force contrôlée. Nous montrons que la proximité des points critiques est le moyen pour le muscle de réagir de manière robuste et rapide aux perturbations externes. La nécessité d'être proches de deux points critiques est liée au caractère non-affine de la réponse mécanique de la fibre musculaire qui place des éléments contractiles individuels dans des conditions de chargements mixtes, intermédiaires entre déplacement imposé et force imposée. Nous avons ensuite étendu le modèle en introduisant des interactions stériques à courte portée susceptibles de concurrencer les interactions à longue portée imposées par les filaments. Nous montrons que les interactions à courte portée antiferromagnétiques peuvent modifier radicalement la réponse qualitative du système musculaire en stabilisant le régime de contraction isométrique. Nous avons utilisé l'approche classique de Landau pour générer le diagramme de phase complet du système, présentant une ligne de transitions de phase de second ordre atteignant un point tricritique, puis se poursuivant par une ligne de transitions de phase de premier ordre. Ce diagramme de phase montre que le système peut en fait être placé au voisinage de plusieurs régimes différents, ce qui permet un vaste répertoire de réponses mécaniques. La vérification expérimentale de nos prévisions devrait être la prochaine étape de ce projet de recherche.

Acknowledgements

First and foremost, I wish to thank my advisor, Lev Truskinovsky. He has been supportive since day one. It was hard not to be motivated by his passion for science. The door to Lev's office was always open whenever I ran into a trouble spot or had a question about my research or writing; for that, I am incredibly grateful.

I also would like to thank my thesis committee: Prof. Hans Herrmann, and Prof. Claude Verdier for accepting to be reporters for my thesis. Moreover, I feel very honored for Prof. Basile Audoly, Prof. Matthieu Caruel, Prof. Pascal Martin, Prof. Jacques Prost, and Prof. Stéphane Roux being part of my thesis committee.

I started my thesis at the LMS, and then for the last year, I was mainly based at PMMH, and I felt very welcomed in both labs. Thanks to Prof. Patrick Le Tallec, director of LMS and Prof. Philippe Petitjeans, director of PMMH, for providing me the structure for carrying out my research in the best conditions. I also want to thank Reinaldo Garcia-Garcia, Matthieu Caruel, Pierre Recho, Sylvain Patinet, and Damien Vandembroucq for the stimulating discussions and advice throughout my Ph.D.

I was fortunate enough to have a great number of friends who participated in my academic path. Early in my high school times, I discovered the wonders of mathematical competitions, and I am very grateful to my friends Elvis Néris and Mário Neto, those "wasted" weekends discussing math problems were really the trigger to follow a path in academia (which at the time I thought would be in mathematics). I was also lucky to have had wonderful professors who encouraged me to pursue a career in science. In particular, I want to mention Prof. Nir Cohen, Prof. Wallace Bessa, and Prof. Roberto Hugo Bielschowsky, for all the excellent advice and for always being supportive.

Moving to a foreign country can be very challenging and scary. However, it is much easier if one is lucky enough to find supporting friends. Half of my thesis, I spent in the isolated campus of the École Polytechnique. I thank Olcyr, Marlen, Charu, Irene, Arthur, Blandine, Livia, and many others for wonderful memories of friendship, which certainly made my stay in the campus more enjoyable.

I am incredibly lucky for having lived two years in the Cité Universitaire, where I met a lot of people from all sorts of backgrounds that were in similar situations than I was. Special thanks to Joanito, Joanita, and Mercedita. They shared with me all the crises that are inherent of a Ph.D. I will always cherish the long talks in the kitchen of the Maison du Portugal. Thanks to Laryssa, Gabs, Sophie, Raquel, Inês, Rita, Rita, Rita (yes, very common name), Virginia, Alice, Alicia, and Lucas (again, a non-exhaustive list). I also want to express my gratitude to Leonor, who supported me throughout the long months of writing and re-writing, even when I retreated to long days with my computer during vacation.

Finalmente não poderia deixar de agradecer à minha familia: à minha mãe, Núbia, ao meu Pai, Macêdo e às minhas irmãs, Nayara e Mayara. Sempre soube que tinha uma torcida muito grande do outro lado do atlântico para que tudo desse certo, e deu!

Contents

To all my friends scattered around the world, to my family, thank you.

Chapter 1

Background

Nature provides an abundance of examples of systems whose overall behavior is extremely complex and yet the fundamental components are very simple. This complexity is due to the interactions between the components, which generate collective effects. Emerging phenomena (”the whole is more than the sum of its parts”) are common in biological systems, and considerable efforts have recently been made to interpret them as physical systems. The main tool used in these studies has been statistical mechanics, which provides a bridge between the microscopic rules and the macroscopic phenomena. A large number of spatially distributed elements involved in the functioning of these systems also suggests that continuum mechanics may be a relevant language to capture the implied complexity.

Biological systems constantly consume energy from metabolism and operate far from thermodynamic equilibrium, which makes the classical methods of equilibrium statistical mechanics and weakly non-equilibrium Onsager theory hardly applicable. The passive behavior of biological systems, however, is an exception. While remaining quite complex, these regimes are often amenable to analysis by the methods of classical theory. In this work, we consider two representative examples of passive behavior: the detachment of cellular adhesive clusters subjected to applied displacements, and the passive response of skeletal muscles to abrupt loading.

These two biomolecular systems share a common architecture, which is somewhat generic and also relevant for many other biological systems. It can be roughly described as a large number of multi-stable units coupled through long-range interactions. Such a purely mechanical system is usually frustrated by quenched disorder and functions in a Brownian environment, which means that it is exposed to thermal noise that cannot be treated as a small perturbation.

In the context of this type of systems, the main effect of interest in the present study is synchronization ensured by long-range interactions. The dominant character of such interactions distinguishes biomolecular systems from conventional crystals. Such interactions are usually mediated by semi-rigid backbones or pads traversing the system and stabilizing affine responses. Alternatively, internal multistability, finite temperature, and quenched disorder act as de-synchronizing agents favoring spatial and temporal inhomogeneities and contributing to non-affine responses.

Given this perspective, we explore the parallelism between muscle cross-bridges and adhesive binders. In both cases, individual elements are bi-stable, exhibiting a folding-unfolding transition in the case of muscle contraction and binding-unbinding transition in the case of cellular adhesion. In both systems, the individual bi-stable elements are connected by much more rigid elastic manifolds represented by the myofilaments in the case of muscle cross-bridges, and the cellular cortex/membrane complex in the case of adhesive binders. Because of the near mean-field structure of the resulting coupling, these systems exhibit critical points and phase transition separating correlated (ferromagnetic) regimes from the uncorrelated (paramagnetic)

one. Other important features of these systems originating from the presence of long-range interactions are the nonconvexity of the free energy, the metastability (freezing) in the thermodynamic limit and, most importantly for our study, the non-equivalence of the displacement-controlled and force-controlled ensembles.

In the description of these systems, the quenched disorder has been usually ignored, and the synchronization was assumed to be confronted only by temperature. To overcome this limitation, we study in this Thesis the effects of the quenched structural inhomogeneity, which brings into both systems the spin glass structure affecting the overall mechanical behavior. Our main finding is that the seemingly deleterious effect of the 'dirt' may be in fact highly functional and even crucially important.

To emphasize the necessity of including quenched disorder in the description of these systems, we recall that the importance of inhomogeneities in muscle mechanics has been already pointed out in the classical contributions of A. Huxley. He argued that the incommensuration between the periodicities of the location of myosin heads and actin binding sites could play an important role in tuning the system towards a particular mechanical regime. In the case of focal adhesion, the role of inhomogeneities is even more apparent because cells have to interact with random backgrounds epitomized by the extracellular matrix. The random position and pre-stretch of such cell adhesion molecules (CAMs), as for instance, integrins, and the inhomogeneity in the spatial distribution of the receptors are therefore inherent elements of cellular adherence.

Although the two systems studied in this Thesis share a common general architecture, they are clearly distinct because of the different nature of the non-convexity of the elementary potential: double well in the case of cross-bridges and Lennard-Jones type in the case of binders. Also, because of the different numerical values of parameters, the effects of temperature and disorder in different systems/regimes may not be the same: one system may be 'cold' (in terms of dimensionless values of parameters) and another one 'hot'.

In our manuscript, which is comprised of two independent parts, the analysis of each of the two systems is presented separately. In this way, we could not only highlight the parallel parts but also emphasize the important differences.

Cellular de-cohesion Cells are enclosed by plasma membranes, which are bilayers of fat-based molecules (phospholipids) that physically prevent hydrophilic, or water-loving substances, from entering or escaping the cell. The plasma membrane is basically a 2D fluid allowing the tangential movement of a variety of membrane-bound proteins and sugars, as well as the multimerization and redistribution of receptors. The membrane is studded with proteins that act as channels and pumps, allowing the movement of different molecules into and out of the cell. They typically act as gatekeepers, determining which substances can cross the membrane. They are also involved in signaling between neighboring cells and the interaction with environment (O'Connor, Adams, and Fairman, 2010).

The space within the membrane is taken mostly by the cytoplasm, a liquid environment carrying cellular machinery and structural elements. Extending throughout the cytoplasm, from the nucleus to the plasma membrane is a highly cross-linked and entangled network of filaments and microtubules, called the cytoskeleton, which is responsible for maintaining the cell shape and mechanical resistance to deformation. The cytoskeleton is able to actively contract, thereby deforming the cell, affecting the cell's environment, and most importantly allowing the cell to

migrate and divide. In the inner face of the plasma membrane, we also find another protein structure: the cell cortex, which is mainly composed of actin filaments, actin-binding proteins, and motor proteins. The cortex modulates the behavior of the plasma membrane and ensures the elastic properties of the cell surface. In particular, it is largely responsible for the rigidity of focal adhesions.

The process of cells attachment to a substrate or another cell is called cell adhesion and is mediated by interactions between molecules of the cell surface. Cell adhesion molecules transmit both mechanical and chemical signals across the plasma membrane, which is necessary for the detection of external objects and the response to mechanical cues in the environment. These adhesion-dependent signals are particularly important for multicellular organisms where the mechanical information received from adjacent cells and extracellular matrix proteins plays a vital role in regulating many aspects of cell behavior, including cell differentiation, proliferation, and migration (Buckley et al., 1998).

In most cases, the nature of the interface between the cell and its environment determines the behavior and even the fate of a cell. For instance, it has been shown that the differentiation of stem cells can be guided by the mechanical or adhesive properties of the substrate (Eroshenko et al., 2013). There is also plenty of evidence that cells actively sense the passive properties of their environment, in particular, perform the rigidity sensing by actively straining the surroundings (Gupta et al., 2016; Sens, 2013; Schwarz, 2007). Such observations have already led to exciting new applications in regenerative medicine and tissue engineering given that mechanical signals are easier to control and observe than biochemical or genetic ones (Schwarz and Safran, 2013). Furthermore, active mechanisms involving biological adhesion in living systems are of considerable theoretical interest because of potential applications in bio-inspired adhesion devices (Puglisi and Truskinovsky, 2013).

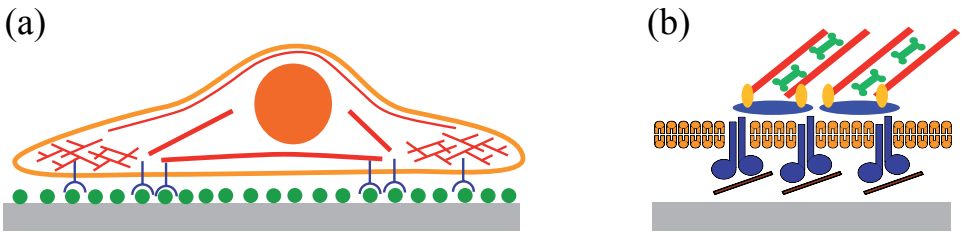

Figure 1.1: Schematic drawing of an adhering cell (a) and the detailled focal adhesion (b). The transmembranes molecules (integrins) bind to the extracellular matrix on the outside and are anchored to the actin network by cytoplasmic proteins, such as talin, vinculin. Adapted from (Schwarz and Safran, 2013)

In the theory of biological adhesion, the dissociation of a single binder is usually perceived as a one dimensional motion of a Brownian particle in a viscous environment. Bell's classical approach to adhesion kinetics, which is fundamentally similar to the Huxley-Simmons modeling of muscle contraction (Huxley and Simmons, 1971), introduces the effect of mechanical forces on the rate of the dissociation of a single bond (Bell, 1978). It was later appreciated that the strength of a bond depends crucially on the rate at which the bond is loaded (Evans and Ritchie, 1997; Seifert, 2002). The dissociation is usually modeled as an escape of a particle from a metastable state. This problem can be treated within the framework of Kramers's escape rate theory (Kramers, 1940; Hänggi, Talkner, and Borkovec, 1990) and the main qualitative result already captured by Bell's theory is that the increase in force decreases the energetic barrier necessary for dissociation. More recently, Schwarz and

coauthors used a stochastic version of Bell's model to describe adhesive clusters incorporating several binders connected in parallel. They showed that the non-linear receptor-ligand dynamics resulted in bistability and concluded that the possibility of rebinding is essential to ensure physiological lifetimes exhibited by adhesive clusters (Erdmann and Schwarz, 2004; Erdmann and Schwarz, 2006).

Recent advances in single-cell force spectroscopy and atomic force microscopy have allowed the adhesive properties of living cells to be studied in near-physiological conditions with unprecedented temporal and spatial resolution. These experiments typically show that the unbinding of a cell attached to a substrate is a sequence of *intermittent* events, in which the cell, pulled away from the substrate, gradually unbinds through a succession of abrupt jumps in the force (Helenius et al., 2008; Friedrichs, Helenius, and Muller, 2010; Müller et al., 2009; Rajan et al., 2017). The distribution of these jumps appears to be long-tailed indicating the possibility of scaling and suggesting near-criticality.

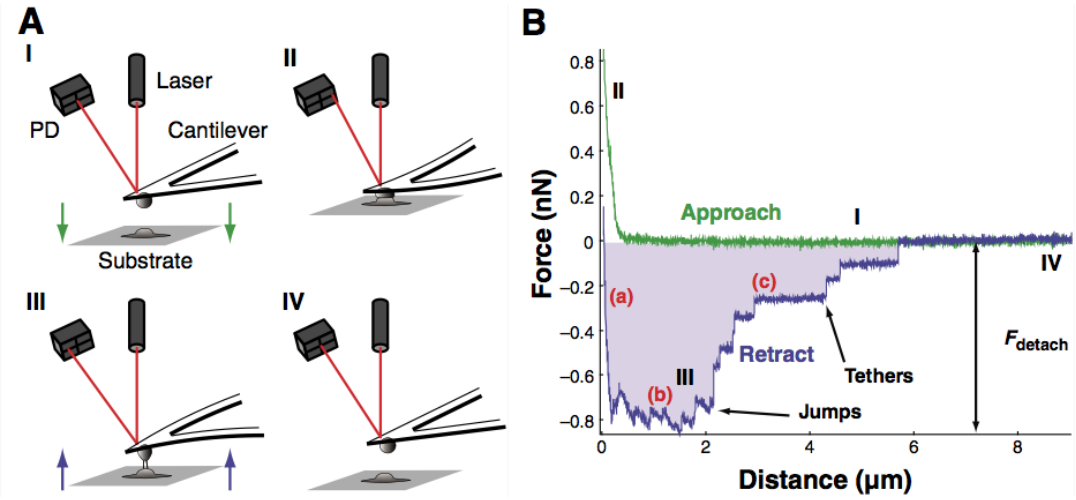

Figure 1.2: Single-cell force spectroscopy. Scheme for measurement of cell-adhesion for which the approach is shown in green and the retraction in blue. During the approach, the cell is pressed onto de subtrate until a pre-set force is reached. After a contact time, the cell is retracted from the substrate. Note the intermittent signature of the retraction. Taken from (Helenius et al., 2008)

The fact that cells do not operate using individual bonds and instead employ clusters, incorporating a large number bonds, suggests a possibility of complex emerging behavior. Distribution of load in the cluster may induce a non-trivial cooperative behavior involving large numbers of adhesive binders. As one bond is disrupted, the load on the remaining bonds increases and the cluster stability is changed; debonding can then propagate spatially, and one can potentially model cell adhesion as a reversible continuum fracture.

In continuum mechanics fracture is modeled as an athermal, irreversible process (Kanninen and Popelar, 1985). Even though thermally activated crack nucleation and propagation has been observed experimentally (Selinger, Wang, and Gelbart, 1991; Brenner, 1962; Cook and Liniger, 1993) and modeled as a kinetic process (Petrov and Orlov, 1976; Xing, 1991; Berdichevsky and Le, 2005; A. S. Krausz, 1988), thermally induced fracture has not attracted much interest in (non-extreme) industrial applications because of the enormous timescales involved in such process (Pomeau, 1992; Ciliberto, Guarino, and Scorretti, 2001; Politi, Ciliberto, and Scorretti, 2002a).

The situation is drastically different in biological applications where, for instance, cell adhesion, is characterized by low binding energies of the order of k_BT, which is ~ 4.1 pN nm at physiological temperatures $T \sim 300$ K. Such weak bonding can be disrupted by thermal activation leading to finite lifetimes of the bonding (Bell, 1978; Schwarz and Safran, 2013; Evans and Ritchie, 1997). As a result, the temperature can be an important factor controlling the debonding processes, in particular, it plays a crucial role in zipping-unzipping phenomena involved in the functioning of biological macromolecules (Chakrabarti and Nelson, 2009; Hyeon and Thirumalai, 2014; Mishra et al., 2015; Bergues-Pupo et al., 2015).

Statistical mechanics has been used in the studies of various minimal models of thermal fracture (Selinger, Wang, and Gelbart, 1991; Selinger et al., 1991; Roux, 2000; Scorretti, Ciliberto, and Guarino, 2001; Alava, Nukala, and Zapperi, 2006; Virgilii, Petri, and Salinas, 2007; Yoshioka, Kun, and Ito, 2015). In the context of cell adhesion, one is often interested in understanding how the external loading affects the stability of the bonding (Erdmann and Schwarz, 2004) and influences its lifetime (Bell, 1978). The simplest approach involves stochastic dynamics of elastically interacting binders (Peyrard and Bishop, 1989) with the phenomenologically postulated dependence of the attachment and detachment rates on the applied load (Manghi and Destainville, 2016; Vologodskii and Frank-Kamenetskii, 2017). Such models have been very successful in the studies of molecular denaturation and unzipping and also advanced our understanding of actomyosin contraction (Erdmann, Albert, and Schwarz, 2013; Caruel and Truskinovsky, 2018) and cell adhesion (Seifert, 2000; Erdmann and Schwarz, 2007; Erdmann and Schwarz, 2006; Lin et al., 2010).

In this Thesis, we focus on the microscopic modeling of collective thermal debonding avoiding explicitly phenomenological assumptions. Our starting point is the democratic fiber bundle model (FBM) (Pradhan, Hansen, and Chakrabarti, 2010; Hansen, Hemmer, and Pradhan, 2015) which we augment by adding a parallel spring allowing us to place the system in a hard device. The ensuing mean-field type coupling permits individual binders to interact and opens a possibility for cooperative behavior. The model remains analytically transparent, and we can compute its equilibrium thermodynamic properties explicitly even in the presence of quenched disorder.

More specifically, we model an adhesive cluster by a collection of N breakable units connected in parallel between two rigid bars. When an individual unit unbind/breaks, the load is redistributed equally between the surviving units. This process may trigger bursts or avalanches of bond dissociation, that either lead to a stable, partially debonded state or causes complete failure of the system. This problem was thoroughly studied in a soft loading device (Peirce, 1926; Daniels, 1945; Sornette, 1989; Herrmann and Roux, 2014; Roux, 2000) where the objective was to find the expected number of bursts before complete failure, as well as the frequency of events when a certain number of fibers breaks simultaneously. In this work, we extend these analyses to the case of cellular adhesion under prescribed displacement, where a bond plays the role of a fiber and the breaking of the fiber is interpreted as disruption of a bond.

In the conventional version of the FBM, when the system is exposed to a constant force (loaded in a soft device), the thermal equilibrium behavior is trivial because even at zero temperature the ground state is formally absent. To handle the hard device case, we augmented the democratic FBM by adding seemingly innocent internal (series to the binders) and external (series to the bundle) springs. For analytical transparency, we also assumed that each fiber has a piece-wise quadratic elastic energy. The quenched disorder is introduced in the breaking thresholds. Through

this assumption, we take into account the inhomogeneity of the substrate and the randomness of the distribution of integrins along the cell membrane.

We begin with the analysis of the mechanics of a single binder and show that it loses its snap through characteristics at any finite temperature. Then, we show that due to the presence of long-range interactions, the system of infinitely many interacting units can maintain its brittle behavior at finite temperatures. We study the emergent properties of the system arising from the collective interaction of the basic units and show that the discontinuous "brittle-to-ductile" transition in adhesion (which is similar to synchronous power stroke in muscle at finite temperatures, see below) is the direct consequence of long-range interactions. We interpret the brittle-to-ductile transition as a phase transition and show how temperature, disorder, and rigidity affect its parameters. Our main result is that the transition is of the second order bringing about all the usual features of criticality.

Criticality and ubiquity of power laws are the issues of great significance in contemporary science, giving a framework for understanding the emergence of complexity in a variety of natural systems, from earthquakes to turbulence. Particularly striking examples of criticality are encountered in biology and include such diverse phenomena as DNA folding, cytoskeleton rheology, healthy heartbeat and group behavior of animals. A characteristic feature of critical systems is minimal or marginal stability. In mechanical terms, this means that the system is non-linearizable and is posed at a bifurcation point. Such degeneracy, which has been in the past avoided in engineering, is presently becoming a design principle because it brings anomalous amplification combined with swift adaptation. Critical systems can be also expected to exhibit strong robustness in front of random perturbations featuring a broad range of scales.

Muscle contraction There are three types of muscle tissues in the body: skeletal, cardiac and smooth. They all share similar properties but differ from one another in anatomy, location and in how they are controlled by the nervous system. In this Thesis, we will be concerned with skeletal (striated) muscles.

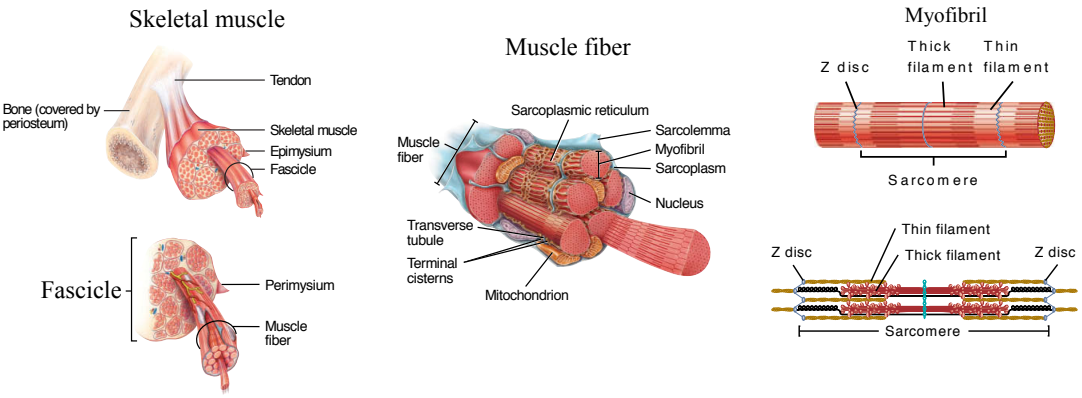

Figure 1.3: Representation of a skeletal muscle with multiple levels of organization. Adapted from (Tortora and Derrickson, 2014)

Skeletal muscles in vertebrates are the most common of the three types of muscle in the body. They work under voluntary control and got this name because most of them are attached to bones through collagen fibers (tendons) and are responsible for bone movement. Among their functions are body movement, active stabilization and even generation of heat.

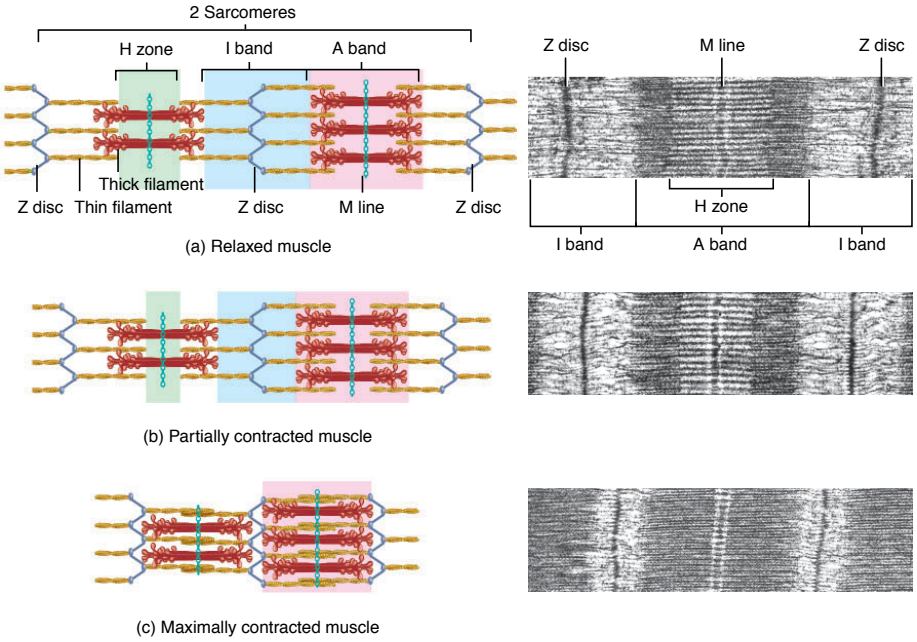

Figure 1.4: Skeletal muscle at the level of a sarcomere. On the left is a schematic representation of the sarcomeres in the sliding filament mechanism, and on the right its electron micrography. The overlap between the myosin and actin corresponds to the dark region. Taken from (Tortora and Derrickson, 2014)

Skeletal muscles are composed of bundles of fibers, which are long cylindrical multi-nucleated cells spanning the whole length of the tissue. Fibers, in turn, are composed of myofibrils, containing contractile units called sarcomeres. They run in series down the length of the myofibril. Each sarcomere, the basic unit of contraction, is composed of alternating bundles of thick and thin myofilaments. The muscles contract when these filaments slide past each other.

The thick filaments (about 15nm in diameter) are mainly formed by a protein myosin. The myosin molecules have the appearance of a golf club, with a tail composed of two intertwined chains and a double globular head projecting away from it. The thin filaments (7nm in diameter) is built primarily of a protein called actin. Actin molecules join together forming chains twisted into a helix configuration. These molecules are essential for the contraction of muscles because each actin molecule has a single 'myosin-binding' site. The other two proteins that are present in the thin filaments are troponin and tropomyosin. The molecules of tropomyosin cover the myosin-binding sites on the actin molecules when the muscle fibers are relaxed.

One of the main goals of muscle mechanics is to understand the working of the active force generating mechanism which operates at sub-myofibril scale and requires for its functioning the ATP hydrolysis. The passive mechanical properties of muscles, which do not require external energy supply, can be studied by applying rapid mechanical perturbation to an isometrically contracting muscle fiber. These types of experiments go back to the 60s, starting with the pioneering work of Podolsky (Podolsky, 1960) and later extended by Huxley (Huxley and Simmons, 1971).

It was found that if an isometrically tetanized muscle is suddenly shortened, the force first abruptly decreases but then partially recovers over ~ 1 *ms* timescale (Podolsky, 1960; Huxley and Simmons, 1971; Irving et al., 1992). The mechanism

behind such fast force recovery does not require the detachment of myosin cross-bridges from actin filaments. It can be viewed as a collective folding-unfolding phenomenon in the system of interacting bistable units. Behind such folding is a conformational change in the actin-bound myosin heads, known as the 'power stroke'. Since the power stroke takes place at the time scale that is much faster than the timescale of the active, ATP driven attachment-detachment ($\sim 100\ ms$) (Howard, 2001; Piazzesi et al., 2002; Kaya et al., 2017), the power-stroke-induced fast force recovery can be modeled as a passive collective folding of a bundle of bistable elements (Vilfan and Duke, 2003; Marcucci and Truskinovsky, 2010a). The resultant snap-spring response is resistant to thermal fluctuations because of the dominance of long-range interactions mediated by elastic backbones (Caruel, Allain, and Truskinovsky, 2013; Caruel and Truskinovsky, 2017).

If the applied force is fixed, the realistic mean-field theory, viewing the backbone as rigid (Caruel and Truskinovsky, 2016), predicts metastability due to synchronization of the cross-bridges and the existence of a critical point (Caruel, Allain, and Truskinovsky, 2013). It has been argued that this critical point is crucial for the functioning of muscle machinery (Caruel and Truskinovsky, 2017). As we have already mentioned, critical systems are ubiquitous in biology most probably because of their adaptive and operational advantages (Balleza et al., 2008; Beggs and Timme, 2012; Mora and Bialek, 2011; Krotov et al., 2014; Kessler and Levine, 2015). Their robustness in the face of random perturbations has been linked to marginal stability, and skeletal muscles indeed exhibit near zero passive rigidity in physiological (isometric contractions or stall) conditions (Huxley and Simmons, 1971; Brunello et al., 2014; Piazzesi et al., 2007; Linari et al., 1998).

The dominance of long-range interactions (Campa, Dauxois, and Ruffo, 2009; Barré, Mukamel, and Ruffo, 2001) leads to different collective behavior of cross-bridges in force (soft device) and length (hard device) ensembles (Caruel, Allain, and Truskinovsky, 2013). An interesting consequence of the ensemble non-equivalence (Gupta and Ruffo, 2017; Touchette, 2015) is that the critical points corresponding to length and force clamp loading conditions do not need to coincide (Caruel and Truskinovsky, 2018). Since individual cross-bridge bundles (half-sarcomeres) are embedded in a complex elastic environment involving series and parallel connections, both tension (at fixed displacement) and displacement (at fixed tension) responses are of relevance and to be robust in the sense of criticality the system should be poised close to both critical points.

In this Thesis, we use an augmented Huxley-Simmons model to show that this type of optimality may actualize in the system of muscle cross-bridges due to inhomogeneity induced by steric incommensuration. The idea that the *disregistry* between the periodicities of myosin and actin filaments brings the system's stiffness to zero was pioneered in (Huxley and Tideswell, 1996); the utility of quenched disorder for the active aspects of muscle mechanics has been recently discussed in (Egan et al., 2017). The beneficial nature of inhomogeneity is well known in many other fields of physics from high-temperature superconductivity (Zaanen, 2010) to Griffiths phases in brain networks (Moretti and Muñoz, 2013).

To explore the reachability of the desired 'double criticality', we represent the system of interacting cross-bridges by a random field Ising model (RFIM) and compute the equilibrium free energy using the techniques of the theory of glassy systems (Castellani and Cavagna, 2005). We then use the available experimental data on skeletal muscles to justify the claim that geometric frustration is the main factor in ensuring the targeted response.

It is generally appreciated that placing the system in the vicinity of a critical point offers the best trade-off between flexibility and robustness (Muñoz, 2017). Concerning fast force recovery, this means that equally synchronous response of the cross-bridges, needed to ensure the appropriate intensity of the strike (robustness), is available for an extensive range of mechanical stimuli (flexibility). Criticality in soft loading ensures stable force recovery while criticality in hard device ensures stable displacement recovery.

We also make another crucial observation that the equilibrium response of a bundle of contractile units connected in series and placed in a hard device cannot be described by local equilibrium constitutive relations obtained in either soft or hard device ensembles. Instead, the system exhibits an intermediate behavior.

To further extend the model we introduce steric short-range interactions, which may compete with the long-range interactions imposed by the filaments. We show that destabilizing anti-ferromagnetic short-range interactions can drastically change the qualitative response of the muscle system, stabilizing the regime of isometric contractions by turning the negative stiffness into the positive one. We used the classical Landau approach to generate the complete phase diagram of the system exhibiting a line of second-order phase transitions that hits a tricritical point and then continues by a line of first-order phase transitions. This phase diagram suggests a much broader potential repertoire of mechanical responses for the muscle system than it was previously thought with the possibility of not only critical but also tricritical behavior.

PART I:
CELLULAR ADHESION

In this Part we present a minimalistic mechanical description of cellular adhesion, which we model as a problem of thermalized fracture in disordered discrete systems. A focal adhesion is described as a collection of breakable units in parallel. Our model is an extension of the fiber bundle model (FBM), which has been used previously as a prototypical description of brittle fracture in systems with random failure thresholds. The democratic FBM has been previously studied only in a soft loading setting, and the described behavior was always brittle. To capture quasi-brittle (ductile) behavior in the same prototypical framework, we augmented the FBM by adding internal (series to fibers) and external (series to the bundle) springs and studied the resulting system in a hard device. By changing the stiffness of the series springs, we are able the crossover from brittle to ductile response. While the former is characterized by intermittent avalanche distribution near the global failure threshold, the latter shows predominantly Gaussian statistics. Near the brittle-to-ductile transition point, correlation length diverges, and the transition becomes of the second order (critical point). We compute the corresponding mean-field critical exponents analytically for both energy minimizing (zero temperature limit of a thermal equilibrium) and marginal (non-equilibrium, zero viscosity limit of an overdamped dynamics) decohesion processes. We then study the effects of finite temperature and finite rate of driving.

Chapter 2

Introduction

In Fig. 1.2 we have already illustrated the intermittent nature of cellular debonding. The presence of avalanches along this curve, clearly associated with collective debonding of groups of molecular binders, has not been explained yet. Here we explore the fact that similar intermittent behavior is routinely observed during the breakdown of disordered solids and the underlying complexity is expressly manifested in the distribution of earthquakes. In fracture mechanics, the simultaneous breaking of several structural elements is usually interpreted as an avalanche, and the subject of interest is often the probability distribution of the energy release associated with breaking and fragmentation.

Power law distributed avalanches, accompanying fracture-type phenomena in disordered elastic solids are of interest from the fundamental point of view because of the intricate interplay in this processes between disorder and long-range interactions. The observed and numerically simulated scale-free behaviors in such systems have been previously linked to spinodal points associated with first-order phase transitions (Alava, Nukala, and Zapperi, 2006; Zapperi et al., 1997). Other authors, however, related the observed scaling to critical points or second-order phase transitions (Moreno, Gómez, and Pacheco, 2000). The mystery is deepened by the fact that athermal fracture (de-cohesion) can be modeled in two ways: as an incremental global energy minimization phenomenon (Francfort and Marigo, 1998; Bourdin, Francfort, and Marigo, 2008) or as an incremental marginal equilibration phenomenon (Selinger, Wang, and Gelbart, 1991; Wang et al., 1991).

In this Part, we use the simplest mean-field model of fracture under controlled displacement to show that already at zero temperature both spinodal and critical point interpretations are relevant, even though the detailed scenarios for the ground state dynamics (zero temperature limit of the equilibrium response) and the marginal dynamics (zero viscosity limit of the overdamped response) are different. To this end, we consider the fiber bundle model (FBM) with global stress redistribution (Peirce, 1926; Daniels, 1945). The fracturing system is then modeled by a parallel bundle of breakable units with random failure thresholds. This model was studied exhaustively in a soft device setting where it exhibits universal scaling behavior of the fracture precursors with a disorder-insensitive mean-field exponents (Hemmer and Hansen, 1992; Hansen, Hemmer, and Pradhan, 2015; Sornette, 1989; M. Kloster and Hemmer, 1997). Various 'non-democratic' settings, implying local load sharing, have also been studied in the soft device framework (Pradhan, Hansen, and Chakrabarti, 2010; Patinet et al., 2014; Delaplace, Roux, and Cabot, 1999).

To capture the ductile behavior, we augment the democratic FBM by adding seemingly innocent internal (series to fibers) and external (series to the bundle) springs and study the resulting system in a hard device. The main advantage of the new model is that by changing the stiffness of the external series springs, we are able to simulate the crossover from brittle to ductile response. The ductile response

is usually associated with the stable development of small avalanches (micro-bursts) representing debonding events at the microscopic level. Instead, the brittle response is associated with large system size events representing macro-crack system size instabilities. In our model, the two types of fracture are distinguished by their statistical distribution of bond-breaking avalanches.

More specifically, we show that brittle fracture is characterized by intermittent avalanche distribution near the global failure threshold with mean-field exponents as in the case of the soft device. Instead, the predominantly Gaussian statistics of bursts characterizes ductile fracture. Near the brittle-to-ductile transition, the structure of the correlations bears a strong resemblance to athermal second-order phase transitions (critical points). We show that the location of the brittle-ductile transition in our generalized FBM is controlled as much by the ratio of the elastic stiffnesses (representing a rigidity measure), as by the variance of the quenched disorder.

Our analysis reveals that in the transition region between brittle and ductile regimes, the system following marginal dynamics exhibits scale-free avalanches with an exponent different from the one observed in the robust spinodal criticality, which we associate with brittle regimes. In the setting of equilibrium dynamics, we observe universal power law distribution of avalanches only in the transition from brittle to the ductile regime with the same exponent as encountered in out-of-equilibrium dynamics.

It has been shown in (Balog, Tissier, and Tarjus, 2014) that the out-of-equilibrium and equilibrium critical behaviors for random-field Ising model (RFIM) are in the same universality class, exhibiting the same critical exponents, scaling functions, and the same avalanche size distribution. We compare the critical exponents for the avalanche distribution in our model in equilibrium and out-of-equilibrium settings and find that the critical exponents indeed agree for the two dynamical models which appears to be a common property for all mean-field systems. Moreover, we show that if dynamics is energy minimizing, as in the case of zero temperature equilibrium systems, the spinodal scaling is lost while the critical system remains in the same universality class as its non-equilibrium analog. When the system size affects rigidity, spinodal avalanches remain, while critical scaling emerges only as a finite size effect. We argue that the observed robust criticality, as in the case of earthquakes and compressed porous materials, can result from self-tuning of the system towards the border separating brittle and ductile behaviors.

We draw analogies between fracture and phase transitions showing that our augmented version of FBM can be mapped onto the mean-field random field Ising model (RFIM). Our study also confirms that the system's rigidity can act as a control parameter sufficient to induce failure. Similar studies in different settings have already shown that rigidity can control the transition from brittle cracking to system-spanning diffuse breaking (Driscoll et al., 2016). In the context of cell adhesion, the internal and external elasticity has been long known as the regulator of the strength and stability of focal adhesions (Fuhrmann and Engler, 2015; Discher, Janmey, and Wang, 2005; Yeung et al., 2004). By building the bridge between these seemingly unrelated research directions, we reveal the complexity of cellular adhesion and hope to shed new light on its near-critical nature.

Chapter 3

The model

In this Chapter we introduce our model. We begin with the phenomenological study of a single binder, represented as a breakable element in series with an elastic element. Next, we study a parallel bundle of interacting bonds that is expected to mimic a realistic adhesive cluster.

3.1 A single binder

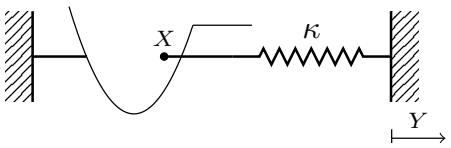

Figure 3.1: Mechanical representation of an individual binding element

We represent an elementary binding unit by a linear spring in series with a breakable element, see Fig. 3.1. For analytical simplicity, we model such element as a 'fuse' with a piece-wise quadratic potential

$$U(X) = \begin{cases} \dfrac{\kappa_p X^2}{2}, & if\ X \leq L \\ \dfrac{\kappa_p L^2}{2}, & if\ X > L. \end{cases} \tag{3.1}$$

Here κ_p is the linear elastic modulus of the binder before its breaking. When the coordinate X reaches the threshold L, the bond dissociates and under further stretching its energy remains constant and equal to $\kappa_p L^2/2$. The total energy of the binder loaded in a hard device[1] takes the form

$$E(X,Y) = U(X) + \frac{\kappa}{2}(Y-X)^2, \tag{3.2}$$

where κ is the elasticity of the series spring and Y is the controlling parameter representing total elongation, see Fig. 3.1.

It will be convenient to work with dimensionless variables. We set the breaking threshold L as the reference length and introduce the dimensionless lengths $x = X/L$, $y = Y/L$ and dimensionless energies $e = E/\kappa_p L^2$, $u = U/\kappa_p L^2$. We also

[1] In continuum mechanics, a machine that prescribes displacements on the boundary is called a hard loading device, and the one that prescribes surface tractions is called a soft loading device (Batra, 2006). From this point forward we call those two loading conditions the *hard device* and the *soft device*, accordingly.

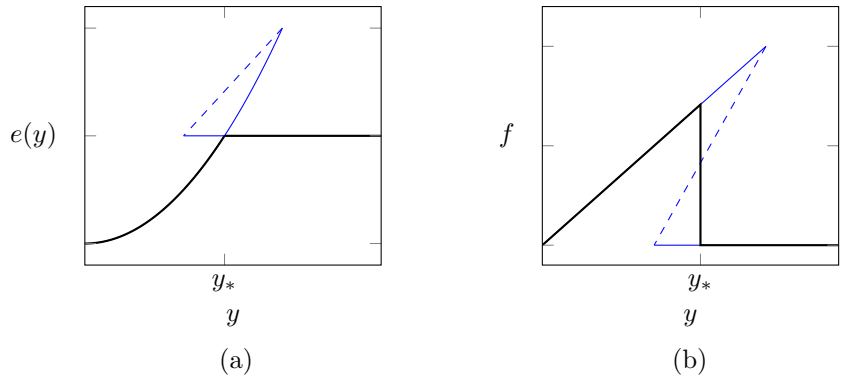

Figure 3.2: Mechanical response of a single binder in a hard device. Solid black lines, global minimum; colored lines, metastable states. Parameters: $\lambda = 1$.

define the dimensionless parameter $\lambda = \kappa/\kappa_p$ controlling the effective elasticity of the binder. Then the non-dimensional energy reads

$$e(x, y) = u(x) + \frac{\lambda}{2}(y - x)^2, \tag{3.3}$$

where,

$$u(x) = \begin{cases} \frac{x^2}{2}, & if\, x \leq 1 \\ \frac{1}{2}, & if\, x > 1. \end{cases} \tag{3.4}$$

In this setting, y is the controlling parameter characterizing the hard loading device. In equilibrium, $\partial e(x, y)/\partial x = 0$ and the internal variable x can be eliminated giving two locally stable branches.

$$e(y) = \begin{cases} \frac{\lambda}{\lambda+1}\frac{y^2}{2}, & \text{for } y \leq \frac{\lambda+1}{\lambda}, \\ \frac{1}{2}, & \text{for } y > 1 \end{cases} \tag{3.5}$$

The ensuing double-valued force-elongation relation $f(y) = \partial e(y)/\partial y$ can be written as

$$f = \begin{cases} \frac{\lambda}{\lambda+1} y, & \text{for } y \leq \frac{\lambda+1}{\lambda} \\ 0, & \text{for } y > 1. \end{cases} \tag{3.6}$$

Observe that at $y_* = \sqrt{\frac{\lambda+1}{\lambda}}$ the ground-state switches from unbroken (unbound) to broken (bound), however, both states can coexist as metastable in the interval $y \in [1, 1 + 1/\lambda]$. Therefore, the role of the series spring, characterized by the parameter λ, is to ensure the mechanical bi-stability of the individual binders. In Fig. 3.3, we show how the size of the bi-stability domain depends on the parameters λ and y. Note that in the limit $\lambda \to \infty$ the bonds behave as simple 'fuses', while at $\lambda \to 0$ the range of bi-stability, where the bonds behave as mechanical snap-springs, diverges.

3.2 Bundle of N binders

Next, consider N parallel binders attached to a pair of rigid backbones. A generic element with index $i = 1, \ldots, N$ is characterized by a random breaking threshold

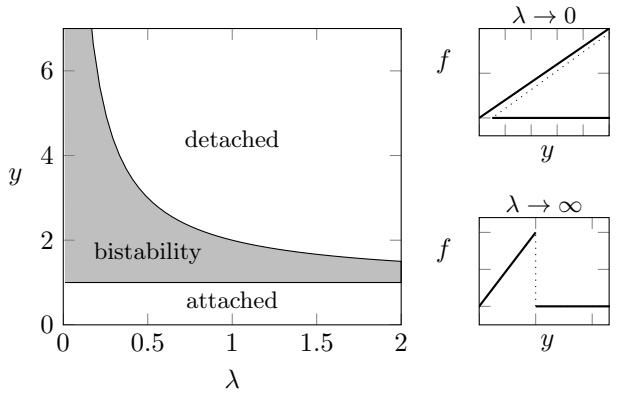

Figure 3.3: The dependence of the boundaries of the domain of metastability for a single binder on the loading y and the stiffness λ

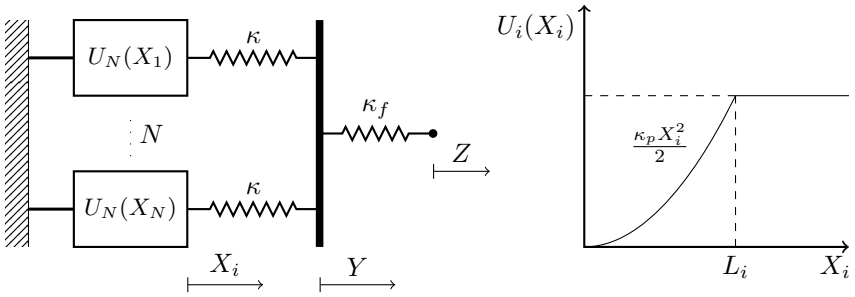

Figure 3.4: Mechanical model of the system and the potential energy of a single bond. X, Y and Z are displacements.

L_i. Assume further that the system is loaded through an external spring with stiffness κ_f, which characterizes elasticity of the environment (Jülicher and Prost, 1995a; Delaplace, Roux, and Cabot, 1999; Seifert, 2000). The total energy of the system is,

$$E = \sum_i^N U_i(X_i) + \frac{\kappa}{2}\sum_i^N (Y - X_i)^2 + \frac{\kappa_f}{2}(Z - Y)^2, \tag{3.7}$$

where Y is a position of the backbone and Z is the total elongation serving as the controlling parameter, see Fig. 3.4(a). The nonlinear breakable element is characterized by the potential,

$$U_i(X_i) = \begin{cases} \dfrac{\kappa_p X_i^2}{2} & \text{for } X_i \le L_i, \\ \dfrac{\kappa_p L_i^2}{2} & \text{for } X_i > L_i. \end{cases} \tag{3.8}$$

It will be again convenient to work with dimensionless variables. We define the average threshold as $\bar{L}$ and then introduce $x_i = X_i/\bar{L}$, $y = Y/\bar{L}$, $z = Z/\bar{L}$ and $l_i = L_i/\bar{L}$. The remaining non-dimensional parameters of the problem are

$$\lambda = \frac{\kappa}{\kappa_p} \tag{3.9}$$

and

$$\lambda_f = \frac{\kappa_f}{N\kappa_p}. \tag{3.10}$$

The dimensionless energy per element in a hard device is given by

$$\mathcal{H}(\boldsymbol{x}, y, z) = \frac{1}{N}\sum_{i=1}^{N}\left[u(x_i) + \frac{\lambda}{2}\left(y - x_i\right)^2\right] + \frac{\lambda_f}{2}(z-y)^2. \tag{3.11}$$

where,

$$u_i(x_i) = \begin{cases} \dfrac{x_i^2}{2} & \text{for } x_i \leq l_i, \\ \dfrac{l_i^2}{2} & \text{for } x_i > l_i. \end{cases} \tag{3.12}$$

We assume that the thresholds l_i are disordered and represented by independent random variables with the same probability distribution $p(l)$. We also introduce the cumulative distribution $P(l) = \int_0^l p(y)dy$ and recall that due to normalization $\int_0^\infty p(l)dl = 1$ and $\int_0^\infty lp(l)dl = 1$.

The soft device loading can be seen as a limiting case of the hard device loading. It can be obtained if we assume that the outer spring is infinitely soft $\lambda_f \to 0$. In this limit $z \to \infty$, but if $\lambda_f z \to f$ we obtain the system with applied force f. The outer spring becomes redundant in the soft device case since in quasi-static conditions the force is transmitted directly to the backbone. In this Thesis, we focus mainly on the less explored case of a hard device.

Chapter 4

Mechanical equilibrium

In this Chapter, we characterize the mechanical equilibrium of the adhesive cluster in the absence of thermal fluctuations. We explore the whole set of the metastable states and study how the internal parameters (internal rigidity and degree of disorder) influence the overall behavior of the system. We then introduce two loading strategies: the global minimum strategy and the marginal stability strategy. The goal is to show that fine-tuning the parameters allows one to change the behavior of the system from brittle-like to ductile (quasi-brittle) -like.

4.1 Metastable states

We first mechanically equilibrate the system with respect to the internal variables x_i's and y and keep z as a control parameter. To this end we need to solve the system of equations:

$$\begin{cases} \dfrac{\partial \mathcal{H}}{\partial x_i} & = 0, \text{for all } 1 \leq i \leq N \\ \dfrac{\partial \mathcal{H}}{\partial y} & = 0. \end{cases} \tag{4.1}$$

Equilibration in $\boldsymbol{x}$ means $u'(x_i) = \lambda(y - x_i)$, or more explicitly,

$$x_i = \begin{cases} \dfrac{\lambda y}{\lambda + 1} & \text{for } \; x_i \leq l_i, \\ y & \text{for } \; x_i > l_i. \end{cases} \tag{4.2}$$

The equilibration in y gives,

$$y(\boldsymbol{x}, z) = \frac{1}{\lambda + \lambda_f} \left(\lambda_f z + \lambda \frac{1}{N} \sum_{i=1}^{N} x_i \right). \tag{4.3}$$

We see the mean-field nature of the coupling through Eq. (4.3): the variable y is affected by the average value of x_i. We obtain

$$\frac{1}{N} \sum_{i=1}^{N} x_i = \frac{k}{N} y + \frac{N-k}{N} \frac{\lambda y}{\lambda + 1}, \tag{4.4}$$

where k is the number of broken elements. This representation allows us to write the backbone elongation $\hat{y}$ as a function of the number of broken elements k and total elongation z:

$$\hat{y}(k, z) = \frac{(1+\lambda)\lambda_f z}{\lambda(1 - k/N) + \lambda\lambda_f + \lambda_f}. \tag{4.5}$$

Moreover, if we substitute Eq. (4.5) in Eq. (4.2) we obtain the equilibrium positions x_i for the closed $\hat{x}_0$ and open $\hat{x}_1$ configurations,

$$\hat{x}_0(k,z) = \frac{\lambda\lambda_f z}{\lambda(1-k/N)+\lambda\lambda_f+\lambda_f}, \tag{4.6}$$

$$\hat{x}_1(k,z) = \frac{(1+\lambda)\lambda_f z}{\lambda(1-k/N)+\lambda\lambda_f+\lambda_f}. \tag{4.7}$$

Finally, substituting in Eq. (3.11) the equilibrium values for y and x_i, we write the energy of the system in terms of z only:

$$\mathcal{H}(k,z) = a_k z^2 + S_k. \tag{4.8}$$

Here $a_k = \frac{1}{2}\frac{\lambda\lambda_f(N-k)}{\lambda(N-k)+N(\lambda\lambda_f+\lambda_f)}$, and S_k is the accumulated energy of the disrupted bonds.

Because of the rigidity of the backbone, individual bonds will fail in sequence according to the value of their thresholds. Let $\bar{x}_i, i = 1, ..., N$ be the ordered sequence of failure thresholds l_i: $\bar{x}_1 \leq \bar{x}_2 \leq \cdots \leq \bar{x}_N$. Then, we can write $S_k = \frac{1}{N}\sum_{i=1}^{k}\frac{\bar{x}_i^2}{2}$ and $S_0 = 0$. Note that a_k is a (strictly) monotonically decreasing sequence while S_k is a (strictly) monotonically increasing sequence. The tension-elongation relation for a microscopic state[1] characterized by the parameter k can be now written as,

$$f(k,z) = \frac{\partial\mathcal{H}(k,z)}{\partial z} = \frac{\lambda\lambda_f(N-k)z}{\lambda(N-k)+N(\lambda\lambda_f+\lambda_f)}. \tag{4.9}$$

The main effect of complementing our fuse elements with the series springs with elasticity λ is the creation of metastability, which means that for a given elongation the binder can be locally stable in two microscopic configurations. The equilibrium values $\hat{x}_0(k,z)$ and $\hat{x}_1(k,z)$ are linear in z (see Eq. (4.6)-(4.7)) and therefore, it is clear that all individual will eventually debond. Each value of k defines an equilibrium branch extending between the two limits $(z_{inf}(k),\ z_{sup}(k))$ induced by the inequalities $\hat{x}_0(k,z) < \bar{x}_k$ and $\hat{x}_1(k,z) > \bar{x}_k$:

$$z_{inf}(k) = \frac{\lambda(1-k/N)+\lambda\lambda_f+\lambda_f}{(1+\lambda)\lambda_f}\bar{x}_k, \text{ for } 0 < k \leq N, \tag{4.10}$$

$$z_{sup}(k) = \frac{\lambda(1-k/N)+\lambda\lambda_f+\lambda_f}{\lambda\lambda_f}\bar{x}_k, \text{ for } 0 \leq k < N, \tag{4.11}$$

These branches are represented by the gray lines in Fig. 4.1 and Fig. 4.2. As we show below, they correspond to the local minima of the energy. The special cases are the homogeneous configurations $k = 0$, defined for $z \in (-\infty, z_{sup}(k=0)]$ and $k = N$, defined for $z \in [z_{inf}(k=N), \infty)$. When the thresholds are disordered, the load path will be characterized by a series of intermittent jumps because the complete synchronization, characteristic of the fully homogeneous system, will be compromised by the disorder.

[1] In our model, due to permutation invariance, the microscopic configuration is fully described by the number of open elements k.

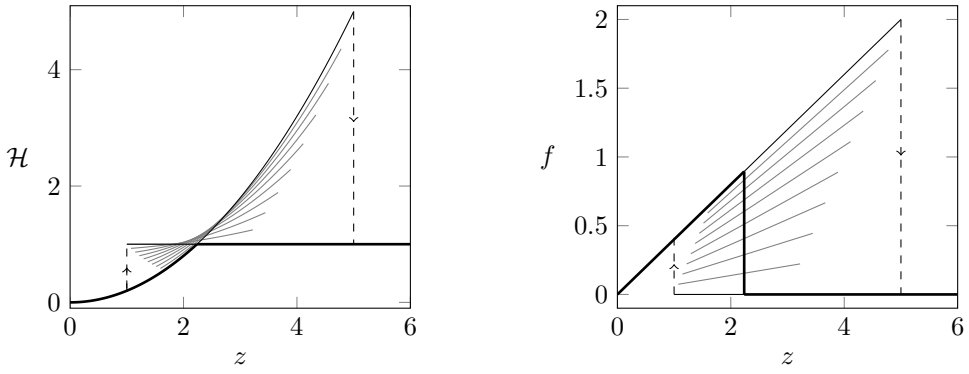

(a) Energy **(b)** Tension-elongation

Figure 4.1: Mechanical response of the model in a hard device. Solid black lines, global minimum, gray lines metastable states. Parameters are $N = 10$, $\lambda = 1$, $\lambda_f = 1$ and $l = \sqrt{2}$.

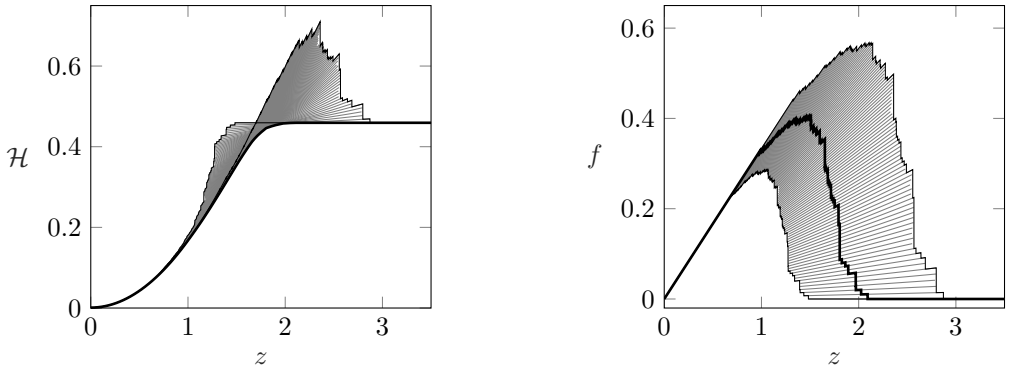

(a) **(b)**

Figure 4.2: Typical mechanical curves for the quenched system with $N = 50$ breakable units. The thick black line corresponds to the global minimum, while the gray lines are the metastable states. (a) is the energy curves for each microscopic configuration. (b) is the tension elongation curve. The thresholds are disordered following the Weibull distribution with shape parameter $\rho = 4$ and parameters are $\lambda = 1$, $\lambda_f = 1$.

4.2 The effect of different elastic moduli

The structure of the homogeneous system is mainly described by two elastic parameters: λ, representing the elasticity of individual units and λ_f, the external elasticity of a series spring through which the load is applied. In Fig. 4.3 we illustrate the separate effects of the parameters λ and λ_f in the overall response of the system. The inner spring λ creates an extended branch of stability for each of the two microscopic configurations; as the inner spring becomes stiffer (λ increases), the domain of metastability shrinks. To see this analytically it is enough to compute the $\lambda \to \infty$ limits of z_{inf} and z_{sup}:

$$\lim_{\lambda\to\infty} z_{inf} = l\left[\frac{(1-k/N)}{\lambda_f} + 1\right] \tag{4.12}$$

$$\lim_{\lambda\to\infty} z_{sup} = l\left[\frac{(1-k/N)}{\lambda_f} + 1\right], \tag{4.13}$$

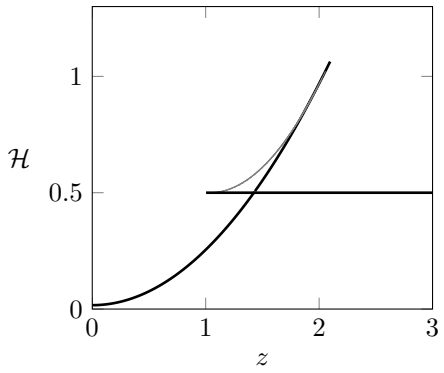

(a) Energy $\lambda = 10$,$\lambda_f = 1$

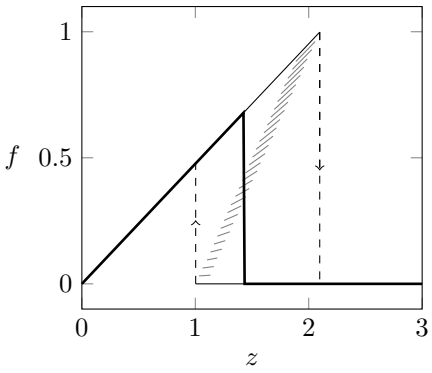

(b) Tension-elongation $\lambda = 10$, $\lambda_f = 1$

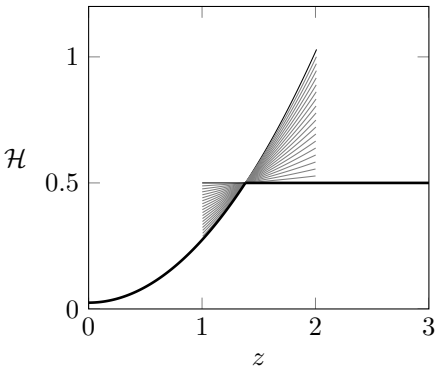

(c) Energy $\lambda = 1$, $\lambda_f = 100$

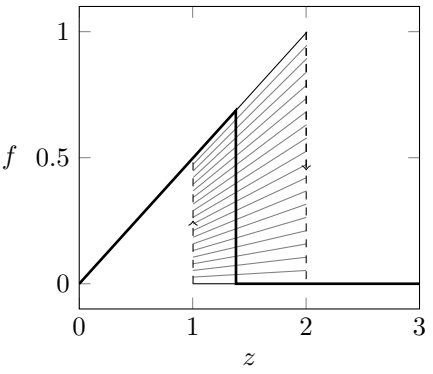

(d) Tension-elongation $\lambda = 1$, $\lambda_f = 100$

Figure 4.3: Mechanical response of the model in a hard device. Solid black lines, the global minimum; grey lines, metastable states. Parameters are $N = 30$ and $l = 1$.

which shows that the interval $[z_{inf}, z_{sup}]$ collapses to a single point $z = l\left[\frac{(1-k/N)}{\lambda_f} + 1\right]$ in this limit.

The rigidity of the external spring, represented by the parameter λ_f, also affects the size of the metastability domain. Even in the limit $\lambda \to \infty$, a finite elasticity λ_f can still be responsible for the metastability and the coexistence of bound and unbound conformations. In the disordered system, a small value of λ_f favors a macroscopic (collective or brittle) fracture, see Fig. 4.4, while at large values of λ_f we see, instead, sequential microfractures. In the classical FBM, neither of the limits $\lambda \to \infty$ and λ_f is relevant because the force is applied directly to the bundle. Note that in the absence of disorder, the fracture of the system is always synchronous (collective).

4.3 Stability analysis

To analyze the stability of the obtained equilibrium states, consider the total energy of N elements loaded at a hard device,

$$\hat{\mathcal{H}} = N\mathcal{H}(\boldsymbol{x}, y, z) = \sum_{i=1}^{N}\left[u(x_i) + \frac{\lambda}{2}(y - x_i)^2 + \frac{\lambda_f}{2}(z - y)^2\right]. \tag{4.14}$$

The equilibrium state is locally stable when the Hessian is positive definite. Since the energy in each of the conformational state is a quadratic form, the second derivatives

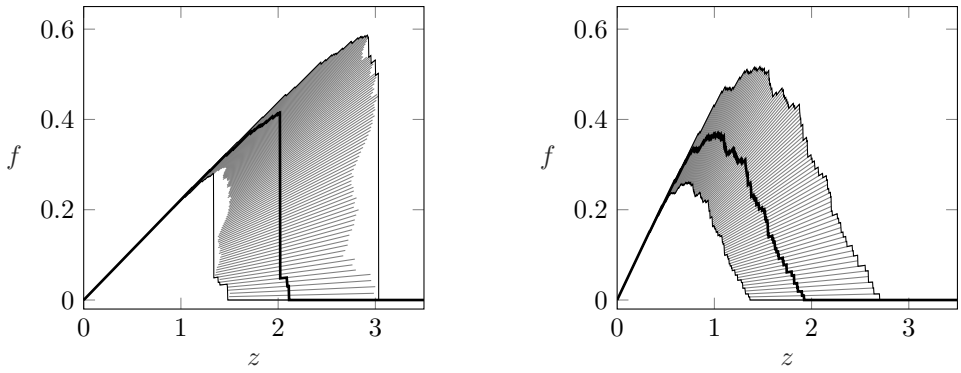

(a) $\lambda_f = 0.4$ **(b)** $\lambda_f \gg 1$

Figure 4.4: Mechanical response of the model in a hard device. Solid black lines, global minimum; grey lines, metastable states. Parameters are $N = 100$, $\lambda = 1$ and thresholds follow a Weibull distribution with $l = 1$ and $\rho = 4$. We compare the effect of the parameter λ_f in the global minimum load. path

do not depend on the variables of the problem. For a given microscopic configuration, characterized by k unbound elements[2],

$$\begin{aligned}
\frac{\partial^2 \hat{\mathcal{H}}(\boldsymbol{x}, y, z)}{\partial x_i^2} &= \begin{cases} h_0 = \lambda + 1 & \text{for } \ 1 \leq i < N - k \\ h_1 = \lambda & \text{for } \ N - k \leq i \leq N \end{cases} \\
\frac{\partial^2 \hat{\mathcal{H}}(\boldsymbol{x}, y, z)}{\partial x_i \partial x_j} &= 0, \ \text{ for } i \neq j \\
\frac{\partial^2 \hat{\mathcal{H}}(\boldsymbol{x}, y, z)}{\partial x_i \partial y} &= -\lambda, \ \text{ for } i = 1, \ldots, N \\
\frac{\partial^2 \hat{\mathcal{H}}(\boldsymbol{x}, y, z)}{\partial y^2} &= N(\lambda + \lambda_f)
\end{aligned} \tag{4.15}$$

Then the Hessian can be presented in the form,

$$\underline{\underline{\boldsymbol{\mathcal{M}}}} = \begin{pmatrix} H_1 & 0 & \ldots & 0 & -\lambda \\ 0 & \ddots & \ddots & \vdots & \vdots \\ \vdots & \ddots & \ddots & 0 & \vdots \\ 0 & \ldots & 0 & H_N & -\lambda \\ -\lambda & \ldots & \ldots & -\lambda & N(\lambda + \lambda_f) \end{pmatrix}, \tag{4.16}$$

where H_i is either h_0 or h_1. The sufficient condition for local stability is that all the principal minors of the Hessian are positive.

Note that the first N minors are just the product of diagonal therms H_i and are therefore always positive. The last principal minor, the determinant, is

$$\det(\underline{\underline{\boldsymbol{\mathcal{M}}}}) = \prod_{i=1}^{N} H_i \sum_{i=1}^{N} \left(\lambda + \lambda_f - \frac{\lambda^2}{H_i} \right). \tag{4.17}$$

Given the allowed values of H_i, each term in the sum is positive. Therefore, the determinant is positive, implying the stability of the equilibrium configurations obtained above. The unstable configurations must contain at least one element in the

[2]Because of permutational invariance, we rearrange the elements such that the first $N-k$ are bound, and the remaining k are unbound

spinodal state represented in our fuse model by a single point separating bound and unbound states.

Chapter 5

Response strategies

Suppose that the loading parameter is changed quasi-statically. The internal dynamics of the system controls the choice of a particular branch of the energy $\mathcal{H}$. Of particular interest are two dynamic responses. The first one is the vanishing viscosity limit of the correspondent viscoelastic problem. In this case, which we called the *marginal stability* (MS) response strategy, the system stays in a given local minimum until it becomes unstable. The second strategy imposes that the system is always in the *global minimum* (GM) of the energy, which can be viewed as the zero temperature limit of the (thermal) equilibrium dynamics (Maddalena et al., 2009).

5.1 Global minimization

Among all the equilibrium states we identify the ground states as the ones where the energy is globally minimized. As it can be seen from Fig. 4.1a and Fig. 4.2a, in a homogeneous system, the loading path defined by the ground states is characterized by a single transition; and when the quenched disorder is present, the system undergoes several intermediate transitions. Below, we first analyze the homogeneous case, when all elements are identical $l_i = l$, for $i = 1, \dots, N$ and then the disordered case, where l_i are randomly distributed with the probability density $p(l)$. In the case when the thresholds are identical, the ground state switches from the fully bound to the fully unbound configuration at $z = z_*$, see Fig. 4.1a, which solves the equation $\mathcal{H}(0, z_*) = \mathcal{H}(N, z_*)$. We can write the solution explicitly

$$z_* = l\sqrt{\frac{\lambda_f + \lambda\lambda_f + \lambda}{\lambda\lambda_f}}. \tag{5.1}$$

It is easy to see that for $z < z_*$ any element with $k \neq N$ increases its energy as the system is loaded. By direct calculation we get, $\mathcal{H}(N, z) \leq \mathcal{H}(k, z)$ for $z \leq z_*$, and $\mathcal{H}(0, z) \leq \mathcal{H}(k, z)$ for $z > z_*$, where $\mathcal{H}$ is given by Eq. (4.8).

We next define the fraction of connected bonds $\phi = 1 - k/N$ and the equation for the energy reads,

$$\mathcal{H}(\phi, z) = \frac{1}{2}\frac{\lambda\lambda_f\phi}{\lambda\phi + \lambda\lambda_f + \lambda_f}z^2 + (1 - \phi)\frac{l^2}{2} \tag{5.2}$$

In the continuum limit $N \to \infty$, one can show that only the homogeneous configurations $\phi = 0$ and $\phi = 1$ minimize the total energy. Indeed, by viewing ϕ as a continuous variable, we can compute the second derivative of $\mathcal{H}$ with respect to ϕ obtaining,

$$\frac{\partial^2\mathcal{H}(\phi, z)}{\partial\phi^2} = -\frac{(1 + \lambda)(\lambda\lambda_f z)^2}{(\lambda\phi + \lambda\lambda_f + \lambda_f)^3} \leq 0. \tag{5.3}$$

This computation shows that the energy is concave in ϕ, which means that the global minimum is always reached on fully synchronized configurations. In Fig. 5.1 we illustrate the energy landscape at different elongations z: at the point $z = z_*$ it is equally favorable to stay bound or unbound, for $z < z_*$ the system prefers to stay in the bound configuration $\phi = 1$, while for $z > z_*$ the stable configuration is $\phi = 0$.

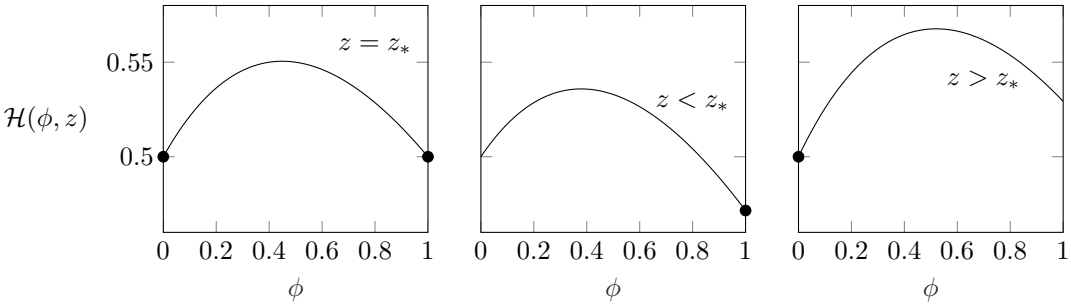

Figure 5.1: Energy profile as a function of the microscopic state ϕ for an applied load z. Black points indicate the microscopic state that minimizes the energy. Parameters are $\lambda = 1$, $\lambda_f = 1$ and $l = 1$.

In the presence of quenched disorder, the loading path defined by the global energy minimization produces several intermediate states and is deterministic for each realization of the quenched disorder. It can be reconstructed by comparing the energies of different equilibrium configurations at a given elongation z and choosing the configuration that minimizes the energy.

Contrary to the homogeneous case, it is now not possible to define analytically the transitions points z_k separating the different states. The main complications are associated with discrete minimization and the stochastic term S_k. However, when $N \gg 1$, we can obtain approximated results by recalling the statistical properties of order statistics, for details see Appendix A.

As the number of thresholds N increases, we can better and better approximate the sum S_k (the energy of dissociation of the first k elements) by an integral

$$S_k = \frac{1}{N}\sum_{i=0}^{k}\frac{\bar{x}_i^2}{2} \approx \int_{\bar{x}_1}^{\bar{x}_k}\frac{x^2}{2}dP(x) = \int_{\bar{x}_1}^{\bar{x}_k}\frac{x^2}{2}p(x)dx. \tag{5.4}$$

Behind this approximation is the fact that $k/N \to P(\bar{x}_k)$, for large N, and we can identify $dP(x)$ with $1/N$, to obtain $S_k \approx \int_{\bar{x}_1}^{\bar{x}_k}\frac{x^2}{2}p(x)dx$, where the lower limit of integration $\bar{x}_1$ is the first element of the ordered sequence $\bar{x}_k$. In Fig. 5.2 the quality of this approximation is illustrated for a set of thresholds drawn from a Weibull distribution.

We can now write the continuous approximation of the discrete energy, Eq. (4.8),

$$\mathcal{H}(x, z) = \frac{\lambda_f(1 - P(x))}{1 - P(x) + \Lambda}\frac{z^2}{2} + \int_0^x p(x')\frac{x'^2}{2}dx', \tag{5.5}$$

where

$$\Lambda = \frac{\lambda_f(\lambda + 1)}{\lambda}. \tag{5.6}$$

From the equilibrium equation $\partial\mathcal{H}(x, z)/\partial x = 0$ we obtain

$$-\frac{\lambda_f \Lambda p(x) z^2}{2(1 - P(x) + \Lambda)^2} + p(x)\frac{x^2}{2} = 0, \tag{5.7}$$

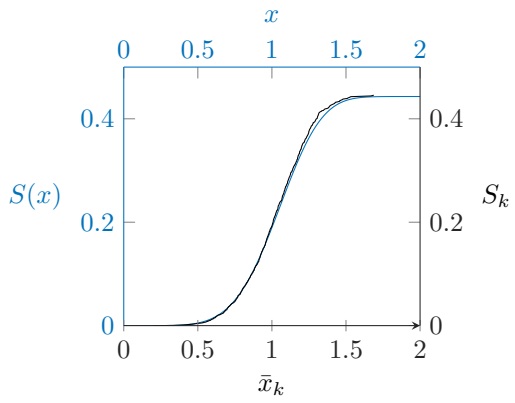

Figure 5.2: Comparison between S_k, composed of 1000 random variables drawn from a Weibul distributio, and the predicted $S(x)$.

which gives,

$$z = (1 - P(x) + \Lambda)\frac{x}{\sqrt{\lambda_f \Lambda}}. \tag{5.8}$$

The idea now is to find x for a given value of the external loading parameter z.

Even though we have performed the calculation using the large N limit, we would like to check how good is the approximation in the case of finite N. To this end, we rewrite the averaged equation, Eq. (5.8), in a discrete form, by assuming that the continuous variable x takes the discrete values $\bar{x}_k$. We obtain

$$z_k = (1 - k/N + \Lambda)\frac{\bar{x}_k}{\sqrt{\lambda_f \Lambda}}. \tag{5.9}$$

In Fig. 5.3, we substitute Eq. (5.9) into Eq. (4.8) in order to approximate the global minimum load path.

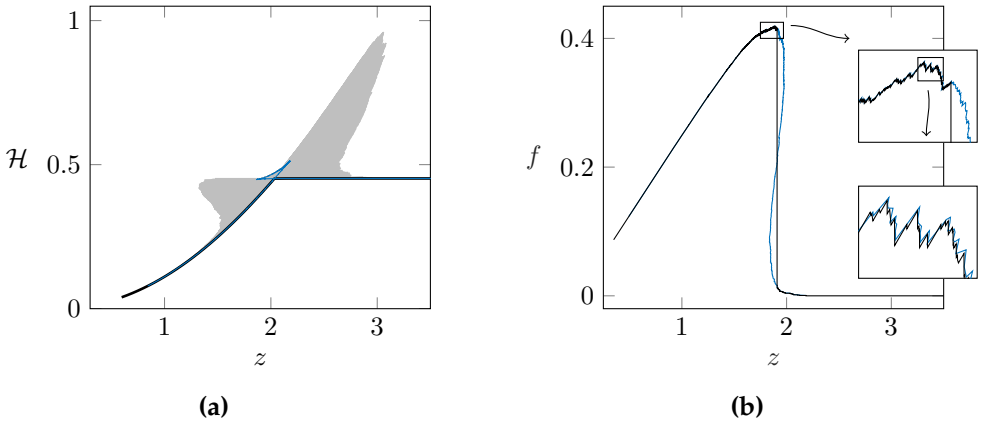

(a) **(b)**

Figure 5.3: (a) Energy-elongation relation, (b) force-elongation. In (a) the light gray region corresponds to the metastable states; (a) and (b): the black thick line is the load path following the global minimum of the energy, the blue curve is the global minimum path as predicted by Eq. (5.9). Parameters: $\rho = 5$, $\lambda = 1$, $\lambda_f = 0.4$, and $N = 500$.

In Fig. 5.3b, we compare in detail the outcome of the numerical global minimization with the theoretical expression, Eq. (5.9). We observe an overall agreement, even at finer scales, even though the approximate theory does not capture every single fluctuation. The theoretical expression is also not able to capture the big jump

associated with macroscopic collective debonding. The reason is that we need to complement the theoretical curve with a Maxwell line establishing the equality of the mechanical energies in the two coexisting states.

5.2 Marginal stability strategy

Observe that each microscopic configuration exists in an extended domain of the loading parameter z. The limiting points of these domains characterize the states with only marginal stability. In the presence of quenched disorder, the points of marginal stability combine into a response protocol that differs considerably from the one predicted by the global minimization (ground state) response. One of the main differences between the marginal path and the global minimum path is that in general the dissociation trajectory and the rebinding trajectory, which coincide in the case of global minimization, differ in the case of marginal minimization, generating a hysteresis loop.

Define z_k as the marginal stability points for the branch with k broken elements. In such branch, $N-k$ elements are still holding the load, experiencing a common elongation $\bar{x}_k$ (the threshold of the k'th element). The force on the bundle is therefore $(N-k)\lambda(y-\bar{x}_k) = N\lambda_f(z_k-y)$, and if we eliminate y using Eq. (4.5) we obtain

$$z_k = \frac{\lambda+1}{\lambda}[(1-\frac{k}{N})\frac{1}{\Lambda}+1]\bar{x}_k \tag{5.10}$$

where Λ is defined in Eq. (5.6).

In the same way, we can construct the sequence of external loading points describing the rebinding process

$$z_k = [(1+\frac{1-k}{N})\frac{1}{\Lambda}+1]\bar{x}_k. \tag{5.11}$$

We now recall that at an elongation x the expected number of broken bonds is $NP(x)$, thus only $N[1-P(x)]$ bonds carry the total load, which means that $\bar{F}(x) = N[1-P(x)]x$. The load per bond is then

$$\bar{f}(x) = [1-P(x)]x. \tag{5.12}$$

The average displacement $\bar{z}(x)$ at elongation x is easy to assess from Eq. (5.10) by using the Glivenko-Cantelli theorem, which ensures that the empirical cumulative distribution function (ECDF) $\hat{P}(x) = k/N$ converges with probability one to the CDF $P(x)$ for $N \gg 1$, see Appendix A. Moreover, the order statistics of $\bar{x}_k$ can be approximated by $P^{-1}\left(\frac{k}{N}\right)$, and hence $\bar{x}_k \to P^{-1}(P(x)) = x$. Now, Eq. (5.10) can be approximated by,

$$\bar{z}_f(x) = \frac{\lambda+1}{\lambda}([1-P(x)]\frac{1}{\Lambda}+1)x. \tag{5.13}$$

In Eq. (5.13) and Eq. (5.12) we can use the elongation x as a parameter to obtain the average force-elongation relation $\bar{f} = \bar{f}(\bar{z})$.

Recall that our parameter λ is responsible for the fact that loading and unloading paths do not coincide. Along the reverse path, the rebinding (healing) of the bonds, is described by the equation

$$\bar{z}_r(x) = \left[\left(1-P(x)\right)\frac{1}{\Lambda}+1\right]x. \tag{5.14}$$

The corresponding force can be found from

$$\bar{f}_r(x) = N\frac{\lambda}{\lambda+1}[1-P(x)]x. \tag{5.15}$$

The (averaged) breaking and healing paths along the maximum delay (marginal stability) paths as well as the global minimum path are illustrated in Fig. 5.4. We see here the important role played by the rigidity parameter λ_f. At a fixed disorder, the system fails continuously when λ_f is large, and we identify this regime in what follows as the *ductile* fracture. Instead, at small values of λ_f we observe a finite abrupt discontinuity and, in what follows, we associate such regimes with *brittle* fracture.

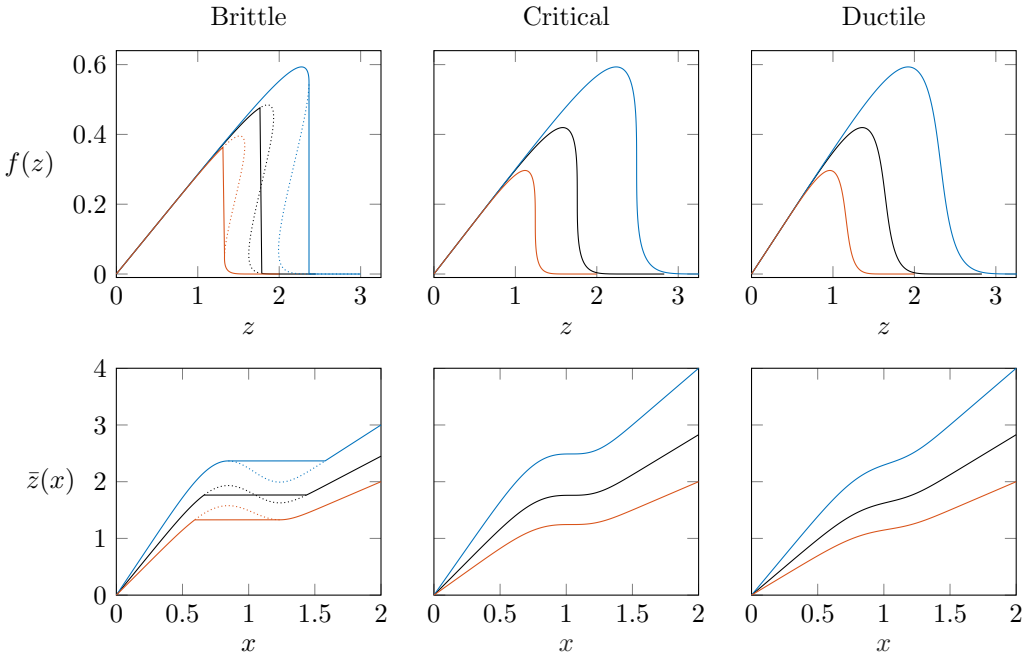

Figure 5.4: First row: force elongation, second row: external elongation as a function of internal variable x. The blue (red) curves correspond to the unbinding (rebinding) path in the MS strategy; The black curves correspond to the GM strategy.

Chapter 6

Brittle to ductile transition

We recall that brittle behavior in our description was associated with a discontinuity in the mechanical response, while ductile behavior was linked to a smooth, sequential breakdown of the system elements, Fig. 5.4. In this Chapter, we study how the rigidity of the system and the level of disorder influence the averaged response of the system, and show, in particular, that in the brittle regime the global minimization response is qualitatively different from the marginal stability response.

Since our averaged force-elongation curves are obtained from the parametric equations for $f(x)$ and $z(x)$, whenever we have a discontinuity in $f(z)$ we also have a discontinuity in $z(x)$. In other words, if at a fixed elongation z, we have multiple solutions x, satisfying (5.8), (5.13) or (5.14) we are in the brittle regime.

6.1 Marginal stability response

We first need to find the roots of the equation $\partial \bar{z}_f(x)/\partial x = 0$, where $\bar{z}_f(x)$ is given by Eq. (5.13). Suppose that the value at the local maximum is z_* and it is achieved at x_* which solves the equation

$$[1 - P(x_*)] - p(x_*)x_* + \Lambda = 0. \tag{6.1}$$

The existence of a maximum z_* in the averaged response is a fingerprint of a system size collective debonding event as it can be seen in Fig. 5.4 and Fig. 4.4a. The existence of such point is then a signature of the brittle behavior. We shall then associate brittle behavior with the case when there exist multiple solutions x_c of Eq. (6.1).

The critical regime, separating brittle from ductile behavior then corresponds to the case when the solution x_c to Eq. (6.1) is an inflection point, which is equivalent to the condition that the two solutions merge into one. Therefore, the point x_c is an inflection point if $\partial^2 \bar{z}_m(x_c)/\partial x^2 = 0$, which can be rewritten as

$$-2p(x_c) - p'(x_c)x_c = 0. \tag{6.2}$$

Therefore, we can find the critical line on the phase diagram implicitly from Eq. (6.1) and Eq. (6.2). If we define the auxiliary function,

$$\Psi_m(\Lambda, p(x_c)) = \begin{cases} [1 - P(x_c)] - p(x_c)x_c + \Lambda \\ -2p(x_c) - p'(x_c)x_c \end{cases} \tag{6.3}$$

the critical condition can be compactly written as $\Psi_m(\Lambda, p(x_c) = 0$.

6.2 Global minimization response

It is easy to see that whenever the system is brittle in the marginal stability response, it is also brittle in the global minimum response. However, the maximum on the

curve $\bar{z}_g(x)$ corresponding to the global minimization path is absent in the brittle regime, because the system switches configuration before such spinodal point is reached. In the 'Brittle' column of Fig. 5.4, the black line corresponds to the collective debonding chosen by the Maxwell construction.

According to Eq. (5.8) the condition for a local maximum of $\bar{z}_g(x)$ is

$$[1 - P(x_c)] - p(x_c)x_c + \Lambda = 0, \tag{6.4}$$

which is exactly Eq. (6.1), in the case of marginal stability path. Similarly, the condition for an inflection point is $-2p(x_c) - p'(x_c)x = 0$. Hence, the critical surface separating brittle from ductile is independent of the loading protocol, and we can again define it by the relation $\Psi_g(\Lambda, p(x_c)) = 0$, where

$$\Psi_g(\Lambda, p(x_c)) = \begin{cases} [1 - P(x_c)] - p(x_c)x_c + \Lambda \\ -2p(x_c) - p'(x_c)x \end{cases} . \tag{6.5}$$

To illustrate these results, we use a Weibull distribution of thresholds, see app. C. In this case, we can solve Eq. (6.1) explicitly to obtain

$$x_c = \left(\frac{1}{\rho} - W\left(-\Lambda \frac{e^{1/\rho}}{\rho} \right) \right)^{1/\rho} , \tag{6.6}$$

where $W(x)$ is the Lambert function, defined by the equation $x = W(x)e^{W(x)}$. Since this function is not injective, the relation $W(x)$ is multivalued everywhere except zero. This function is defined for $x \geq -1/e$, which gives the inequality

$$\Lambda \leq e^{-\frac{1}{\rho}-1}\rho. \tag{6.7}$$

This relation defines, in the averaged description, the boundary between the brittle and ductile regimes, see Fig. 6.2. Fig. 6.1 (b) shows the values of the critical tension f_c for the fixed disorder ρ and varying rigidity parameter Λ. The point Λ_c where the two curves meet marks the transition between brittle and ductile behavior.

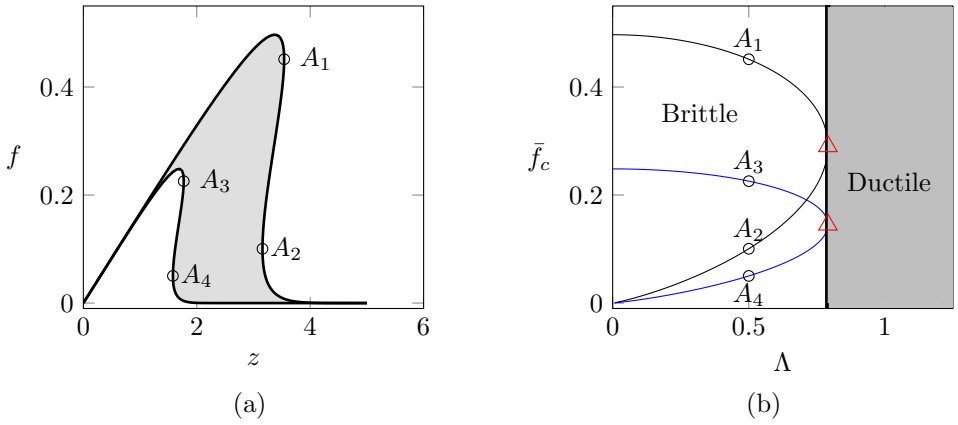

Figure 6.1: (a) Typical stress-strain behavior in the brittle regime ($\Lambda = 0.5$). In the hard device loading A_1, A_2 are the spinodal points for the forward loading path, while A_3, A_4 are the spinodal points for the unloading path. (b) Brittle to ductile transition at $\rho = 3$.

We observe that in the brittle regime, when, for instance, along the loading path the control parameter z reaches the value corresponding to point A_1 in Fig. 6.1a the

system undergoes a collective debonding. Similar collective bonding takes place at the value of the control parameter z corresponding to point A_4. In the ductile regimes, such jumps are absent, and the evolution of the system is gradual. The behavior of the spinodal stress at points A_1 and A_4, as a function of the rigidity Λ, shows that the loading and unloading critical points coincide and describe super-critical pitchfork bifurcations. The corresponding phase diagram in the space rigidity-disorder is presented in Fig. 6.2, for the case of Weibull distribution.

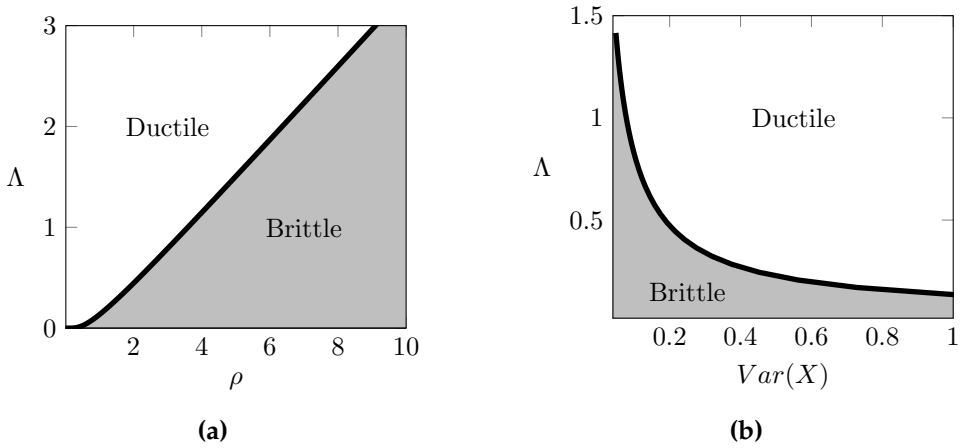

Figure 6.2: The phase diagram constructed based on Eq (6.7). In (a) we use the shape parameter ρ of the Weibull distribution as the measure of disorder. In (b) we used the variance of the Weibull distribution as the disorder coordinate.

6.3 Conclusions

We studied here the averaged mechanical behavior of a parallel bundle of breakable units that can both debond and rebind. The inner spring with stiffness λ placed in series with the breakable element is responsible for creating a domain of metastability as one varies the applied load z. The external stiffness λ_f can be understood as the measure of the interaction among the elements, the bigger the λ_f, the less sensitive the binders are to a change in the configuration of their neighbors.

We focused on the differences in the mechanical response to loading between homogeneous and disordered systems. The homogeneous system responds as an equivalent linear spring up to the rupture point, where all bonds break simultaneously. The introduction of a quenched disorder is responsible for the force-elongation curve exhibiting intermittent breaking events involving collective debonding of many springs. Since disorder tends to desynchronize the bonds, we observed a crossover from correlated debonding at small disorder to uncorrelated debonding at large disorder. We interpreted this crossover as a brittle to ductile transition.

We characterized these two main types of behavior in the case of two dynamic strategies: marginally stable response when the system is always minimally stable and the global minimization response when the system is always maximally stable. We were able to describe the critical transition between brittle and ductile behaviors for both types of responses analytically. We constructed the phase diagram in the disorder-rigidity plane for the averaged behavior of the system, showing that the larger is the disorder (larger is its variance), the more ductile the system is. Ductility

can also be achieved by decreasing the degree of interaction/connectivity among individual binders measured by our rigidity parameter (achieved by increasing λ_f).

Chapter 7

Avalanche distribution

In the previous Chapter we focused on the average behavior of the large system, thus neglecting fluctuations that take place at a small scale. In this Chapter, we change focus and study the statistics of avalanches as the system is continuously driven in the hard loading device.

It will be even more important for us now that an athermal fracture can be modeled in two ways: as an incremental energy minimization phenomenon (Francfort and Marigo, 1998; Bourdin, Francfort, and Marigo, 2008) and as incremental marginal equilibration phenomenon (Selinger, Wang, and Gelbart, 1991; Wang et al., 1991). We study the distribution of avalanches in both equilibrated systems (global minimum strategy) and the out-of-equilibrium system (marginal stability strategy). We justify analytically our numerical simulations showing rather different statistics of avalanches for brittle, ductile and critical systems. We derive explicit formulas for the power law exponents of the avalanche distribution in the brittle and critical regimes using asymptotic analysis and show that they are fundamentally different, distinguishing spinodal from critical fracture. Critical exponents were found to be the same for both types of responses, which is in agreement with numerical simulations for a finite size bundle and agrees with general predictions for mean-field theories.

7.1 Marginally stable response

In Fig. 7.1a we present a typical force-elongation curve showing the marginal response of a small bundle with only five elements. The endpoints of the metastable branches, z_k, which define such limiting out-of-equilibrium path, are given by Eq. (5.10). We see that after the first element breaks the system skips one metastable branch before it reaches the stable one, as a result of an avalanche of size one. As the load increases further the next marginal stable endpoint z_3 is reached, and the system jumps to the new configuration, breaking at once two more elements, and thus exhibiting an avalanche of size two.

We see that the occurrence of avalanches can be predicted if we know of the breaking sequence $\{z_k\}$. It is easy to see that the sequence $\{z_k\}$ is not monotonically increasing or decreasing and instead exhibits random oscillations. From Eq. (5.10) we see that the sequence z_k is the product of a monotonically increasing fluctuating factor $\bar{x}_k$[1] and a monotonically decreasing factor $(N-k)$, not counting a constant. Suppose that an applied displacement z 'endangers' the configuration with $k-1$ already dissociated bonds. This is equivalent to saying that $z_k > z > z_j$, for all $j < k$. Assume that $z_{k+j} \leq z_k$, with $j = 1, 2, \ldots, \Delta - 1$, but $z_{k+\Delta} > z_k$, which means that all the fibers characterized by the thresholds $z_k, z_{k+1}, \ldots, z_{k+\Delta-1}$ will

[1] Recall that $\bar{x}_k$ is the ordered sequence of breaking thresholds.

break simultaneously at the same value of the external load. Such a synchronous failure will be interpreted as an avalanche of size Δ that takes place because of the collective redistribution of the load. We are interested in the expected number of bursts D of size Δ. The burst counting method involved in the construction of the function $D(\Delta)$ is illustrated in the Fig. 7.1b.

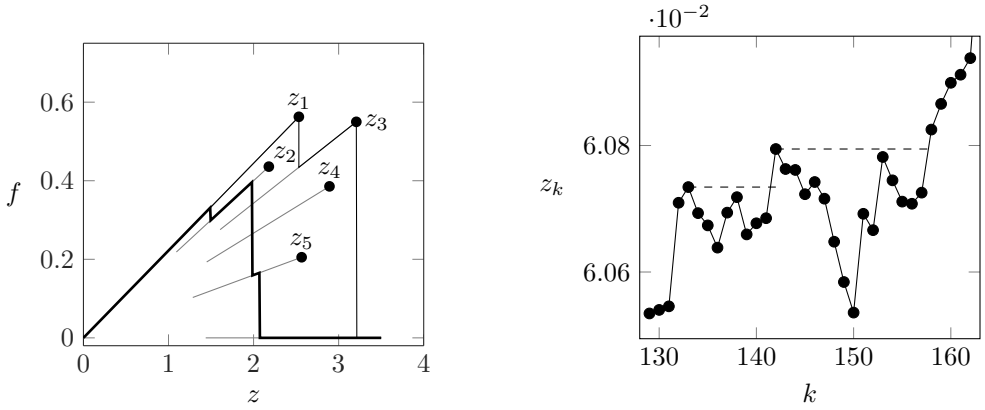

Figure 7.1: (a) Load path for a system with $N = 5$. (b) Fluctuations of the burst thresholds z_k for a bundle containing $N = 1000$ in the window with $129 \leq k \leq 162$. The first dashed black line ilustrates a burst of size $\Delta = 8$ and the second line marks a burst of size $\Delta = 15$.

For a standard democratic FBM loaded in a soft device, it has been shown analytically that in the limit of infinite number of elements, the distribution of avalanches is a power law[2] $D(\Delta)/N \propto \Delta^{-\xi}$ with the exponent $\xi = 5/2$, see (Pradhan, Hansen, and Chakrabarti, 2010) for more detail. In Fig. 7.2, we present the empirical (found numerically) avalanche distribution in our augmented FBM loaded in the hard device in the brittle ($\lambda_f = 0.4$), critical ($\lambda_f = 0.573$) and ductile ($\lambda_f = 0.75$) regimes under the assumption of 'maximum delay' dynamics. In the brittle regime, we found the power law with exponent $5/2$, the same one as in the classical FBM, however, the distribution is only super-critical because of the presence of the peak, representing system size events associated with brittleness. In the critical regime, we observe the power law with exponent $9/4$, which was not known in the classical FBM. Finally, in the ductile regime, the distribution is a power law only for very small events but then exhibits an exponential decay characteristic for Gaussian distribution.

7.2 Maximally stable response

Consider now the same system exhibiting global minimization (equilibrium) response. We can again obtain numerically the force-elongation curve and study the statistics of avalanches in the same way as it was done in the marginal (out of equilibrium) response case.

Our numerical experiments show that the overall structure for the breaking sequence along the global minimum path is similar to the one in the out-of-equilibrium

[2]We define the cumulative probability function of the avalanches $\mathbb{P}(\Delta)$ as the probability of observing avalanches greater than or equal Δ. As opposed to $D(\Delta)/N$, which is the point probability of finding an avalanche of size Δ. Fig. 7.2 shows the probability $D(\Delta)/N$ of finding an avalanche of size Δ in the out-of-equilibrium load path.

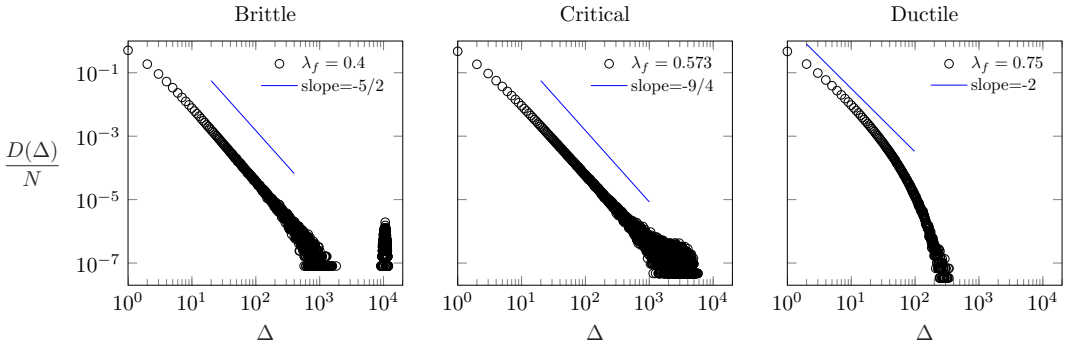

Figure 7.2: Avalanche distribution for a system with $N = 20000$ fibers, $\lambda = 1$ and thresholds following a Weibull distribution with $l = 1$ and $\rho = 4$. The distribution is averaged over 10000 realizations of the disorder. (From left to write: Brittle, critical and ductile)

case. For instance, the avalanche statistics in the critical and ductile regimes is identical to the one in the out-of-equilibrium system. However, as we can see in Fig. 7.3, the statistics for the brittle regime differs. While in the out-of-equilibrium case we see a power law with a peak, in the global minimization response we see a power law with exponential decay followed by a peak. The reason is that in the latter case the system collectively debonds before it reaches the state where the stiffness diverges.

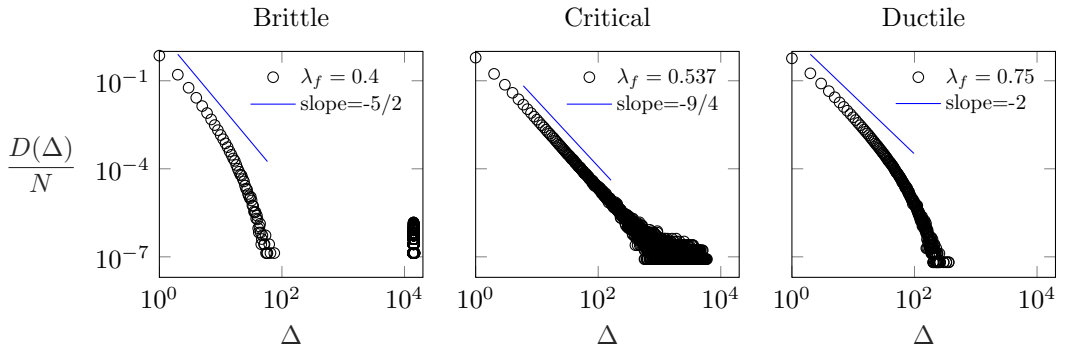

Figure 7.3: Avalanche distribution in the global minimum dynamic strategy. The left figures shows avalanches for system in brittle regime, the central figure shows avalanches for the critical system and the right figure shows avalanches for the ductile regime. It was realized 2000 experiments in a bundle of $N = 20000$ fibers with thresholds following the one dimensional Weibull distribution $P(x) = 1 - \exp(-x^\rho)$, with $\rho = 4$. (From left to write: Brittle, critical and ductile)

7.3 Analytical study of the avalanche distribution

To derive the avalanche distribution in a length-controlled ensemble, we follow the work of Hansen and collaborators, who studied the case of the classical, force-controlled FBM (Hansen, Hemmer, and Pradhan, 2015; Hansen and Hemmer, 1994; Hemmer and Hansen, 1992; M. Kloster and Hemmer, 1997; Pradhan, Hansen, and Chakrabarti, 2010).

To determine the statistics of the avalanches, it is sufficient to know the sequence z_k of transition points. Here we present the derivation for the *out-of-equilibrium* loading (debonding) path; it will be clear that the procedure remains valid for the rebinding process and the global minimization path, see below. The differences between the out-of-equilibrium and global minimization responses will be highlighted in the asymptotic analysis, where we would need to differentiate them particularly in the brittle regime.

Recall that when the k'th element is about to debond, the total elongation per fiber is given by[3]

$$z_k = \frac{\lambda+1}{\lambda N\Lambda}[N-k+N\Lambda]\bar{x}_k \tag{7.1}$$

For an avalanche of size Δ to start when the kth fiber is about to debond the following two condition must be satisfied. The first condition will be called the *forward condition* because it says that $\Delta-1$ fibers will fail after the breaking of the kth fiber. More specifically, this condition states that

$$z_{k+j} \leq z_k, \text{ for } j = 1, 2, \ldots, \Delta-1 \tag{7.2}$$

and

$$z_{k+\Delta} > z_k. \tag{7.3}$$

We must also secure that z_k is larger than all the previous thresholds so that the current avalanche is not a part of a bigger one. The corresponding condition, which we call the *backward condition*, reads

$$z_j \leq z_k, \text{ for all } j < k. \tag{7.4}$$

Since we are interested in the asymptotics for the avalanche distribution at large N, we assume that during the avalanche of size Δ, the involved thresholds cover just a small part of the total range of the thresholds and therefore $\Delta \ll N$. Using Eq. (7.1) in the forward and in the backward conditions we can obtain similar relations for the ordered thresholds $\bar{x}_i$. Thus

$$z_{k+j} \gtrless z_k \tag{7.5}$$

is equivalent to

$$\bar{x}_{k+j} \gtrless \bar{x}_k \frac{N-k+N\Lambda}{N-k-j+N\Lambda} \tag{7.6}$$

which can be also rewritten as

$$\bar{x}_{k+j} \gtrless \bar{x}_k \left(1 + \frac{j}{N-k-j+N\Lambda}\right). \tag{7.7}$$

Defining $\delta_k = \dfrac{\bar{x}_k}{N-k-j+N\Lambda} \simeq \dfrac{\bar{x}_k}{N-k+N\Lambda}$, and using the assumption that $j \ll N-k$, we can simplify the above relation further, obtaining

$$z_{k+j} \gtrless z_k \Leftrightarrow \bar{x}_{k+j} \gtrless \bar{x}_k + j\delta_k \tag{7.8}$$

Because the breaking sequence for the rebinding process is $z_k^r = \frac{\lambda}{\lambda+1} z_k$, the condition $z_{k+j}^r \gtrless z_k^r$ leads to the same relation in terms of the ordered thresholds $\bar{x}_k$;

[3] Refer to Eq. (5.10) for the breaking along the out-of-equilibrium path, to Eq. (5.11) in the case of rebinding and to Eq. (5.9) for the global minimization path. From our combinatorial argument, it will be clear why any of the three relations could be used to obtain the distribution of avalanches. Special care in the final steps is necessary as one considers out-of-equilibrium or global minimization path.

therefore, the procedure remains valid for the rebinding process. Moreover, assuming that for the maximally stable response we can describe the breaking sequence z_k^g from Eq. (5.9), it is easy to see that $z_k^g = z_k\sqrt{\frac{\lambda}{\lambda+1}}$ and the procedure will also be valid in the maximally stable regime.

Now we note that breaking of one fiber at the elongation z_k, corresponding to a threshold $\bar{x}_k = x$, raises the load on the remaining fiber by δ_k. The average number of fibers that breaks as a result of this load increase is equal to the number of thresholds in the interval $(x, x+\delta_k)$, which is $Np(x)\delta_k$. Thus, the average number of fibers breaking as a result of the failure of the kth fiber is,

$$g(x) = \frac{p(x)x}{1 - P(x) + \Lambda} \tag{7.9}$$

We used here that $k/N = P(x)$. If $g(x) > 1$ the current failure would produce further failures. Recall that the condition $g(x) = 1$, or $1 - P(x) + \Lambda - p(x)x = 0$, means that there exists a local maximum on the $z(x)$ curve, see Eq. (6.1), and therefore the condition $g(x) \leq 1$ characterizes the ductile regime where the function $z(x)$ is monotone.

For an avalanche of size Δ, the increase in load will be approximate $\Delta\delta$, which implies the average number $g(x)\Delta$ of breaking fibers. The probability that the additional $\Delta - 1$ fibers break is then given by a Poisson distribution[4] with the rate $g(x)\Delta$,

$$\frac{(g(x)\Delta)^{\Delta-1}}{(\Delta-1)!}e^{-g(x)\Delta} \tag{7.10}$$

We still need to secure that all the $\Delta - 1$ inequalities of the forward condition

$$\begin{aligned} \bar{x}_{k+1} &< x + \delta_k \\ \bar{x}_{k+2} &< x + 2\delta_k \\ &\vdots \\ \bar{x}_{k+\Delta-1} &< x + (\Delta-1)\delta_k \end{aligned} \tag{7.11}$$

holds. We can visualize these inequalities in the figure

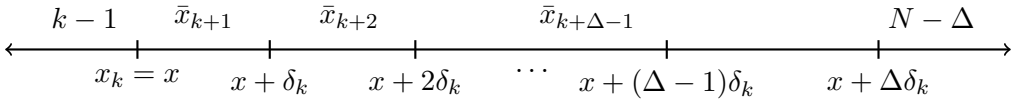

This figure can be interpreted as follows. We divide the interval $(x, x+\Delta\delta_k)$ into Δ intervals of size δ_k. For the forward condition to be satisfied we must have at least one threshold value in the first interval $(x, x+\delta_k)$, at least two in the first two intervals, and at least $\Delta - 1$ in the first $\Delta - 1$ intervals. There should be no threshold values in the last interval $(x+(\Delta-1)\delta_k, x+\Delta\delta_k)$ to ensure that $z_{k+\Delta} > z_k$.

To summarize, we obtain the following combinatorial problem: distribute $\Delta - 1$ balls randomly in Δ numbered boxes. Find the probability that there are at least h balls in the first h boxes taken together, for $h = 1, \ldots, \Delta - 1$, while the last one is empty. As argued in (Hansen, Hemmer, and Pradhan, 2015), the condition that there is at least one ball in the first box implies that there should be at most $\Delta - 2$ balls in the last $\Delta - 1$ boxes. At least two balls in the first two boxes implies at most

[4] If the number n of fibers that break as a consequence of the failure of a fiber k is independent of the previous events and the failure takes place at a rate r the probability distribution of the events is given by the Poisson distribution $p(n) = \frac{r^n}{n!}e^{-r}$ (Hansen, Hemmer, and Pradhan, 2015).

$\Delta - 3$ balls in the last $\Delta - 2$ boxes, and so on. This problem is stated and resolved in the Appendix B, where it is shown that the answer to our combinatorial problem is,

$$p_{\Delta-1,\Delta} = \frac{1}{\Delta}. \tag{7.12}$$

Hence, the forward condition imposes the following general structure on the probability distribution of avalanches

$$\mathcal{P}_f = \frac{(g(x)\Delta)^{\Delta-1}}{\Delta!} e^{-g(x)\Delta}. \tag{7.13}$$

Now, the remaining backward condition states that z_k must be bigger than its predecessors, which is necessary to ensure that the avalanche actually starts at the z_k, and that it is not a part of a larger avalanche starting with another weaker element. Consider a finite number d of such elements, $k-1, k-2, \ldots, k-d$ and compute the probability $\psi(d, x, k)$ that none of the values $z_{k-1}, z_{k-2}, \cdots, z_{k-d}$ exceeds z_k, for $d \ll N$. According to (7.8), this condition is equivalent to

$$\begin{aligned} \bar{x}_{k-1} &< x - \delta_k \\ \bar{x}_{k-2} &< x - 2\delta_k \\ &\vdots \\ \bar{x}_{k-d} &< x - d\delta_k \end{aligned} \tag{7.14}$$

If there are no thresholds in $(x - \delta_k, x)$, at most one in $(x - 2\delta_k, x)$, at most two in $(x - 3\delta_k, x), \ldots$, and at most $d - 1$ in $(x - d\delta_k, x)$, then all the inequalities (7.14) are fulfilled. This implies that the number h, not exceeding $d-1$, must be in the interval $(x - d\delta_k, x - \delta_k)$, while all the remaining $k - 1 - h$ thresholds must be smaller than $x - d\delta_k$. As in the case of the forward condition, the probability of finding h elements in the interval $(x - d\delta_k, x)$ is given by a Poisson distribution,

$$\frac{(g(x)d)^h}{h!} e^{-g(x)d}. \tag{7.15}$$

We still have to secure that all conditions (7.14) are satisfied. Consider a uniform probability distribution in the interval $(x - d\delta_k, x)$, and divide it in d small intervals of size δ_k. We can now compute the probability that h thresholds are randomly distributed among these d intervals such that no threshold value lies in the interval $(x - \delta_k, x)$, at most one in the interval $(x - 2\delta_k, x - \delta_k)$, at most two in the interval $(x - 3\delta_k, x - 2\delta_k)$, and so on (Hansen, Hemmer, and Pradhan, 2015). This is again a combinatorial problem that can be stated as follows: having d numbered slots, what is the probability of distributing h particles among these slots in such a way that the first slot contains no particles, the second slot contains at most one particle, and in general, the slot number n contains at most $n - 1$ particles. The solution to this problem is given in Appendix B and the desired probability is

$$p_{h,d} = 1 - \frac{h}{d}. \tag{7.16}$$

Now, the probability distribution imposed by the backward condition is the product of equations (7.16) and (7.15). If we sum over the allowed values of h we obtain,

$$\mathcal{P}_b = e^{-gd} \sum_{h=0}^{d-1} \frac{(gd)^h}{h!d} (d - h), \tag{7.17}$$

Rearranging the summation in Eq. (7.17) we can re-write it as,

$$\mathcal{P}_b = (1-g)\, e^{-gd} \sum_{h=0}^{d-1} \frac{(gd)^h}{h!} + e^{-gd} \frac{(gd)^h}{d!}. \tag{7.18}$$

Finally, we need to take the limit $d \to \infty$. First note that $\sum_{h=0}^{d-1} \frac{(gd)^h}{h!} \to e^{gd}$. In the last term, we can use Stirling approximation $d! \approx d^d e^{-d}\sqrt{2\pi d}$ to show that it vanishes for $g \leq 1$. Then we can write

$$\mathcal{P}_b = 1 - g = 1 - \frac{xp(x)}{1 - P(x) + \Lambda}. \tag{7.19}$$

The probability of the avalanche of size Δ starting at the element k with the threshold value $x_k = x$ can be now written as the product of the forward (7.13) and the backward (7.19) probabilities,

$$\frac{\Delta^{\Delta-1}}{\Delta!} g(x)^{\Delta-1} e^{-\Delta g(x)} (1 - g(x)), \tag{7.20}$$

where $g(x) = p(x)x/(1-P(x)+\Lambda)$. Since the number of elements with thresholds in $(x, x+dx)$ is $Np(x)dx$, the number of avalanches of size Δ starting inside $(x, x+dx)$ is given by

$$\Phi(\Delta, x) = \frac{\Delta^{\Delta-1}}{\Delta!} g(x)^{\Delta-1} e^{-\Delta g(x)} (1 - g(x)) N p(x) dx. \tag{7.21}$$

In order to compute $D(\Delta)$, the total number of avalanches of size Δ, we have to integrate over all the possible values of x. The final expression for the avalanche distribution takes the form

$$\begin{aligned} \frac{D(\Delta)}{N} = & \int_0^{x_c} \frac{\Delta^{\Delta-1}}{\Delta!} \left[\frac{p(x)\, x}{1 - P(x) + \Lambda}\right]^{\Delta-1} \\ & \times \exp\left[-\Delta \frac{p(x)\, x}{1 - P(x) + \Lambda}\right] \left[1 - \frac{p(x)\, x}{1 - P(x) + \Lambda}\right] p(x) dx, \end{aligned} \tag{7.22}$$

where x_c is the critical threshold where the (local) maximum of the averaged curve $z(x)$ is achieved.[5] In other words, we consider only the distribution of thresholds prior to the system size avalanche characterizing the brittle regime. As indicated at the beginning of this Section, the obtained relation is valid for both out-of-equilibrium and equilibrium paths.

Note that the distribution (7.22) is similar to the distribution obtained in the classical FBM for the case of applied force (Hansen, Hemmer, and Pradhan, 2015; Hemmer and Hansen, 1992; Halász and Kun, 2010), except for the appearance of quantity Λ, which describe the system's rigidity and can differentiate and ductile behaviors. Numerical simulations, Fig. 7.2 and Fig. 7.3, suggest different avalanches distributions in different regimes and loading protocols and the analysis of Eq. (7.22) should confirm these empirical observations.

7.4 Asymptotic analysis

To capture all of the observed distributions we need to conduct an asymptotic analysis of Eq. (7.22) focusing on the tail of the distribution $D(\Delta)/N$ when $N \to \infty$.

[5] Such maximum is given by the solution of Eq. (6.1). For the ductile case, the domain of integration covers the whole domain of existence of thresholds

The results for the critical and ductile regimes will be similar for out-of-equilibrium and equilibrium protocols. In the brittle regime, we would need to treat each case separately.

We first rewrite Eq. (7.22) as

$$\frac{D\left(\Delta\right)}{N} = \frac{\Delta^{\Delta-1}}{\Delta!}\int_0^{x_c} \phi(x) e^{[-g(x)+\ln g(x)]\Delta} dx \tag{7.23}$$

where $\phi(x) = \left[1-g(x)\right]\dfrac{p(x)}{g(x)}$ and $g(x) = \dfrac{p\left(x\right)x}{1-P(x)+\Lambda}$.

We then use the standard saddle-point approximation by focusing on the global minimum of the function $h(x) = g(x) - \ln g(x)$. If the minimum, say $x = x_0$, exists then for large Δ the main contribution to the integral will come from the vicinity of x_0. To find x_0, we need to solve the equation

$$h'(x) = \frac{g'(x)}{g(x)}(g(x)-1) = 0. \tag{7.24}$$

The two classes of solutions are obtained if either $g(x_0) = 1$ or $g'(x_0) = 0$, which leads to three possibilities,

1. $g(x_0) \neq 1$ and $g'(x_0) = 0$,
2. $g(x_0) = 1$ and $g'(x_0) = 0$ and
3. $g(x_0) = 1$ and $g'(x_0) \neq 0$.

Not surprisingly, these different possibilities are related to our three regimes with a different mechanical response: brittle, critical and ductile.

Indeed, the condition $g(x_0) = 1$ is equivalent to,

$$p(x_0)x_0 = 1 - P(x_0) + \Lambda. \tag{7.25}$$

This is our condition of brittleness, derived based on the averaged behavior of the system, see Eq. (6.1). The condition $g'(x_0) = 0$ can be rewritten as

$$\frac{2}{x_0} + \frac{p'(x_0)}{p(x_0)} = 0, \tag{7.26}$$

and is therefore equivalent to the condition $\partial^2 \bar{z}(x)/\partial x^2 = 0$. This is a signature of an inflection point on the $z(x)$ curve, which, in the absence of a local maximum, $g(x_0) \neq 1$, is a characteristic of ductile response. When both conditions $g(x_0) = 1$ and $g'(x_0) = 0$ are met, we have critical behavior: a crossover between brittle and ductile regimes. While for the marginal, out-of-equilibrium response all three possibilities can be realized, we saw, while studying the averaged behavior, that in the brittle regime the global minimum response is characterized by a jump taking place before the local maximum on the $z(x)$ curve is reached.

We now turn to the study of the avalanche distribution in these three regimes. Suppose first that we are in the situation when the minimum of $h(x)$ is defined by the conditions $g'(x_0) = 0$ and $g(x_0) \neq 1$. We can then write,

$$h(x) \approx g(x_0) - \ln g(x_0) + \frac{g''(x_0)}{2g(x_0)}(g(x_0)-1)(x-x_0)^2. \tag{7.27}$$

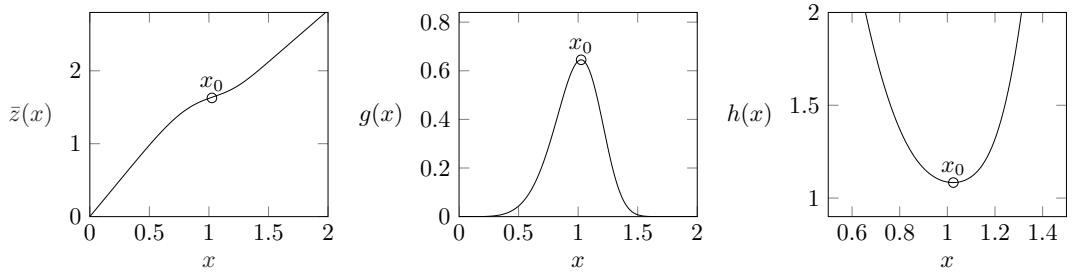

Figure 7.4: Behavior of the functions $z(x)$, $g(x)$ and $h(x)$ when the system is in the ductile regime.

Then the direct application of the saddle-point approximation in (7.23) gives

$$\frac{D\left(\Delta\right)}{N} = \frac{\Delta^{\Delta-1}}{\Delta!} e^{-\Delta h(x_0)} \phi(x_0) \sqrt{\frac{2\pi}{\Delta |h''(x_0)|}} \propto \Delta^{-2} e^{-\Delta(h(x_0)-1)}. \tag{7.28}$$

Here the asymptotic behavior of the distribution is clearly dominated by an exponential cut-off. We are then in the ductile regime which can be seen in Fig. 7.8 where the pair (ρ, Λ) should be above the critical line. It is interesting to note the initial power law slope of -2 relevant for small Δ, is recovered by our asymptotic analysis (7.28) as well as the subsequent exponential cut-off.

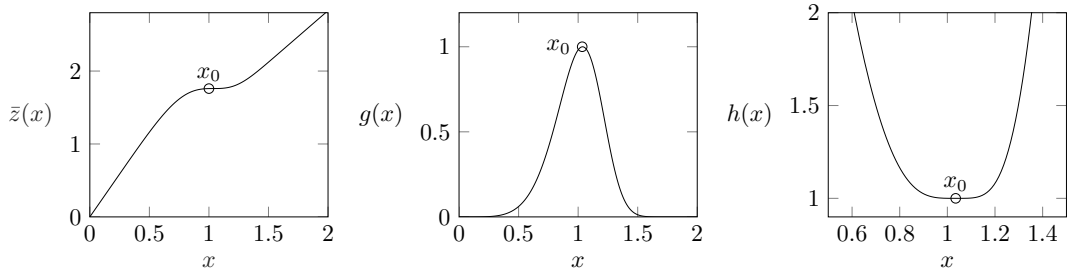

Figure 7.5: Behavior of the functions $z(x)$, $g(x)$ and $h(x)$ when the system is in the critical regime.

The next special case is when simultaneously $g(x_0) = 1$ and $g'(x_0) = 0$. Since then $h''(x_0) = 0$, higher order terms have to be included into the expansion of the function $h(x)$. The third derivative term also vanishes $h'''(x_0) = g^{(3)}(x_0) - \frac{g^{(3)}(x_0)}{g(x_0)} - \frac{2g'(x_0)^3}{g(x_0)^3} + \frac{3g'(x_0)g''(x_0)}{g(x_0)^2} = 0$ and therefore the Taylor approximation of $h(x)$ starts with the fourth order term

$$h(x) \approx \frac{h^{(4)}(x_0)}{4!}(x - x_0)^4. \tag{7.29}$$

Here,

$$\begin{aligned} h^{(4)}(x_0) &= g^{(4)}(x_0) - \frac{g^{(4)}(x_0)}{g(x_0)} + \frac{3g''(x_0)^2}{g(x_0)^2} + \frac{6g'(x_0)^4}{g(x_0)^4} + \frac{4g^{(3)}(x_0)g'(x_0)}{g(x_0)^2} - \frac{12g'(x_0)^2 g''(x_0)}{g(x_0)^3} \\ &= 3g''(x_0)^2. \end{aligned} \tag{7.30}$$

Moreover, we can write

$$\phi(x) \approx \frac{\phi''(x_0)}{2}(x - x_0)^2,$$

with $\phi''(x_0) = -p(x_0)g''(x_0)$, which allows us to re-write the integral (7.23) as

$$\frac{D(\Delta)}{N} = \frac{\Delta^{\Delta-1}}{\Delta!}e^{-\Delta}\int_0^{x_0} -p(x_0)g''(x_0)(x-x_0)^2 e^{-\Delta\frac{3g''(x_0)^2}{4!}(x-x_0)^4}dx. \tag{7.31}$$

Computing the integral explicitly we obtain

$$\frac{D(\Delta)}{N} = \frac{\Delta^{-3/2}}{\sqrt{2\pi}}\frac{p(x_0)g''(x_0)}{4\left(\Delta\frac{3g''(x_0)^2}{4!}\right)^{3/4}}\Gamma\left(\frac{3}{4}, \Delta\frac{3g''(x_0)^2}{4!}(x-x_0)^4\right)\Bigg|_0^{x_0}. \tag{7.32}$$

Here we introduced the incomplete gamma function $\Gamma(s,x) = \int_x^\infty t^{s-1}e^{-t}dt$. The lower limit of the integral does not contribute when Δ is large and we can write the following asymptotic representation for the avalanche size distribution,

$$\frac{D(\Delta)}{N} = C\Delta^{-9/4}, \tag{7.33}$$

where $C = \frac{p(x_0)\sqrt[4]{2}}{\sqrt{2\pi g''(x_0)}}\Gamma\left(\frac{3}{4}\right)$. In particular, this result suggests that the universality classes of equilibrium and out-of-equilibrium systems are the same. Similar equivalence has been previously proven for the random-field Ising model (Balog, Tissier, and Tarjus, 2014).

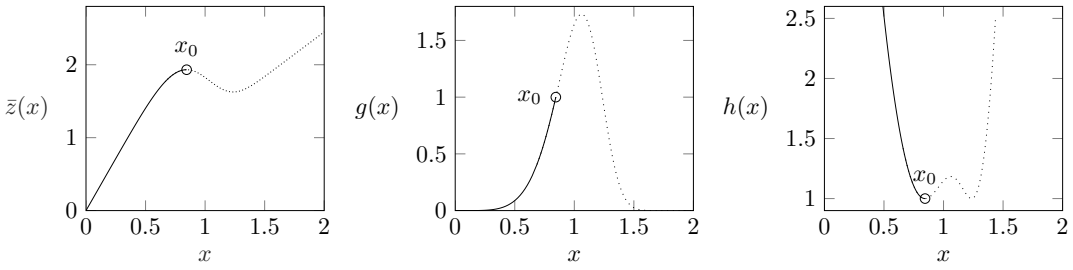

Figure 7.6: Behavior of the functions $z(x)$, $g(x)$ and $h(x)$ when the system is in the brittle regime in the marginally stable response.

Finally, we turn to the study of the case when x_0 is the root of the equation $g(x_0) = 1$. This condition can be rewritten as $1 - P(x_0) + \Lambda - xp(x_0) = 0$, and we observe that it is precisely Eq. (6.1), which is the condition of brittle behavior. The avalanches are then counted until the point x_0 where the system undergoes a system size collective debonding (snap event).

Consider the expansion $h''(x) = g''(x) + \frac{g'(x)^2 - g(x)g''(x)}{g(x)^2}$. The conditions $g(x_0) = 1$ and $g'(x_0) \neq 0$ ensure that $h''(x_0) = g'(x_0)^2 > 0$, when we deal with a local minimum. We then expand the function $h(x) = g(x) - \ln g(x)$ up to second order to obtain

$$h(x) \approx h(x_0) + h'(x_0)(x-x_0) + \frac{h''(x_0)}{2}(x-x_0)^2. \tag{7.34}$$

Here, $h(x_0) = g(x_0) - \ln g(x_0) = 1$, $h'(x_0) = 0$ and $h''(x_0) = [g'(x_0)]^2$.

When $g(x_0) = 1$ we also have $\phi(x_0) = \left[1 - g(x_0)\right]\frac{p(x_0)}{g(x_0)} = 0$, so in addition to $h(x)$ we can also expand $\phi(x)$ to obtain

$$h(x) \approx 1 + \frac{g'^2(x_0)}{2}(x-x_0)^2 \tag{7.35}$$

and

$$\phi(x) \approx \phi'(x_0)(x - x_0) = -g'(x_0)p(x_0)(x - x_0). \tag{7.36}$$

These expansions allow us approximate the integral (7.23) by

$$\frac{D(\Delta)}{N} = \frac{\Delta^{\Delta-1}}{\Delta!}e^{-\Delta}\int_0^{x_0} g'(x_0)p(x_0)(x_0 - x)e^{-\Delta\frac{g'(x)^2}{2}(x-x_0)^2}dx. \tag{7.37}$$

Since we are in the brittle regime and the avalanches are counted up to $x = x_0$ we can compute the Gaussian integral explicitly. Using the Stirling approximations $\Delta! \approx \Delta^{\Delta}e^{-\Delta}\sqrt{2\pi\Delta}$, we finally obtain

$$\frac{D(\Delta)}{N} = \frac{\Delta^{-5/2}}{\sqrt{2\pi}}\frac{g'(x_0)p(x_0)}{\left[g'(x_0)\right]^2}e^{-\Delta\frac{g'(x)^2}{2}(x-x_0)^2}\Big|_0^{x_0}. \tag{7.38}$$

for large Δ the lower limit gives a vanishing contribution, which allows us to write the following asymptotic formula for the avalanche size distribution,

$$\frac{D(\Delta)}{N} \approx C\Delta^{-5/2}, \tag{7.39}$$

where the constant is $C = p(x_0)/(\sqrt{2\pi}g'(x_0))$. As we mentioned before, the exponent $-5/2$ has already appeared in the studies of the classical FBM loaded in the soft device (Hemmer and Hansen, 1992) and has been previously associated with spinodal criticality (Alava, Nukala, and Zapperi, 2006). Our model can be viewed as an extension of this earlier model in the sense that the soft device case can be obtained as a limit c of our hard/mixed device case when $\Lambda \propto \kappa_f \to 0$. We can then conclude that scaling in our brittle regime is also of the spinodal type; however, the presence in our model of the global events makes the system only super-critical.

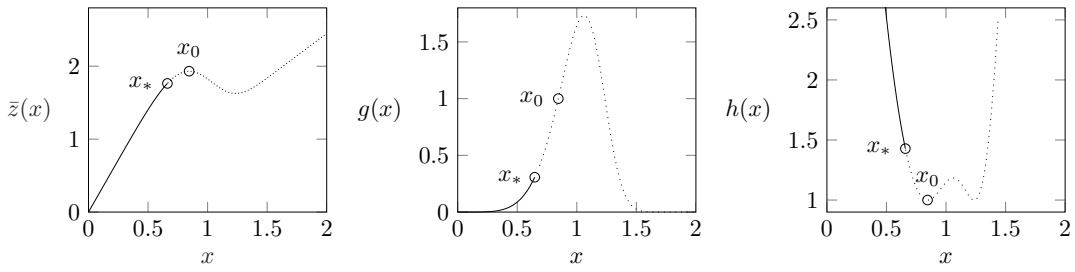

Figure 7.7: Behavior of the functions $z(x)$, $g(x)$ and $h(x)$ when the system is in the brittle regime in the global minimum respone.

We now turn to the subtle difference between the scaling behavior of equilibrium (energy minimizing) and out of equilibrium (marginally stable) systems in the brittle regime. We recall that the condition $g(x_0) = 1$, being rewritten as $1 - P(x_0) + \Lambda - xp(x_0) = 0$ is exactly our Eq. (6.1), stating that the averaged curve $z(x)$ has a (local) maximum. The problem is that along the global minimum path the system size (snap) debonding takes place necessarily before the point x_0 is reached because it corresponds to a metastable state which is only marginally stable. Suppose that the actual equilibrium snap event takes place at some $x_* < x_0$ given by the corresponding Maxwell condition and illustrated in Fig. 7.7. The counting of avalanches should be then performed only up to the point x_* and in the integral (7.23) we must put $x_c = x_*$. Moreover, in this case, the function $h(x)$ will attain its minimum in the boundary point x_* which is the upper limit of integration.

For a function with maximum at the boundary we can still obtain the asymptotic formulas for the avalanche distribution. Suppose $h(x)$ a continuous function such that $h(x)$ attains its maximum at $x = x_*$, $h'(x_*)$ exists and $h'(x_*) > 0$. Assume further that $h(x) \to \infty$, as $x \to -\infty$ and that $\int_{-\infty}^{x_*} e^{-h(x)}dx$ converges. Then, the following asymptotic representation holds at $N \to \infty$ (Bruijn, 2014)

$$\int_{x_{inf}}^{x_{sup}} e^{-Nh(x)}dx \to \frac{e^{Nh(x_*)}}{Nh'(x_*)} \tag{7.40}$$

This allow us to re-write the integral (7.23) in the form

$$\frac{D(\Delta)}{N} = \frac{\Delta^{\Delta-1}}{\Delta!}\frac{e^{-\Delta h(x_*)}}{\Delta h'(x_*)}\phi(x_*). \tag{7.41}$$

Finally, using the Stirling approximations $\Delta! \approx \Delta^{\Delta}e^{-\Delta}\sqrt{2\pi\Delta}$, we obtain

$$\frac{D(\Delta)}{N} = \frac{\phi(x_*)}{h'(x_*)}\frac{\Delta^{-5/2}}{\sqrt{2\pi}}e^{-\Delta(1-h(x_*))}. \tag{7.42}$$

This result can be rewritten more succinctly

$$\frac{D(\Delta)}{N} \approx C\Delta^{-5/2}e^{-\Delta(1-h(x_*))}, \tag{7.43}$$

where the constant $C = \phi(x_*)/(\sqrt{2\pi}h'(x_*))$. This distribution has the same exponent $-5/2$ as in the classical FBM loaded in soft device (Hemmer and Hansen, 1992) however the power law scaling is now compromised at the large sizes by an exponential cut off. The numerical simulations supporting this results were previously reported in our Fig. 7.3.

7.5 Phase diagram

We have shown the existence of two scaling exponents characterizing the behavior of our augmented FBM. In the brittle regime, the classical exponent $5/2$ has appeared, however, due to the presence of the snap event we cannot call such regimes critical. We have also shown that the transition from brittle to the ductile regime is associated with actual criticality and scale-free distribution of avalanches characterized by the new exponent $9/4$. Such crossover criticality must be tuned as in the random field Ising model (RFIM) and can be interpreted as the presence of a classical *critical* point. The super-criticality observed in the brittle regime with exponent $5/2$ is instead robust and can be associated with the presence of a *spinodal* point.

The global phase diagram in the rigidity-disorder parameter space is presented in Fig. 7.8 for the out-of-equilibrium dynamics and Weibull distribution of thresholds. The red crossover region was determined by numerical evaluation of the Kolmogorov-Smirnoff statistic for the case of finite N and applying the corresponding criterion of the quality of the power law distribution, for details see Appendix E. The thick black line behind the crossover region identifies the values of parameters (ρ, Λ) for which there exists a solution of the equation $g(x_0) = 1$.

In Fig. 7.9 we illustrate, using the cumulative distribution of avalanches, the crossover from the exponent $3/2$ associated with the spinodal criticality to the exponent $5/4$ characterizing the actual critical point.

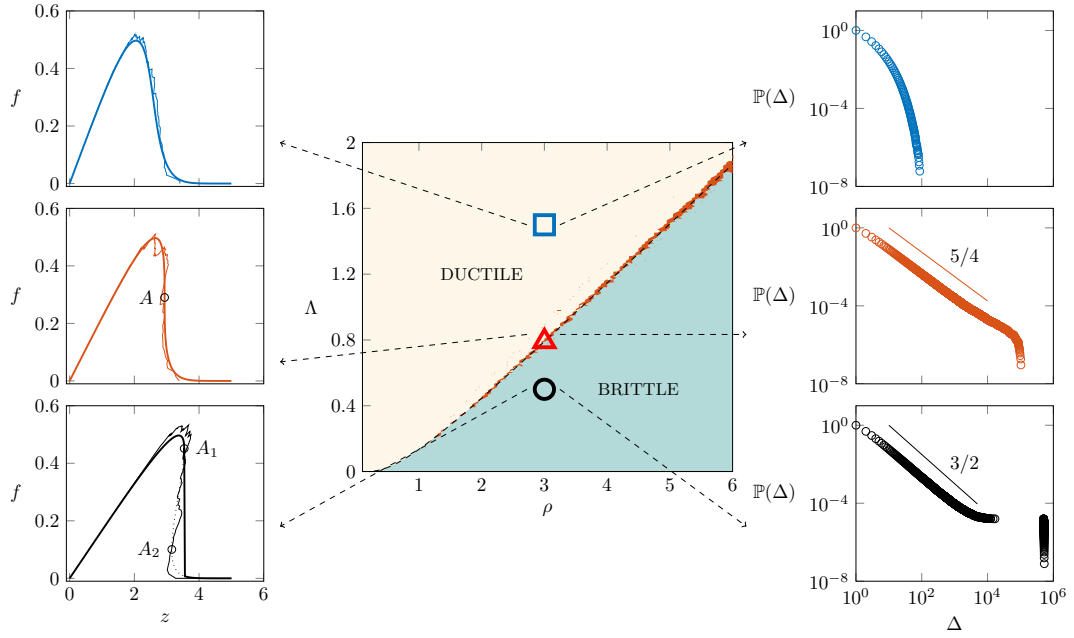

Figure 7.8: Brittle-to-ductile transition (critical) line in the (ρ, Λ) phase diagram. On the left is the the superposition of the average force-elongation curve with a realization of system of size $N = 100$. On the right is the avalanche distribution for the the system with the corresponding parameters with $N = 10^6$.

7.6 Finite size scaling

So far we have been mostly interested in the behavior of the system in the thermodynamic limit. However, in many situations, we need to understand the effects of finite N. For instance, in cell adhesion, the area density of integrins is of the order of a few hundred to few thousands per μm^2 (Bell, 1978; Erdmann and Schwarz, 2007) and the total number of receptors in adhesion contacts can range from just a few (in the initial states of adhesion), to $\sim 10^5$ in mature cell-matrix contact (Schwarz and Safran, 2013; Erdmann and Schwarz, 2004).

In this perspective, it is reasonable to consider a situation when one is allowed to change the number of binding elements while the external spring, representing the elasticity of the backbone and the environment is kept fixed. In the simulations the distribution of avalanches is typically bounded by upper cut-offs related to the system size, see Fig. 7.10

To understand the structure of the cut-off functions, also expected to be universal near the critical point, we can write the probability distribution for the avalanches in the form

$$P(\Delta) = \Delta^{-\tau} \mathcal{G}(\Delta/\Delta_c), \tag{7.44}$$

When the system size goes to infinity, the cutoff parameter can be expected to diverge near the critical point as $\Delta_c \sim N^{\xi}$. Under such finite size scaling assumption, the set of exponents $\{\tau, \xi\}$ characterizes the universality class of the model.

To test such finite size scaling (FSS) picture and to find the critical exponents we performed numerical simulations with initial values of parameters ρ, Λ taken on the critical line, as it is predicted by the study of the averaged behavior of the system. We performed simulations at several values of the system size N, adjusting the values

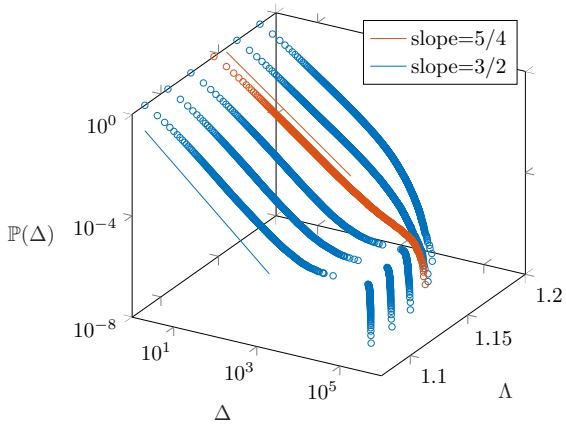

Figure 7.9: Avalanche distribution along the brittle to ductile transition at a given disorder and varying rigidity.

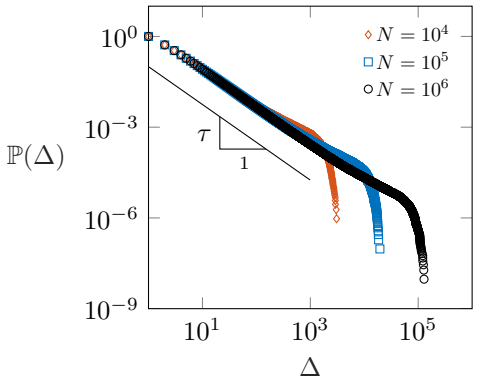

Figure 7.10: Avalanche cumulative distribution for the system in the critical state for several system sizes.

of ρ, Λ until we reach the analytically predicted value of the cumulative avalanche distribution exponent $\tau = 9/4 - 1 = 5/4$ [6]

The computation of the exponent ξ was performed through the standard method of moments $P(\Delta, N)$ (Chessa, Vespignani, and Zapperi, 1999). More specifically, we defined the q-moment of Δ for a system of size N as $\langle \Delta^q \rangle_N = \int \Delta^q P(\Delta) d\Delta$. If the FSS hypothesis, Eq. (7.44), is valid, we can use the transformation $s = \Delta / N^\xi$ to obtain

$$\langle \Delta^q \rangle_N = N^{\xi(q+1-\tau)} \int s^{q-\tau} \mathcal{G}(s) ds. \tag{7.45}$$

Therefore, one can expect to have $\langle \Delta^q \rangle_q \sim N^{\xi(q+1-\tau)}$. The exponent $\xi(q+1-\tau)$ can be then computed as the slope of the log-log plot of $\langle \Delta^q \rangle_N$ versus N. Furthermore, we have that $\langle \Delta^{q+1} \rangle_N / \langle \Delta^q \rangle_N \sim N^\xi$, so that the slope of $\xi(q+1-\tau)$ as a function of q is exactly the cutoff exponent ξ.

In Fig. 7.11a, we show the results obtained from the momentum analysis of the cumulative distribution of avalanches $P(\Delta) = \int d\Delta D(\Delta)$. One observes a clearly linear behavior starting from $q = 1.8$. As a final consistency test of the finite size scaling (FSS) hypothesis, we verified the data collapse for the distribution $P(\Delta, N)$ when we use the exponents obtained from the momentum analysis. More specifically, the FSS hypothesis states that after rescaling $q_\Delta \equiv \Delta N^{-\xi}$ and $P_{q_\Delta} \equiv P(\Delta, N)\Delta^\tau$, the

[6] For a power law with pdf $p(x) \sim x^{-\alpha}$ the corresponding CDF goes as $P(x) \sim x^{\alpha-1}$.

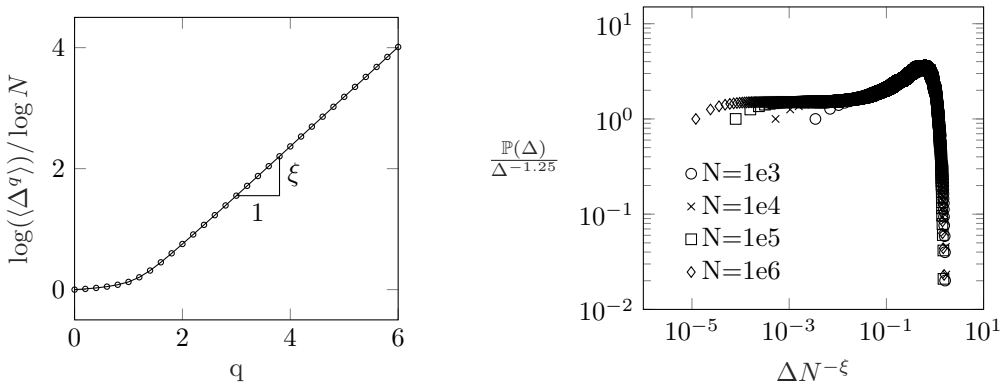

Figure 7.11: (a) Plot of the momentum spectrum for the distribution of avalanches Δ. The linear part has a slope $\xi \approx 0.8$. (b) Data collapse analysis for the avalanche distribution. The values for the critical exponents are $\tau = 1.25$ and $\xi = 0.8$.

data for different N must collapse onto a single curve. In Fig. 7.11b, we show that the quality of such data collapse is indeed very good.

7.7 Finite size criticality

Note that since

$$\Lambda = (1 + 1/\lambda)\lambda_f = (1 + 1/\lambda)\kappa_f/\kappa N$$

increasing Λ at fixed λ should be equivalent to either increasing κ_f or decreasing N. For instance, if we assume that κ_f is fixed, varying Λ can be viewed as a size effect because it is equivalent to varying N. In this case, one can interpret Fig. 7.8 as a statement that in smaller systems there is a limit on the size of the bursts, which makes large events less frequent and ductile response more relevant.

A related size effect was studied for 2D fuse models of disordered materials in (Shekhawat, Zapperi, and Sethna, 2013), where the analog of our ductile regime was interpreted as damage percolation, and the analog of our brittle regime was associated with crack nucleation. The scaling in the crossover region was interpreted as a finite size criticality. Other similar studies have also been conducted in (Herrmann and Roux, 2014; Toussaint and Hansen, 2006; Delaplace, Pijaudier-Cabot, and Roux, 1996; Arcangelis and Herrmann, 1989). Similar to our case, three types of breakdown processes were identified: localization regime, diffuse localization regime, and percolation-like regime. These three regimes were studied using a mean-field theory predicting a passage from the localization regime to a percolation-like regime through a diffuse localization as a function of the system size. Later, using the renormalization group approach, a phase diagram relating the disorder and system size was constructed separating the regions of localization and percolation. It was also predicted that there is a region of intermediate system sizes and disorders where critical scaling takes place.

To explain such finite size criticality within our approach, we need to change the setting to make sure that the critical state is only observed in a window of system sizes at a given disorder. The ductile (quasi-brittle) regime should also be a finite size effect at a given disorder disappearing in the thermodynamic limit where only the brittle regime should be able to survive.

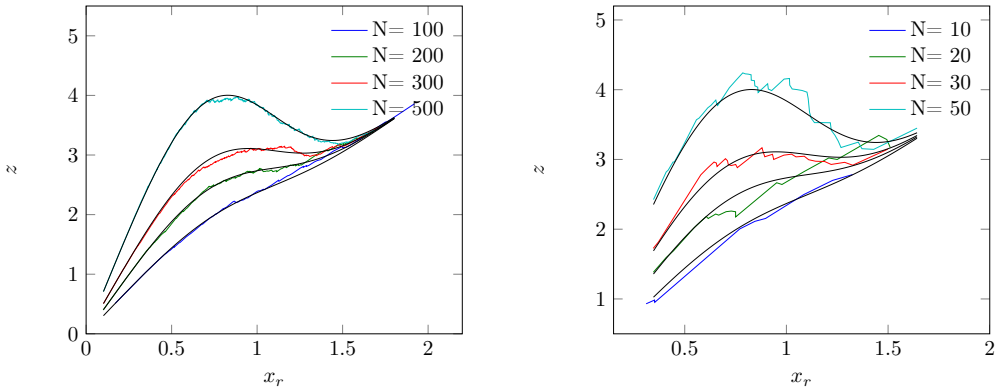

(a) $\rho = 3$ **(b)** $\rho = 4$

Figure 7.12: The effect of the system size in the overall response of the system is shown for two values of disorder. The external stiffness is fixed $\tilde{\Lambda} = 200$ and in (a) $\tilde{\Lambda} = 20$ in (b). The colored curves are single realizations obtained for the given size N and disorder (Weibull distribution characterized by ρ) the black lines are obtained by the averaged equation (5.13).

Note that so far, we have been acting under the assumption that the stiffness κ_f is a size-independent constant. Formally, this stiffness parameter characterizes a single spring connected in series with our parallel bundle of binders. However, the mean-field nature of the model compromises the actual spatial structure of the system where each breakable element may interact indirectly with any other breakable element as it is the case, for instance, in a 2D fuse network. Such interactions can be represented effectively in our model by various assumptions about the N dependence of the stiffness parameter κ_f.

Assume, for instance, that the external loading (controlled displacement) is applied to the bundle through the 'spring' with effective stiffness $\kappa_f \propto N^\alpha$, $0 \leq \alpha \leq 1$ where α can be seen as the dimensionality of the load transmitting network. The simplest assumption would be that there is indeed an external spring which would mean that $\alpha = 0$. Then $\Lambda \propto 1/N$. Another limiting case is when $\kappa_f \propto N$ which would mean that $\alpha = 1$ and Λ is size independent as in our original approach. One can also argue that in the simple tension test for a 3D body whose volume scales as $L^3 \sim N$, the load is applied on a surface with dimension $L^2 \sim N^{2/3}$. Then, if κ_f is to represent the elasticity of the coupling between the load device and the body, we should have $\kappa_f \propto N^{2/3}$ which means that $\alpha = 2/3$ and $\Lambda \propto N^{-1/3}$.

While the focus of our previous analytical computations was usually the thermodynamic limit $N \to \infty$, one can show that the N dependence of Λ represents a higher order effect and one can still consider $\Lambda(N)$ in the expressions obtained taking a formal thermodynamic limit for Λ equal to a constant. We show some numerical simulations below to support this claim.

Suppose, for instance, that $\alpha = 0$. The size effect is then hidden in the N dependence of the stiffness $\lambda_f \propto 1/N$. We can then write $\Lambda = \tilde{\Lambda}/N$, and assume that the rigidity is characterized by the parameter $\tilde{\Lambda}$. Consider first the question of existence of a local maximum (indicating brittleness) on the curve $z(x)$ for $x \leq x_{max}$, where x_{max} is the biggest threshold value. It is related to the question whether brittleness only emerges in sufficiently large systems. In Fig. 7.12 we increase N at fixed rigidity $\tilde{\Lambda}$ and show how the system undergoes a transition from ductile to brittle. The

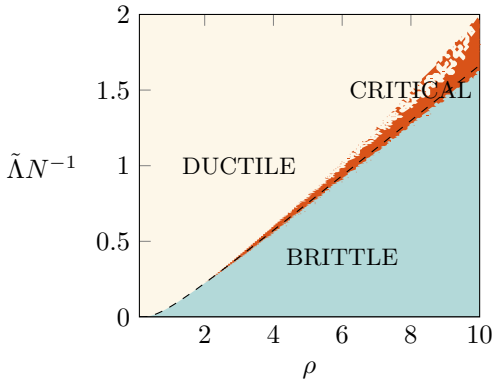

Figure 7.13: The effect of the system size N in the overall response of the bundle for $\tilde{\Lambda} = 2 \times 10^4$ and $\lambda = 1$. We distiguish three regions: brittle, where theres is a big snap event scaled with the system size, critical, where burst events distribution is a power law, and ductile (quasi brittle), with the predominance of small bursts.

transition, however, is not abrupt at the fixed disorder, and we see the evidence of a critical region, instead of a critical point expected at $N \to \infty$ in the system with $\alpha = 1$.

In Fig. 7.13 we show the phase diagram in the disorder-system size space that is based on direct numerical simulations of the system at a given (ρ, N). The diagram shows three domains with a structurally different distribution of avalanches. In the red perforated domain, we observed the power law distribution of avalanches with exponent with exponent -9/4 indicating criticality.

In the green domain, we have super-critical distribution with exponent -5/2 and the peak corresponding to persistent system size events. This is our brittle regime exhibiting robust spinodal criticality. Finally, in the yellow domain, the scaling was absent and we identified such regimes as ductile. To assess the quality of the power laws we estimated the scaling exponent using maximum likelihood estimation (MLE), and then tested the power law hypothesis using the Kolmogorov-Smirnov approach, as suggested in (Clauset, Shalizi, and Newman, 2009; Newman, 2005; Baró and Vives, 2012), and discussed in detail in Appendix E.

According to the phase diagram presented in Fig. 7.13, large systems will be brittle with pseudo-critical avalanche distribution dominated by a large system size event (SNAP). However, for finite size systems, this big event disappears, giving rise to an extended domain of scaling regimes that can be associated with finite size criticality. In this domain, such pseudo-criticality will be robust with correlation length reaching the system size and fluctuations (avalanches) taking the form of a crackling noise with a cut-off. The real (percolation type) criticality in such setting will be observed in a single point corresponding to an infinite (brittle) system with an infinitely broad disorder.

As the system size is decreased further the correlation length becomes microscopic and the system enters the ductile (quasi-brittle) regime (POP) with largely Gaussian statistics of avalanches. We believe that this scenario is rather general and can be associated with the behavior of many other complex systems that are otherwise vaguely interpreted as being critical. It remains to be seen experimentally if cellular adhesion can also be interpreted in the same framework (despite the finite temperature effects, some of which will be discussed in the next Chapter)

7.8 Conclusions

We have shown that in contrast to the standard FBM, our augmented bundle model exhibits two types of scaling. The first type, which can be interpreted as resulting from spinodal instability, is observed in brittle regimes near the ultimate failure threshold. This robust regime, however, cannot be called critical because of the presence of the system size event. The second type of scaling, reflecting the presence of a real critical point, is not robust in the absence of a feedback mechanism. It is observed at the brittle-to-ductile transition, and the corresponding critical exponents differ from the ones characterizing the spinodal criticality. We studied the behavior of the athermal system under two different response protocols, the out-of-equilibrium or marginal stability response when the system remains in a metastable state until it becomes unstable, and the equilibrium or global minimization protocol when the system always remains in a ground state. In the former case, we predicted the existence of a robust scaling prior to final breakdown, as well as the critical behavior at the brittle-to-ductile transition, while in the latter case, our analysis showed that scaling could be only present in the critical point with the same exponents as in the case out-of-equilibrium criticality. Natural generalizations of the underlying model were shown to be compatible with the phenomenon of finite scale criticality.

Chapter 8

Quasi-static loading at finite temperature

In this Chapter, we study the equilibrium mechanical response of our augmented FBM at finite temperature viewed as an annealed disorder. Although at physiological temperatures reaching thermal equilibrium may take a prohibitively long time, it is of interest to see to what extent the quenched and annealed disorder are interchangeable and how effective each of these sources of inhomogeneity in suppressing the collective debonding.

We begin with a study of a single elastic binder and show that it loses its snap-through response at any nonzero temperature. We then extend this analysis to the case of a parallel bundle of N elastic binders and show how the presence of long-range interactions allows the system to recover the brittle behavior in the thermodynamic limit. Finally, we study the mean-field critical point in this system and link it to the brittle-ductile transition. We also demonstrate that similar to the case of quenched disorder, not only temperature but also the system's rigidity may affect the mode of failure in this system.

8.1 Single binder

Consider a single binder described in Section 3.1, which can be described by the potential (3.3). To compute the averaged mechanical response at finite temperature, we need to know the free energy as a function of the loading parameter

$$\mathcal{F}(\beta, y) = -\frac{1}{\beta} \log \mathcal{Z}(y, \beta). \tag{8.1}$$

Here $\mathcal{Z}(\beta, y) = \displaystyle\int_{-\infty}^{\infty} \exp\left[-\beta e(x; y)\right] dx$ is the partition function, $\beta = (\kappa_p L^2)/(k_b T)$ is the non-dimensional inverse temperature and k_b is the Boltzmann constant. We can compute the partition function explicitly

$$\begin{aligned} \mathcal{Z}(\beta, y) &= \int_{-\infty}^{1} \exp\left[-\beta e(x; y)\right] dx + \int_{1}^{\infty} \exp\left[-\beta e(x; y)\right] dx \\ &= \int_{-\infty}^{1} e^{-\beta\left[\frac{x^2}{2} + \frac{\lambda}{2}(y-x)^2\right]} dx + \int_{1}^{\infty} e^{-\beta\left[\frac{1}{2} + \frac{\lambda}{2}(y-x)^2\right]} dx. \end{aligned} \tag{8.2}$$

Here

$$\int_{-\infty}^{1} e^{-\beta\left[\frac{x^2}{2} + \frac{\lambda}{2}(y-x)^2\right]} dx = \sqrt{\frac{\pi}{2\beta(1+\lambda)}} e^{-\frac{\lambda\beta}{2(1+\lambda)} y^2} \left\{ \operatorname{erf}\left[\sqrt{\frac{\beta}{2(1+\lambda)}}(1 + \lambda - \lambda y)\right] + 1 \right\} \tag{8.3}$$

and

$$\int_1^\infty e^{-\beta\left[\frac{1}{2}+\frac{\lambda}{2}(y-x)^2\right]}dx = \sqrt{\frac{\pi}{2\beta\lambda}}e^{-\frac{\beta}{2}}\left\{\operatorname{erf}\left[\sqrt{\frac{\beta\lambda}{2}}(y-1)\right]+1\right\}. \tag{8.4}$$

Bringing all these expressions together, we obtain

$$\begin{aligned}\mathcal{Z}(\beta,y) = \sqrt{\frac{\pi}{2\beta(1+\lambda)}}e^{-\frac{\lambda\beta}{2(1+\lambda)}y^2}\left\{\operatorname{erf}\left[\sqrt{\frac{\beta}{2(1+\lambda)}}(1+\lambda-\lambda y)\right]+1\right\}+ \\ \sqrt{\frac{\pi}{2\beta\lambda}}e^{-\frac{\beta}{2}}\left\{\operatorname{erf}\left[\sqrt{\frac{\beta\lambda}{2}}(y-1)\right]+1\right\},\end{aligned} \tag{8.5}$$

where $\operatorname{erf}(x) = \frac{2}{\sqrt{\pi}}\int_0^x e^{-t^2}dt$. The equilibrium tension can be now obtained by direct differentiation $f(\beta,y) = \partial\mathcal{F}(\beta,y)/\partial y$.

The ensuing force-elongation relations are illustrated in Fig. 8.1. Note that the metastability of the zero temperature model has disappeared and that the reversible transition from the detached state is now gradual at any nonzero temperature. One can say that a single binder exhibits 'ductile' behavior while becoming 'brittle' only at zero temperature. This will also be the case in the standard FBM model with N elements and controlled elongation because in such model individual binders are effectively independent. Below we show that 'brittleness' at finite temperature can be recovered in a hard device if individual binding elements interact sufficiently strong and can therefore bind and unbind cooperatively.

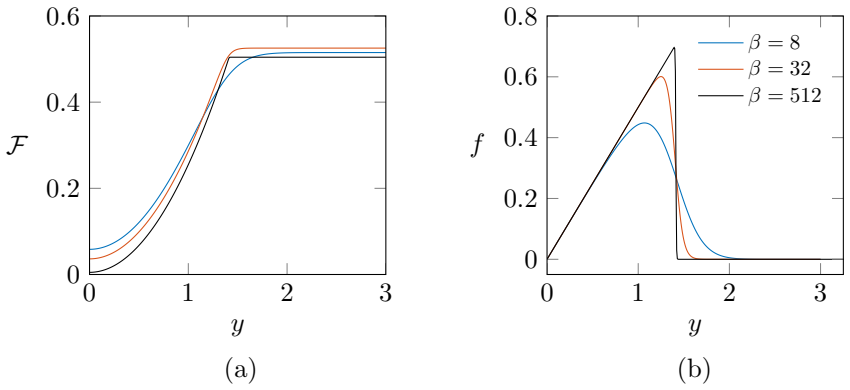

Figure 8.1: Mechanical response of a single bond in a hard device (imposed y) at several values of temperature for $\lambda = 1$: (a) free energy; (b) averaged tension.

8.2 Parallel bundle of N binders

Since we are interested in equilibrium behavior, the challenge is again to compute the partition function

$$\mathcal{Z}(\beta,z) = \int_\Omega \exp\left[-\beta\mathcal{H}(\boldsymbol{x};y;z)\right]d\boldsymbol{x}dy \tag{8.6}$$

where now $\Omega = \mathbb{R}^N \times \mathbb{R}$. Given that the problem is permutationally invariant, we may say that in a given configuration the first $N\phi$ bonds, $x_1,\ldots,x_{N\phi}$, are attached

while the remaining bonds $x_{N\phi+1}, \ldots, x_N$ are detached. We may then write

$$\mathcal{H}(x_1, \ldots, x_N, y, z, \phi) = N\frac{\lambda_f}{2}(z-y)^2 + \sum_{i=1}^{N\phi} V_1(x_i, y) + \sum_{i=N\phi+1}^{N} V_0(x_i, y). \tag{8.7}$$

Here $V_1(x_i, y) = \frac{x_i^2}{2} + \frac{\lambda}{2}(y - x_i)^2$ defined for $x_i \leq 1$, and $V_0(x_i, y) = \frac{1}{2} + \frac{\lambda}{2}(y - x_i)^2$ defined for $x_i > 1$. Since for each value of ϕ, there are $\binom{N}{N\phi} = \frac{N!}{(N\phi)!(N-N\phi)!}$ ways of choosing $N\phi$ bonds we can write the expression for the marginal partition function at fixed ϕ and y in the form

$$\begin{aligned}\mathcal{Z}(\beta, z, y, \phi) = \binom{N}{N\phi} e^{-\beta N\frac{\lambda_f}{2}(z-y)^2} \int_{-\infty}^{1} \cdots \int_{-\infty}^{1} \exp\left[-\beta \sum_{i=1}^{N\phi} V_1(x_i, y)\right] dx_1 \ldots dx_{N\phi} \\ \int_{1}^{\infty} \cdots \int_{1}^{\infty} \exp\left[-\beta \sum_{i=N\phi+1}^{N} V_0(x_i, y)\right] dx_{N\phi+1} \ldots dx_N.\end{aligned} \tag{8.8}$$

After some straightforward manipulations we obtain

$$\mathcal{Z}(\beta, z, y, \phi) = \exp\left[-\beta N\left(\bar{v}(y, \phi, z) - \frac{1}{\beta}\bar{S}(\beta, y, \phi) - \frac{1}{\beta N}\ln\binom{N}{N\phi}\right)\right]$$

where

$$\bar{v}(z, y, \phi) = \frac{\lambda_f}{2}(z-y)^2 + \phi\frac{\lambda}{2(1+\lambda)}y^2 + (1-\phi)\frac{1}{2},$$

and

$$\begin{aligned}\bar{S}(\beta, y, \phi) = \phi \ln\left[\sqrt{\frac{\pi}{2\beta(1+\lambda)}}\left\{\operatorname{erf}\left[\sqrt{\frac{\beta}{2(1+\lambda)}}(1+\lambda-\lambda y)\right] + 1\right\}\right] \\ +(1-\phi)\ln\left[\sqrt{\frac{\pi}{2\beta\lambda}}\left\{\operatorname{erf}\left[\sqrt{\frac{\beta\lambda}{2}}(y-1)\right] + 1\right\}\right].\end{aligned} \tag{8.9}$$

To eliminate the variable ϕ we need to sum over corresponding microconfigurations:

$$\mathcal{Z}(\beta, z, y) = \sum_{N\phi=0}^{N} \mathcal{Z}(\beta, z, y, \phi) \tag{8.10}$$

Note that in the thermodynamic limit $N \to \infty$ we can replace the sum over ϕ in the above expression by an integral over the interval $[0, 1]$. We then obtain the marginal (with y fixed) partition function

$$\mathcal{Z}(\beta, z, y) = \exp\left[-\beta N\left(\hat{v}(y, z) - \frac{1}{\beta}g(\beta, y)\right)\right]$$

where

$$\hat{v}(y, z) = \frac{\lambda_f}{2}(z-y)^2$$

and

$$g(\beta, y) = \ln \left[\sqrt{\frac{\pi}{2\beta(1+\lambda)}} e^{\frac{-\lambda\beta}{2(1+\lambda)} y^2} \left\{ \operatorname{erf}\left[\sqrt{\frac{\beta}{2(1+\lambda)}} (1 + \lambda - \lambda y) \right] + 1 \right\} + \sqrt{\frac{\pi}{2\beta\lambda}} e^{-\frac{\beta}{2}} \left\{ \operatorname{erf}\left[\sqrt{\frac{\beta\lambda}{2}} (y - 1) \right] + 1 \right\} \right]. \tag{8.11}$$

The corresponding (marginal) free energy function is given by

$$\mathcal{F}_y(\beta, z, y) = \hat{v}(y, z) - \frac{1}{\beta} g(\beta, y) \tag{8.12}$$

and is illustrated in Fig. 8.2.

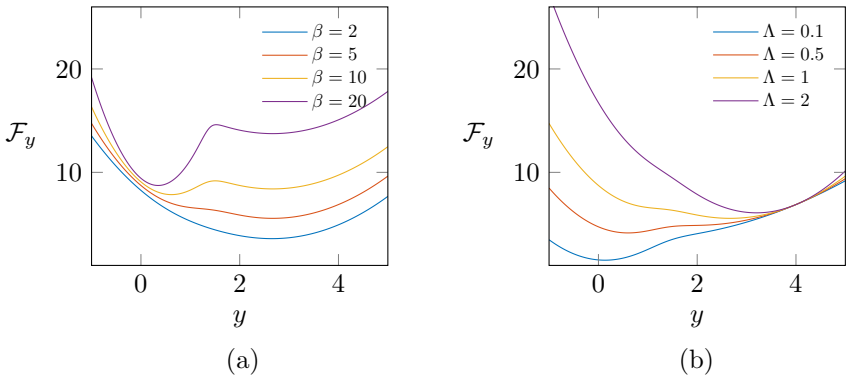

Figure 8.2: Free energy (8.12) for $\lambda = 1$ and $z = 4$. In (a) we fix $\lambda_f = 1$ and vary β, and in (b) we fix $\beta = 5$ and vary λ_f.

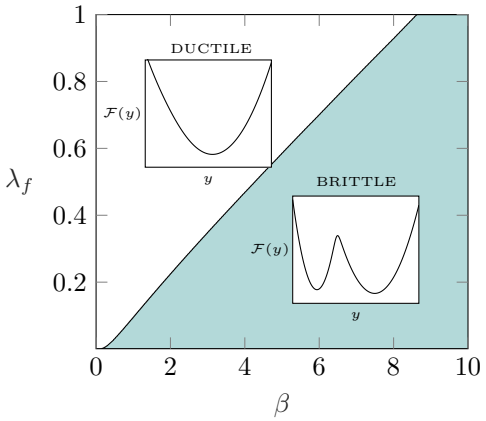

Figure 8.3: Phase diagram showing different convexity domains of the marginal free energy (8.12).

An interesting feature of this free energy is its non-convexity at sufficiently small temperatures (large β) and sufficiently strong coupling between individual binders (small λ_f). This is a result of the presence in the system of long-range interactions (Campa, Dauxois, and Ruffo, 2009). The two macroscopic energy wells in the parameter range of non-convexity represent synchronized states and indicate the possibility of highly coherent transitions between bound and unbound states. In Fig. 8.3

we show the domain of nonconvexity of $\mathcal{F}_y(y)$ in the plane (β, λ_f). The presence of such a domain is an indication of the 'brittle' behavior characterized by collective debonding. The debonding in the domain of convexity of $\mathcal{F}_y(y)$ can be expected to be gradual and can be associated with ductile behavior.

To recover the macroscopic behavior, we still need to integrate over the order parameter y and compute the equilibrium partition function $\mathcal{Z}(\beta, z) = \int_{-\infty}^{\infty} \mathcal{Z}(\beta, z, y)dy$. Using the Laplace method we obtain $\mathcal{Z}(\beta, z) \sim \exp\left[-N\beta\mathcal{F}_y(y_0(\beta, z), \beta, z)\right]$ where $y_0(\beta, z)$ is the global minimum of the function $\mathcal{F}_y(y, \beta, z)$. We can then obtain the equilibrium free energy $\mathcal{F}(\beta, z) = \mathcal{F}_y(y_0(\beta, z), \beta, z)$ and study the equilibrium force-elongation $f(\beta, z) = \partial\mathcal{F}(\beta, z)/\partial z$. The nontrivial mechanical response of the ensuing system is due to the double well nature of the marginal free energy density $\mathcal{F}_y(y)$ which is responsible for the discontinuous dependence of y_0 on the loading parameter z.

8.3 Brittle to ductile transition

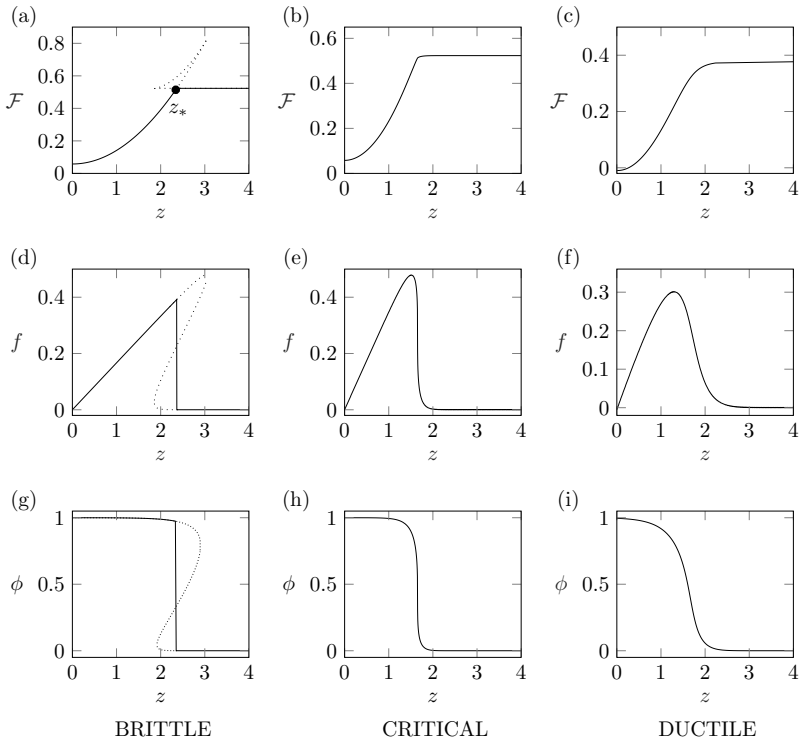

Figure 8.4: Mechanical response of system in ductile, critical and brittle regimes. Brittle: $\beta = 8$, $\lambda = 1$, $\lambda_f = 0.25$. Critical: $\beta = 8.62$, $\lambda = 1$, $\lambda_f = 1$. Ductile: $\beta = 4$, $\lambda = 1$, $\lambda_f = 1$.

Our main results, summarizing the mechanical response of the system in the thermodynamic limit $N \to \infty$, are presented in Fig. 8.4. Depending on the location in the parameter space rigidity-disorder (see Fig. 8.3), the behavior of the system can be again qualified as brittle or ductile.

In the ductile regime, the response is continuous in the whole range of values of the loading parameter in the sense that the bound state becomes unzipped gradually as the loading parameter z increases from zero to infinity. In such systems, the average fraction of attached binders ϕ changes continuously under loading, and the

force f decreases progressively. Instead, in the brittle regime, the system undergoes at some $z = z_*(\beta, \lambda_f)$ a singular macroscopic transition from bound to unbound state with an abrupt drop of tension. The transition is associated with a jump in the number of attached binders which means that it is a collective phenomenon and that behind it is a synchronized switch of the significant fraction of binding elements from one macro energy well to another.

Brittle and ductile regimes are separated in Fig. 8.3 by a line of critical points which can also be interpreted as the boundary of a second order phase transition. The situation is formally similar to what is observed in mean-field spin systems describing the transition from para to ferromagnetism. In the brittle (ferromagnetic) phase the marginal free energy $\mathcal{F}(y)$ is non-convex for some z and the equilibrium free energy $\mathcal{F}(z)$ has a singularity at $z = z_*$ while in the ductile (paramagnetic) phase the marginal free energy is always convex and the equilibrium free energy is analytic. We emphasize, however, that the discontinuous (brittle) tension-elongation response associated with the singularity of the equilibrium free energy is possible only in the thermodynamic limit. In other words, at finite N the free energy is always smooth, and the mechanical response is always ductile even though it may be arbitrarily sharp.

In Fig. 8.5 we illustrate a peculiar effect of temperature on the behavior of the system in the brittle regime. Thus, with the inverse temperature (β) increasing at the fixed elongation z one would expect to see an abrupt thermal debonding (denaturation) when the temperatures reach a particular threshold and the bonds collectively disassociate. This is indeed how the system behaves in general. However, we also see in Fig. 8.5 that some partial bonding serves as a precursor of the eventual macroscopic debonding. The detailed study of this phenomenon, which can be associated with negative thermal expansion, remains to be done.

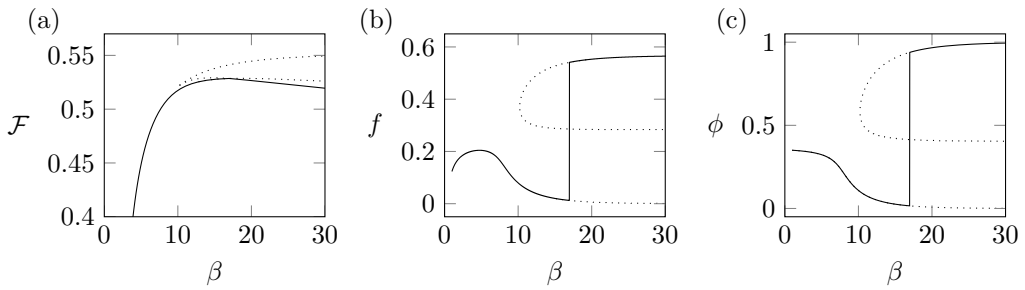

Figure 8.5: Mechanical response of the system at a fixed elongation $z = 1.7$ and varying inverse temperature β. parameters: $\lambda = 1$, $\lambda_f = 1$. Solid lines represent equilibrium behavior, dotted lines – metastable branches.

Suppose now that both, the elongation z and the temperature β, are fixed. In this case the discontinuous transition between the bound configuration with $\phi \sim 1$ and the unbound configuration with $\phi \sim 0$ can be induced by changing the 'internal' stiffness λ, see Fig. 8.6c, or the 'external' stiffness λ_f, see Fig. 8.7c. For this behavior, which may be of particular interest in biological applications, e.g., (Puglisi and Truskinovsky, 2013; Sheshka, Recho, and Truskinovsky, 2016), to be relevant the temperature of the system must be, of course, sufficiently low.

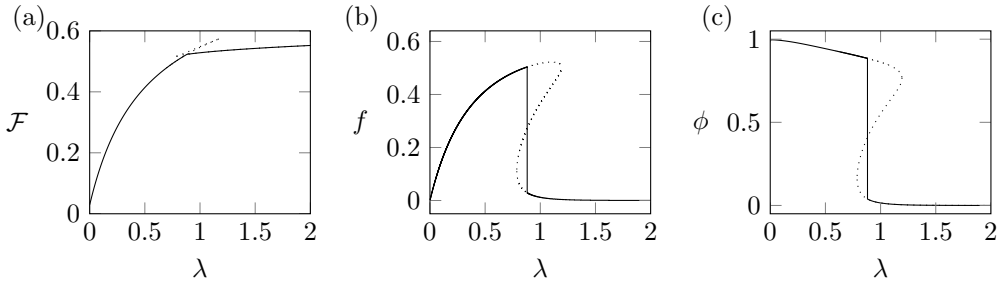

Figure 8.6: Mechanical response of the system at a fixed elongation $z = \sqrt{3}$, temperature $\beta = 15$ and varying internal stiffness λ. Parameters: $\lambda_f = 1$. Solid lines represent the equilibrium response, dotted lines represent metastable branches.

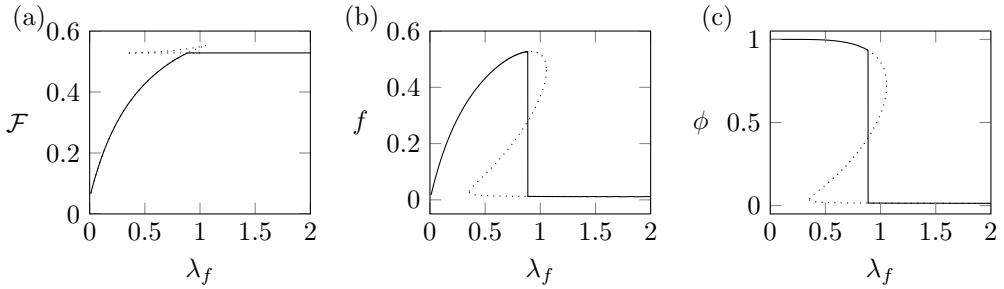

Figure 8.7: Mechanical response of the system at a fixed elongation $z = \sqrt{3}$, temperature $\beta = 15$, and varying external stiffness λ_f. Parameters: $\lambda = 1$. Solid lines represent the equilibrium response, dotted lines represent metastable branches.

8.4 Conclusions

We presented in this Chapter a mean-field model of displacement controlled equilibrium debonding at finite temperature showing that the interplay between the rigidity and temperature may change the overall response of the system from ductile, where the debonding is gradual, to brittle, where it is discontinuous. The elastic interaction through the external spring can effectively 'freeze' the binders in one of the macroscopic (metastable) energy wells allowing only a cooperative switch between the attached and the detached states. We constructed a phase diagram in the temperature-rigidity space showing that a line of critical points separates brittle (cooperative) and ductile (non-cooperative) behaviors. One of our important observations is that tuning of the overall rigidity can induce a discontinuous debonding in such systems. As it has been recently shown, in biological systems this kind of tuning can be achieved actively (Sheshka, Recho, and Truskinovsky, 2016) and our study suggests that active rigidity manipulation may be an important biological adhesion, see also (Puglisi and Truskinovsky, 2013)

Chapter 9

Finite rate of loading

In this Chapter, we collect some, still clearly incomplete, results on the kinetic behavior of our system under time-dependent loading. The kinetics is understood in the sense of overdamped Langevin dynamics at a fixed temperature and time-dependent loading.

To capture the cohesion-decohesion phenomena accompanying self-propulsion of a cell, we define a periodic potential representing the binding sites. We assume that after breaking from one site, the bond can rebind again at another site. The rigid backbone is assumed to be pulled through a linear spring which is by itself dragged with constant velocity ν.

As before, we begin with characterizing the dynamics of a single bond in the presence of a single binding site but under time-dependent load. The primary goal here is to compute the mean time of breaking. We then analyze numerically the Langevin system describing a bundle of elements. We draw a parallel with models of friction and characterize two modes of cohesion-decohesion, stick-slip motion and smooth sliding, which we link with brittle and ductile regimes under the quasi-static driving. We then study how the internal elasticity and the ambient temperature choose a particular type of frictional cohesion-decohesion motion of a cell.

Similar approaches have been employed previously to model friction from a molecular perspective (Vanossi et al., 2013) and were also used to study force fluctuations in an elastic chain (Lacombe, Zapperi, and Herrmann, 2001). Thermal activation is specifically crucial in nano-friction, which is closer to our bio-molecular bonding because it can be easily disrupted by thermal fluctuations. In molecular systems, one usually differentiates between the two types of behaviors: stick-slip motion, characterized by intermittent detachments and associated with a collective behavior of the bonds (Filippov, Klafter, and Urbakh, 2004), and smooth sliding, characterized by gradual detachments and associated with uncorrelated disruptions of individual bonds.

9.1 Single bond

Consider the model of a single bond attached to a support that is traveling at constant velocity ν. We assume that the bond is exposed to a periodic potential, representing binding sites, see Fig. 9.1. This system shares similarities with the problem of a sliding nano-tip on a rough molecular surface (Riedo and Gnecco, 2004). The formation and disruption of bound connections can be thermally activated, and we model the mechanical behavior of this system by an overdamped Langevin equation.

The overdamped Langevin dynamics implies the presence of viscous friction with coefficient γ and the surrounding heat bath with temperature T. To satisfy the fluctuation-dissipation theorem, we must assume that the reservoir is described by

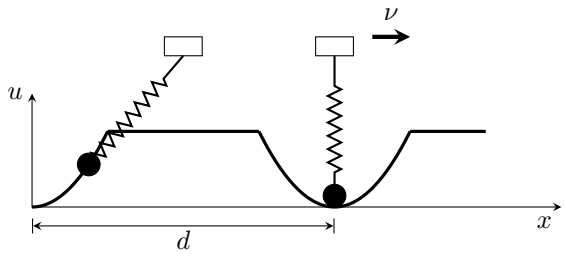

Figure 9.1: Schematic representation of a single particle moving through a periodic potential of parabolas describind the binding sites. The centers of the parabola are separated by a distance d.

the fluctuating force $\sqrt{2\gamma k_B T}\tilde{\xi}(\bar{t})$, where $\left\langle \tilde{\xi}(t) \right\rangle = 0$ and $\left\langle \tilde{\xi}(t)\tilde{\xi}(t') \right\rangle = \delta(t-t')$. We choose the timescale $\tau = \gamma/\kappa_p$, and introduce the non-dimensional inverse temperature $\beta = (\kappa_p L^2)/(k_B T)$ to obtain a non-dimensionalized version of our Langevin equation,

$$\frac{dx}{dt} = -\frac{\partial e(x,y)}{\partial x} + \sqrt{2\beta^{-1}}\xi(t), \tag{9.1}$$

where $e(x,y)$ is the potential describing a single bond, Eq. (3.3). We assume that the applied load is a linear function of time $y(t) = \nu t + y_0$, where ν is a characteristic of the rate of driving. We write the corresponding Fokker-Planck equation in the form (Gardiner, 2009),

$$\frac{\partial P(x,t)}{\partial t} = -\frac{\partial}{\partial x}A(x,t)P(x,t) + \frac{1}{2}\frac{\partial^2}{\partial x^2}B(x,t)P(x,t), \tag{9.2}$$

where the time-dependent drift coefficient $A(x,t) = -x\mathcal{H}(1-x) + \lambda(y(t)-x)$ accounts for the finite rate of driving while the diffusion coefficient is simply $B(x,t) = 2/\beta$.

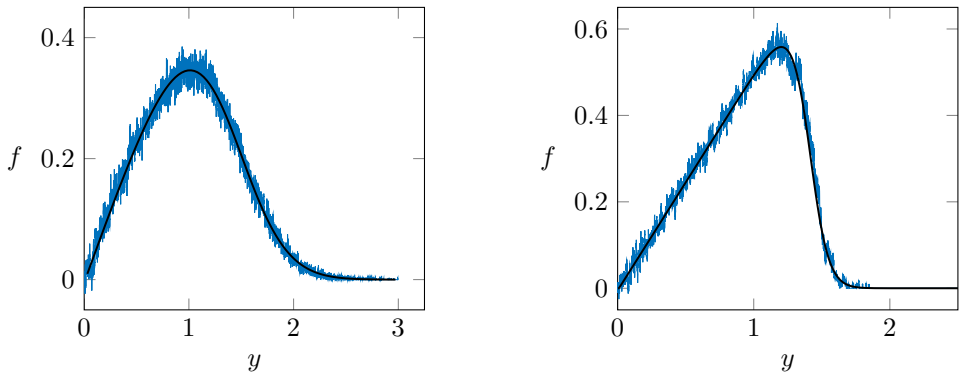

Figure 9.2: We present in blue the Langevin trajectory, Eq. (9.1) and in black the equilibrium response predicted by the stationary Fokker-Planck equation, $\nu \to 0$, which is exactly the curve predicted thorough equilibrium statistical mechanics, in Section 8.2. (a) $\beta = 4$, $\lambda = 1$ and (b) $\beta = 20$, $\lambda = 1$.

When the load y is applied quasi-statically $y(t) = y$, the stationary solution of our Fokker-Planck equation is exactly the Boltzmann distribution studied above. Moreover, $\frac{\partial P}{\partial t} = 0$, which gives the solution (Gardiner, 2009; Van Kampen, 1992),

$$P_{st}(x) = \frac{C}{B(x)} \exp\left(2\int^{x} \frac{A(x')}{B(x')} dx'\right) \tag{9.3}$$

where C is the integration constant, which has to be chosen such that $P_{st}(x)$ is normalized.

$$P_{st}(x) = C\frac{\beta}{2} \exp\left(-\beta e(x,y)\right) \tag{9.4}$$

with

$$C^{-1} = \frac{\beta}{2}\left[\int_{-\infty}^{1} e^{-\beta\left[\frac{x^2}{2}+\frac{\lambda}{2}(y-x)^2\right]} dx + \int_{1}^{\infty} e^{-\beta\left[\frac{1}{2}+\frac{\lambda}{2}(y-x)^2\right]} dx\right] \tag{9.5}$$

We can then identify $C = \frac{\beta}{2}\mathcal{Z}$, where $\mathcal{Z}$ is the partition function of the single binder, found in Section 8.1. From the knowledge of P_{st} we can compute the force $f = \lambda(y - \langle x\rangle)$, where $\langle x\rangle = \int dx P_{st}(x)x$. In Fig. 9.2, we show the force-elongation curve for the Langevin system loaded with infinitesimal rate $\nu \to 0$, which we superpose with the equilibrium force-elongation curve obtained from the stationary solution of the Fokker-Planck equation (9.4).

For a time dependent loading, we are able to analytically solve the associated Fokker-Planck equation. Because of the piece-wise nature of the drift coefficient A, we solve the Fokker-Planck equation by dividing the domain of x in two regions, $x \leq 1$ and $x > 1$ (Owedyk and Kociszewski, 1985; Felderhof, 2008b; Felderhof, 2008a; Frisch et al., 1990).

$$P(x,t) = P_{on}(x,t)\mathcal{H}(1-x) + P_{off}(x,t)\mathcal{H}(x-1) \tag{9.6}$$

We then obtain an equivalent Fokker-Planck equation for each one of the two regions. For each region we have the initial conditions,

$$\begin{aligned} P_{on}(x = x_0, 0) &= C_1\delta(x - x_0) \\ P_{off}(x = x_0, 0) &= C_2\delta(x - x_0). \end{aligned} \tag{9.7}$$

Furthermore, we need to use a boundary condition ensuring continuity of the solution in the point of separation of the domains, which is simply

$$P_{on}(x = 1, t) = P_{off}(x = 1, t). \tag{9.8}$$

For $x \leq 1$ we obtain,

$$\frac{\partial P(x,t)}{\partial t} = -\frac{\partial}{\partial x}\left[\left(-x(\lambda+1) + \lambda y(t)\right) P(x,t)\right] + \frac{1}{\beta}\frac{\partial^2}{\partial x^2}P(x,t). \tag{9.9}$$

For simplicity we write the FP equation as

$$\frac{\partial P(x,t)}{\partial t} = \frac{\partial}{\partial x}\left[(ax + bt + c)P(x,t)\right] + D\frac{\partial^2}{\partial x^2}P(x,t), \tag{9.10}$$

where $a = (\lambda + 1)$, $b = -\lambda\nu$, $c = -\lambda y_0$ and $D = \dfrac{1}{\beta}$. To solve this equation we first apply the Fourier transform with respect to x,

$$\hat{P}(k,t) = \mathcal{F}\left\{P(x,t)\right\} = \int_{-\infty}^{\infty} P(x,t)e^{-ikx}dx \tag{9.11}$$

The initial condition for the Fourier transform is $\hat{P}(k,0) = e^{-ikx}$. Noting that

$$\begin{aligned}
\mathcal{F}\left\{\frac{\partial P(x,t)}{\partial t}\right\} &= \frac{\partial \hat{P}(k,t)}{\partial t}, \\
\mathcal{F}\left\{\frac{\partial P(x,t)}{\partial x}\right\} &= ik\hat{P}(k,t), \\
\mathcal{F}\left\{\frac{\partial}{\partial x}(xP(x,t))\right\} &= -k\frac{\partial \hat{P}(k,t)}{\partial k}.
\end{aligned} \tag{9.12}$$

We obtain,

$$\frac{\partial \hat{P}}{\partial t} + ak\frac{\partial \hat{P}}{\partial k} = \left[-Dk^2 + ik(bt+c)\right]\hat{P} \tag{9.13}$$

We use the method of characteristics to solve this first order PDE. The characteristic equation are

$$\frac{dt}{1} = \frac{dk}{ak} = \frac{d\hat{P}}{\left[-Dk^2 + ik(bt+c)\right]\hat{P}}, \tag{9.14}$$

from which we obtain,

$$k = k_0 e^{at} \tag{9.15}$$

and

$$\begin{aligned}
\frac{d\hat{P}}{\hat{P}} &= \left[-Dk^2 + ik(bt+c)\right]dt \\
&= \left[-Dk_0^2 e^{2at} + ik_0 e^{at}(bt+c)\right]dt.
\end{aligned} \tag{9.16}$$

Integrating this equation and applying the initial condition $\hat{P}(k,0) = C_1 e^{-ik_0 x_0}$ leads to

$$\hat{P} = C_1 \exp\left[-\frac{Dk_0^2}{2a}(e^{2at}-1) + \frac{ik_0}{a}\left[(e^{at}-1)\frac{b-ca}{a} - \frac{b}{a}te^{at} + x_0 e^{-at}\right] - ik_0 x_0\right]. \tag{9.17}$$

Recalling that $k_0 = ke^{-at}$ we can write

$$\begin{aligned}
\hat{P} &= C_1 \exp\left\{-ik\left[\frac{b-ca}{a^2}\left(1-e^{-at}\right) + e^{-at}x_0 - \frac{b}{a}t\right] - \frac{k^2}{2}\left[\frac{D}{a}\left(1-e^{-2at}\right)\right]\right\} \\
&= C_1 \exp\left[-ikM(t) - \frac{k^2}{2}\sigma^2(t)\right]
\end{aligned} \tag{9.18}$$

This is just the Fourier transform of a Gaussian distribution times the constant C_1,

$$P_{on}(x,t) = \frac{C_1}{\sqrt{2\pi\sigma_1^2(t)}} \exp\left[-\frac{\left(x - M_1(t)\right)^2}{2\sigma_1^2(t)}\right], \tag{9.19}$$

with mean

$$M_1(t) = \frac{b-ca}{a^2}\left(1-e^{-at}\right) + e^{-at}x_0 - \frac{b}{a}t \tag{9.20}$$

and variance

$$\sigma_1^2(t) = \frac{D}{a}\left(1 - e^{-2at}\right). \tag{9.21}$$

For $x > 1$ the FP equation is

$$\frac{\partial P(x,t)}{\partial t} = -\frac{\partial}{\partial x}\left[\lambda\left(y(t) - x\right)P(x,t)\right] + \frac{1}{\beta}\frac{\partial^2}{\partial x^2}P(x,t). \tag{9.22}$$

As above, we rearrange the drift coefficient for simplicity, writing the FP equation in the form

$$\frac{\partial P(x,t)}{\partial t} = \frac{\partial}{\partial x}\left[(\tilde{a}x + bt + c)P(x,t)\right] + D\frac{\partial^2}{\partial x^2}P(x,t), \tag{9.23}$$

where $\tilde{a} = \lambda\, b = -\lambda\nu$, $c = -\lambda y_0$.

Using the same method as in the case $x \leq 1$ we obtain a non-normalized Gaussian distribution

$$P_{off}(x,t) = \frac{C_2}{\sqrt{2\pi\sigma_2^2(t)}}\exp\left[-\frac{\left(x - M_2(t)\right)^2}{2\sigma_2^2(t)}\right] \tag{9.24}$$

with mean

$$M_2(t) = \frac{b - c\tilde{a}}{\tilde{a}^2}\left(1 - e^{-\tilde{a}t}\right) + e^{-\tilde{a}t}x_0 - \frac{b}{a}t \tag{9.25}$$

and variance

$$\sigma_2^2(t) = \frac{D}{\tilde{a}}\left(1 - e^{-2\tilde{a}t}\right). \tag{9.26}$$

Therefore, we can finally write

$$P(x,t) = \mathcal{N}(M_1(t), \sigma_1^2(t))\mathcal{H}(1-x)C_1 + \mathcal{N}(M_2(t), \sigma_2^2(t))\mathcal{H}(x-1)C_2 \tag{9.27}$$

To find C_1 and C_2 we can use the normalization and the continuity condition, expressed by a boundary condition at $x = 1$. The normalization condition gives,

$$\int_{-\infty}^{\infty} P(x,t)dx = C_1\int_{-\infty}^{1}\mathcal{N}(M_1(t), \sigma_1^2(t)dx + C_2\int_{1}^{\infty}\mathcal{N}(M_2(t), \sigma_2^2(t))dx = 1, \tag{9.28}$$

we also knnow that

$$\int_{-\infty}^{1}\mathcal{N}(M_1(t), \sigma_1^2(t))dx = \frac{1}{2}\left[1 + \mathrm{erf}\left(\frac{1 - M_1(t)}{\sigma_1(t)\sqrt{2}}\right)\right] \equiv N_1(t), \tag{9.29}$$

and

$$\int_{1}^{\infty}\mathcal{N}(M_2(t), \sigma_2^2(t))dx = \frac{1}{2}\left[1 - \mathrm{erf}\left(\frac{1 - M_2(t)}{\sigma_2(t)\sqrt{2}}\right)\right] \equiv N_2(t). \tag{9.30}$$

The boundary condition $P_{on}(1,t) = P_{off}(1,t)$ leads to the relation

$$\frac{C_1}{C_2} = \frac{\sigma_1}{\sigma_2}\exp\left[\frac{\left(1 - M_1(t)\right)^2}{2\sigma_1^2(t)} - \frac{\left(1 - M_2(t)\right)^2}{2\sigma_2^2(t)}\right] \equiv Q(t). \tag{9.31}$$

Assembling both boundary and normalization conditions, we obtain,

$$\begin{aligned} C_1(t) &= \frac{Q}{QN_1 + N_2} \\ C_2(t) &= \frac{1}{QN_1 + N_2}. \end{aligned} \tag{9.32}$$

This complete our characterization of the probability density and provides the desired solution of the FPE. The time evolution of the PDF for a rate dependent load is shown in Fig. 9.3.

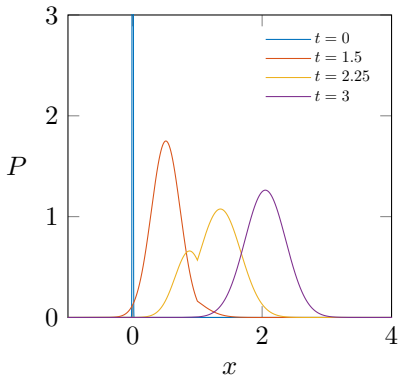

Figure 9.3: Probability density function of the reaction coordinate x of a single bond to a load varying in time as $y(t) = \nu t + y_0$, where $\nu = 1$, $y_0 = 0$, $\lambda = 1$, and $\beta = 10$.

$$P(x,t) = P_{on}(x,t)\mathcal{H}(1-x) + P_{off}(x,t)\mathcal{H}(x-1), \tag{9.33}$$

In Fig. 9.4, we illustrate the effect of finite rate of loading. Notice that at finite velocity of the driving the non-zero force is recorded even after rupture. Indeed, the averaged response of the system after rupture can be described by the equation $\frac{dx}{dt} = \lambda(\nu t - x)$, from where we have $x(t) = \nu t - \nu/\lambda$. Therefore, the residual force is simply $f(t) = \lambda(\nu t - x(t)) = \nu$.

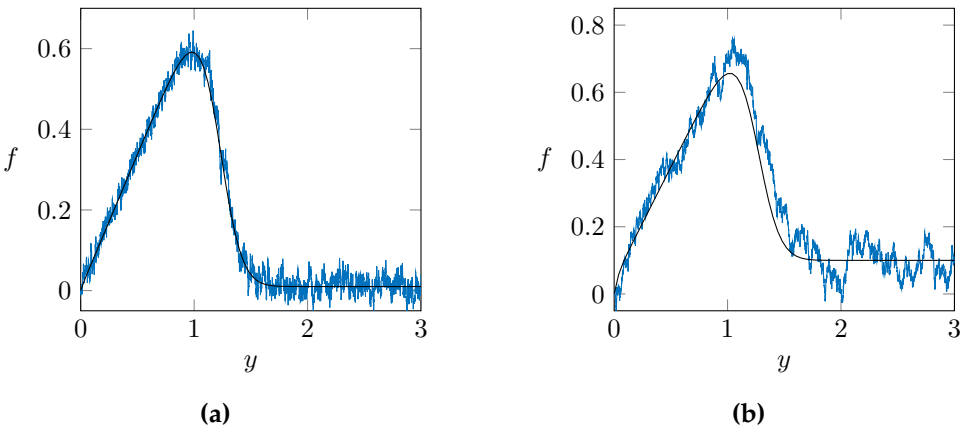

Figure 9.4: Dynamic response of a single bond with time dependent load. The Black curves are the averages force from the Fokker-Planck equation, while the blue curves are Langevin simulations, the curve is an average of 100 simulations. Common parameters: $\beta = 10$ and $\lambda = 2$ (a) $\nu = 0.01$ (b) $\nu = 0.1$.

9.2 Escape rate

Next, we shall be interested in the average time a particle remains in a specific binding site while being subjected to a constant rate of loading. More precisely, we study the transition time for a single bond as it switches from the bound (or closed) state to the unbound (or open) state.

Consider a stochastic process with initial data $x = x_0$ at time $t = 0$, where x_0 is in the interval $[a, b]$. The question is for how long the system will remain in the interval $[a, b]$. We define the probability of finding the particle inside the interval at time t as $P_{in}(t, x_0)$. It is equivalent to the probability that the exit time, $\mathcal{T}$ is greater than t. We impose an absorbing boundary condition at $x = b$ and a reflecting condition at $x = a$. We need to compute the integral of the distribution $P(x, t|x_0, 0)$ representing the solution of the FP equation, over the interval $[a, b]$

$$\text{Prob}(\mathcal{T} > t) = P_{in}(t, x_0) = \int_a^b P(x, t|x_0, 0)dx \tag{9.34}$$

Then the desired probability that the time to exit, $\mathcal{T}$, is smaller than t is

$$\text{Prob}(0 \leq \mathcal{T} \leq t) = 1 - P_{in}(t, x_0). \tag{9.35}$$

The probability density for $\mathcal{T}$ is

$$P_{\mathcal{T}}(t) = \frac{\partial}{\partial t}\text{Prob}(0 \leq \mathcal{T} \leq t) = -\frac{\partial}{\partial t}p_{in}(t, x_0) \tag{9.36}$$

and we can now write the expression for the mean first-passage time in the form

$$\langle \mathcal{T} \rangle = \int_0^\infty tP_T(t)dt = -\int_0^\infty t\frac{\partial}{\partial t}P_{in}(t, x_0)dt = \int_0^\infty P_{in}(t, x_0)dt \tag{9.37}$$

The last step is to integrate by parts and use the fact that $tP_{in}(t, x_0) \to \infty$ as $t \to \infty$, which follow from the assumption that $\mathcal{T}$ has a finite mean. Then, finally,

$$\langle \mathcal{T} \rangle = \int_0^\infty \int_a^b P(x, t|x_0, 0)dxdt. \tag{9.38}$$

In Fig. 9.5 we show the average escape time from our parabolic potential, which can be interpreted as the time of breaking under a fixed rate of loading.

9.3 Cohesion-decohesion phenomena

We now discuss the solutions of Eq. (9.1) when the potential $u(x)$ is periodic in x and the system is subjected to a constant loading rate, experiencing periodic attachment and detachment.

Suppose that $u(x)$ is a periodic potential built of parabolas separated by the same distance d. The rates of bonding ν_{on} and breaking ν_{off} are defined by the corresponding energy barriers ΔE_{on} and ΔE_{off}. The size of the barriers depend on y, hence on f. In the quasi-static limit, $\nu \to 0$, the system is in thermal equilibrium. In this simplest case, the breaking path is the same as the rebinding path and therefore the average force experienced by the bond is equal to zero.

To analyze the effects of the finite rate of loading we first address the limiting case when temperature tends to zero. In this limit, the system can no longer cross barriers and will disconnect/connect only in the marginally stable spinodal points.

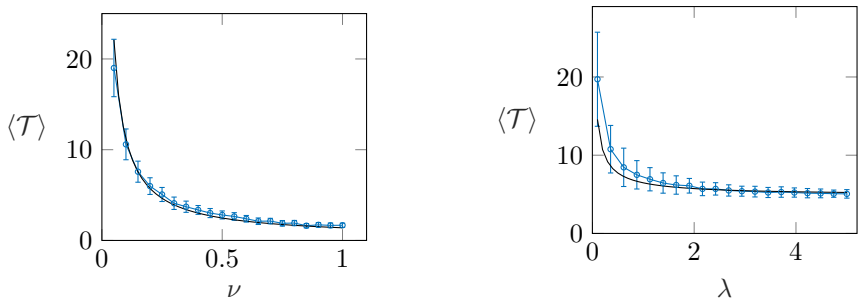

Figure 9.5: Mean escape time for the bond initially being placed at the bottom of the parabola $u(x)$. The black line is the predicted value from Eq. (9.38) and the blue line is a result of numerical simulations based on the associated Langevin equation. (a) Mean escape time versus the rate of loading ν, at $\beta = 10$ and $\lambda = 1$. (b) Mean escape time as a function of the modulus λ, at $\beta = 10$ and $\nu = 0.2$.

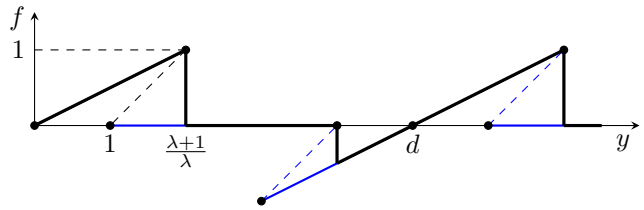

Figure 9.6: The load path of the bond as it moves at a high velocity (black thick line). Note that the transition points are following the spinodal points in both detaching and attaching.

The dependence of force on time, in this case, is illustrated in Fig. 9.6. We implicitly assumed here that the relaxation time is much smaller than the loading time.

The average force can be now easily computed by noting that the bond breaks when the force is equal to 1 and rebuilds when the force has the magnitude $\frac{\lambda}{\lambda+1}$, corresponding to $y_{off} = 1 + 1/\lambda$ and $y_{on} = 1$, respectively. The average force depends on the distance between the binding sites d. From Fig. 9.6 one can see that the average force is equal to the area under the corresponding segment of the metastable force-elongation curve, divided by the distance d

$$\bar{f} = \frac{2\lambda + 1}{2d\lambda(\lambda + 1)}. \tag{9.39}$$

In Fig. 9.7a we illustrated the typical average force $\bar{f}$ computed in this way and superimposed on the results of numerical simulations at low temperatures (high β). The value $\bar{f}$ also defines the maximum average force for a given λ because any finite temperature will make the breaking happen before the spinodal point is reached. The average force given by the formula above does not take into account the viscous contribution, hence in the graphs, we presented the value $f = \lambda(y - x) - \nu$. We observe that for high temperatures the force diminishes smoothly to zero as the driving velocity decreases while at low temperatures our computations predict an abrupt transition as in Bingham rheological model, see Fig. 9.7b, and suggest a possibility of stick-slip behavior.

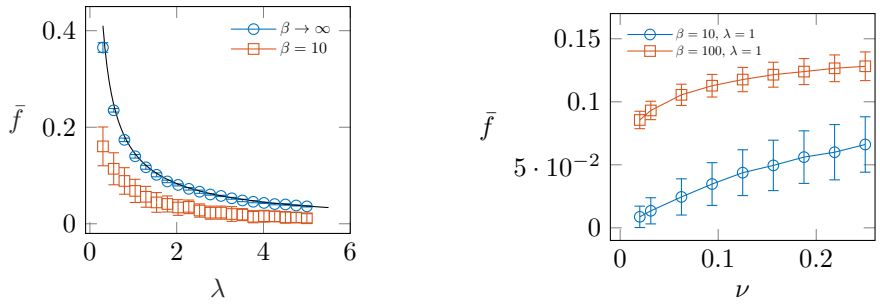

(a) **(b)**

Figure 9.7: (a) Average force on the bond as a function of λ, for a fixed $\nu = 0.1$. (b) Average force as a function of the driving velocity, for a fixed $\lambda = 1$.

The typical time dependence of the force is illustrated in Fig. 9.8, and we point out the possibility of two qualitatively different types of behavior. Thus, in Fig. 9.8a-d we see a stick-slip motion, while in Fig. 9.8c-f we see smooth sliding. The microscopic nature of the motion becomes more clear if we define the spin parameter ϕ which takes the value one when the binder is connected and zero otherwise. It can be then viewed as a probability of the binder being connected, see its typical behavior illustrated in Fig. 9.8d-f.

Note that the stick-slip motion has been recorded at low values of temperatures and large values of elastic modulus λ. Low temperatures prevent the system from crossing energetic barrier, and large λ decreases the domain of metastability. Smooth sliding is instead observed at high temperatures and small values of λ. It should be noted that the distance between the binding sites d also plays an important role: if the binding sites are close, the metastable domain extends, and a binder can jump from one binding site to another. In this sense, d plays a role similar to λ: large d will ensure that the bond is disconnected for a long time before it reconnects again at the next binding site.

Next, we study the average force developed by a collection of binding elements, each behaving as it was described in the previous section. We already know that both rigidity and temperature can drastically affect the mechanical response of the system by inducing a brittle-ductile transition. We will observe that the force-velocity curves are also different depending on whether the system is in brittle or in the ductile state.

In the same framework as for a single bond, we can derive the non-dimensional Langevin system describing the stochastic evolution of a bundle of N elements

$$\begin{cases} \dfrac{dx_i}{dt} = -x_i \mathcal{H}(1-x_i) + \lambda(y - x_i) + \sqrt{2\beta^{-1}}\xi(t) \quad \text{for } 1 \le i \le N \\ \dfrac{dy}{dt} = -\dfrac{N\lambda}{\eta}(y - \dfrac{1}{N}\sum_{i=1}^{N} x_i) + \dfrac{N\lambda_f}{\eta}(z - y) + \dfrac{1}{\eta}\sqrt{2\eta\beta^{-1}}\xi(t). \end{cases} \tag{9.40}$$

In Fig. 9.9, we illustrate stationary solutions of the system (9.40). The simulation was performed by applying fixed elongation z and numerically integrating the equations until the system reaches an equilibrium state. In the ductile regime, shown in Fig. 9.9(a), the simulation nicely approximated the predicted equilibrium path, while in the brittle regime, Fig. 9.9(c), the system was not able to find the global minimum of the energy and instead exhibited a hysteresis. This is related to the fact that the

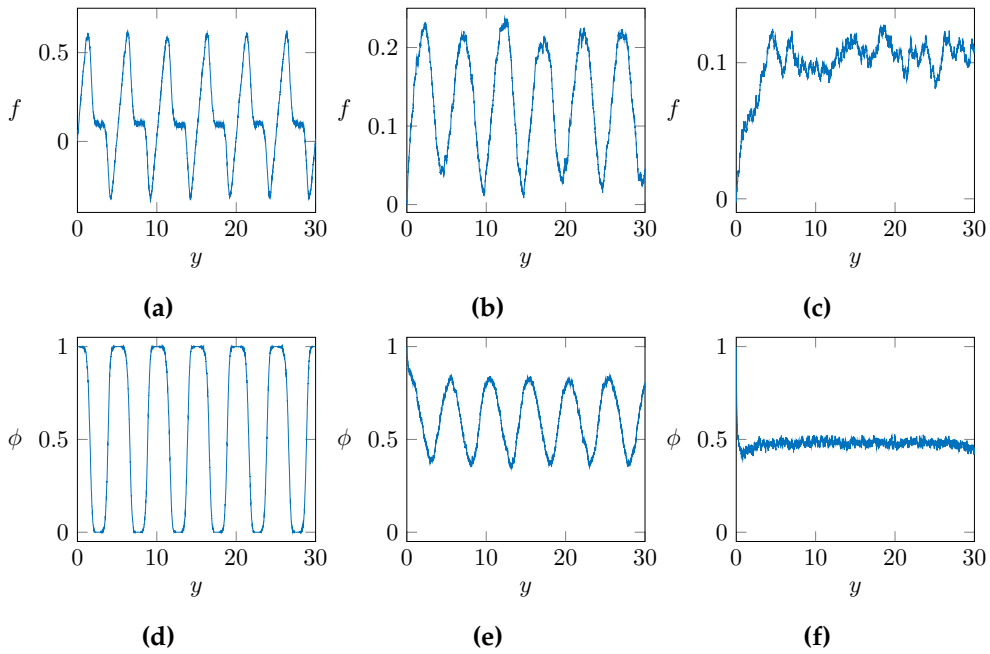

Figure 9.8: Time series of the force (top figures) and the fraction of bounded bonds (bottom figures), for a bundle of $N = 100$ bonds on a periodic potential of $d = 6$. The results are the averaged trajectories of 1000 paths. (a) and (d) $\beta = 20$, $\lambda = 1$, $\lambda_f = 1$ and $\nu = 0.03$; (b) and (e) $\beta = 2$, $\lambda = 1$, $\lambda_f = 1$ and $\nu = 0.3$; (c) and (f) $\beta = 2$, $\lambda = 0.1$, $\lambda_f = 0.25$ and $\nu = 0.3$.

time of the simulation was not long enough for the system to cross the energy barrier necessary to follow the global minimum path.

9.4 Stick-slip vs smooth sliding

As we have already mentioned, in the studies of thermally activated friction, one is often interested in distinguishing between the two types of behavior: sliding and stick-slip. The former refers to the smooth evolution of the bonds along the periodic potential, while the latter invokes sudden collective breaking and reconnections of the bonds. We can obtain sliding in our setting by broadening the metastability region and increasing temperature, which allows the system to jump back and forth between different states. If, however, the temperature is low and metastability region is narrow, the averaged response of the bonds will be sudden and can be interpreted as the stick-slip behavior. It was claimed in (Filippov, Klafter, and Urbakh, 2004) that in order to have stick-slip behavior one should consider necessarily an aging effect, which would prevent a rapid rebinding of the broken bonds. In our framework, the "age" of the bond is related to the distances between the binding sites: once a bond is disrupted, it can only bind again when approaching sufficiently close the next binding site.

Given that we can associate brittleness with stick-slip sliding and ductile with smooth sliding, we note that these different behaviors can be achieved by changing the rigidity of the system. For instance, low values of λ mean a broad domain of metastability for each microscopic configuration, in particular, the size of the metastable branch grows as $1/\lambda$. In this sense, the lowering λ would have the same effect as decreasing the distance between the binders d. On the other hand,

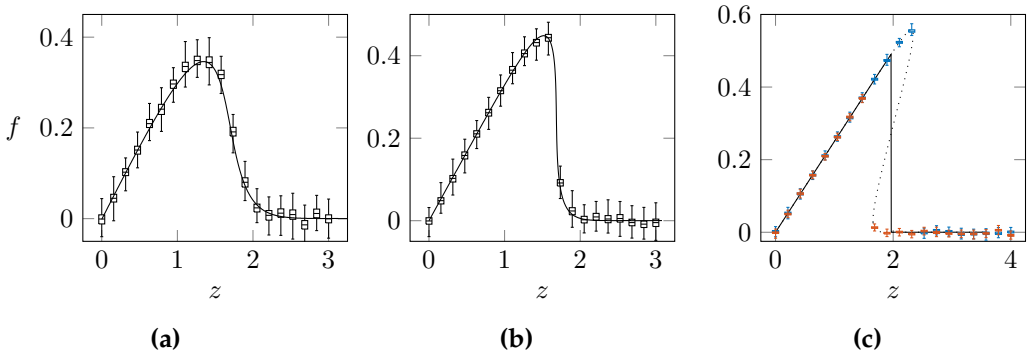

Figure 9.9: Force elongation curves. Boxplots are the result of the simulations using Eq. (9.40). Solid curves correspond to the equilibrium path predicted by the canonical description in the last section (a) Ductile, $\beta = 4$, $\lambda = 1$ and $\lambda_f = 1$. (b) Critical, $\beta = 8$, $\lambda = 1$ and $\lambda_f = 1$, and (c) Brittle, $\beta = 20$. The blue (red) boxplots are the equilibrated response at the fixed elongation in the undinding (rebinding) path. $\lambda = 1$, $\lambda_f = 0.5$. The equilibration time is finite and set to $t = 1000$ and the time step $dt = 10^{-4}$.

increasing temperature favors crossing of the energy barriers, thus also biasing the sliding mode vis-a-vis the stick-slip mode. In the latter, because of the large macroscopic barriers, even at very low loading rates the system will not be able to find the global minimum, see Fig. 9.9. Even though we expect that the average force should tend to zero when the driving velocity approaches zero, this behavior is not observed in the thermodynamic limit when the system is brittle because of the developing metastability. Instead, the force-velocity curve exhibits abrupt drop at zero velocity as we have observed numerically, see Fig. 9.11.

9.5 Conclusions

To understand the effects of time-dependent loading, we developed in this Chapter a kinetic model based on the overdamped Langevin dynamics. We first studied the dynamics of a binder attached to a single binding site and obtained an analytical solution of the corresponding Fokker-Planck equation, which allowed us to compute the force-elongation curve and the mean time of dissociation of a bond. Our study of kinetics at a fixed rate of loading revealed a spurious viscous force, that was also captured by the solution of the Fokker-Planck solution. We then studied a single binder traveling through a periodic potential and identified two limiting regimes, stick-slip and smooth. We then formulated the Langevin system for a bundle of N binders and studied its different modes of sliding when the system is driven at a constant velocity through an elastic spring. Temperature, internal rigidity and the distance between the binding sites have been identified as the main parameters affecting the dynamical response of the system. We associated stick-slip motion with brittle fracture and smooth sliding with the ductile fracture, which also suggests that there is an interesting crossover regime of sliding that should show scaling and should be the dynamic analog of the critical fracture. This regime may be of interest not only for cellular adhesion/friction but also for the mechanics of earthquakes.

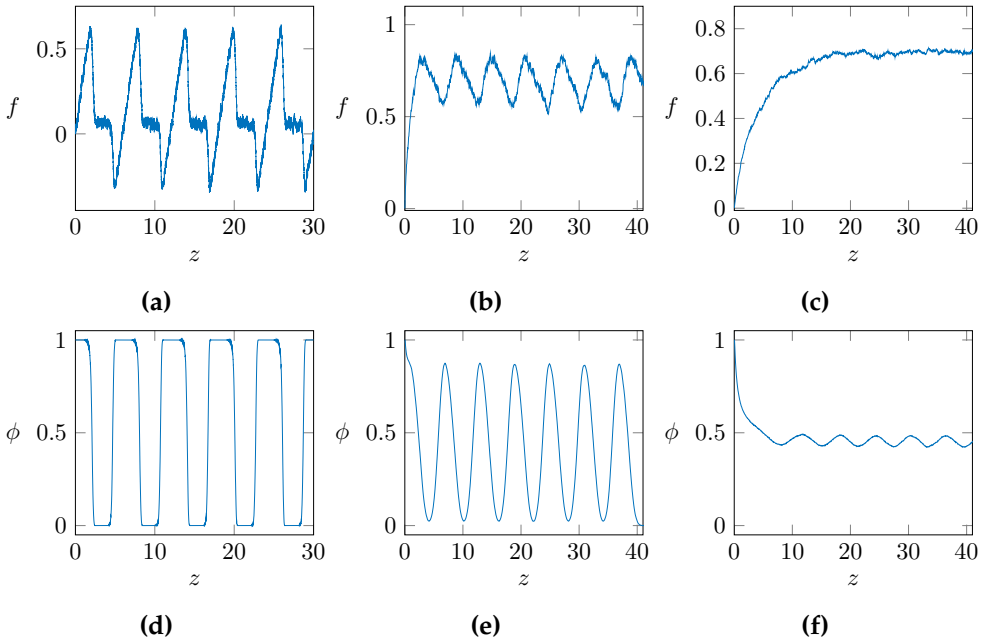

Figure 9.10: Time series of the force (top figures) and the fraction of bounded bonds (bottom figures), for a bundle of $N = 100$ bonds on a periodic potential of $d = 6$. The results are the averaged trajectories of 1000 paths. (a) and (d) $\beta = 20$, $\lambda = 1$, $\lambda_f = 1$ and $\nu = 0.03$; (b) and (e) $\beta = 2$, $\lambda = 1$, $\lambda_f = 1$ and $\nu = 0.3$; (c) and (f) $\beta = 2$, $\lambda = 0.1$, $\lambda_f = 0.25$ and $\nu = 0.3$.

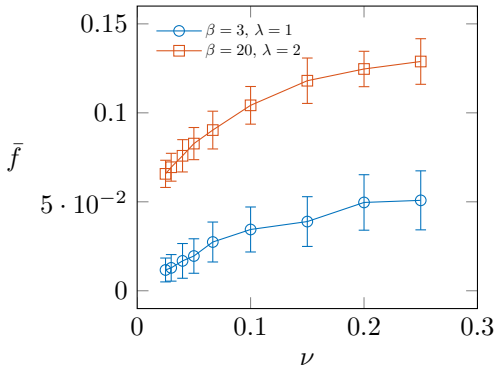

Figure 9.11: Average force as a function of the velocity. In red, a characteristic brittle regime is submitted to several loading rates. In blue, the system is ductile. The outer spring $\lambda_f = 1$ in both cases.

Chapter 10

Random decohesion and Burgers turbulence

To describe the interplay of disorder and temperature analytically, we now simplify our system even further. Assume that individual breakable elements are represented by two-state spin variables differentiating between bound and unbound configurations. Such a model will still capture the brittle-ductile transition, but will now allow us to quantify the combined effects of the disorder, temperature and internal rigidity of the system. The use of a spin variable instead of double well energy makes the energy multi-valued. However, this does not affect the behavior of our system at strongly 'below-melting' temperatures which are of most interest to this study.

In this Chapter, we reduced the equilibrium description of such spin system to the solution of a Burgers equation governing the behavior of the force developed by the bundle. The inverse of the rigidity plays the role of time while the applied load becomes the spatial coordinate. In this setting, the ductile-brittle transition can be interpreted as a formation of a shock wave. In particular, we show that for a finite system and non-zero temperature the shock wave is spread/diffusive, meaning that no discontinuities/brittleness can be observed. In the thermodynamic limit, the Burgers equation becomes inviscid (Hopf equation), and the emerging discontinuous shock is then able to capture the phenomenon of brittleness. The resulting phase diagram shows that brittleness can be associated with the first-order phase transition while the scaling crossover regime is the direct analog of the classical critical point.

Even though the Burgers equation can be in principle integrated analytically (Cole, 1951; Hopf, 1950), the solutions can be represented only implicitly. It has been shown to describe the asymptotic behavior for several nonlinear dissipative systems, which triggered a recent interest to makes the solution constructive for the case of random initial data (Bec and Khanin, 2007). This setting is close to our case where random initial data for the Burgers equation represent the quenched disorder in the system. This observation builds a link between the problem of cellular cohesion and the problem of decaying Burgers turbulence (Kida, 1979; Gurbatov et al., 1997).

10.1 The spin version of the model

Consider again N parallel fibers attached to a pair of rigid backbones. Each fiber, identified by a subscript $i = 1, \dots, N$, contains an elastic element with stiffness κ connected in series with a bi-stable spin unit. The two spin configurations represent the bound ($X_i = 0$) and the unbound ($X_i = a$) configurations of the bond. The system is loaded through a spring of stiffness κ_f in series with the backbone. As before, this external spring can be viewed as a lump description of the external elastic environment.

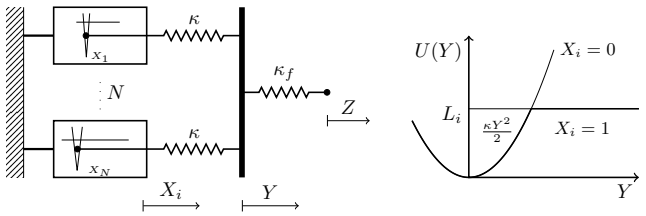

Figure 10.1: Mechanical model of the bundle structure and the potential energy of a single bond.

If we non-dimensionalize lengths by a and total energy by κa^2 we can write the energy of the system in the form

$$\mathcal{H}(\mathbf{x}, y, z) = \sum_{i=1}^{N} \left[l_i x_i + \frac{1}{2} y^2 (1 - x_i) \right] + N \frac{\lambda_f}{2} (z - y)^2 \tag{10.1}$$

where $\lambda_f = \kappa_f/(\kappa N)$; $x_i = X_i/a = \{0, 1\}$, $y = Y/a$, $z = Z/a$ are the non-dimensional lengths and $l_i = L_i/a$, $i = 1 \dots N$ is the energetic bias, which is assumed to be a random variable drawn from a continuous distribution with the probability density $p(l)$.

The mechanical properties of such system exposed to a thermal bath can be obtained by computing the partition function,

$$\mathcal{Z}(\beta, z) = \int dy \sum_{x \in \{0,1\}^N} \exp\left[-\beta \mathcal{H}(\mathbf{x}, y, z) \right]. \tag{10.2}$$

The independence of the spin variables allows us to rewrite it as

$$\begin{aligned} \mathcal{Z}(\beta, z) &= \int dy\, e^{-\beta N \frac{\lambda_f}{2}(z-y)^2} \prod_{i=1}^{N} \left(e^{-\beta l_i} + e^{-\beta y^2/2} \right) \\ &= \int dy\, e^{-\beta N \left[\frac{\lambda_f}{2}(z-y)^2 - \frac{1}{\beta N} \sum_{i=1}^{N} \ln \tilde{\mathcal{Z}}\{l_i\} \right]} \end{aligned} \tag{10.3}$$

where $\tilde{\mathcal{Z}} = e^{-\beta l_i} + e^{-\beta y^2/2}$. We now introduce new notations: $\nu = 1/\lambda_f$ (inverse rigidity) and $\varepsilon = z$ (applied strain) and rewrite Eq. (10.3) in the form:

$$\mathcal{Z}(\beta, \varepsilon) = \sqrt{\frac{N\beta}{2\pi\nu}} \int_{-\infty}^{\infty} e^{-\frac{N\beta}{2\nu}(\varepsilon - y)^2} \Phi(y) dy, \tag{10.4}$$

where,

$$\Phi(y) = \sqrt{\frac{2\pi\nu}{N\beta}} \prod_{i=1}^{N} \left(e^{-\beta l_i} + e^{-\beta y^2/2} \right). \tag{10.5}$$

Following (Mungan and Yolcu, 2010), we can identify Eq. (10.4) with the Green's function solution of the 1D heat equation where ν is time, ε is space, while the function $\Phi(y)$ represents initial data. The Cole-Hopf transformation (Cole, 1951; Hopf, 1950)

$$\sigma(\varepsilon, \nu) = -\frac{1}{\beta N} \frac{\partial}{\partial \varepsilon} \log \mathcal{Z}(\beta, \varepsilon)$$

allows one to view the function $\sigma(\varepsilon, \nu)$ as a solution of the Burgers equation:

$$\frac{\partial \sigma(\varepsilon, \nu)}{\partial \nu} + \sigma(\varepsilon, \nu) \frac{\partial \sigma(\varepsilon, \nu)}{\partial \varepsilon} = \eta \frac{\partial^2 \sigma(\varepsilon, \nu)}{\partial \varepsilon^2}, \quad (\varepsilon, \nu) \in \mathbb{R} \times (0, \infty), \tag{10.6}$$

where viscosity is $\eta = \frac{1}{2\beta N}$. The 'initial' conditions are

$$\sigma(\varepsilon, 0) = \sigma_0(\varepsilon) = -\frac{1}{\beta N}\frac{\partial}{\partial \varepsilon}\log \Phi(\varepsilon) = \frac{1}{N}\sum_{i=1}^{N}\frac{\varepsilon}{2}[1 + \tanh\frac{\beta}{2}(l_i - \varepsilon^2/2)].$$

The inviscid Burgers (Hopf) equation with $\eta = 0$ emerges in either to the thermodynamic limit $N \to \infty$ or to the zero temperature limit $\beta \to \infty$

$$\begin{cases} \dfrac{\partial \sigma(\varepsilon,\nu)}{\partial \nu} + \sigma(\varepsilon,\nu)\dfrac{\partial \sigma(\varepsilon,\nu)}{\partial \varepsilon} = 0 & (\varepsilon,\nu) \in \mathbb{R}\times(0,\infty), \\ \sigma(\varepsilon,0) = \sigma_0(\varepsilon) & \varepsilon \in \mathbb{R}. \end{cases} \tag{10.7}$$

This problem can be solved if we know the field of characteristics

$$\varepsilon(\nu) = \sigma_0(\varepsilon_0)\nu + \varepsilon_0 \tag{10.8}$$

where $\varepsilon_0 = \varepsilon(\nu = 0)$. Along each characteristic curve the solution is given by the implicit relation

$$\sigma(\varepsilon, \nu) = \sigma_0(\varepsilon - \sigma_0(\varepsilon_0)\nu, \nu). \tag{10.9}$$

Below we consider in more detail each of the two cases: first the thermodynamic limit $N \to \infty$ and then the zero temperature limit $\beta \to \infty$.

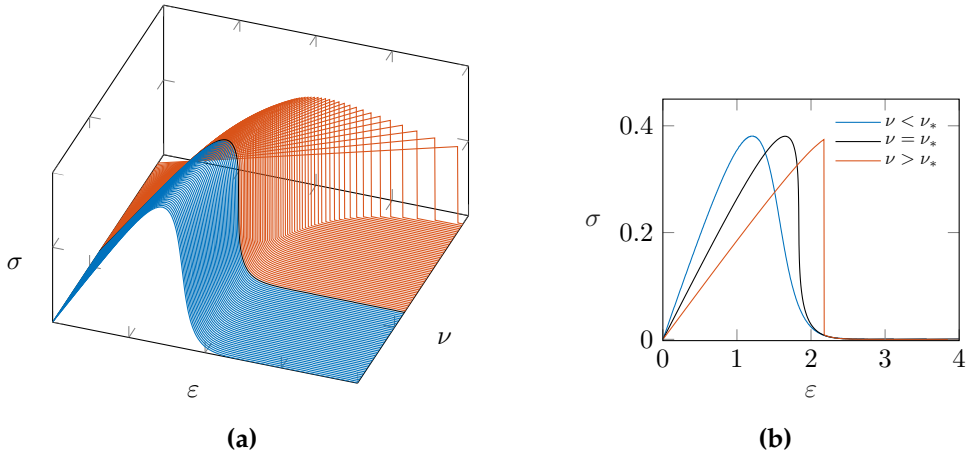

(a) **(b)**

Figure 10.2: Formation of shock wave at increasingg $\nu = 1/\lambda_f$. (a) The initial data evolves smoothly (blue) until the formation of a discontinuity (red).

10.2 Thermodynamic limit

Introduce the probability density $\rho_N(l) \equiv \frac{1}{N}\sum_{i=1}^{N}\delta(l - l_i)$. Then we can write the initial data in the form:

$$\sigma_0(\varepsilon) = \int dl\, \rho_N(l)\frac{\varepsilon}{2}[1 + \tanh\frac{\beta}{2}(l - \varepsilon^2/2)]. \tag{10.10}$$

By the law of large numbers, when $N \to \infty$, the discrete probability density $\rho_N(l)$ converges to a continuous distribution, $p(l)$, and the sample average converges to the expected value

$$\sigma_0(\varepsilon) = \int dl\, p(l)\frac{\varepsilon}{2}[1 + \tanh\frac{\beta}{2}(l - \varepsilon^2/2)]. \tag{10.11}$$

If we assume that all thresholds are identical, $p(l) = \delta(l - l_0)$, we can write $\sigma_0(\varepsilon) = \frac{\varepsilon}{2}[1 + \tanh \frac{\beta}{2}(l_0 - \varepsilon^2/2)]$. We illustrate the solution of such problem in Fig. 10.2a where we see the formation of a discontinuity (shock), when ν becomes sufficiently large. The shock formation takes place when the characteristic curves intersect. The corresponding *breaking time* is $\nu_* = \min_{\varepsilon \in \mathbb{R}} \left\{ -\frac{1}{\sigma_0'(\varepsilon)} \right\}$ (Whitham, 2011). Fig. 10.2b shows the the solutions at different stages of the evolution, both before and after the shock formation.

Note that by construction $\sigma = \mathcal{F}_\varepsilon$ is the tension developed in the system. The formation of the shock wave can be then interpreted as the transition from ductile to brittle behavior and the breaking time ν_* represent the critical value of the rigidity λ_f at which the system becomes critical. In Fig. 10.3 we show the corresponding phase diagram showing the critical point and the line of the first order phase transition separating broken and unbroken states. Remarkably, this diagram has the same structure as the phase diagram for the liquid-gas phase transition.

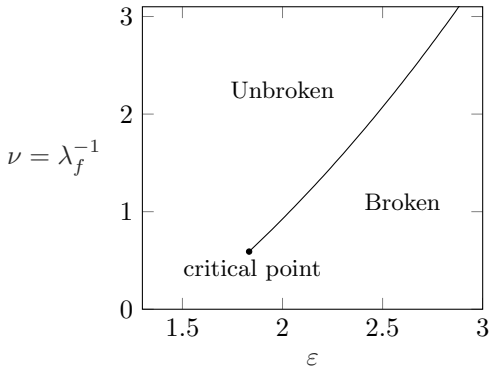

Figure 10.3: Phase diagram at fixed temperature $\beta = 4$ and no disorder.

10.3 Zero temperature limit

Another way to obtain the inviscid Burgers equation is to consider the limit $\beta \to \infty$. In this case, the initial condition for the Burgers/Hopf equation can be written as

$$\sigma_0(\varepsilon) = \frac{1}{N} \sum_{i=1}^{N} \varepsilon H(l_i - \varepsilon^2/2), \tag{10.12}$$

where $H(x)$ is the Heaviside function and we used the fact that

$$H(x) = \lim_{k \to \infty} \frac{1}{2}(1 + \tanh kx). \tag{10.13}$$

The initial condition is then a discontinuous function with shocks in random locations. Once the thresholds are assigned to each bond, the system is deterministic. For the distribution of thresholds we used the one-parameter Weibull distribution with the probability density $p(x) = \rho x^{\rho - 1} e^{-x^\rho}$. In Fig. 10.4a we show that as 'time' increases, the shocks progressively merge until finally, only one shock survives, representing the regime of brittle fracture. In Fig. 10.4b we track of the position of individual shocks to visualize their coalescence sequence. One can show that the

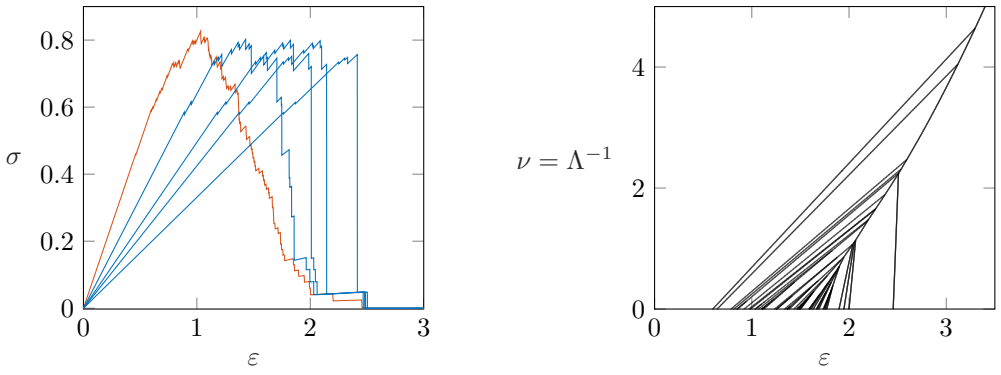

(a) **(b)**

Figure 10.4: (a) Shock evolution in the athermal limit, with thresholds randomly distributed according to Weibull distribution. A system of $N = 50$ elements. The initial data $\sigma_0(\varepsilon)$ is presented in red. (b) Shock trajectories from a random initial condition. System of $N = 50$ elements, and thresholds following a Weibull distribution with $\rho = 2$.

most complex structure of shocks is observed at the value of ν (which indicate a particular moment of our 'time') corresponding to the critical point of the problem with ensemble averaged initial data.

Indeed, consider the 'time-dependent' statistics for the number of shocks $n_i(\nu)$ corresponding to different realizations of the quenched disorder parameterized by the initial number of shocks N_r. In particular, we can track the mean number of shocks $\mu(\nu) = \frac{1}{N_r}\sum_{i=1}^{N_r} n_i$ and their standard deviation $s(\nu) = \sqrt{\frac{1}{N_r}\sum_{i=1}^{N_r}(n_i - \mu)^2}$. These time dependencies are illustrated in Fig. 10.5. When we normalize the mean by the number of units, N and the standard deviation by $\sqrt{N}$ all the curves collapse onto one, as seen in Fig. 10.6. We observed that while the mean number of shocks is monotonously decreasing as 'time' (ν) increases, the standard deviation shows a peak for some intermediate value of ν. This maximum indicates the largest complexity of the distribution of shocks. Not surprisingly, it is located close to the critical point where fluctuations are scale-free. We note that in the conventional decaying Burgers turbulence the initial data are assumed to have a zero average, which postpones the scaling regime till $t = \infty$. Instead, here we assumed the nontrivial averaged behavior for the initial data, which has shifted the scaling regime to finite time.

To summarize, we have drawn a parallel between the ground-state mechanical response of our mean-field system and the formation of shock waves in the Burgers equation. By viewing the inverse of the rigidity of the system as time and the applied strain as space, we represented the 'dynamics' of stress as the nonlinear wave propagation phenomenon, with viscosity proportional to the temperature and inversely proportional to the system size. We have shown that any finite system at non-zero temperature has diffusive shocks that exclude discontinuities and makes the system ultimately ductile. In the thermodynamic limit, the viscosity vanishes, and we retrieve the inviscid Burgers equation supporting discontinuous solutions and allowing for ductile to brittle transition. An interesting prediction of the model is that the shock formation 'time/rigidity' corresponds to the crossover (critical) regime marking the transition from ductile to brittle behavior. Brittleness, representing cooperativity and synchronization, can then be viewed as an emergent property arising in

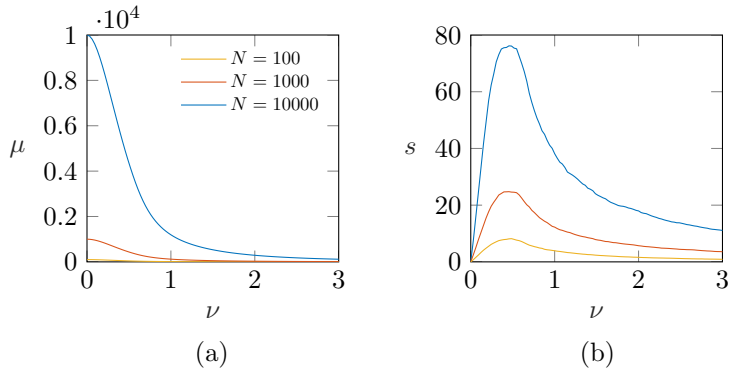

Figure 10.5: (a) Mean number of shocks; (b) Standard deviation of the number of shocks. The statistics consists of 1000 realizations of the quenched disorder (Weibull distribution $\rho = 3$) of several system sizes.

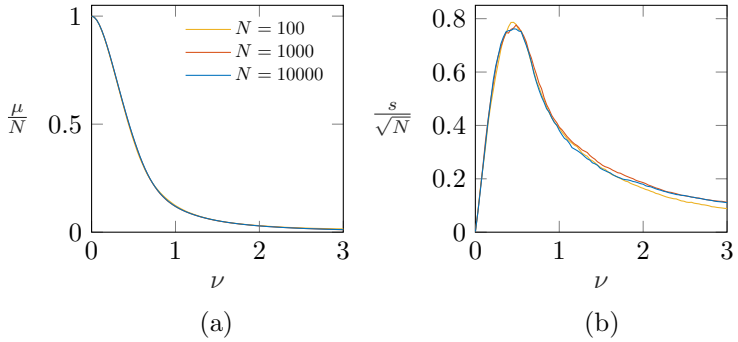

Figure 10.6: (a) Normalized mean number of shocks; (b) Normalized standard deviation of the number of shocks. The statistics consists of 1000 realizations of the quenched disorder (Weibull distribution $\rho = 3$) of several system sizes.

the thermodynamic limit as a result of the interaction of the infinite number of individual units. Instead, a finite system behaves as ductile material at any non-zero temperatures.

Chapter 11

Conclusions

In this Part, we presented a mean-field mechanical description of cellular adhesion, which we interpreted as a problem of thermalized fracture in a disordered discrete system. A focal adhesion is described as a collection of breakable units connected in parallel and interacting through a common series spring. We studied the equilibrium and the non-equilibrium marginal behavior of this system under quasistatic loading and at a finite rate of loading. By changing the stiffness of the series springs, we were able to obtain the crossover from brittle to ductile response. At zero temperature the fluctuational behavior in the brittle regime is supercritical with spinodal exponents and a finite peak in the distribution of avalanches. In the ductile regime, the system exhibits subcritical or 'pop' behavior with a Gaussian distribution of fluctuations. The crossover regime separating brittle and ductile behavior show scaling with the new exponent, not previously known in the FBM studies. We computed the corresponding mean-field critical exponents analytically for both energy minimizing (zero temperature limit of a thermal equilibrium) and marginal (non-equilibrium, zero viscosity limit of an overdamped dynamics) decohesion processes. We then studied the effects of finite temperature and finite rate of driving. Our main finding is that the interplay between the rigidity, disorder, and temperature can drastically change the overall response of the system not only in quasistatic conditions but also in dynamic loading where brittleness can be associated with stick-slip frictional behavior while ductility means continuous quasi-viscous sliding. These results may be used in the modeling of cell motility in complex environments where our rigidity and disorder may be identified with particular rheological and structural conditions.

PART II:
SKELETAL MUSCLES

In this Part, we study the peculiarities of the mechanics of passive force generation in skeletal muscles. Under an abrupt mechanical perturbation, a tetanized muscle fiber will first respond elastically but then show a counter-intuitive tension recovery in the millisecond timescale. Such fast force recovery is mostly ATP independent, and experiments show that it is due to the collective conformational change in the myosin heads binding the actin filaments. We study a minimalistic purely mechanical model of a half-sarcomere, the basic unit of contraction, which is still able to capture the synchronous conformational change in a large number of myosin heads. We show that the direct analogy between our model and the random field Ising model (RFIM) allows one to compute the thermodynamic properties of the disordered muscle system by using the classic replica trick. The new result is the demonstration that the geometrical frustration, caused by disregistry between the periodicities of the extruding myosin heads and the actin binding sites, is the factor in ensuring the optimal functioning of the system. The optimality is understood here as the closeness to the critical point, and we show that the muscle machinery operates in the vicinity of two adjacent, but distinct critical points corresponding to elongation-controlled and force-controlled ensembles. We argue that criticality is the way for the muscle to respond robustly and swiftly to external perturbations. The necessity of double criticality is linked to the non-affinity of the mechanical response of the muscle fiber which places individual contractile elements in the mixed, soft-hard loading conditions. We then extended the model by introducing steric short-range interactions which may compete with the largely long-range interactions imposed by the filaments. We show that destabilizing anti-ferromagnetic short interactions can drastically change the qualitative response of the muscle system stabilizing the regime of isometric contractions by turning the negative stiffness into the positive one. We used the classical Landau approach to generate the complete phase diagram of the system exhibiting a line of second-order phase transitions that hits a tricritical point and then continues by a line of first-order phase transitions. This phase diagram shows that the system may be in fact placed in the vicinity of several different regimes which allows for the broadest repertoire of mechanical responses. The experimental verification of our predictions should be the next step of this research project.

Chapter 12

Introduction

In this Chapter, we discuss the phenomenology of the passive force generation under fast loading and introduce the main constitutive elements of the model. In particular, we show how the quenched disorder can model steric incommensuration between the myosin heads and actin binding sites in the cross-bridge assembly. We present the mechanical description of the cross-bridge and discuss the relation of this model with the classical Huxley-Simmons model, which can also account for the presence of quenched disorder.

12.1 Passive force generation

Sudden application of a mechanical perturbation to an active muscle fiber is one of the oldest method of studying the mechanical properties of active muscle fibers (Huxley and Simmons, 1971; Podolsky, 1960). The time course of such experiments is illustrated in Fig. 12.1. When a quick length perturbation (0.12ms) is applied to an isometrically contracting muscle (T_0), we first observe an abrupt drop in the tension during the length step (T_1) due to the elasticity of the CB, followed by a fast recovery of the tension level (T_2) caused by a synchronous conformation change in myosin shape, the power stroke (Irving et al., 1992; Piazzesi et al., 2002).

The response illustrated by Fig. 12.1(b) suggests the presence of two structural elements,

1. An elastic element whose length is altered abruptly, producing the large initial change of tension. It is described here by a Hookean linear spring with stiffness κ_0.

2. A power-stroke element with viscous and elastic properties, whose length re-adjusts itself during the period of a few milliseconds immediately after the applied length change which results in the change of tension. It is described here by a two-state element. It can be described by a soft-spin like variable representing the angular position of the myosin head with respect to actin in the pre and post-power-stroke. In a hard spin version of the model, each energy well is infinitely sharp. The bottoms of the two wells are separated by the distance a representing the characteristic size of the power-stroke.

The power-stroke in the actomyosin system can be interpreted as passive folding which takes place in the myosin heads that are bounded in parallel to actin filaments. The thermomechanical behavior of this system was first studied by A.F. Huxley and R. M. Simmons (HS) in (Huxley and Simmons, 1971), who interpreted the pre- and post-power stroke conformations of the myosin heads as discrete chemical states (spin model). In this work, we follow a soft-spin statistical mechanical approach,

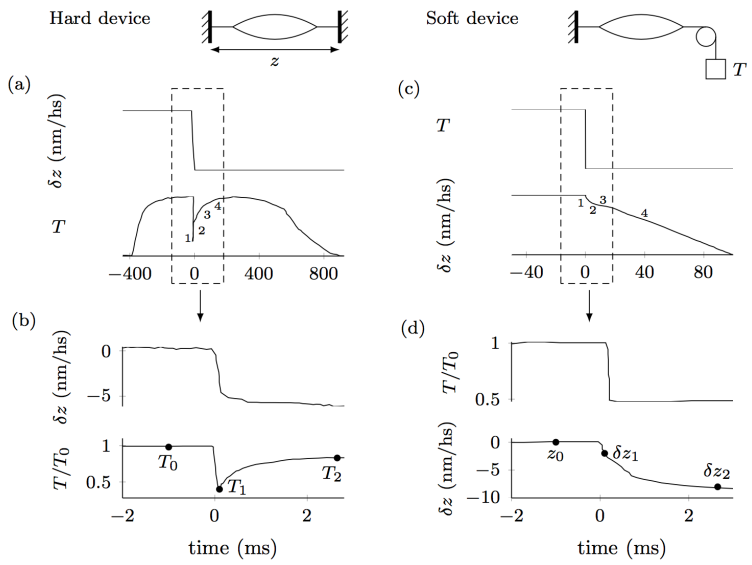

Figure 12.1: Fast transients in mechanical experiments on single muscle fibers in length clamp [hard device, (a) and (b)]; and in force clamp [soft device, (c) and (d)]. Typical experimental responses are shown on a slow timescale [(a) and (c)] and on a fast time scale [(b) and (d)]. In (a) and (c) the numbers indicate the 4 distinctive steps of the transient responses reflecting the elastic response (1), the processes associated with passive power strokes (2) and the ATP driven steady state (3-4). Figure extracted from (Caruel and Truskinovsky, 2018).

developed in(Marcucci and Truskinovsky, 2010a; Marcucci and Truskinovsky, 2010b; Caruel and Truskinovsky, 2016; Caruel, Allain, and Truskinovsky, 2015).

The original Huxley-Simmons Model successfully reproduced the measurements of the tension T_2 attained at the end of phase 2 of fast force recovery in a hard device, see Fig. 12.1. However, the observed behavior was obtained using an underestimated value of the stiffness of the myosin head (0.25pN nm^{-1} (Huxley and Simmons, 1971)), which was far by at least one order of magnitude from the one measured directly. Most recent measurements of the myosin stiffness (2.7$\pm$0.9 pN.nm^{-1}) (Brunello et al., 2014; Piazzesi et al., 2007; Linari et al., 1998) lead to the controversial prediction of a negative stiffness in the physiological regime of isometric contractions (Caruel, Allain, and Truskinovsky, 2013). In a later work, Huxley and Tideswell (Huxley and Tideswell, 1996) proposed that this discrepancy can be due to the inherent inhomogeneity of the actomyosin system. This inhomogeneity can be described as a quenched disorder in the positions of myosin molecules relative to attachment sites. Although some numerical simulations were performed by Huxley and Tideswell which took these new effects into account, the theoretical understanding of the obtained results was missing. This suggests the necessity of the thorough theoretical study of the effects of quenched disorder on the passive mechanical behavior of the muscle system.

12.2 Structure of a cross-bridge

Following (Huxley and Simmons, 1971; Caruel and Truskinovsky, 2016), we model a single cross-bridge as an elastic element (with stiffness κ_0) connected in series with

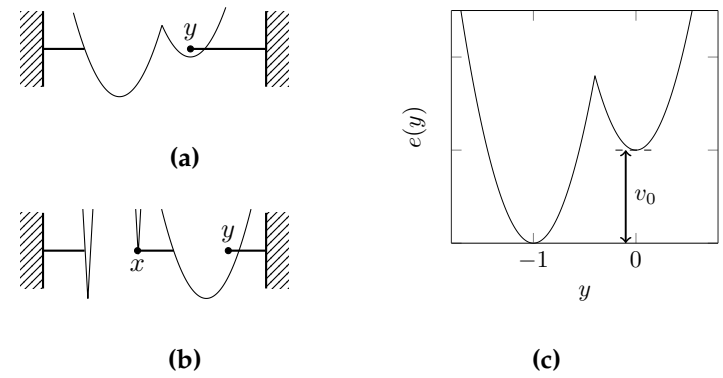

Figure 12.2: Huxley-Simmons (HS) model of a single cross-bridge: (a) mechanical representation of a myosin head as a bistable element. (b) Equivalent bistable element with the introduction of a spin variable x. (c) Internal energy landscape of the CB as function of its total elongation y.

a bi-stable spin unit. The bi-stable element mimics the power stroke: the two configurations, described by the internal variable x, represent conformational states of the myosin head, see Fig. 12.2. We set $\bar{x} = 0$ for pre-power-stroke (unfolded conformation) and $\bar{x} = -a$ for the post-power-stroke configuration (folded conformation). We assume that the two unloaded states have different energy levels, with the parameter $\bar{v}_0$ characterizing the energy bias. While x is a spin variable, the length $\bar{y}$, representing the displacement of the myosin relative to the actin, is a continuous variable. We chose a, the distance between the wells, as the reference length size. This parameter also represents the characteristic size of the power stroke: the overall displacement caused by the change in shape of the myosin head.

We perform the non-dimensionalization of the model by introducing dimensionless variables $x = \bar{x}/a$, taking values 0 and -1, and $y = \bar{y}/a$ and defining $v_0 = \bar{v}_0/\kappa_0 a$ as the non dimensional energy bias. The total energy of a single CB is normalized by $\kappa_0 a^2$ will then take the form

$$e(x, y) = (1 + x)v_0 + \frac{1}{2}(y - x)^2, \text{ for } x = \{0, -1\}. \tag{12.1}$$

This energy function is illustrated in Fig. 12.2c. If we denote $y_0 = v_0 - 1/2$ we can say that for $y > y_0$ the global minimum of the energy Eq. (12.1) is in the pre-power-stroke state, and otherwise it is in the post-power-stroke state .

12.3 Axial offset of the binding sites

Experimental studies using electron microscopy (EM) and x-ray diffraction have shown that the binding of cross-bridges is restricted to limited segments of the actin filament known as target zones (Tregear et al., 1998; Suzuki and Ishiwata, 2011). These zones are represented by two to three actin monomers, see Fig. 12.3. Moreover, it was found (Tregear et al., 2004) that the probability distribution of axial offsets from the target zone center is approximately Gaussian and that at least 60% of the attached cross-bridges are displaced within half of the spacing between actin monomers which corresponds to the offset of 2.76nm.

In our model, the offset for the individual cross-bridge can be represented by the reference elongation $y_0 = v_0 - 1/2$ which marks the boundary between pre and post-power stroke states. Because parameters v_0 and y_0 differ by a constant, the variance of v_0 is equal to the variance y_0. Hence, placing disorder in the energetic bias v_0 will be equivalent in our description to introducing a variable axial offset.

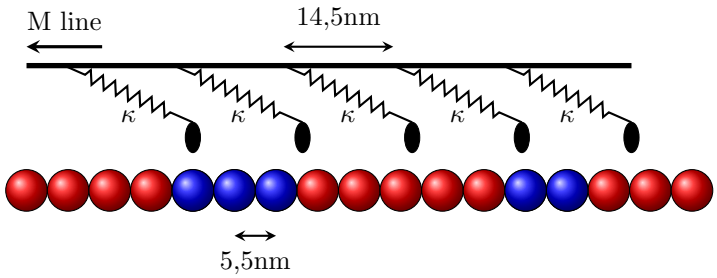

Figure 12.3: Schematic representation of the attachment sites. Each sphere represents an actin monomer; blue color delineate target zones.

To asses the statistical properties of such disorder we recall that if X is a random variable (v_0 or y_0 in our case) with finite mean $\mu = E(X)$ and finite variance $\sigma^2 = Var(X)$. If we suppose that the distribution of axial offsets between the myosin head and the actin-binding site is Gaussian, we can estimate its standard deviation by noting that the probability for the variable to be in the range $\pm k\sigma$ is given by,

$$\Pr(\mu - k\sigma \leq X \leq \mu + k\sigma) = \mathrm{erf}(\frac{k}{\sqrt{2}}). \tag{12.2}$$

We can then use the fact that for 60% of the cross-bridges the offset is in the range $\pm$2.76nm to find $k = 0.842$ and $\sigma = 3.3$nm.

We can alternatively assume the uniform distribution of disorder which attributes the same probability to all the range of the random variable. This is in a reasonable agreement with the range of the half-spacing of the actin monomer, and that is what Huxley and Tideswell postulated in their paper. If we follow their reasoning we get a standard deviation $\sigma \approx 1.6$nm, since $\sigma^2 = (b-a)^2/12$, where a and b are the extremities of the distribution and the assumption in (Huxley and Tideswell, 1996) is equivalent to setting $b - a = 5.5$nm.

However, as the Ref. (Tregear et al., 2004) indicates, there is a fraction of the myosins that are subjected to a greater value of stretching. Then, if we suppose that the random values of axial offset are uniform the statement that 60% of the CBs are within the $\pm$2.76nm means that 5.5 accounts for 60% of $a - b$, or $5.5/(b - a) = 0.6$. Therefore, $b - a \approx 9.2$, which would imply a standard deviation $\sigma_U \approx 2.65$nm, which is a larger value than the standard deviation used in (Huxley and Tideswell, 1996). This is because Huxley and Tideswell assumed that myosin could only bind within the $\pm$2.76nm range.

12.4 Modeling disorder in the HS framework

The intrinsic variation in the pre-stretch of the cross-bridges can be represented by the spatial inhomogeneity of the parameter $\bar{y}$. The analytical model of a single cross bridge, given by Eq. (12.1) allows us to express the degree of inhomogeneity in terms

of the energy bias between the two states. To this end, we replace a variable v_0 by the vector v_i, where the index i represents particular cross-bridge attached to an actin site. The two variables are simply related $\bar{y}_0 = \bar{v}_0/\kappa_0$ (dimensional), and therefore we can assume that their distributions are identical.

The original HS approach assumed that the behavior of the muscle fiber could be reduced to the behavior of the basic contractile unit, a half sarcomere, and treated the thick filament as a rigid backbone, in which the total elongation y is prescribed for all the N cross-bridges (CB) attached to actin. Here we allow the energetical bias to take random values within a given probability distribution. Then, the total energy of the bundle with a particular realization of the disorder can be written as,

$$E(\boldsymbol{x}, y)\{v_i\} = \sum_{i=1}^{N} \left[(1 + x_i)v_i + \frac{1}{2}(y - x_i)^2 \right] \tag{12.3}$$

where v_i, $i = 1 \dots N$ is the random realization of a variable distributed with probability density $p(v)$.

To study the equilibrium behavior of the system, we first compute the partition function for a given realization of disorder,

$$\mathcal{Z}(\beta, y)\{v_i\} = \sum_{x \in \{0,-1\}^N} \exp\left[-\beta E(\boldsymbol{x}, y)\{v_i\}\right]. \tag{12.4}$$

Here the argument $\{v_i\}$ indicates the dependence on the quenched disorder. The spin variables are independent, which allows us to write

$$\begin{aligned} \mathcal{Z}(\beta, y)\{v_i\} &= \prod_{i=1}^{N} \left(e^{-\frac{\beta}{2}(y+1)^2} + e^{-\beta(y^2/2+v_i)} \right) \\ &= e^{-N\left[-\frac{1}{N}\sum_{i=1}^{N} \log \tilde{\mathcal{Z}}\{v_i\}\right]} \end{aligned} \tag{12.5}$$

Here $\tilde{\mathcal{Z}}\{v_i\} = e^{-\frac{\beta}{2}(y+1)^2} + e^{-\beta(y^2/2+v_i)}$, which is the partition function for a single element.

Next, we introduce the empirical density $\rho_N(v) \equiv \frac{1}{N}\sum_{i=1}^{N} \delta(v - v_i)$. This allow us to re-write the partition function as

$$\mathcal{Z}(\beta, y)\{v_i\} = \exp\left[N \int_{\Omega_e} \rho_N(v) \log \tilde{\mathcal{Z}}\{v_i\} dv \right] \tag{12.6}$$

When $N \to \infty$, the discrete distribution converges to its continuum analog, $\rho_N(v) \to p(v)$, where $p(v)$ is the probability density function of the continuously distributed thresholds. Moreover, by the law of large numbers, the sample average converges to the expected value, so that we can write,

$$\mathcal{Z}(\beta, y) = e^{N\left\langle \log \tilde{\mathcal{Z}}\{v\} \right\rangle}. \tag{12.7}$$

If we assume a Gaussian distribution of the disorder, such that $p(v) = \frac{1}{\sqrt{2\pi\sigma^2}} e^{\frac{-(v-\mu)^2}{2\sigma^2}}$, we obtain the free energy[1],

$$\begin{aligned} \mathcal{F}(\beta, y) &= -\frac{1}{\beta} \int \frac{dv}{\sqrt{2\pi\sigma^2}} e^{\frac{-(v-\mu)^2}{2\sigma^2}} \log\left[e^{-\beta(v+y^2/2)} \left(e^{-\beta(y-v+1/2)} + 1 \right) \right] \\ &= \frac{y^2}{2} + \frac{y}{2} + \frac{1}{4} + \frac{\mu}{2} - \frac{1}{\beta} \int \frac{dh}{\sqrt{2\pi\sigma^2}} e^{-\frac{(h-\mu)^2}{2\sigma^2}} \log\left[2\cosh\left[\frac{\beta}{4}(-2h + 2y + 1) \right] \right]. \end{aligned} \tag{12.8}$$

[1] Refer to Eq. (13.3) for the self-averaged free energy.

Having the free energy, we can compute the force elongation relation

$$t = \partial \mathcal{F}(\beta, y)/\partial y = y + \frac{1}{2} - \frac{1}{2}\int \frac{dh}{\sqrt{2\pi\sigma^2}} e^{-\frac{(h-\mu)^2}{2\sigma^2}} \tanh\left[\frac{\beta}{4}(1-2h+2y)\right]. \quad (12.9)$$

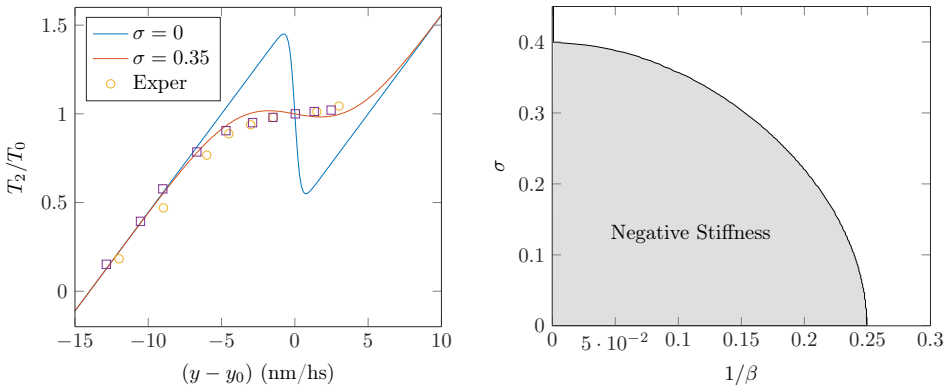

(a) **(b)**

Figure 12.4: (a) Comparison of the original HS model $\sigma = 0$ and the disordered model for $\sigma = 0.35$. The dimensional parameters are a=10nm, $\kappa_0 = 2$pN/nm, $T = 277.15$K, y_0 =4nm. Experimental results are represented by the circles and squares. (b) Negative stiffness phase diagram for the disordered system with Gaussian distribution.

In Fig. 12.4b we show a phase diagram of the system in the plane (temperature, disorder) that distinguishes domain with positive and negative stiffness in the regime of isometric contractions. To match experiments, suggesting zero stiffness in these conditions, the system must be on the boundary of the two regions. For a non-disordered system $\sigma = 0$ this can be achieved if the absolute temperature is two orders of magnitude higher than in real muscles ($T \approx 5,8 \times 10^4$, $\beta = 0.25$), see In Fig. 12.4a. The presence of a quenched disorder allows the system to have zero stiffness at smaller temperatures, in particular muscle conditions can be met at σ =0.4nm. This value of disorder is close to the one suggested by the measured axial offset.

Note, however, that in the original HS setting we do not observe a collective behavior of cross-bridges because in the case of hard device loading they are completely independent. Indeed, since the control parameter is the elongation of the backbone, the behavior of a single element is not felt by the other elements. That is why, despite zero stiffness in the regime of isometric contractions, the system is not critical.

To account for elastic interactions among cross-bridges we need to take the elasticity of the backbone into consideration. This will be done in the next Chapter for the inhomogeneous system of cross-bridges subjected to quenched disorder. Because of the spin glass nature of the resulting system, its equilibrium properties can be obtained by using the *Replica trick*, which is the main technique used in the computation of the partition functions for disordered systems, see Appendix G. We start with a case of mean-field elastic interaction which we study exhaustively and then present a partial analysis of the effect of short-range interactions.

Chapter 13

Mean-field model

In this Chapter, we study an augmented model of the Huxley-Simmons system in which cooperativity can be achieved in hard-device loading (Caruel, Allain, and Truskinovsky, 2013). The idea is to introduce an external spring that can be viewed as a lump description of the filament elasticities. Then the switch of an individual element will trigger a change in the overall elasticity of the ensemble of cross-bridges, which has to equilibrate with the backbone elastic spring. The outer spring is then the key element inducing long-range (mean-field) interactions and ensuring collectivity of the bundle response in a displacement controlled setting.

We study the equilibrium properties of such system and show that the quenched disorder, due to disregistry between the periodicities of myosin and actin filaments, places the system between two adjacent but distinct critical points. The equilibrium analysis shows that the disorder in skeletal muscles may be functional, ensuring that the system is posed near the critical points. We then use the available experimental data on muscle contraction to justify the implied criticality of muscle machinery.

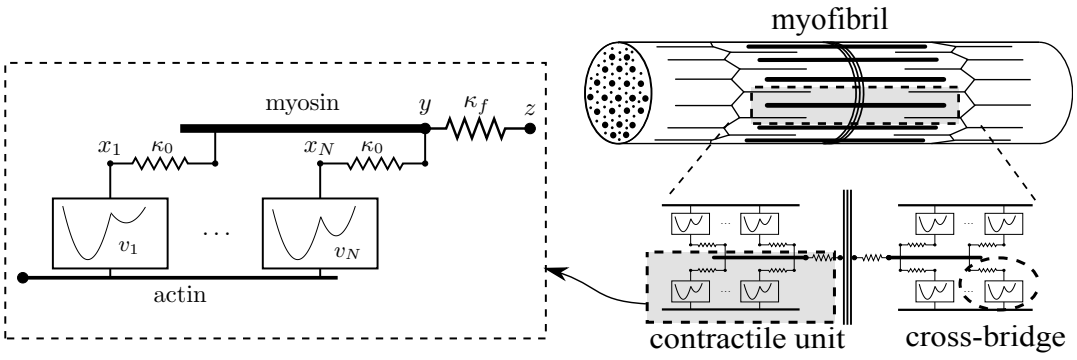

Figure 13.1: Mechanical model of a cluster of N HS elements submitted to an applied displacement z through an elastic link k_f.

The basic contractile unit, already implicitly identified in the original Huxley-Simmons model (Huxley and Simmons, 1971), is schematically represented in Fig. 13.1. The structure consists of N attached cross-bridges in parallel, bounded together by two backbones. Each CB is represented by an energy potential as defined in Eq. (12.1).

In contrast to previous studies of muscle contraction, the cross-bridges in our model are non-identical, due to the disordered energy bias between the two conformational states v_i, $i = 1, \dots, N$. This means that different cross-bridges will perform the power-stroke at different levels of elongation. As we have already mentioned, the finite elasticity of both myosin and actin is accounted for by introducing an elastic spring in series with the bundle κ_f (Caruel, Allain, and Truskinovsky,

2015; Jülicher and Prost, 1995b). The system is loaded through hard device through the external spring, whose non-dimensional stiffness is $\lambda_f = \kappa_f/(N\kappa_0)$.

13.1 Hard device

A schematic mechanical representation of the system in a hard device is given in Fig. 13.1. The total energy of the bundle for a given realization of disorder reads,

$$E(\bar{\boldsymbol{x}}, \bar{y}, \bar{z})\{\bar{v}\} = \sum_{i=1}^{N} \left[(a + \bar{x}_i)\bar{v}_i + \frac{\kappa_0}{2}(\bar{y} - \bar{x}_i)^2 \right] + \frac{\kappa_f}{2}(\bar{z} - \bar{y})^2. \tag{13.1}$$

We introduce a as the length scale, allowing us to define the non-dimensional lengths $x_i = \bar{x}_i/a$, with $i = 1, \ldots, N$, $y = \bar{y}/a$ and $z = \bar{z}/a$, along with the reference energy $\kappa_0 a^2$. The non-dimensional energy is then,

$$E(\boldsymbol{x}, y, z)\{v\} = \sum_{i=1}^{N}(1 + x_i)v_i + \frac{1}{2}(y - x_i)^2 + \frac{\lambda_f}{2}(z - y)^2, \tag{13.2}$$

where $\boldsymbol{x} = \{x_1, \ldots, x_N\}$ is the vector representing all the internal variables x_i, y is the total elongation in the CB, z is the control parameter, the applied displacement. The vector $v_i = \bar{v}_i/(\kappa_0 a)$, $i = 1 \ldots N$ is the disordered non-dimensional energy bias between the pre and post power-stroke states, taking values from a continuous probability distribution $p(v)$, with correspondent cumulative probability function $P(v)$. We use the notation $\{v\}$ to stress the realization dependence of the energy of the system. For this system we further introduce a reference elongation $z_0 = (1 + \lambda_f)\langle v \rangle/\lambda_f - 1/2$ for which the equilibrated system presents an equal energy for the folded and unfolded configurations.

In the analysis of disordered systems, any physical property would need to be averaged over all disorder realizations. When the system size is large enough, we do not expect that its behavior will differ from its averaged behavior, so that some properties of the system would no longer depend on its particular realization of the disorder. Quantities that behave like this in the thermodynamic limit are called *self-averaging quantities*. For self-averaging quantities, sample-to-sample fluctuations with respect to the mean value are expected to be $O(\frac{1}{N^a})$ with $a > 0$. In principle, observables that involve summing over the entire volume of the system are expected to be self-averaging, which includes the Helmholtz free-energy (Sherrington and Kirkpatrick, 1975; Mezard, Parisi, and Virasoro, 1987; Castellani and Cavagna, 2005; Schneider and Pytte, 1977).

These observations allow us to write the Helmholtz free-energy per particle as,

$$\lim_{N\to\infty} \mathcal{F}(\beta, z)\{v\} = \lim_{N\to\infty} \left\langle \mathcal{F}(\beta, z) \right\rangle_v = -\frac{1}{N\beta} \left\langle \log \mathcal{Z}\{v\}(\beta, z) \right\rangle_v, \tag{13.3}$$

where $\beta = \frac{\kappa_0 a^2}{k_B T}$ is the non-dimensional measure of thermal fluctuations (non-dimensional temperature) and $\mathcal{Z}(\beta, z)\{v\}$ is the partition function

$$\mathcal{Z}(\beta, z)\{v\} = \int dy \sum_{x\in\{0,-1\}^N} e^{-\beta E(\boldsymbol{x}, y, z)\{v\}}. \tag{13.4}$$

Here the sum is over all the internal spin variables x_i's,

$$\sum_{x\in\{0,-1\}^N} = \sum_{x_1\in\{0,-1\}} \sum_{x_2\in\{0,-1\}} \cdots \sum_{x_N\in\{0,-1\}}.$$

To obtain a partition function that depends on the temperature β and the controlled displacement z we need to eliminate the internal variables y and x_i. We calculate the partition function using the Eq. (13.2) for the energy into Eq. (13.4). Since the spin variables x_i are independent (there is no short-range interaction between the spins) we can then write the partition function in the form

$$\begin{aligned}\mathcal{Z}(\beta,z)\{v_i\} &= \int dy\, e^{-\beta N\frac{\lambda_f}{2}(z-y)^2}\prod_{i=1}^{N}\left(e^{-\frac{\beta}{2}(y+1)^2}+e^{-\beta(y^2/2+v_i)}\right)\\ &= \int dy \exp\left\{-\beta N\left[\frac{\lambda_f}{2}(z-y)^2-\frac{1}{\beta N}\sum_{i=1}^{N}\log\tilde{\mathcal{Z}}\{v_i\}\right]\right\}\end{aligned} \tag{13.5}$$

where $\tilde{\mathcal{Z}}\{v_i\} = e^{-\frac{\beta}{2}(y+1)^2}+e^{-\beta(y^2/2+v_i)}$. The latter expression is the partition function for a single Huxley-Simmons element (bi-stable unit in series with elastic spring).

Let us again introduce the density $\rho_N(v) \equiv \frac{1}{N}\sum_{i=1}^{N}\delta(v-v_i)$. This allow us to re-write the expression for the partition function in the form

$$\mathcal{Z}(\beta,z)\{v_i\} = \int dy\, e^{-\beta N\left(\frac{\lambda_f}{2}(z-y)^2-\frac{1}{\beta}\int_{\Omega_e}\rho_N(v)\log\tilde{\mathcal{Z}}\{v_i\}dv\right)}. \tag{13.6}$$

In the thermodynamic limit, when $N\to\infty$, we can again identify the discrete density ρ_N with its continuum analog, $\rho_N(v)\to p(v)$, where $p(v)$ is the probability density function of the distributed thresholds. Moreover, using the law of large numbers (see above), we can write,

$$\mathcal{Z}(\beta,z) = \int e^{-\beta N\left(\frac{\lambda_f}{2}(z-y)^2-\frac{1}{\beta}\left\langle\log\tilde{\mathcal{Z}}\{v\}\right\rangle_v\right)}dy. \tag{13.7}$$

Here the symbol $\langle\cdot\rangle_v$ denotes the average over the disorder.

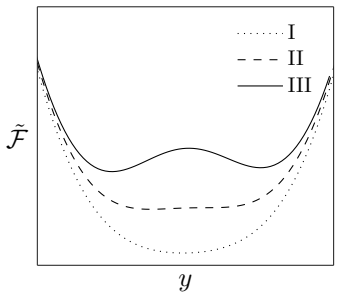

Figure 13.2: Sketch of the free energy $\tilde{\mathcal{F}}(\beta,z,y)$ as a function of y for different values of temperature, we observe the possibility of multiple values of the minimum, corresponding to y_0, which is related to the multiple solutions of the self-consistent relation

To compute this integral we use a saddle point approximation. First, we define $\tilde{\mathcal{F}}(y,\beta,z) = \beta\frac{\lambda_f}{2}(z-y)^2-\left\langle\log\tilde{\mathcal{Z}}\{v\}(\beta,y,z)\right\rangle_v$ and y_0, the minimum of $\tilde{\mathcal{F}}(y,\beta,z)$, which gives $\mathcal{Z}(\beta,z) = \exp\left[-\tilde{\mathcal{F}}(y_0,\beta,z)\right]$. Once calculated, the partition function

may be substituted into Eq. (13.3) to obtain the self-averaged free energy,

$$\begin{aligned}\mathcal{F}(\beta,z) &= \left\langle \frac{\lambda_f}{2}(z-y_0)^2 - \frac{1}{\beta}\left\langle \log \tilde{\mathcal{Z}}\{v_i\}(\beta,y_0,z)\right\rangle_v \right\rangle_v \\ &= \frac{\lambda_f}{2}(z-y_0)^2 + \frac{1}{4}(y_0+1)^2 + \frac{1}{2}(y_0^2/2+v_0) \\ &- \frac{1}{\beta}\int dv\, p(v)\log\left[2\cosh[\frac{\beta}{4}(1+2y_0-2v)]\right]\end{aligned} \tag{13.8}$$

To find the saddle-point y_0 we must look for the extrema of $\tilde{\mathcal{F}}(y,\beta,z)$, which requires finding solutions of the equation $\partial\tilde{\mathcal{F}}(y,\beta,z)/\partial y = 0$. This gives us the following self-consistency relation,

$$y_0 = \Phi(y_0) = z + \frac{1}{\lambda_f\beta}\int_{\Omega_e} dv p(v)\frac{\partial}{\partial y}\log\tilde{\mathcal{Z}}\{v\}(\beta,y_0,z) \tag{13.9}$$

or more explicitly,

$$y_0 = \frac{2\lambda_f z - 1}{2(\lambda_f+1)} + \int dv\,\frac{p(v)}{2(1+\lambda_f)}\tanh\left[\frac{\beta}{4}(1-2v+2y)\right]. \tag{13.10}$$

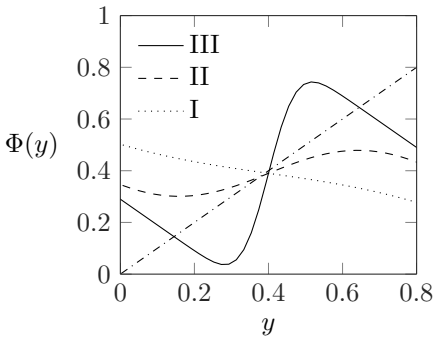

Figure 13.3: Graphical representation of Eq. (13.10). In Phase III, we observe that the solid curve Φ crosses three times the dashed-dotted curve, presenting the multiple solutions that are characteristic of the phase III.

The multiplicity of solutions of the self-consistency relation Eq. (13.10) would be a result of the non-convexity of the free energy with respect to the variable y. The typical behavior of the free energy as a function of y is shown in Fig. 13.2. We observe that when the function $\tilde{\mathcal{F}}(y,\beta,z)$ is non-convex the self-consistency equation has indeed multiple solutions y_0, see Fig. 13.3.

To describe the state of the system, in addition to the free energy we compute the tension $t(\beta,z)$ developed by the bundle at an applied displacement z

$$t(\beta,z) = \frac{\partial\mathcal{F}}{\partial z} = \lambda_f(z-y_0). \tag{13.11}$$

If we assume that the disorder is Gaussian, $p(v) = \frac{1}{\sqrt{2\pi\sigma^2}}e^{-\frac{(v-\mu)^2}{2\sigma^2}}$, the behavior of the system can be specified further. It will be fully defined by the temperature $1/\beta$, the variance of disorder σ^2 and the parameter λ_f, characterizing the degree of cooperativity in the system. The full diagram is presented in Fig. 13.5. The section

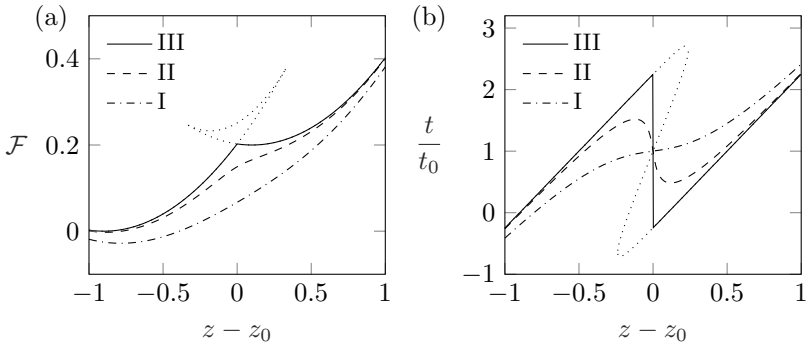

Figure 13.4: (a) Representative Helmholtz free energies in each of the phases and (b) The corresponding force-elongation relations; $z_0 = (1 + \lambda_f)\mu/\lambda_f - 1/2$ is the reference elongation.

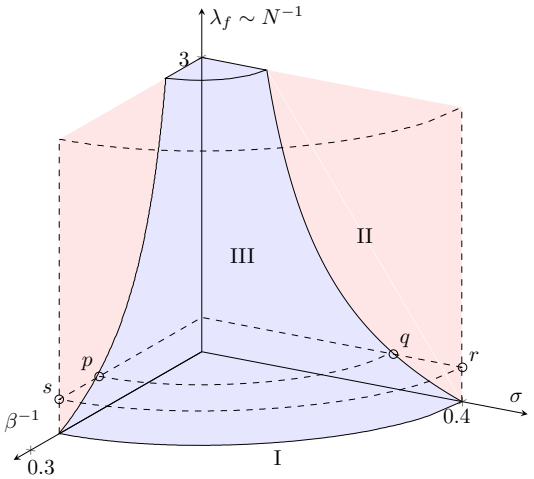

Figure 13.5: Configuration of phases I, II and III in the extended parameter space ($1/\beta$, σ , λ_f). The phase diagram shown in Fig. 14.3 is a marked section of this more complete phase diagram.

$\sigma = 0$ was studied in (Caruel and Truskinovsky, 2018) . We note that at $\sigma > 0$ the system responds as if it were subjected to a higher effective temperature (Roux, 2000; Politi, Ciliberto, and Scorretti, 2002b).

The behavior of the Helmholtz free energy and the tension-elongation relation in the three 'phases' I, II and III is shown in Fig. 13.4. In phase I the cooperativity is absent and the cross-bridges fluctuate independently. In phase III the discontinuity in the tension-elongation relation corresponds to a synchronous switch between two pure states. In the intermediate phase II the tension-elongation relation exhibits negative stiffness in the regimes where the system fluctuates between pure states. The space of parameters that characterizes each phase is illustrated in Fig. 13.5.

13.2 Soft device

In the soft device (force clamp) the presence of the series spring λ_f is irrelevant and we can assume that $\lambda_f \to 0$, $z \to \infty$, but $\lambda_f z \to t$, where t is now the control force.

The relevant potential is,

$$G = \sum_{i=1}^{N} \left[(1 + x_i)v_i + \frac{1}{2}(y - x_i)^2 \right] - ty. \tag{13.12}$$

Following the approach used in the case of hard device, we obtain the expression for the Gibbs free energy

$$\begin{aligned} \mathcal{G}(\beta, t) = &-ty_0 + \frac{1}{4}(y_0 + 1)^2 + \frac{1}{2}(\frac{y_0^2}{2} + v_0) \\ &- \frac{1}{\beta} \int dv\, p(v) \log \left[2\cosh[\frac{\beta}{4}(1 + 2y_0 - 2v)] \right] \end{aligned} \tag{13.13}$$

where now y_0 solves the equation

$$t = y_0 + \frac{1}{2} - \frac{1}{2} \int dv\, p(v) \tanh \left[\frac{\beta}{4}(1 - 2v + 2y_0) \right]. \tag{13.14}$$

The tension elongation relation is then a solution of $y = -\partial\mathcal{G}/\partial t$.

In Fig. 13.6 we show that the soft device tension-elongation relation in phase II is monotone but discontinuous. On the boundary $r - s$ in Fig. 13.5 the system exhibits zero stiffness in stall conditions, which means that it corresponds to the set of critical points in the soft device ensemble. This line, targeted numerically in (Huxley and Tideswell, 1996), represents regimes that can be expected to deliver the optimal trade-off between robustness and flexibility in the soft device (Kauffman, 1993; Darabos et al., 2011).

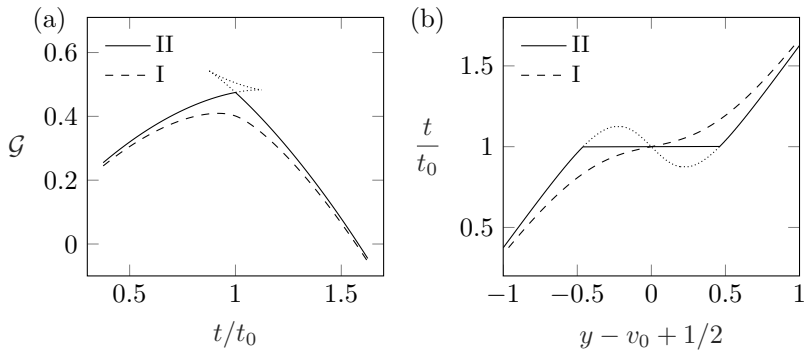

Figure 13.6: Typical Gibbs free energies and force-elongation curves in the force clamp loading conditions (soft device) in phases I and II; $t_0 = v_0$.

Chapter 14

Phase diagrams

We now discuss in more detail the obtained phase diagram of the system in hard and soft devices.

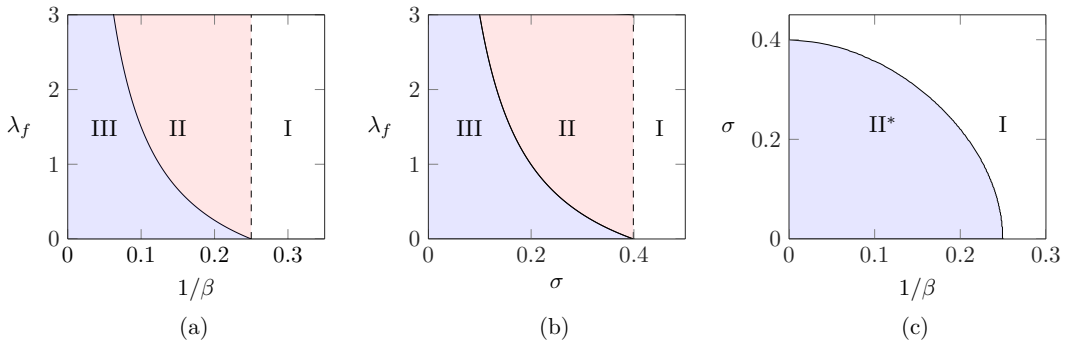

Figure 14.1: Phase diagrams separating different qualitative responses of the tension elongation curve. (a) corresponds to the non-disordered case, $\sigma \to 0$; (b) represents the zero temperature behavior, $1/\beta \to 0$. and (c) correspond to a vanishing value of the external elasticity $\lambda_f \to 0$. In (c) we marked II* to express that although the tension elongation curve is similar to that of phase II, in a force clamp mode it corresponds to collective behavior.

In a setting of controlled displacement we obtained three main types of behavior as far as the tension elongation response of the system is concerned, see Fig. 13.4. First, for large values of temperature and disorder, we have a monotonically increasing tension curve, represented by the 'phase I'. Second, the red region, 'phase II', represents a response in which the tension elongation presents a negative stiffness. Lastly, for a set of parameters, the self-consistent relation may have several solutions, representing the non-convexity of the free energy with respect to y. This creates a response with a discontinuity in the tension elongation curve, represented by a finite jump, corresponding to a synchronous switch between the two conformational states, 'phase III'. This cooperative response is represented by the blue region in the phase diagram pictured in Fig. 13.5 and Fig. 14.1. The cooperative behavior is lost by tuning the parameters, such that the free energy is convex.

Now we show how the boundaries separating these different qualitative behaviors can be obtained analytically in the particular case of the disorder being represented by a Gaussian distributed energetic bias with variance σ^2.

14.1 Boundary between phases II and III: criticality in the hard device

To compute the critical surface, separating the blue (I) and the red (II) regions in Fig. 14.1 and Fig. 13.5, we must obtain the condition where the free energy becomes convex in y. To do so, we must check that the second derivative of the free energy with respect to y is non negative, $\partial^2\tilde{\mathcal{F}}(\beta, z, y)/\partial y^2 \geq 0$. This equality can be written as,

$$\lambda_f + 1 - \frac{\beta}{4}\int dv\, p(v)\,\mathrm{sech}^2\,\frac{\beta}{4}(1 - 2v + 2y_0) = 0. \tag{14.1}$$

The region II corresponds to the set of parameters where Eq. (14.1) has a unique solution y_0. From this equation, if we consider the quenched disorder following a Gaussian distribution, we can obtain the phase diagram as seen in Fig. 13.5.

If we use the Gaussian distribution of disorder and use new variables $\eta = \beta(1 + 2y_0)/2$ and $\bar{v} = \beta v$ we can rewrite this equation in the form

$$\lambda_f + 1 - \frac{\beta}{4}\int d\bar{v}\frac{e^{-\frac{(\bar{v}-\beta v_0)^2}{2\sigma^2\beta^2}}}{\sqrt{2\pi\sigma^2\beta^2}}\,\mathrm{sech}^2\,\frac{1}{2}(\eta - \bar{v}) = 0. \tag{14.2}$$

Note that the variance of disorder appears in this formula only in the combination $\sigma^2\beta^2$. This means that, modulo some obvious adjustments, the small disorder $\sigma \to 0$ and large temperature $\beta \to 0$ limits are complimentary. The same can be said about the small temperature $\beta \to \infty$ and the large disorder $\sigma \to \infty$ limits.

14.2 Zero disorder limit

In the limit $\sigma \to 0$ we have $p(v) \to \delta(v - v_0)$ and the boundary between phase II and III is defined by the equation

$$\lambda_f + 1 = \frac{\beta}{4}\,\mathrm{sech}^2\,\frac{\beta}{4}(1 - 2v_0 + 2y_0). \tag{14.3}$$

Since $\mathrm{sech}^2\, x \in [0, 1]$, this equation does not have solutions y_0 for $\beta > 4(\lambda_f + 1)$ and therefore the point p in Fig. 13.5 is defined by the condition $\beta = 4(\lambda_f + 1)$.

To get the next term of the asymptotic expansion we introduce the new variable $\xi = (1 - 2v + 2y_0)/4$ and assume that the temperature is large, $\beta \to 0$. Then we can expand $\log \mathrm{sech}^2\,\beta\xi \approx -\beta^2\xi^2 + O(\beta^4)$, which implies that $\mathrm{sech}^2\,\beta\xi \approx e^{-\beta^2\xi^2}$. Using this approximation we can compute the integral and represent the boundary between phase II and III in the form

$$\lambda_f + 1 = \frac{e^{\frac{-(y_0 - v_0 + 1/2)^2}{2(2T^2+\sigma^2)}}}{2\sqrt{2(2T^2 + \sigma^2)}}, \tag{14.4}$$

where $T = 1/\beta$. Since $e^{-x^2} \in (0, 1]$ the criticality condition is

$$(\lambda_f + 1)2\sqrt{2(2T^2 + \sigma^2)} = 1. \tag{14.5}$$

The equivalent quenched disorder is then defined by the condition $\sigma_{eq}^2 = 2T^2 + \sigma^2$.

14.3 Zero temperature limit

In the zero temperature limit, $\beta \to \infty$, we use the fact that

$$\lim_{k\to\infty} \frac{k}{2} \operatorname{sech}^2 kx \to \delta(x)$$

to rewrite the equation defining the boundary between phase II and III in the form

$$(\lambda_f + 1)\sqrt{2\pi\sigma^2} = e^{-\frac{(y_0+1/2-v_0)^2}{2\sigma^2}}. \tag{14.6}$$

Here the *r.h.s* is defined in the interval $(0, 1]$ and therefore there are no solutions y_0 if $(\lambda_f + 1)\sqrt{2\pi\sigma^2} > 1$, where we used the fact that $\sigma, \lambda_f > 0$. The point q in Fig. 13.5 is then defined by the condition $(\lambda_f + 1)\sqrt{2\pi\sigma^2} = 1$ or,

$$\lambda_f + 1 = \frac{1}{\sqrt{2\pi\sigma^2}}. \tag{14.7}$$

Which is the equation for the solid black line separating the regions II and III in Fig. 14.1. For $\lambda_f = 0$ we would obtain $\sigma = 1/\sqrt{2\pi}$.

To obtain the next term of the asymptotic expansion we assume that disorder is large $\sigma \to \infty$. In this case we can still approximate the function $\operatorname{sech}^2(x)$ by the Gaussian distribution but now the approximation should be good not only at $x = 0$ but globally. To this end we need to require that the two functions are equally normalized

$$\frac{1}{4T}\int dv \operatorname{sech}^2 \frac{1-2v-y_0}{4T} = \frac{1}{\sqrt{4\pi T^2}}\int dv e^{-\frac{(v-y_0-1/2)^2}{4T^2}} = 1,$$

where again $T = 1/\beta$. With this normalization the integral can be again computed and we obtain the condition

$$(\lambda_f + 1)\sqrt{2\pi} = \frac{e^{\frac{-(y-v_0+1/2)^2}{2(2T^2+\sigma^2)}}}{\sqrt{2T^2+\sigma^2}}.$$

The criticality criterion is then

$$(\lambda_f + 1)\sqrt{2\pi(2T^2+\sigma^2)} = 1,$$

which allows us to re-introduce the effective disorder $\sigma_e^2 = 2T^2 + \sigma^2$.

14.4 Boundary between phases I and II: criticality in soft device

Region III in Fig. 13.5 represents a monotonous stress strain response of the system and it is determined by the condition that the free energy is convex in z, or $\partial^2\mathcal{F}/\partial z^2 \geq 0$. Note first that $\frac{\partial t}{\partial z} = \lambda_f(1 - \frac{\partial y_0}{\partial z})$, and therefore to get zero stiffness we must have $\partial y_0/\partial z = 1$, Here y_0 is found from the self-consistency condition, given by Eq. (13.10), and therefore

$$\frac{\partial y_0}{\partial z} = \frac{\lambda_f}{\lambda_f + 1} + \frac{\beta}{4(1+\lambda_f)}\int dv\, p(v) \operatorname{sech}^2\left[\frac{\beta}{4}(1-2v+2y_0)\right]\frac{\partial y_0}{\partial z}, \tag{14.8}$$

which is equivalent to

$$1 = \frac{\beta}{4} \int dv\, p(v) \operatorname{sech}^2 \left[\frac{\beta}{4}(1 - 2v + 2y_0) \right]. \tag{14.9}$$

For the stress strain curve to be monotonous we need to find a y_0 such that Eq. (14.9) is satisfied. Because Eq. (14.9) does not involve λ_f, y_0 is independent of the external elastic properties, and hence the region in the phase diagram where the system present a monotonous stress strain curve is λ_f independent, as it can be observed by the red region in Fig. 13.5.

14.5 Zero disorder limit

In the limit $\sigma \to 0$, we can again assume that the probability density $p(v)$ is infinitely localized and compute the integral explicitly. We obtain

$$\frac{4}{\beta} = \operatorname{sech}^2 \frac{\beta}{4}(1 - 2v + 2y_0).$$

Since $\operatorname{sech}^2 x \in [0, 1]$, this equation does not have solutions y_0 if $\beta < 4$, hence $\beta_c = 4$, which is the coordinate of our point s in Fig. 13.5. The higher order asymptotic expansion can be obtained following the same procedure as in the case of the boundary between phases II and III.

14.6 Zero temperature limit

In the limit $\beta \to \infty$, we can again use the fact that the function $\frac{k}{2} \operatorname{sech}^2 kx$ converges to the delta function as $k \to \infty$. Therefore, assuming that the probability distribution $p(v)$ is Gaussian we obtain,

$$1 = \frac{1}{\sqrt{2\pi\sigma^2}} e^{-\frac{(y_0 + 1/2 - v_0)^2}{2\sigma^2}}.$$

Using the same arguments as in the zero disorder limit and noticing that $e^{-x^2} \in (0, 1]$, we conclude that this equation has solution only if $\sigma \geq 1/\sqrt{2\pi}$. Therefore, the critical value of the disorder in this limit is $\sigma_c = 1/\sqrt{2\pi}$, which corresponds to our point r, see Fig. 13.5. The expansion around this point can be obtained as in the case of the boundary between phases II and III considered above.

14.7 Edwards-Anderson order parameter

In the absence of disorder, a natural order parameter is

$$\phi = \frac{1}{N} \sum_{i=1}^{N} \langle s_i \rangle_T \,,$$

where $s_i = 2x_i + 1$. To find $\phi(z, \beta)$ we notice that since all cross-bridges are the same we can write $\phi = 2 \langle x_i \rangle_T + 1$ where

$$\langle x_i \rangle_T = -Z(\beta, z)^{-1} e^{-\beta E(x_i = -1, y_0, z)}$$

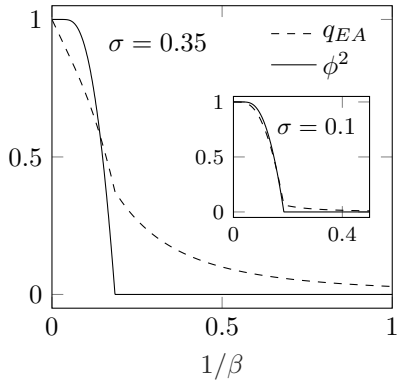

Figure 14.2: The behavior of the parameter ϕ^2 (solid lines) and the Edwards-Anderson parameter q_{EA} (dashed lines) near the boundary $p-q$ at the realistic value of disorder. Inset illustrates the case of weak disorder.

with

$$Z(\beta, z) = e^{-\beta N\left[\frac{\lambda_f}{2}(z-y_0)^2 - \frac{1}{\beta}\log(e^{-\frac{\beta}{2}(y_0+1)^2} + e^{-\beta(y_0^2/2+v)})\right]}.$$

By combining these expressions we obtain

$$\langle x_i \rangle_T = -\frac{1}{1+e^{\beta(y_0-v+1/2)}}.$$

In the presence of disorder, the average values $\langle x_i \rangle_T$ are different for different cross-bridges and the macroscopic parameter $\phi(z,\beta)$ is no longer sufficient to differentiate between microscopic configurations. To this end we can introduce an analogue of the Edwards-Anderson parameter from the theory of spin glasses

$$q_{EA} = \frac{1}{N}\sum_{i=1}^{N}\left\langle \langle s_i \rangle_T^2 \right\rangle_v.$$

where we distinguish between the thermal average $\langle\cdot\rangle_T$ and the ensemble average $\langle A\rangle_v = \int dv p(v) A(v)$. If the parameter ϕ characterizes the average occupancy of the pre-power stroke state, the nonzero value of q_{EA} means that individual cross bridges are 'frozen' either in pre- or post-power-stroke states even if in average, both states appear to be equally occupied. The knowledge of this parameter is needed, for instance, if one is interested in computing the effect of the random field on mechanical susceptibility (stiffness) (Vilfan and Cowley, 1985).

In terms of the variables x_i, the definition of q_{EA} reads

$$q_{EA} = \frac{1}{N}\sum_{i=1}^{N}\left[4\left\langle \langle x_i \rangle_T^2 \right\rangle_v + 4\left\langle \langle x_i \rangle_T \right\rangle_v + 1\right],$$

where

$$\left\langle \langle x_i \rangle_T^2 \right\rangle_v = \int dv \frac{p(v)}{(1+e^{\beta(y_0-v+1/2)})^2},$$

and

$$\left\langle \langle x_i \rangle_T \right\rangle_v = -\int dv \frac{p(v)}{1+e^{\beta(y_0-v+1/2)}}.$$

The boundary between phases II and III corresponds to the second order phase transition: the order parameter $\phi = N^{-1}\sum_{i=1}^{N}\langle s_i \rangle_\beta$, where $< \cdot >_\beta$ is the thermal

average, is double-valued in phase III and single-valued in phase II, see Fig. 14.6. To distinguish between different microscopic configurations, we also compute the Edwards-Anderson (overlap) parameter q_{EA}. Fig. 14.2 shows that q_{EA} is different from zero in the 'paramagnetic' phase II close to the $p-q$ boundary, which indicates weakly *glassy* behavior (Schneider and Pytte, 1977; Vilfan, 1987; Krzakala, Ricci-Tersenghi, and Zdeborová, 2010). This is an indication that in a more realistic model, where the backbone elasticity is taken into account, one can expect the emergence in this range of parameters of a real 'strain glass' phase (Wang, Ren, and Otsuka, 2006; Vasseur et al., 2012).

14.8 Calibration of the model

Note that we have operated under an implicit assumption that in the thermodynamic limit $\kappa_f \to \infty$, while λ_f remains finite. This assumption is based on the picture of the myosin filament as a parallel arrangement of N myosin tails, all contributing to the lump stiffness of the backbone. A more realistic assumption may be that the effective stiffness of the backbone κ_f depends only weakly on the number of attached cross-bridges N and in this case we have a different scaling $\lambda_f \sim N^{-1}$. Then the phase diagram, presented in Fig. 13.5, shows the size effect and suggests that scaling may be narrowly linked to a particular number of attached cross-bridges.

To apply our results to a realistic muscle system, we use the data for *rana temporaria* at $T = 277.15K$ (Caruel and Truskinovsky, 2018). From structural analysis we obtain the value $a = 10 \pm 1$nm (Dominguez et al., 1998; Rayment et al., 1993b; Rayment et al., 1993a). Measurements of the fiber stiffness in *rigor mortis*, where all the 294 cross-bridges per half-sarcomere were attached, produced the estimate $\kappa_0 = 2.7 \pm 0.9$ pN/nm (Brunello et al., 2014; Piazzesi et al., 2007). The number of attached cross-bridges in physiological conditions is $N = 106 \pm 11$ and experimental measurements at different N converge on the value $\kappa_f = 154 \pm 8$pN.nm^{-1} for the lump filaments stiffness (Wakabayashi et al., 1994; Huxley et al., 1994; Piazzesi et al., 2002). This gives $\lambda_f = 0.54 \pm 0.2$. Given κ_0 and a we are able to estimate the non-dimensional inverse temperature $\beta = 71 \pm 26$.

Recall next that for $y > y_*$, where $y_* = v_0 - 1/2$, the ground state of a single cross-bridge is in the pre-power-stroke, while for $y < y_*$ it is in the post-power-stroke, so y_* represents the characteristic offset for an individual cross-bridge. Knowing that $y_* \sim 4$nm (Huxley and Simmons, 1971; Huxley and Tideswell, 1996) we conclude that $v_0 \sim 24.3\text{pN}\ /(\kappa_0 a)$. It was experimentally shown in (Tregear et al., 2004) that at least 60% of the cross-bridges are axially displaced within half of the spacing between actin monomers, which corresponds to ~ 2.76 nm shift from the nearest actin binding site, see also (Huxley and Tideswell, 1996). Given the linear dependence between v_0 and y_*, the variances of these two quantities are the same. If the axial offsets are Gaussian random numbers, we can estimate the standard deviation of the energetic bias $\sigma \sim 3.3\text{nm}/a$, see Sec 12.3.

Based on these data we find that, rather remarkably, the system appears to be operating in a narrow domain of stability of phase II, close to both critical lines $p-q$ and $r-s$, see the point marked by a triangle in Fig. 14.3. The gap between these boundaries corresponds to ~ 1 nm difference in the cross-bridge attachment positions which is rather small given that the size of a single actin monomer is about

5.5nm. The mechanical responses in the adjacent critical regimes A and B are structurally similar, however, if in the hard device ensemble we imply coherent fluctuations of tension (infinite rigidity), in the soft device we expect system size correlations of strain (zero rigidity).

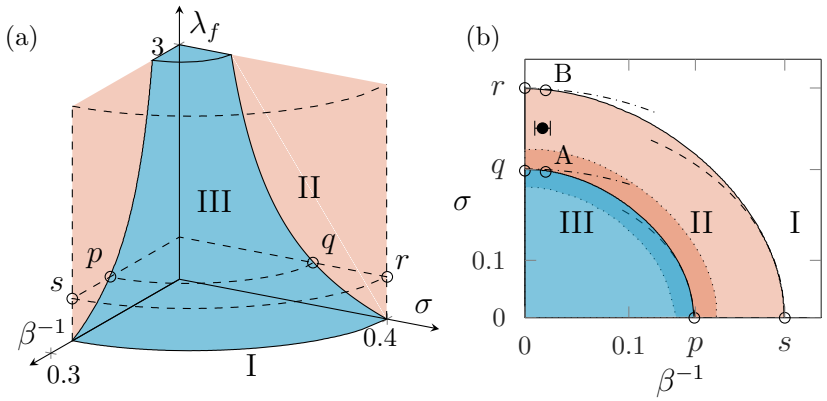

Figure 14.3: (a) Configuration of phases I, II and III in the parameter space $(1/\beta, \sigma, \lambda_f)$. (b) A section of this phase diagram corresponding to $\lambda_f = 0.54 \pm 0.2$; the shadowed region near the boundary II/III reflects the uncertainty in λ_f. The realistic data set for skeletal muscles is presented in (b) by a filled circle with the superimposed error bars indicating uncertainty in temperature. Analytic approximations in (b): dashed-dotted lines – low temperature; dashed lines – low disorder.

14.9 Critical response in soft and hard ensembles

In Fig. 14.4 we illustrate the mechanical responses in the adjacent critical regimes marked as A and B in Fig. 14.3. In the associated critical points, indicated here by small circles and intended to represent the physiological regime of isometric contractions, the susceptibilities diverge. The closeness of these two regimes in the parameter space allows the system to exhibit the whole repertoire of behaviors from zero to infinite rigidity.

To emphasize the necessity to be close to critical behavior in both ensembles, we now present an elementary illustration of the fact that the equilibrium response of a bundle of contractile units connected in series and placed in a hard device, cannot be described by local equilibrium constitutive relations obtained in either soft or hard device ensembles. Instead, the system exhibits an intermediate behavior.

Consider two elementary contractile units in series, see (Caruel and Truskinovsky, 2018) for the analysis of M such elements. Each of the two elements represents a parallel connection of N cross-bridges. The total energy per cross bridge in dimensionless form for a system placed in a hard device reads

$$E_2 = \frac{1}{2}\left\{ \frac{1}{N}\sum_i^N [(1+x_{i1})v_{i1} + \frac{1}{2}(y_1 - x_{i1})^2 + \frac{\lambda_f}{2}(z_1 - y_1)^2] \right. \\ \left. + \frac{1}{N}\sum_i^N [(1+x_{i2})v_{i2} + \frac{1}{2}(y_2 - x_{i2})^2 + \frac{\lambda_f}{2}(z_2 - y_2)^2] \right\} \tag{14.10}$$

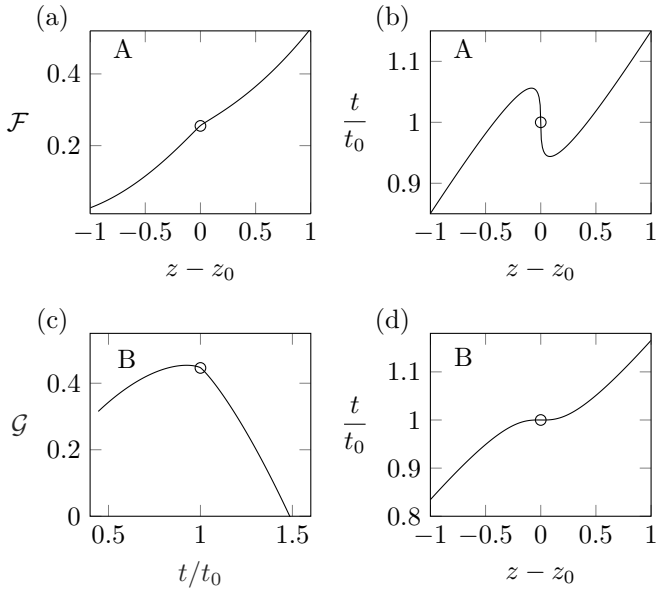

Figure 14.4: The response of the system in the critical regimes A and B shown in Fig. 2 of the main text : (a) and (b) are the Helmholtz free energy and the tension-elongation curve in the hard device ensemble; (c) and (d) are the Gibbs free energy and the associated tension-elongation curve in the soft device ensemble. Critical points are marked by the small circles.

The equilibrium response of the system is obtained by computing the partition function

$$\mathcal{Z}_2(z,\beta) = \int \exp[-2\beta N E_2]\delta(z_1 + z_2 - 2z)d\boldsymbol{x}$$

where $d\boldsymbol{x} = \prod_i^N dx_{i1}dy_1 \prod_j^N dx_{j2}dy_2$ and z is the (average) elongation imposed on the system. We can rewrite the expression for $\mathcal{Z}_2$ in the form

$$\begin{aligned}\mathcal{Z}_2(z,\beta) = \int dy_1 dy_2 \exp\Big\{-\beta N[-\frac{\lambda_f}{2}(z - y_1 - y_2)^2 \\ -\frac{1}{\beta}\int dv p(v)\log\tilde{\mathcal{Z}}_1(y_1,v)\tilde{\mathcal{Z}}_2(y_2,v)]\Big\}\end{aligned} \tag{14.11}$$

where $\tilde{\mathcal{Z}}_i(y_i,v) = e^{-\frac{\beta}{2}(y_i+1)^2} + e^{-\beta(y_i^2/2+v)}$. The free energy per cross-bridge is then $\mathcal{F}_2(z,\beta) = -\frac{1}{2N}\log\mathcal{Z}_2(z,\beta)$. The equilibrium tension-elongation relation for this system, obtained from the relation $t(z,\beta) = \partial\mathcal{F}_2(z,\beta)/\partial z$, is shown by the thick line in Fig. 14.5(a). Similar thick line in Fig. 14.5(b) shows the equilibrium response of a single contractile element placed in the hard device.

We now compare this behavior with the one obtained under the assumption that the two elements in series are characterized by their equilibrium free energies computed either in a hard or a soft ensemble.

For instance, using the hard device ensemble we can write the total (Helmholtz) free energy of the two element system in the form $E_2^{hd} = \mathcal{F}(z_1,\beta) + \mathcal{F}(z - z_1,\beta)$, where $\mathcal{F}$ is the free energy of a half-sarcomere given by Eq. 15.23. The extra variable z_1 can be eliminated using the equilibrium condition $\partial\mathcal{F}(z_1,\beta)/\partial z_1 = \partial\mathcal{F}(z - z_1,\beta)/\partial z_1$. The resulting tension elongation curve is shown in Fig. 14.5 (a) by a dotted line.

A similar analysis can be performed based on the response functions for the elements loaded in a soft device. Here we need to use equilibrium (Gibbs) free energies of the elements, Eq. (13.13), and since the elements in series share the value of tension, we obtain $G_2^{SD} = 2\mathcal{G}(t, \beta)$. The ensuing response of the series bundle is shown in Fig. 14.5(a) by a dashed line. In Fig. 14.5(b), the dashed line shows the equilibrium response of a single contractile element loaded in a soft device.

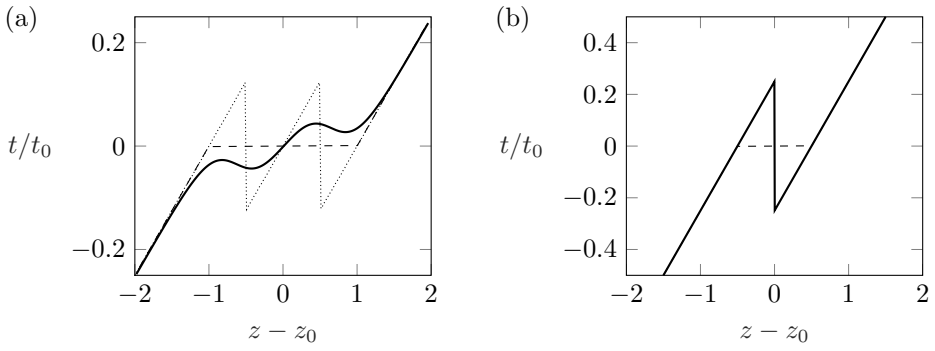

Figure 14.5: (a) Tension elongation relations for a system containing two half-sarcomeres in series placed in a hard device. Thick line: equilibrium response. Dotted (dashed) line: the response of two contractile elements in series, each one endowed with its own equilibrium the hard (soft) device constitutive law. (b) Response of a single half-sarcomere. Thick line: hard device; dashed line: soft device. Parameters are: $\beta = 30$, $\sigma = 0$, $v_0 = 0$, $\lambda_f = 1$.

Observe that the equilibrium response predicted by the two 'constitutive models' contains discontinuities, while the response of the truly equilibrated system (two half-sarcomeres in series) is smooth. Note also that the actual response curves do not coincide with either of the two 'constitutive models' and exhibit some intermediate behavior with features mimicking both models simultaneously. The observed discrepancy stems from the fact that in a fully equilibrated system none of the contractile elements is loaded in either soft or hard device and that the overall response of the system is fundamentally non-affine, see also (Vilfan and Duke, 2003; Caruel and Truskinovsky, 2018).

14.10 Functionality of criticality

The special nature of the critical regimes is illustrated in Fig. 14.6 for the case of a hard device. We first note that in phase I the passive response of the system reminds rubber elasticity: small stimuli lead to small responses and synchronization is absent, see Fig. 14.6(a, d). If the individual contractile units were operating in this regime, the collective power-stroke observed in experiments would not be possible. In phase III we can expect finite synchronized jumps, but such cooperativity comes at the cost of crossing an energetic barrier, see Fig. 14.6(b, e). This barrier is proportional to N (recall that $\mathcal{F}$ is the free energy *per* cross-bridge), which leads to macroscopic metastability and dramatic slowing down of the response. In the vicinity of a critical point, see Fig. 14.6(c, f), the system is able to perform the collective stroke without crossing a prohibitively high macroscopic barrier. We argue that this is a targeted behavior, achieved in the course of evolution.

Note also that the emergence of arbitrarily large correlation lengths at criticality is an important feature that can be exploited by living systems to induce coordinated behavior of individual units across space and time. The power stroke is a synchronous conformational change of myosin heads spanning the whole myofibril. The fast-recovery experiments show that this synchronous response takes place for a range of input length increments (imposed slacks). We link this robustness to criticality, which is expected to offer the best trade-off between the resilience of the system to external perturbations (a property of ordered phases) and responsiveness to environmental cues and stimuli (a feature of disordered phases).

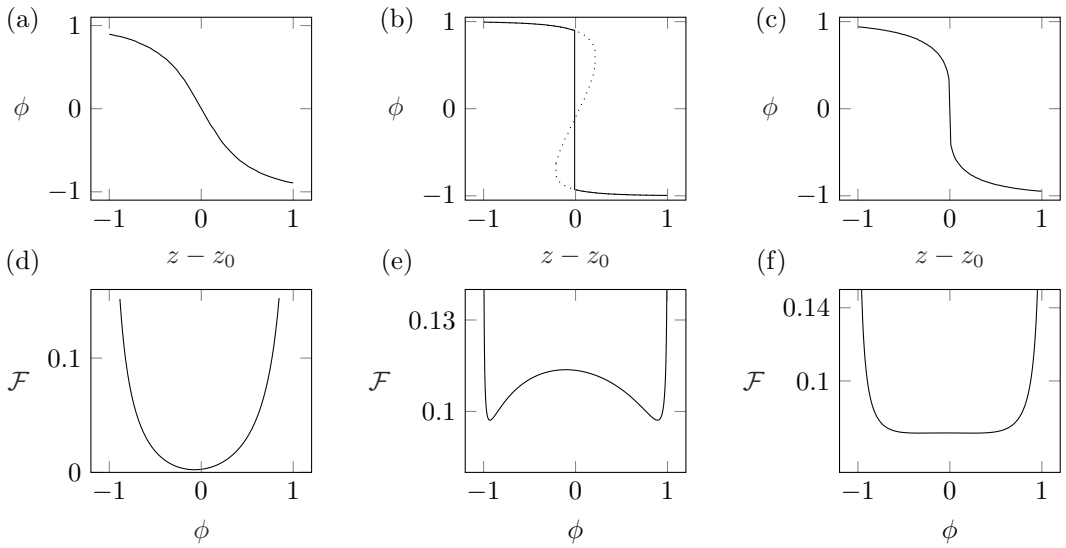

Figure 14.6: The structure of the energy barriers in different regimes for the case of hard device. The upper row: z dependence of the order parameter $\phi = N^{-1}\sum_{i=1}^{N}\langle s_i\rangle$ in different regimes; Lower row: matching free energies at fixed $z = z_0$. (a) and (d): phase I ($\beta = 4$, $\sigma = 0.2$); (b) and (e): phase III ($\beta = 10$, $\sigma = 0.1$) and (c) and (f): critical state ($\beta = 6$, $\sigma = 0.1$). $\lambda_f = 0.35$ and $v_0 = 0.1$

To summarize, our study suggests that evolution might have used geometrical frustration to tune the muscle machinery to perform near the conditions where both the Helmholtz and the Gibbs free energies are singular. Such design is highly functional when elementary force producing units affect each other performance and are therefore loaded in a mixed, soft-hard device. We recall that the muscle architecture is characterized by hierarchical structures with coupled modular elements loaded both in parallel and in series. In such systems, the proximity to only one of our two critical points will not be sufficient to ensure high performance in a sufficiently broad range of environment (Muñoz, 2017; Bialek, 2018). Moreover, as we show in the very idea of ensemble independent *local* constitutive relations for such a system may have to be abandoned.

14.11 Conclusions

In this Chapter, we established new links between muscle physiology and the theory of spin glasses and revealed a tight relation between steric incommensuration and the optimal mechanical performance of force generating machinery. While we neglected in this study many important features of actual muscles, we drew attention

to the beneficial role of geometrical frustration for the functioning of this biological system. The predicted strain glassiness in the regime of isometric contractions opens access to the whole spectrum of rigidities from zero (adaptability, fluidity) to infinite (control, solidity) and may serve as the factor ensuring the largest dynamic repertoire of the 'muscle material'. Similar disorder-mediated tuning towards criticality can be expected in other biological systems relying on long-range interactions including hair cells (Bormuth et al., 2014) and focal adhesions (Schwarz and Safran, 2013).

Chapter 15

Short-range interactions

As we have already mentioned, it has been long realized that the passive mechanical response of muscle sarcomeres is characterized by the negative stiffness in the physiologically relevant regime of isometric contractions which should lead to instabilities in a set of sarcomeres connected in series. In this Chapter, we argue that if destabilizing short-range interactions are introduced into the model of Huxley and Simmons, the homogeneous state of isometric contractions can be stabilized.

We consider a parallel bundle of Huxley-Simmons bi-stable units with competing short-range (nearest neighbor) and long-range (mean-field type) interactions. We show that in such the state of isometric contraction can be made stable and that the phase diagram of such a system is controlled by a tricritical point separating the lines of first and second order phase transitions.

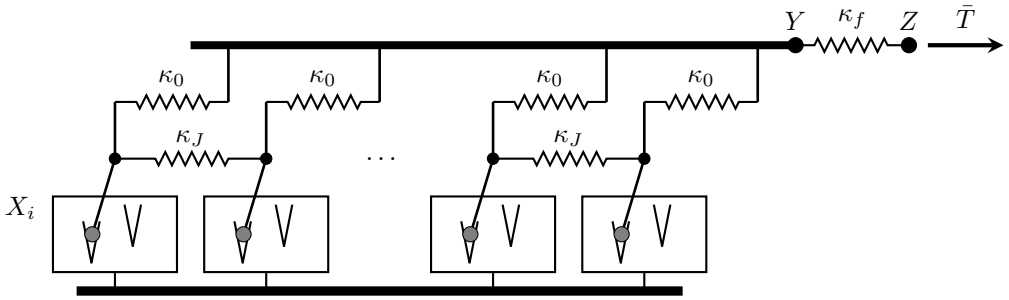

Figure 15.1: Cluster of interacting Huxley-Simmons units with short range interactions.

The system is represented by a collection of N interconnected units. A single unit, indicated by the subscript $i = 1, \ldots, N$, is the association of an elastic spring κ_0 in series with a bi-stable unit. We assume that the spin variable X_i represents the two conformational positions of the myosin head. In the pre-power stroke state $X_i = 0$, and in the post-power stroke $X_i = -a$, where a is the amount by which the myosin head pulls the actin during the power stroke. The different conformations differ by the energy bias $\bar{v}_0$.

Each element is assumed to interact with its nearest neighbors via a linear spring of stiffness κ_J. This spring is perceived as describing some kind of steric interaction that can destabilize homogeneous distribution of conformational states and therefore the parameter κ_J will be allowed to take negative values.

We assume that the bundle is loaded through an elastic spring $\kappa_f > 0$, which can be again viewed as representing a lumped description of the combined elasticities of actin and myosin filaments. An imposed displacement Z is applied to the external spring κ_f if the system is loaded in a hard device.

We write the energy of the system as,

$$\tilde{E}(\boldsymbol{X}, Y, Z) = \sum_{i}^{N} (a + X_i)\bar{v}_0 + \frac{\kappa_0}{2}(Y - X_i)^2 + \frac{\kappa_J}{2}(X_{i+1} - X_i)^2 + \frac{\kappa_f}{2}(Z - Y)^2. \quad (15.1)$$

To non-dimensionalize the problem we define the reference length a, and normalize the spatial variables accordingly: $x_i = X_i/a$, $y = Y/a$ and $z = Z/a$. Note that now the variable x_i takes values 0 and -1 for the pre and post-power stroke, respectively. By defining the non-dimensional energy $E(\boldsymbol{x}, y, z) = \tilde{E}(\boldsymbol{X}, Y, Z)/\kappa_0 a^2$, we write,

$$E(\boldsymbol{x}, y, z) = \sum_{i}^{N} (1 + x_i)v_0 + \frac{1}{2}(y - x_i)^2 + \frac{\lambda_J}{2}(x_{i+1} - x_i)^2 + \frac{\lambda_f}{2}(z - y)^2. \quad (15.2)$$

For finite systems, we consider periodic boundary conditions: $x_{N+1} = x_1$, but in the thermodynamic limit, the choice of the boundary conditions should become irrelevant (Yeomans, 1992; Goldenfeld, 1992).

To summarize, the ensuing system contains both short-range interactions, scaled with λ_J, and long-range interaction scaled with λ_f; the latter is executed through a backbone imposing a uniform elongation y.

If the system is loaded with an applied force instead of displacement, we may neglect the external spring κ_f, because κ_f is in series with the bundle. The corresponding total energy is,

$$W(\boldsymbol{x}, y, t) = \sum_{i}^{N} (1 + x_i)v_0 + \frac{1}{2}(y - x_i)^2 + \frac{\lambda_J}{2}(x_{i+1} - x_i)^2 - ty. \quad (15.3)$$

Here $t = \bar{T}/\kappa_0 a$ is the non-dimensional force applied to the bundle. In the case of a soft device, the long-range interaction is ensured by the presence of an applied force which is transmitted to all the elements.

To study the equilibrium properties of the system, we need to determine its free energy, which can be done through the computation of the partition function. Assume that the entire system is in contact with a reservoir at a fixed temperature T that remains fixed.

The canonical partition function in the *hard device* (controlled displacement) ensemble case can be written as,

$$\mathcal{Z}(\beta, z) = \int dy \sum_{\{x\}} e^{-\beta E(x_i, y, z)}, \quad (15.4)$$

where $\{x\}$ represents the trace over all possible states of the system, or the sum over $x_i = \{0, -1\}$ for all x_i, $\beta = \kappa_0 a^2/k_B T$ is the non-dimensional inverse temperature and k_B is the Boltzmann constant. In the *soft device* (controlled force) case the partition function reads,

$$\mathcal{Q}(\beta, t) = \int dy \sum_{\{x\}} e^{-\beta W(x_i, y, t)}. \quad (15.5)$$

Since $x_i = \{-1, 0\}$ we have that $\sum_i x_i^2 = -\sum_i x_i$, and this allows us to write the partition functions in both ensembles as,

$$\begin{aligned} \mathcal{Z}(\beta, z) &= \int dy e^{-\beta N\left[\frac{\lambda_f}{2}(z-y)^2 + v_0 + \frac{y^2}{2}\right]} \sum_{\{x\}} e^{\beta\lambda_J \sum_i x_i x_{i+1} + \beta(\lambda_j + y + 1/2 - v_0)\sum_i x_i} \\ &= \int dy e^{-\beta N \varphi(y,z)} \mathcal{Z}_0(\beta, y). \end{aligned} \quad (15.6)$$

and

$$\begin{aligned}\mathcal{Q}(\beta,t) &= \int dy e^{-\beta N\left[-ty+v_0+\frac{y^2}{2}\right]} \sum_{\{x\}} e^{\beta\lambda_J \sum_i x_i x_{i+1}+\beta(\lambda_j+y+1/2-v_0)\sum_i x_i} \\ &= \int dy e^{-\beta N\psi(y,t)} \mathcal{Z}_0(\beta,y).\end{aligned} \tag{15.7}$$

Here $\varphi(y,z)=\frac{\lambda_f}{2}(z-y)^2+v_0+\frac{y^2}{2}$, $\psi(y,t)=-ty+v_0+\frac{y^2}{2}$. The function $\mathcal{Z}_0(\beta,y)$ is the partition function for an Ising ring with spin values 0,-1 instead of the usual ± 1:

$$\begin{aligned}\mathcal{Z}_0(\beta,y) &= \sum_{\{x\}} \exp\left[\beta\lambda_J \sum_i x_i x_{i+1} + \beta\left(\lambda_j+y+1/2-v_0\right)\sum_i x_i\right] \\ &= \sum_{\{x\}} \exp\left[\beta J \sum_i x_i x_{i+1} + \beta H \sum_i x_i\right].\end{aligned} \tag{15.8}$$

Here, $J=\lambda_J$ and $H(y)=\lambda_j+y+1/2-v_0$.

To compute $\mathcal{Z}_0(\beta,y)$ we use the transfer matrix method. The general idea is to write the partition function as a product of equal matrices (Yeomans, 1992; Goldenfeld, 1992). The thermodynamic properties of the system will be then described by the eigenspectrum of the underlying (transfer) matrix.

First, we rewrite $\mathcal{Z}_0$ as,

$$\mathcal{Z}_0(\beta,y) = \sum_{\{x\}} e^{\beta J(x_1x_2+x_2x_3+\cdots+x_Nx_1)+\beta H(y)(x_1+x_2+\cdots+x_N)} \tag{15.9}$$

This is equivalent to

$$\mathcal{Z}_0(\beta,y) = \sum_{x_1}\cdots\sum_{x_N} e^{Jx_1x_2+\frac{H}{2}(x_1+x_2)} \times e^{Jx_2x_3+\frac{H}{2}(x_2+x_3)} \times \cdots \times e^{Jx_Nx_1+\frac{H}{2}(x_N+x_1)}. \tag{15.10}$$

Now we can think of each term as being an element of a 2×2 matrix

$$\boldsymbol{T}_{x_1x_2} = e^{Jx_1x_2+\frac{H}{2}(x_1+x_2)}. \tag{15.11}$$

Here x_1 and x_2 are the labels of the matrix elements. If we denote $x'=0$ and $x''=-1$ we can write $\boldsymbol{T}$ explicitly,

$$\boldsymbol{T} = \begin{pmatrix} T_{x'x'} & T_{x'x''} \\ T_{x''x'} & T_{x''x''} \end{pmatrix} = \begin{pmatrix} 1 & e^{-\frac{\beta H}{2}} \\ e^{-\frac{\beta H}{2}} & e^{\beta(J-H)} \end{pmatrix}. \tag{15.12}$$

Then,

$$\mathcal{Z}_0 = \sum_{x_1}\cdots\sum_{x_N} \boldsymbol{T}_{x_1x_2}\boldsymbol{T}_{x_2x_3}\cdots\boldsymbol{T}_{x_Nx_1}. \tag{15.13}$$

The sums $\sum_{x_1}\cdots\sum_{x_N}$ in Eq. (15.10) represent matrix multiplication. Therefore we can write

$$\mathcal{Z}_0 = \sum_{x_1} \boldsymbol{T}^N_{x_1x_1} = \mathrm{Tr}(\boldsymbol{T}^N) \tag{15.14}$$

so that only the summation over x_1 of the diagonal elements of $\boldsymbol{T}^N$ remains. Since $\boldsymbol{T}$ is real and symmetric it can be diagonalized

$$\boldsymbol{T}' = \begin{pmatrix} \lambda_1 & 0 \\ 0 & \lambda_2 \end{pmatrix} \tag{15.15}$$

Here λ_1 and λ_2 are the eigenvalues of the matrix $\boldsymbol{T}$

$$\lambda_{1,2} = e^{\frac{\beta}{2}(J-H)}\left[\cosh\frac{\beta}{2}(H-J) \pm \sqrt{\sinh^2\frac{\beta}{2}(H-J)+e^{-\beta J}}\right] \tag{15.16}$$

Since $\operatorname{Tr}\boldsymbol{T} = \operatorname{Tr}\boldsymbol{T}'$, we have

$$\mathcal{Z}_0 = \lambda_1^N + \lambda_2^N. \tag{15.17}$$

Now, assume that $\lambda_1 > \lambda_2$, and write,

$$\mathcal{Z}_0 = \lambda_1^N\left[1+\left(\frac{\lambda_2}{\lambda_1}\right)^N\right]. \tag{15.18}$$

In the thermodynamic limit $N \to \infty$,

$$\mathcal{Z}_0 \approx \lambda_1^N\left[1+\mathcal{O}(e^{-\alpha N})\right], \tag{15.19}$$

where $\alpha \equiv \log(\lambda_1/\lambda_2)$ is a positive constant. Therefore, in the thermodynamic limit, only the largest eigenvalue of the transfer matrix is important for the computation of the partition function.

15.1 Hard device

In order to obtain the thermodynamic properties of the system we need to calculate the free energy

$$\mathcal{Z}(\beta,z) = \int dy\, e^{-N\beta\left[\varphi(y,z)-\frac{1}{2}(J-H)-\frac{1}{\beta}\log\left[\cosh\frac{\beta}{2}(H-J)+\sqrt{\sinh^2\frac{\beta}{2}(H-J)+e^{-\beta J}}\right]\right]} \tag{15.20}$$

We recall that H is a function of y. To compute this integral, we may apply the saddle point approximation, which reduces to finding the minimum of the exponent with respect to y. This allows us to write,

$$\mathcal{Z}(\beta,z) = \sqrt{\frac{2\pi}{N|\Phi''(\beta,z,y_0)|}}e^{-N\beta\Phi(\beta,z,y)}. \tag{15.21}$$

Here $\Phi(\beta,z,y) = \varphi(y,z)-\frac{1}{2}(J-H)-\frac{1}{\beta}\log\left[\cosh\frac{\beta}{2}(H-J)+\sqrt{\sinh^2\frac{\beta}{2}(H-J)+e^{-\beta J}}\right]$. We use the notation $\Phi''(\beta,z,y_0)$ for the second derivative with respect to y. The free energy per element of the system is $\mathcal{F}(\beta,y) = -\frac{1}{N\beta}\log\mathcal{Z}(\beta,z)$. In the thermodynamic limit $N\to\infty$, we can write

$$\begin{aligned}\mathcal{F}(\beta,z,y_0(z)) = \varphi(y_0) &- \frac{1}{2}(J-H(y_0)) \\ &- \frac{1}{\beta}\log\left[\cosh\frac{\beta}{2}(H(y_0)-J)+\sqrt{\sinh^2\frac{\beta}{2}(H(y_0)-J)+e^{-\beta J}}\right],\end{aligned} \tag{15.22}$$

or more explicitly,

$$\begin{aligned}\mathcal{F}(\beta,z,y_0(z)) =& \frac{\lambda_f}{2}(z-y_0)^2 + v_0 + \frac{y_0^2}{2} + \frac{1}{2}(y_0+1/2-v_0) \\ &- \frac{1}{\beta}\log\left[\cosh\frac{\beta}{2}(y_0+1/2-v_0)+\sqrt{e^{-\beta\lambda_J}+\sinh^2\frac{\beta}{2}(y_0+1/2-v_0)}\right],\end{aligned} \tag{15.23}$$

where y_0 is a solution of a transcendental equation derived from the saddle point approximation. Since Φ is identical to the free energy $\mathcal{F}$, we need to solve

$$\frac{\partial \mathcal{F}(\beta, z, y)}{\partial y} = 0. \tag{15.24}$$

We can rewrite this equation as a self-consistent relation $y_0 = \Psi(y_0)$,

$$y_0 = \lambda_f z - \lambda_f y_0 - \frac{1}{2} + \frac{e^{\beta\lambda_J} \sinh \frac{\beta}{2}(y_0 + 1/2 - v_0)\sqrt{e^{-\beta\lambda_J} + \sinh^2 \frac{\beta}{2}(y_0 + 1/2 - v_0)}}{2e^{\beta\lambda_J} \sinh^2 \frac{\beta}{2}(y_0 + 1/2 - v_0) + 2}. \tag{15.25}$$

We may have more than one solution to Eq. (15.25) because of the non-convexity of the free energy with respect to y. This would mean the possibility of the coexistence of several phases in thermal equilibrium, each one corresponding to a different value of y_0. A graphical representation of the solutions of the self-consistent relation is shown in Fig. 15.2. We obtain three different scenarios, with one, three or five solutions.

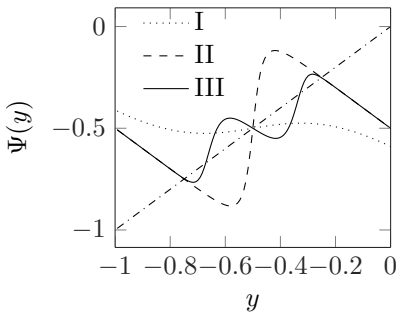

Figure 15.2: The self-consistent equation, Eq. (15.25), may have from one to five solutions, depending on the parameters. Here we show three possible scenarios. In scenario I the solution is unique, while in scenarios II and III we have multiple solutions.

To understand better the behavior of the system we can also compute the tension $t(\beta, z)$ developed by the bundle at an applied displacement z. It can be calculated as $t(\beta, z) = \frac{\partial \mathcal{F}(\beta, z, y_0(z))}{\partial z}$. Computing the total derivative of the free energy with respect to the displacement we obtain,

$$t(\beta, z) = \frac{\partial \mathcal{F}(\beta, z, y_0(z))}{\partial z} = \frac{\partial \mathcal{F}}{\partial z} + \frac{\partial \mathcal{F}}{\partial y_0}\frac{dy_0}{dz}, \tag{15.26}$$

Noticing that $\frac{\partial \mathcal{F}}{\partial y_0} = 0$, we finally write

$$t(\beta, z) = \frac{\partial \mathcal{F}}{\partial z} = \lambda_f (z - y_0). \tag{15.27}$$

We now fix the value for the external stiffness $\lambda_f = 1$ and study the behavior of the system at different values of λ_J and temperatures β. We assume, for simplicity, that $v_0 = 0$, $\lambda_f = 1$. For the interpretation of the results, it will be useful to introduce the reference elongation $z_0 = (1 + 1/\lambda_f)v_0 - 1/2$, which describes the state where the fully folded and unfolded configurations have the same energy.

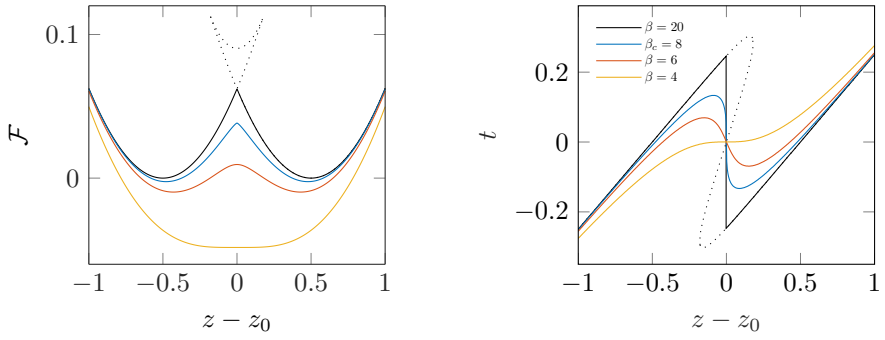

(a) **(b)**

Figure 15.3: Mechanical response of the system with varying temperature, here the system is non-interacting $\lambda_J = 0$, $\lambda_f = 1$ and $v_0 = 0$

In Fig. 15.3 we show the mechanical response of a system without short-range interactions ($\lambda_J = 0$). As we increase the temperature (decrease β), we proceed from a discontinuous jump in the tension to a critical state in the hard device, where the derivative of the tension with respect to z is infinite. Increasing further the temperature we obtain a response with negative stiffness. At much higher temperatures we recover the positive stiffness response, which indicates the recovered convexity of the free energy (with respect to the control parameter z).

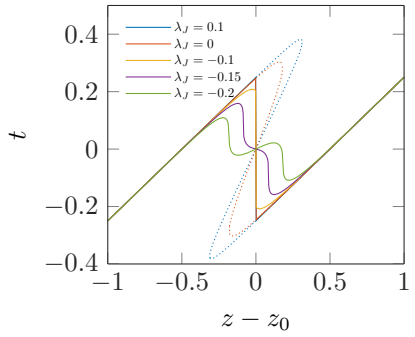

Figure 15.4: Tension developed by the system at a fixed temperature $\beta = 20$ and varying levels of interaction λ_J. The remaining parameters are $\lambda_f = 1$ and $v_0 = 0$.

When the sort range interaction is present, we observe a new feature in the response of the system. In Fig. 15.4 we show that positive values of λ_J act as an increase in β (or decrease in temperature), favoring cooperativity and destabilizing the point $z = z_0$. However, at negative values for λ_J we observe regimes where the initially unstable point $z = z_0$ gets stabilized while the two regimes with negative stiffness are pushed side-wise.

To illustrate all possible behaviors we construct a phase diagram in the $1/\beta, \lambda_J$ plane, by fixing $\lambda_f = 1$ and $v_0 = 0$. It is shown in Fig. 15.5. The different tension curves, corresponding to different indicated points in the phase diagram are presented in Fig. 15.6. The construction of the phase boundaries is based on the convexity properties of $\mathcal{F}(\beta, z, y_0)$ with respect to y_0, and individual phases differ by the number of solutions to the self-consistent relation, Eq. (15.25).

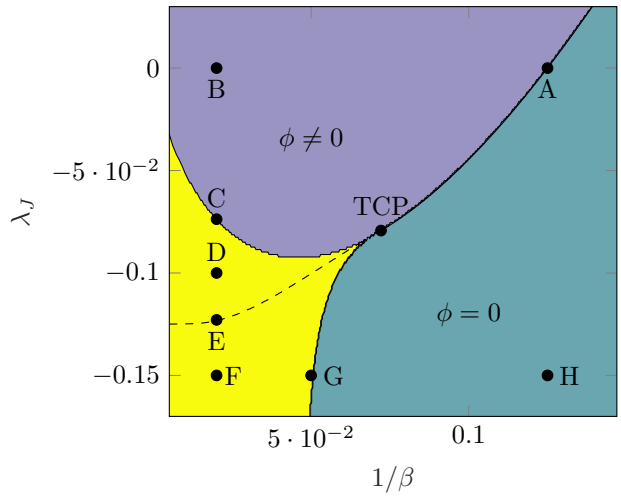

Figure 15.5: Phase diagram for the system. In the canonical ensemble the transition is continuous (bold solid line) down to the tricritical point TCP, where it becomes first-order (dashed line).

15.2 Soft device

In order to obtain the thermodynamic properties of the system in the soft device, we need to calculate the Gibbs free energy. If we substitute the expression for $\mathcal{Z}_0(\beta, y)$ in Eq. (15.7) we obtain,

$$\mathcal{Q}(\beta, z) = \int dy\, e^{-N\beta\left[\psi(y,z)-\frac{1}{2}(J-H)-\frac{1}{\beta}\log\left[\cosh\frac{\beta}{2}(H-J)+\sqrt{\sinh^2\frac{\beta}{2}(H-J)+e^{-\beta J}}\right]\right]} \tag{15.28}$$

To compute this integral, we again apply a saddle-point approximation and obtain

$$\mathcal{Z}(\beta, t) = \sqrt{\frac{2\pi}{N|\Psi''(\beta, t, y_0)|}} e^{-N\beta\Psi(\beta,t,y)}, \tag{15.29}$$

where $\Psi(\beta, t, y) = \psi(y, t) - \frac{1}{2}(J-H) - \frac{1}{\beta}\log\left[\cosh\frac{\beta}{2}(H-J) + \sqrt{\sinh^2\frac{\beta}{2}(H-J) + e^{-\beta J}}\right]$.
The Gibbs free energy per element is $\mathcal{G}(\beta, t) = -\frac{1}{N\beta}\log\mathcal{Q}(\beta, t)$ and in the thermodynamic limit $N \to \infty$ we can write

$$\begin{aligned}\mathcal{G}(\beta, t, y_0(z)) = \psi(y_0, t) - \frac{1}{2}(J - H(y_0)) \\ - \frac{1}{\beta}\log\left[\cosh\frac{\beta}{2}(H(y_0) - J) + \sqrt{\sinh^2\frac{\beta}{2}(H(y_0) - J) + e^{-\beta J}}\right],\end{aligned} \tag{15.30}$$

or more explicitly,

$$\begin{aligned}\mathcal{G}(\beta, t, y_0(z)) = - ty_0 + v_0 + \frac{y_0^2}{2} + \frac{1}{2}(y_0 + 1/2 - v_0) \\ - \frac{1}{\beta}\log\left[\cosh\frac{\beta}{2}(y_0 + 1/2 - v_0) + \sqrt{e^{-\beta\lambda_J} + \sinh^2\frac{\beta}{2}(y_0 + 1/2 - v_0)}\right],\end{aligned} \tag{15.31}$$

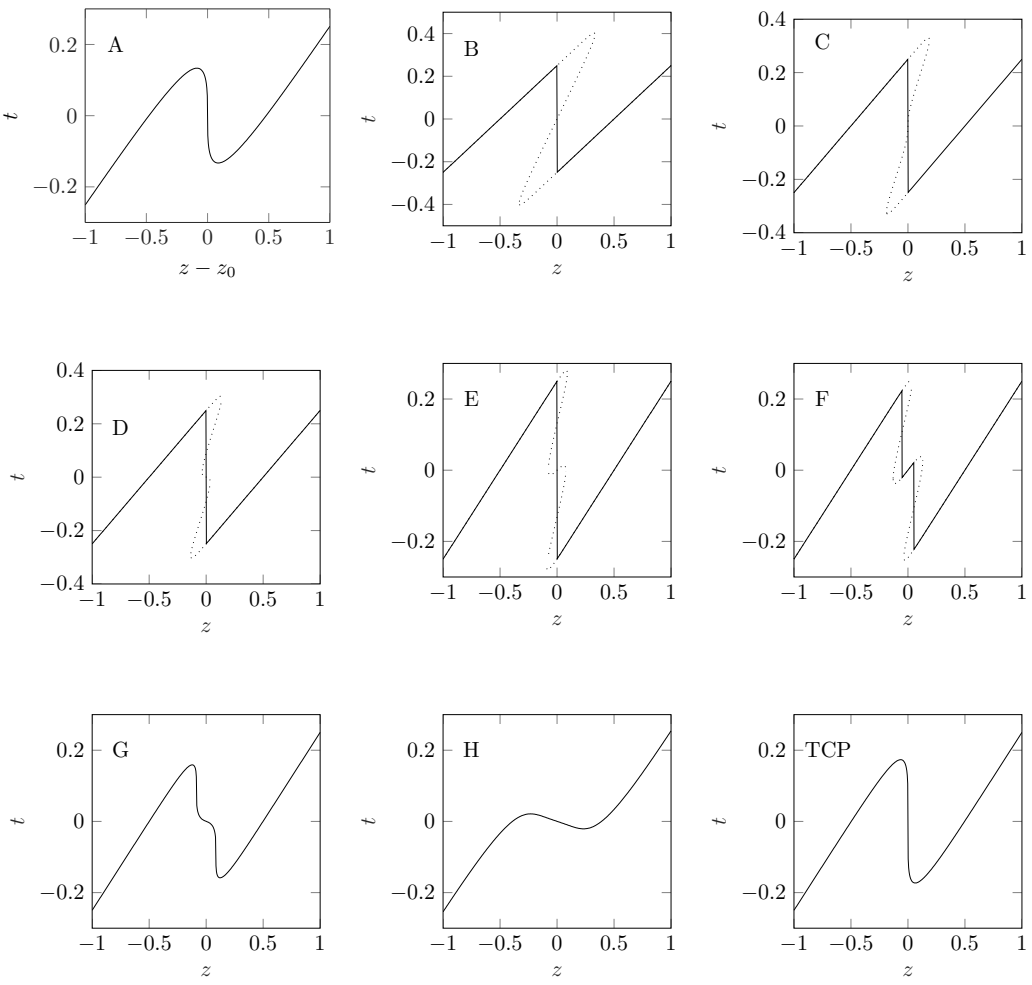

Figure 15.6: Force-elongation curves illustrating the multiple types of behavior presented in the phase diagram in Fig. 15.5.

where y_0 is the solution to a transcendental equation derived as a part of the saddle-point approximation. Since Ψ is identical to $\mathcal{G}$, we can write

$$\frac{\partial \mathcal{G}(\beta, t, y)}{\partial y} = 0, \tag{15.32}$$

which gives the self-consistency relation,

$$y_0 = t - \frac{1}{2} + \frac{e^{\beta\lambda_J} \sinh \frac{\beta}{2}(y_0 + 1/2 - v_0)\sqrt{e^{-\beta\lambda_J} + \sinh^2 \frac{\beta}{2}(y_0 + 1/2 - v_0)}}{2e^{\beta\lambda_J} \sinh^2 \frac{\beta}{2}(y_0 + 1/2 - v_0) + 2}. \tag{15.33}$$

As in the hard device, parameter λ_J plays the major role in the behavior of the system, which we illustrate by showing the free energy and the force-elongation relation.

To summarize, we developed a model for interacting cross-bridges and introduced different elastic parameters characterizing short-range interactions (λ_J) and long-range interactions (λ_f). Positive values of λ_J, produce ferromagnetic interactions and have a similar effect to decreasing the temperature on the response of the

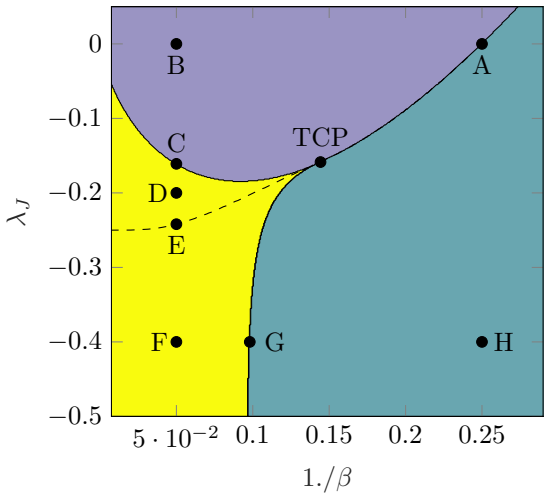

Figure 15.7: Phase diagram for the system in soft device. In the canonical ensemble the transition is continuous (bold solid line) down to the tricritical point TCP, where it becomes first-order (dashed line).

system: as short-range interaction get stronger, the system is more prone to behave collectively (synchronously). For negative λ_J the effect of short-range interaction is anti-ferromagnetic. Then, in a specific region of the parameter space, we observe the creation of a new macroscopic energy well. This new well replaces the energy saddle which in this way becomes stabilized (at the point z_0). This result holds for both hard and soft device ensembles even if stabilization takes place at different values of parameters.

Landau's phenomenological description To apply Landau's mean-field description (Goldenfeld, 1992; Pathria and Beale, 1996) to our problem we first need to define an order parameter. First, notice that the equilibrium of the system with respect to the variable y implies,

$$y = \frac{\lambda_f z}{\lambda_f + 1} + \frac{1}{\lambda_f + 1}\frac{1}{N}\sum_i x_i. \tag{15.34}$$

We can then obtain a relation between the average value of the internal spin variable $\langle x \rangle = \frac{1}{N}\sum_i x_i$ and y :

$$\langle x \rangle = (\lambda_f + 1)y - \lambda_f z. \tag{15.35}$$

As we see below, it will be natural to define the order parameter as $\phi = \langle x \rangle + \frac{1}{2}$.

15.3 Hard device

We study the system at a given elongation $z = z_0 = (1 + 1/\lambda_f)v_0 - 1/2$, which is the value at which the equilibrated system has the same energy for the fully folded and unfolded configurations. At this elongation it is expected that the mean fraction of folded elements is equal to the unfolded elements, since $E(x_i = 0, z_0) = E(x_i = -1, z_0)$, leading to $\langle x \rangle (\beta, z_0) = -1/2$, which justifies the definition of ϕ. We can then write

$$\phi = (\lambda_f + 1)y - \lambda_f z + \frac{1}{2}. \tag{15.36}$$

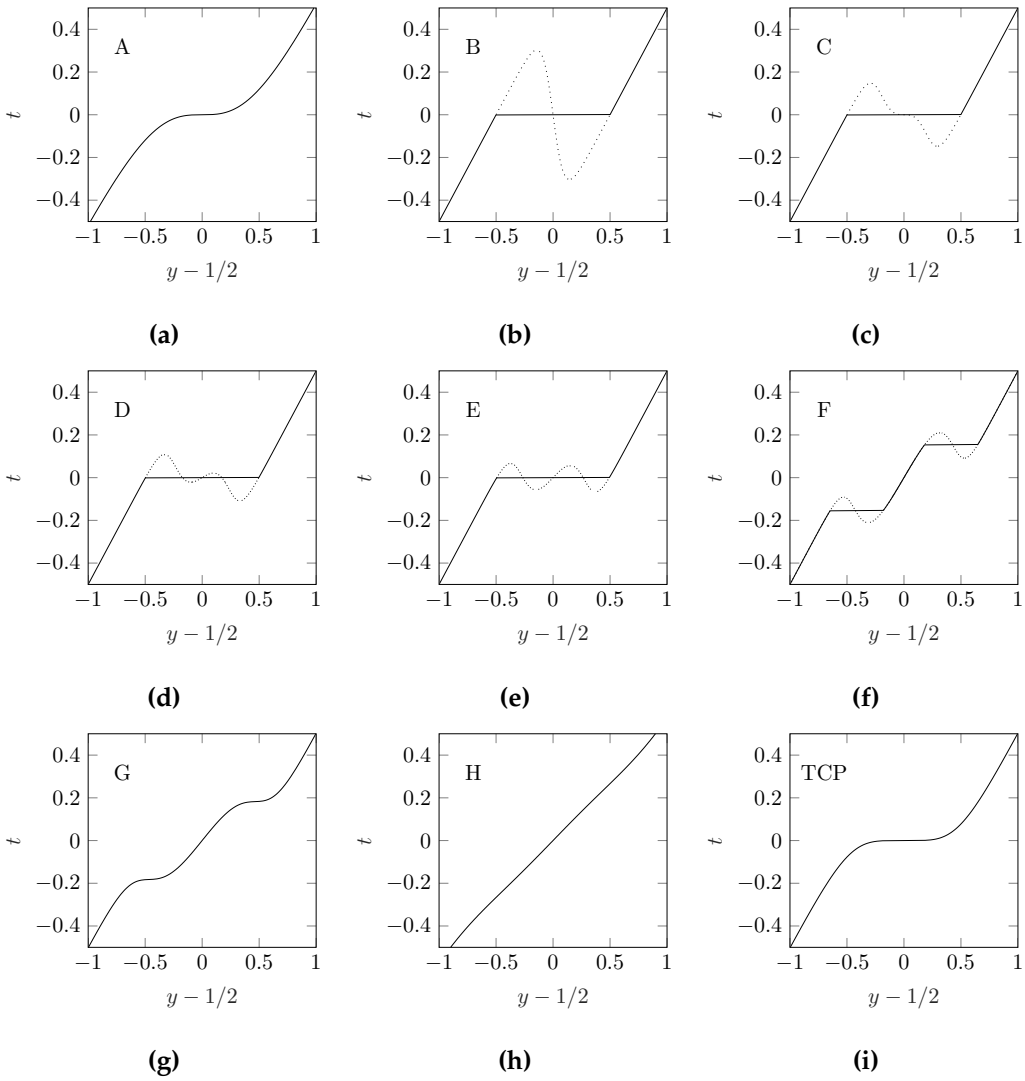

Figure 15.8: Force-elongation curves illustrating the multiple types of behavior presented in the phase diagram in Fig. 15.7.

Assume, for simplicity, $v_0 = 0$, $\lambda_f = 1$. Then we can write

$$\mathcal{F}(\beta,\phi) = \frac{1}{8} + \frac{\phi^2}{4} - \frac{1}{\beta}\log\left[\cosh\frac{\beta\phi}{4} + \sqrt{e^{-\beta\lambda_J} + \sinh^2\frac{\beta\phi}{4}}\right], \tag{15.37}$$

The corresponding self-consistency relation in terms of ϕ is,

$$\phi = \frac{\sinh\frac{\beta\phi}{4}}{2\sqrt{e^{-\beta\lambda_J} + \sinh^2\frac{\beta\phi}{4}}}. \tag{15.38}$$

The main assumption of Landau approach is that near T_c we can expand the free energy for small ϕ, *i.e.* that $\mathcal{F}$ is an analytical function of the order parameter. To describe in this way the second-order phase transition in our system we perform a Taylor expansion of the free-energy Eq. (15.37) around $\phi = 0$ leading to,

$$\mathcal{F}(\beta,\phi) = \frac{1}{8} - \frac{\log\left(\sqrt{e^{-\beta\lambda_J}}+1\right)}{\beta} + \left(1 - \frac{\beta}{8\sqrt{e^{-\beta\lambda_J}}}\right)\phi^2 + \frac{\beta^3\left(3e^{\beta\lambda_J}-1\right)}{384\sqrt{e^{-\beta\lambda_J}}}\phi^4 + \mathcal{O}(\phi^5). \tag{15.39}$$

Due to the symmetry of the free energy $\mathcal{F}(\beta, \phi) = \mathcal{F}(\beta, -\phi)$ the Taylor expansion around $\phi = 0$ contains only even powers of ϕ. In this expansion we must ensure that the fourth-order term is positive; otherwise the free energy would be minimized by $|\phi| \to \infty$. Hence, we must require that

$$3e^{\beta\lambda_J} - 1 > 0. \tag{15.40}$$

Next, we find the equilibrium value of the order parameter by minimizing the free energy

$$\frac{\partial \mathcal{F}}{\partial \phi} = 0 = 2\left(1 - \frac{\beta}{8\sqrt{e^{-\beta\lambda_J}}}\right)\phi + \frac{\beta^3\left(3e^{\beta\lambda_J} - 1\right)}{96\sqrt{e^{-\beta\lambda_J}}}\phi^3. \tag{15.41}$$

Clearly, one of the solutions is $\phi = 0$ but there are also two other solutions

$$\phi = \pm\sqrt{\frac{24\left(\beta - 8\sqrt{e^{-\beta\lambda_J}}\right)}{\beta^3\left(3e^{\beta\lambda_J} - 1\right)}}. \tag{15.42}$$

The critical inverse temperature, β_c is such that the second-order term in the expansion is equal to zero, hence

$$1 - \frac{\beta_c}{8\sqrt{e^{-\beta_c\lambda_J}}} = 0. \tag{15.43}$$

In the limit $\lambda_J \to 0$ we obtain $\beta_c = 8$. In general, we can write an explicit expression for β_c

$$\beta_c = \frac{2W(4\lambda_J)}{\lambda_J} \tag{15.44}$$

where $W(x)$ is the Lambert function, defined by the functional equation $z = W(z)e^{W(z)}$. This function is defined for $z \geq -1/e$. The typical shape of the resulting free energy is shown in Fig. 15.9a.

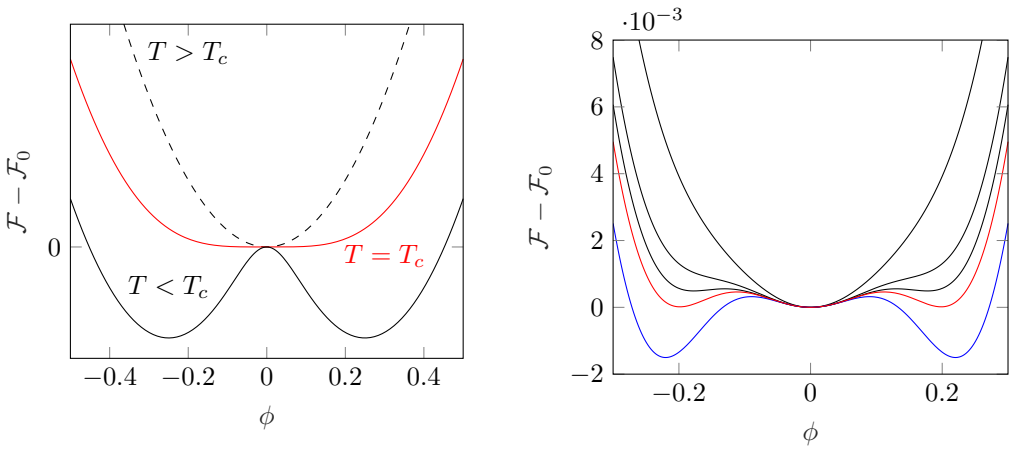

(a) Second-order phase transition. **(b)** First-order phase transition.

Figure 15.9

The constructed Landau model exhibits a second-order phase transition. However, we also know that in the (β, λ_J) phase diagram there is a tricritical point (TCP), where the transition becomes of the first order.

We can capture this effect in the Landau's framework by introducing the sixth-order term in the expansion. It must be positive so that the system is globally stable.

However, now the fourth-order term may be negative. The expansion reads

$$\begin{aligned}\mathcal{F}(\beta,\phi) = \frac{1}{8} - \frac{\log\left(\sqrt{e^{-\beta\lambda_J}}+1\right)}{\beta} + \left(1 - \frac{\beta}{8\sqrt{e^{-\beta\lambda_J}}}\right)\phi^2 \\ + \frac{\beta^3\left(3e^{\beta\lambda_J}-1\right)}{384\sqrt{e^{-\beta\lambda_J}}}\phi^4 + \frac{\beta^5\left(30e^{\beta\lambda_J}-45e^{2\beta\lambda_J}-1\right)}{46080\sqrt{e^{-\beta\lambda_J}}}\phi^6 + \mathcal{O}(\phi^7).\end{aligned} \tag{15.45}$$

Again, due to the symmetry of the free energy we only have even powers of ϕ.

The minimization of this free energy with respect to the order parameter yields,

$$\frac{\partial\mathcal{F}}{\partial\phi} = 2a_2\phi + 4a_4\phi^3 + 6a_6\phi^5 = 0, \tag{15.46}$$

where $a_2 = 1 - \frac{\beta}{8\sqrt{e^{-\beta\lambda_J}}}$, $a_4 = \frac{\beta^3\left(3e^{\beta\lambda_J}-1\right)}{384\sqrt{e^{-\beta\lambda_J}}} < 0$ and $a_6 = \frac{\beta^5\left(30e^{\beta\lambda_J}-45e^{2\beta\lambda_J}-1\right)}{46080\sqrt{e^{-\beta\lambda_J}}} > 0$. Out of the five solutions of this equation, at most three are real and stable. The trivial solution is $\phi = 0$ and for solutions with $\phi \neq 0$ we have an explicit expression

$$\phi = \pm\sqrt{\frac{-a_4 + \sqrt{a_4^2 - 3a_2a_6}}{3a_6}}. \tag{15.47}$$

Our analysis shows that the ensuing system indeed exhibits a second-order phase transition up to the tricritical point, where the transition becomes first-order. The tricritical point can be linked to the vanishing of the fourth-order term in the expansion. Therefore, if we recall that at the transition $\beta = 8e^{-\beta\lambda_J/2}$, from the second-order term and $e^{-\beta\lambda_J/2} = \sqrt{3}$ from the fourth-order term, we obtain the tricritical point TCP at $\beta_{TCP} = 8\sqrt{3}$ and $\lambda_J = -\log 3/8\sqrt{3}$. The first-order transition line (Maxwell line) is obtained by requiring that $\mathcal{F}(\beta,\phi=0) = \mathcal{F}(\beta,\phi=\phi^*)$.

We can now build the full phase diagram in the (λ_J,β) plane showing separately the region where the state with $\phi = 0$ is stable from the regions where the stable configurations have $\phi \neq 0$.

Similar analysis can be performed for the system in the soft device, see Appendix K.

To summarize, we have formally introduce the Landau free energy capturing the whole complexity of the phase transitions between synchronous and asynchronous behavior. It is interesting to notice that hard- and soft-device systems are characterized by qualitative similar but quantitatively different phase diagrams. In both systems the tricritical point was found to be located in the region of anti-ferromagnetic short range interactions.

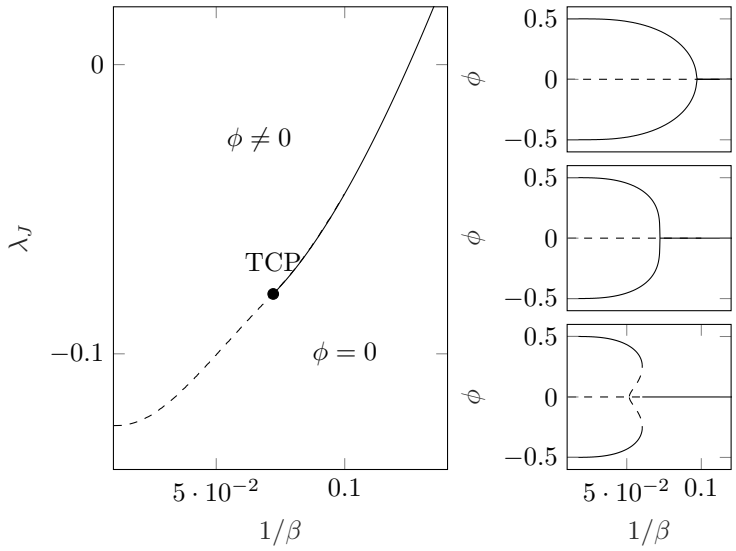

Figure 15.10: Phase diagram for the system. In the canonical ensemble the transition is continuous (bold solid line) down to the tricritical point TCP, where it becomes first-order (dashed line).

Chapter 16

Conclusions

In this Part, we studied a mathematical model describing the passive mechanical behavior of muscle fibers, which is relevant for the analysis of experiments involving fast mechanical perturbations.

Under an assumption that the fast force recovery is due to the synchronous conformational change involving myosin heads attached to the actin, known as the power stroke (Piazzesi et al., 2002; Kaya et al., 2017), we generalized the Huxley-Simmons model (Huxley and Simmons, 1971) along the lines proposed in (Caruel, Allain, and Truskinovsky, 2013) and assumed that the bi-stable nature of the myosin head could be represented by a soft spin variable. In our simplified representation of the half-sarcomere, the cross-bridges were arranged in parallel. The bundle of parallel cross-bridges connects to a linear spring, representing a lump description of the myofilament elasticity. The parallel structure of the system and the presence of the series spring are responsible for long-range interactions – the main ingredient allowing the system to act synchronously.

The main new step was the account of the intrinsic geometrical frustration, caused by the disregistry between the periodicity of myosin heads and actin binding sites. Such inhomogeneity makes muscles systems, commonly believed to be regular, crystal-like materials, resembling rather structural glasses. We explored the direct analogy between our model and the random field Ising model (RFIM) which allowed us to compute the thermodynamic properties of the disordered muscle system explicitly by using the classic replica trick.

Our main focus was on the study of the equilibrium properties of the muscle system. Finite temperature ($1/\beta$) and finite quenched disorder (σ) act as desynchronizing factors, while long-range interactions act as synchronizing mechanism scaled by λ_f. We constructed a phase diagram in (β, σ, λ_f) space distinguishing cooperative from non-cooperative behavior. The transition was found to be of the second-order.

We explored the consequences of the fact that in the presence of long-range interactions (Campa, Dauxois, and Ruffo, 2009; Barré, Mukamel, and Ruffo, 2001) the collective behavior of cross-bridges is different in force (soft device) and length (hard device) ensembles. Our main result is the phase diagram where we presented two critical surfaces corresponding to the hard- and soft-device criticality loci. We have shown that the experimental data point to the fact that the system is placed in a narrow region between the two critical lines, which we argue to be highly functional. Such posing of the system depends crucially on the presence of the quenched disorder.

We then introduced a destabilizing short-range interaction between the cross-bridges and studied its competition with stabilizing long-range interactions. We have shown that while an increase in strength of ferromagnetic interaction ($\lambda_J > 0$) has the same effect as a decrease of temperature leaving the overall qualitative behavior is unchanged, anti-ferromagnetic interactions ($\lambda_J < 0$) drastically change

the qualitative behavior of the system. Fine tuning of λ_J allows one to introduce a third energetic well and stabilize the stall state. For a fixed long-range interaction strength (fixed λ_f), the phase diagram in (β, λ_J) space, has a line of second-order phase transition that ends in a tricritical point, followed by a line of first-order phase transition.

Arguing for the importance of being close to both critical points, we proposed that such design is necessary when elementary force producing units affect each other's mechanical performance and are, effectively loaded in a mixed, soft-hard device. Parallel sarcomeres would then need to synchronize under imposed displacement, while series connections would have to sync under imposed force. We also observed that because of a generically non-affine response of a system of elastically interacting half-sarcomeres the very idea of ensemble independent *local* constitutive relation for such system may have to be abandoned.

Finally, we used the classical Landau approach to generate the complete phase diagram of the system. The Landau potential for the muscle system was shown to be at least of the sixth order. The main feature of the ensuing diagram is the presence of the tricritical point separating the lines of first-order and second-order phase transitions. This phase diagram broader potential repertoire of mechanical responses for the muscle system comparing to the mean-field system with the possibility of not only critically but also tri-critically tuned behavior. The exploration of this possibility depends crucially on the adequate account of the quenched disorder which will remain our next task. The experimental verification of our predictions is also a natural next step of this research project.

Chapter 17

General discussion

In this Ph.D. Thesis, we explored several simple models whose goal is to understand the very basic features of the passive mechanical response of focal adhesion and skeletal muscles. Both systems were analyzed in a mean-field framework as a bundle of interacting bistable elements subjected to thermal fluctuations and exposed to quenched inhomogeneities. The only difference between adhesion and contraction in such a prototypical representation is that in the case of the binding one of the two states is degenerate while in the case of the power stroke both states are characterized by finite rigidity.

Despite the similarity of the underlying systems, we were interested in different aspects for each one of them. Thus, we focused mainly on the athermal fluctuational characteristics of the debonding process because of recent experiments showing intermittency in the response of focal adhesions. We also studied the response of a focal adhesion to a time-dependent loading, which ultimately defines the effective friction mechanism during cell's crawling. In the case of muscles, one of the most intriguing phenomena is the passive fast force recovery, which we modeled within an extended version of the Huxley-Simmons model, with the main novelty in the systematic account of intrinsic inhomogeneity, which we found to be functional. For both systems, we studied the effect of finite temperatures to make sure that in the conditions of interest the systems do not 'melt' and preserve their crucial snap-through mechanical behavior. An important general conclusion is that the macroscopic bi-stability requires self-organization and cooperative response of individual elements which is ensured in both systems by the dominance of long-range interactions.

Our more detailed conclusions are collected below where we also briefly mention some unsolved problems which we plan to attack in the future.

Cellular adhesion We modeled cellular adhesion as a problem of thermalized fracture in a disordered system. A focal adhesion was described as a collection of breakable units loaded in parallel through a rigid backbone that imposed long-range interactions. The classic theory of FBM deals with a force-controlled ensemble and predicts brittle behavior (abrupt collective debonding) independently of the level of disorder. To capture ductile behavior, we introduced an external spring in series with the bundle and viewed it as a lump description of the connecting pad, extracellular matrix or another type of elastic environment. The elasticity of this spring is a measure of the system's rigidity, which is by itself a measure of the degree of interaction between individual binding elements. We showed that by tuning the degree of disorder, the rigidity, and the temperature of the system one can externally (or internally) induce a brittle to ductile transition. This transition is of the second-order, and the associated scaling can be interpreted as critical debonding. We studied the

fluctuational behavior of the system in ductile, brittle and critical regimes analytically and computed the exponents characterizing the long tails of the corresponding distributions. We have also studied how the scaling behavior in this disordered athermal system is affected by finite temperature and finite rate of driving.

In the perspective of the analogy between thermal fracture and cellular adhesion, one of our principal results is that in- or out-of-equilibrium systems are in the same universality class, with the same avalanche size distribution in the critical regimes. We have shown that the fluctuational behavior in brittle regime is supercritical, with spinodal exponents and a finite peak, similar to what was previously found in the classical FBM. However, while in the out-of-equilibrium system we found a robust power-law distribution of avalanches prior to the final breakdown, in the equilibrium system we observed a size-independent exponential cut off. The ductile responses in both types of internal protocols are similar (subcritical) with close to the Gaussian distribution of avalanches.

Recent studies using atomic force microscopy (AFM), where rupture/failure events were detected using indentation of a cantilever in a living cell, revealed the intermittent mechanical response characterized by a long-tailed distribution of fluctuations. Moreover, the notion of brittle to ductile transition and the associated criticality, previously introduced in amorphous plasticity, was found relevant in quantifying cellular response (Polizzi et al., 2018). In the studies of debonding of focal adhesions from substrates, several authors also reported intermittent behavior along the force-elongation curve (Helenius et al., 2008; Friedrichs, Helenius, and Muller, 2010; Müller et al., 2009; Rajan et al., 2017; Sundar Rajan, 2016). Our work provides a theoretical quantification of such intermittency. It suggests that distribution of avalanches should become a focus of future experimental studies aimed at the characterization of the mechanistic pathways involved in regulation and passive control of cellular debonding and deformation.

We reiterate that there seems to be an ever increasing evidence of criticality in the behavior of cellular systems. For instance, plasma membranes of mammalian cells have compositions which appear to be tuned near a critical point at physiological temperatures. Such proximity to criticality is believed to be necessary to explain the observed heterogeneity and may be functional (Machta et al., 2011; Machta, Veatch, and Sethna, 2012). As we have shown, similar heterogeneity, involved in the activity of focal adhesions, may influence the robustness of the debonding process.

More generally, we have shown that in systems with long-range interactions, the interplay between rigidity, disorder, and temperature can significantly affect the overall response of the debonding system not only in quasistatic conditions but also under dynamic loading, where brittleness can be associated with stick-slip frictional behavior, while ductility would mean continuous/smooth sliding. The most interesting crossover regimes of critical sliding need to be further investigated theoretically, and the associated fluctuations should be studied experimentally. However, even the results already obtained in this Thesis can be directly used in the modeling of cell motility in complex environments, where the rigidity and disorder parameters of the model would have to be linked to the particular rheological and structural states of the environment. We emphasize that critical debonding can be achieved by tuning the overall rigidity, which cells can in principle perform actively. This suggests that active rigidity manipulation may be an important factor controlling cell friction and ultimately affecting the choice of the prevailing mode of cell motility.

Many important questions have been left for future research. For instance, more realistic geometries can be considered in the FBM framework with non-democratic, elasticity controlled stress redistribution which would account for the possibility of

stress concentration and crack propagation. Similarly, the complex rheology of the background and the nontrivial rigidity of the supporting cortex/cytoskeleton, implying force-chain-based transmission of mechanical interactions, have not been yet accounted for. Last but not least, the active processes involved in cellular adhesion and fueled by ATP hydrolysis remain to be introduced into the model. Incorporating all these elements in the comprehensive geometrical setting with the state of the art biochemical regulation will allow one to obtain an engineering level of control in cellular adhesion which will then open the way to genuinely adequate modeling of cell crawling and the development of artificial devices imitating this complex biological phenomenon.

Skeletal muscles In parallel with the study of adhesive clusters, we also developed a model describing the passive mechanical behavior of muscle fibers, which is relevant for the analysis of physiological experiments involving muscle response to fast mechanical perturbations. The proposed model is therefore aimed at reproducing the passive force generation in skeletal muscles. By assuming that it is due to synchronous power stroke in actin-bound myosin heads, we built upon the extension of the Huxley-Simmons model proposed in (Caruel, Allain, and Truskinovsky, 2013).

The new developments include the account of geometrical inhomogeneity, introduced in the form of a quenched disorder, and the incorporation of steric interaction between myosin heads in the form of nearest neighbor interactions. Both, quenched inhomogeneity and destabilizing short-range interactions make muscles systems, commonly believed to be crystal-like materials, looking more like structural glasses.

A muscle fiber is a complex hierarchical structure of parallel and series connections. Therefore, for the system to strike synchronously it should do so in both length and force ensembles: parallel sarcomeres would need to sync under imposed displacement, while series connection under imposed force. We used the fact that due to the dominance of long-range interactions, the overall behavior of the system is different in force- and length-controlled ensembles and computed a phase diagram in temperature, disorder and rigidity space, identifying two critical surfaces corresponding to either hard or soft device loading. The experimental data place the system in a narrow region between these two critical surfaces, and such positioning is crucially dependent on the presence of the quenched disorder.

Our study then suggests that evolution might have used geometrical frustration to tune muscle machinery to perform near the conditions where both Helmholtz and the Gibbs free energies are singular. Our study also suggests that to achieve such proximity to a critical surface by only tuning temperature would have been impossible. The ensuing organization of individual cross bridges appears to be highly functional when elementary contractile units affect each other performance and are loaded in a mixed, soft-hard device. Because of a generically non-affine response of a system of elastically interacting half-sarcomeres, the very idea of ensemble independent local constitutive relation for such system becomes questionable which makes the task of continuum modeling of skeletal muscles rather challenging.

To make the model more adequate, we also considered destabilizing steric short-range interactions of neighboring cross-bridges allowing them to compete with the stabilizing, long-range interactions imposed by the filaments. We showed that antiferromagnetic short-range interactions could drastically change the qualitative response of the muscle system stabilizing the stall regime by turning the apparently negative stiffness into the positive one. We used the classical Landau approach to generate the complete phase diagram of the system controlled by a tricritical point.

This phase diagram offers a broad potential repertoire of mechanical responses for the muscle system with the possibility of not only critically but also tri-critically tuned behavior. The exploration of this possibility depends crucially on the adequate account of the quenched disorder which will remain the task for future research.

Other subjects to be considered in the muscle framework include a more adequate modeling of the realistic multiscale (hierarchical) organization of the elementary force producing units (half sarcomeres) and the correct account for the distributed elasticity of the filaments, the cross-linking disks and the connectivity induced by other supporting proteins, first of all, titin. An even more radical step would be to include into the model the active force generation involving the collective action of a large number of interacting molecular motors. This will allow one to link the relatively simple phenomenon of passive fast force recovery with complex active phenomena of tetanization and ATP supported force homeostasis. These developments will open the way to the construction of adequate macroscopic continuum representations of striated muscles, which can be used, for instance, in the modeling of heart tissue. The critical nature of muscle response, implying the absence of scale separation, makes this task particularly challenging.

Bibliography

A. S. Krausz, K. Krausz (auth.) (1988). *Fracture Kinetics of Crack Growth*. 1st ed. Mechanical Behavior of Materials 1. Springer Netherlands. ISBN: 978-94-010-7116-1,978-94-009-1381-3.

Alava, Mikko J., Phani K. V. V. Nukala, and Stefano Zapperi (2006). "Statistical models of fracture". In: *Advances in Physics* 55.3-4, pp. 349–476. DOI: 10.1080/00018730300741518.

Arcangelis, L. de and H. J. Herrmann (1989). "Scaling and multiscaling laws in random fuse networks". In: *Phys. Rev. B* 39 (4), pp. 2678–2684. DOI: 10.1103/PhysRevB.39.2678.

Arnold, B.C., N. Balakrishnan, and H.N. Nagaraja (1992). *A First Course in Order Statistics*. Classics in Applied Mathematics. Society for Industrial and Applied Mathematics. ISBN: 9780898719062.

Balleza, Enrique et al. (June 2008). "Critical Dynamics in Genetic Regulatory Networks: Examples from Four Kingdoms". In: *PLOS ONE* 3.6, pp. 1–10. DOI: 10.1371/journal.pone.0002456.

Balog, Ivan, Matthieu Tissier, and Gilles Tarjus (2014). "Same universality class for the critical behavior in and out of equilibrium in a quenched random field". In: *Phys. Rev. B* 89 (10), p. 104201. DOI: 10.1103/PhysRevB.89.104201.

Baró, Jordi and Eduard Vives (2012). "Analysis of power-law exponents by maximum-likelihood maps". In: *Phys. Rev. E* 85 (6), p. 066121. DOI: 10.1103/PhysRevE.85.066121.

Barré, Julien, David Mukamel, and Stefano Ruffo (2001). "Inequivalence of Ensembles in a System with Long-Range Interactions". In: *Phys. Rev. Lett.* 87 (3), p. 030601. DOI: 10.1103/PhysRevLett.87.030601.

Batra, R.C. (2006). *Elements of Continuum Mechanics*. AIAA education series. American Institute of Aeronautics & Astronautics. ISBN: 9781600860485.

Bec, Jérémie and Konstantin Khanin (2007). "Burgers turbulence". In: *Physics Reports* 447.1, pp. 1 –66. ISSN: 0370-1573. DOI: https://doi.org/10.1016/j.physrep.2007.04.002.

Beggs, John and Nicholas Timme (2012). "Being Critical of Criticality in the Brain". In: *Frontiers in Physiology* 3, p. 163. ISSN: 1664-042X. DOI: 10.3389/fphys.2012.00163.

Bell, GI (1978). "Models for the specific adhesion of cells to cells". In: *Science* 200.4342, pp. 618–627. DOI: 10.1126/science.347575.

Berdichevsky, Victor and Khanh Chau Le (2005). "On The Microcrack Nucleation In Brittle Solids". In: *International Journal of Fracture* 133.4, pp. L47–L54. ISSN: 1573-2673. DOI: 10.1007/s10704-005-0632-4.

Bergues-Pupo, A. E. et al. (2015). "Thermal and inertial resonances in DNA unzipping". In: *The European Physical Journal E* 38.5, p. 41. ISSN: 1292-895X. DOI: 10.1140/epje/i2015-15041-4.

Bialek, William (2018). "Perspectives on theory at the interface of physics and biology". In: *Reports on Progress in Physics* 81.1, p. 012601.

Bormuth, Volker et al. (2014). "Transduction channels' gating can control friction on vibrating hair-cell bundles in the ear". In: *Proceedings of the National Academy of Sciences* 111.20, pp. 7185–7190. DOI: 10.1073/pnas.1402556111.

Bourdin, Blaise, Gilles A Francfort, and Jean-Jacques Marigo (2008). "The variational approach to fracture". In: *Journal of elasticity* 91.1-3, pp. 5–148.

Brenner, S. S. (1962). "Mechanical Behavior of Sapphire Whiskers at Elevated Temperatures". In: *Journal of Applied Physics* 33.1, pp. 33–39. DOI: 10.1063/1.1728523.

Bruijn, N.G. de (2014). *Asymptotic Methods in Analysis*. Dover Books on Mathematics. Dover Publications. ISBN: 9780486150796.

Brunello, Elisabetta et al. (2014). "The contributions of filaments and cross-bridges to sarcomere compliance in skeletal muscle". In: *The Journal of Physiology* 592.17, pp. 3881–3899. ISSN: 1469-7793. DOI: 10.1113/jphysiol.2014.276196.

Buckley, Christopher D. et al. (1998). "Cell adhesion: More than just glue (Review)". In: *Molecular Membrane Biology* 15.4, pp. 167–176.

Campa, Alessandro, Thierry Dauxois, and Stefano Ruffo (2009). "Statistical mechanics and dynamics of solvable models with long-range interactions". In: *Physics Reports* 480.3-6, pp. 57–159. ISSN: 0370-1573. DOI: 10.1016/j.physrep.2009.07.001.

Caruel, M., J.-M. Allain, and L. Truskinovsky (2015). "Mechanics of collective unfolding". In: *Journal of the Mechanics and Physics of Solids* 76, pp. 237 –259. ISSN: 0022-5096. DOI: http://dx.doi.org/10.1016/j.jmps.2014.11.010.

Caruel, M. and L. Truskinovsky (2016). "Statistical mechanics of the Huxley-Simmons model". In: *Phys. Rev. E* 93 (6), p. 062407. DOI: 10.1103/PhysRevE.93.062407.

— (2017). "Bi-stability resistant to fluctuations". In: *Journal of the Mechanics and Physics of Solids* 109, pp. 117 –141. ISSN: 0022-5096. DOI: https://doi.org/10.1016/j.jmps.2017.08.007.

Caruel, Matthieu, J-M Allain, and Lev Truskinovsky (2013). "Muscle as a Metamaterial Operating Near a Critical Point". In: *Physical Review Letters* 110.24, p. 248103.

Caruel, Matthieu and Lev Truskinovsky (2018). "Physics of muscle contraction". In: *Reports on Progress in Physics* 81.3, p. 036602.

Castellani, Tommaso and Andrea Cavagna (2005). "Spin-glass theory for pedestrians". In: *Journal of Statistical Mechanics: Theory and Experiment* 2005.05, P05012.

Chakrabarti, Buddhapriya and David R. Nelson (2009). "Shear Unzipping of DNA". In: *The Journal of Physical Chemistry B* 113.12, pp. 3831–3836. DOI: 10.1021/jp808232p.

Chessa, Alessandro, Alessandro Vespignani, and Stefano Zapperi (1999). "Critical exponents in stochastic sandpile models". In: *Computer physics communications* 121, pp. 299–302.

Ciliberto, S., A. Guarino, and R. Scorretti (2001). "The effect of disorder on the fracture nucleation process". In: *Physica D: Nonlinear Phenomena* 158.1, pp. 83 –104. ISSN: 0167-2789. DOI: https://doi.org/10.1016/S0167-2789(01)00306-2.

Clauset, Aaron, Cosma Rohilla Shalizi, and M. E. J. Newman (2009). "Power-Law Distributions in Empirical Data". In: *SIAM Review* 51.4, pp. 661–703. DOI: 10.1137/070710111.

Cole, Julian D (1951). "On a quasi-linear parabolic equation occurring in aerodynamics". In: *Quarterly of applied mathematics* 9.3, pp. 225–236.

Cook, Robert F. and Eric G. Liniger (1993). "Kinetics of Indentation Cracking in Glass". In: *Journal of the American Ceramic Society* 76.5, pp. 1096–1105. DOI: 10.1111/j.1151-2916.1993.tb03726.x.

Daniels, H. E. (1945). "The Statistical Theory of the Strength of Bundles of Threads. I". In: *Proceedings of the Royal Society of London A: Mathematical, Physical and Engineering Sciences* 183.995, pp. 405–435. DOI: 10.1098/rspa.1945.0011.

Darabos, Christian et al. (2011). In: *Advances in Artificial Life. Darwin Meets von Neumann*. Ed. by George Kampis, István Karsai, and Eörs Szathmáry, pp. 281–288. ISBN: 978-3-642-21283-3. DOI: 10.1007/978-3-642-21283-3_35.

David, H.A. and H.N. Nagaraja (2004). *Order Statistics*. Wiley Series in Probability and Statistics. Wiley. ISBN: 9780471654018.

Delaplace, Arnaud, Gilles Pijaudier-Cabot, and Stéphane Roux (1996). "Progressive damage in discrete models and consequences on continuum modelling". In: *Journal of the Mechanics and Physics of Solids* 44.1, pp. 99 –136. ISSN: 0022-5096. DOI: http://dx.doi.org/10.1016/0022-5096(95)00062-3.

Delaplace, Arnaud, Stéphane Roux, and Gilles Pi jaudier Cabot (1999). "Damage cascade in a softening interface". In: *International Journal of Solids and Structures* 36.10, pp. 1403 –1426. ISSN: 0020-7683. DOI: https://doi.org/10.1016/S0020-7683(98)00054-7.

Discher, Dennis E., Paul Janmey, and Yu-li Wang (2005). "Tissue Cells Feel and Respond to the Stiffness of Their Substrate". In: *Science* 310.5751, pp. 1139–1143. ISSN: 0036-8075. DOI: 10.1126/science.1116995.

Dominguez, Roberto et al. (1998). "Crystal Structure of a Vertebrate Smooth Muscle Myosin Motor Domain and Its Complex with the Essential Light Chain". In: *Cell* 94.5, pp. 559–571. DOI: 10.1016/S0092-8674(00)81598-6.

Driscoll, Michelle M. et al. (2016). "The role of rigidity in controlling material failure". In: *Proceedings of the National Academy of Sciences* 113.39, pp. 10813–10817. ISSN: 0027-8424. DOI: 10.1073/pnas.1501169113.

Egan, Paul F. et al. (2017). "Robust mechanobiological behavior emerges in heterogeneous myosin systems". In: *Proceedings of the National Academy of Sciences* 114.39, E8147–E8154. DOI: 10.1073/pnas.1713219114.

Erdmann, T. and U. S. Schwarz (2004). "Stability of Adhesion Clusters under Constant Force". In: *Phys. Rev. Lett.* 92 (10), p. 108102. DOI: 10.1103/PhysRevLett.92.108102.

Erdmann, T. and U.S. Schwarz (2007). "Impact of receptor-ligand distance on adhesion cluster stability". In: *Eur. Phys. J. E* 22, pp. 123–137.

Erdmann, Thorsten, Philipp J. Albert, and Ulrich S. Schwarz (2013). "Stochastic dynamics of small ensembles of non-processive molecular motors: The parallel cluster model". In: *The Journal of Chemical Physics* 139.17, p. 175104. DOI: 10.1063/1.4827497.

Erdmann, Thorsten and Ulrich S. Schwarz (2006). "Bistability of Cell-Matrix Adhesions Resulting from Nonlinear Receptor-Ligand Dynamics". In: *Biophysical Journal* 91.6, pp. L60 –L62. ISSN: 0006-3495. DOI: https://doi.org/10.1529/biophysj.106.090209.

Eroshenko, Nikolai et al. (2013). "Effect of substrate stiffness on early human embryonic stem cell differentiation". In: *J Biol Eng* 7.7.

Evans, E. and K. Ritchie (1997). "Dynamic strength of molecular adhesion bonds". In: *Biophysical Journal* 72.4, pp. 1541 –1555. ISSN: 0006-3495. DOI: https://doi.org/10.1016/S0006-3495(97)78802-7.

Felderhof, B.U. (2008a). "Diffusion in a bistable potential". In: *Physica A: Statistical Mechanics and its Applications* 387.21, pp. 5017 –5023. ISSN: 0378-4371. DOI: https://doi.org/10.1016/j.physa.2008.04.034.

Felderhof, BU (2008b). "Escape by diffusion from a parabolic well across a parabolic barrier". In: *Physica A: Statistical Mechanics and its Applications* 387.8-9, pp. 1767–1785.

Filippov, A. E., J. Klafter, and M. Urbakh (2004). "Friction through Dynamical Formation and Rupture of Molecular Bonds". In: *Phys. Rev. Lett.* 92 (13), p. 135503. DOI: 10.1103/PhysRevLett.92.135503.

Francfort, G.A. and J.-J. Marigo (1998). "Revisiting brittle fracture as an energy minimization problem". In: *Journal of the Mechanics and Physics of Solids* 46.8, pp. 1319 –1342. ISSN: 0022-5096. DOI: https://doi.org/10.1016/S0022-5096(98)00034-9.

Friedrichs, Jens, Jonne Helenius, and Daniel J. Muller (2010). "Quantifying cellular adhesion to extracellular matrix components by single-cell force spectroscopy". In: *Nature Protocols* 5.7, pp. 1353–1361. ISSN: 17502799. DOI: 10.1038/nprot.2010.89.

Frisch, H L et al. (1990). "Exact solution of the diffusion in a bistable piecewise linear potential". In: *Journal of Physics A: Mathematical and General* 23.21, p. L1147.

Fuhrmann, Alexander and Adam J. Engler (2015). "The Cytoskeleton Regulates Cell Attachment Strength". In: *Biophysical Journal* 109.1, pp. 57 –65. ISSN: 0006-3495. DOI: https://doi.org/10.1016/j.bpj.2015.06.003.

Gardiner, Crispin (2009). *Stochastic methods*. Vol. 4. springer Berlin.

Glivenko, V. (1933). "Sulla determinazione empirica della legge di probabilita". In: *Giorn. Ist. Ital. Attuari* 4, pp. 92–99.

Goldenfeld, N. (1992). *Lectures on phase transitions and the renormalization group*. Frontiers in physics. Addison-Wesley, Advanced Book Program. ISBN: 9780201554083.

Goldstein, M. L., S. A. Morris, and G. G. Yen (2004). "Problems with fitting to the power-law distribution". In: *The European Physical Journal B - Condensed Matter and Complex Systems* 41.2, pp. 255–258. ISSN: 1434-6036. DOI: 10.1140/epjb/e2004-00316-5.

Gumbel, E.J. (2004). *Statistics of Extremes*. Dover books on mathematics. Dover Publications. ISBN: 9780486436043.

Gupta, Mukund et al. (2016). "Single cell rigidity sensing: A complex relationship between focal adhesion dynamics and large-scale actin cytoskeleton remodeling". In: *Cell Adhesion & Migration* 10.5. PMID: 27050660, pp. 554–567. DOI: 10.1080/19336918.2016.1173800.

Gupta, Shamik and Stefano Ruffo (2017). "The world of long-range interactions: A bird's eye view". In: *International Journal of Modern Physics A* 32.09, p. 1741018. DOI: 10.1142/S0217751X17410184.

Gurbatov, SN et al. (1997). "On the decay of Burgers turbulence". In: *Journal of Fluid Mechanics* 344, pp. 339–374.

Halász, Z. and F. Kun (2010). "Slip avalanches in a fiber bundle model". In: *EPL (Europhysics Letters)* 89.2, p. 26008.

Hänggi, Peter, Peter Talkner, and Michal Borkovec (1990). "Reaction-rate theory: fifty years after Kramers". In: *Rev. Mod. Phys.* 62 (2), pp. 251–341. DOI: 10.1103/RevModPhys.62.251.

Hansen, A and P C Hemmer (1994). *Criticality in fracture: the burst distribution*. Tech. rep. T-TPS-94-8. Trondheim-TPS-8-1994. Trondheim: Trondheim TU. Inst. Phys.

Hansen, A., P.C. Hemmer, and S. Pradhan (2015). *The Fiber Bundle Model: Modeling Failure in Materials*. Statistical Physics of Fracture and Breakdown. Wiley. ISBN: 9783527412143.

Helenius, Jonne et al. (2008). "Single-cell force spectroscopy". In: *Journal of Cell Science* 121.11, pp. 1785–1791. ISSN: 0021-9533. DOI: 10.1242/jcs.030999.

Hemmer, Per C. and Alex Hansen (Dec. 1992). "The Distribution of Simultaneous Fiber Failures in Fiber Bundles". In: *Journal of Applied Mechanics* 59.4, pp. 909–914.

Herrmann, H.J. and S. Roux (2014). *Statistical Models for the Fracture of Disordered Media*. Random Materials and Processes. Elsevier Science. ISBN: 9781483296128.

Hopf, Eberhard (1950). "The partial differential equation $u_t + uu_x = \mu u_{xx}$". In: *Communications on Pure and Applied mathematics* 3.3, pp. 201–230.

Howard, J. (2001). *Mechanics of Motor Proteins and the Cytoskeleton*. Sinauer Associates, Publishers. ISBN: 9780878933341.

Huxley, A. F. and R. M. Simmons (Oct. 1971). "Proposed Mechanism of Force Generation in Striated Muscle". In: *Nature* 233.5321, pp. 533–538.

Huxley, A. F. and S. Tideswell (1996). "Filament compliance and tension transients in muscle". In: *Journal of Muscle Research & Cell Motility* 17.4, pp. 507–511. DOI: 10.1007/BF00123366.

Huxley, H.E. et al. (1994). "X-ray diffraction measurements of the extensibility of actin and myosin filaments in contracting muscle". In: *Biophysical Journal* 67.6, pp. 2411 –2421. ISSN: 0006-3495. DOI: http://dx.doi.org/10.1016/S0006-3495(94)80728-3.

Hyeon, Changbong and Devarajan Dave Thirumalai (2014). "Minimal Models for the Structure and Dynamics of nucleic Acids". In: *Molecular Modeling at the Atomic Scale: Methods and Applications in Quantitative Biology*, p. 141.

Irving, Malcolm et al. (May 1992). "Myosin head movements are synchronous with the elementary force-generating process in muscle". In: *Nature* 357.6374, pp. 156–158.

Jülicher, Frank and Jacques Prost (1995a). "Cooperative Molecular Motors". In: *Phys. Rev. Lett.* 75 (13), pp. 2618–2621. DOI: 10.1103/PhysRevLett.75.2618.

— (1995b). "Cooperative Molecular Motors". In: *Phys. Rev. Lett.* 75 (13), pp. 2618–2621. DOI: 10.1103/PhysRevLett.75.2618.

Kanninen, M.F. and C.H. Popelar (1985). *Advanced Fracture Mechanics*. Oxford engineering science series. Oxford University Press. ISBN: 978-0-19-503532-2.

Kauffman, S.A. (1993). *The Origins of Order: Self-Organization and Selection in Evolution*. Oxford University Press. ISBN: 9780199826674.

Kaya, Motoshi et al. (2017). "Coordinated force generation of skeletal myosins in myofilaments through motor coupling". In: *Nature Communications* 8, p. 16036. DOI: 10.1038/ncomms16036.

Kessler, D. A. and H. Levine (Aug. 2015). "Generic Criticality in Ecological and Neuronal Networks". In: *ArXiv e-prints*. arXiv: 1508.02414.

Kida, Shigeo (1979). "Asymptotic properties of Burgers turbulence". In: *Journal of Fluid Mechanics* 93.2, pp. 337–377. DOI: 10.1017/S0022112079001932.

Kramers, H.A. (1940). "Brownian motion in a field of force and the diffusion model of chemical reactions". In: *Physica* 7.4, pp. 284 –304. ISSN: 0031-8914. DOI: https://doi.org/10.1016/S0031-8914(40)90098-2.

Krotov, Dmitry et al. (2014). "Morphogenesis at criticality". In: *Proceedings of the National Academy of Sciences* 111.10, pp. 3683–3688. DOI: 10.1073/pnas.1324186111.

Krzakala, Florent, Federico Ricci-Tersenghi, and Lenka Zdeborová (2010). "Elusive Spin-Glass Phase in the Random Field Ising Model". In: *Phys. Rev. Lett.* 104 (20), p. 207208. DOI: 10.1103/PhysRevLett.104.207208.

Lacombe, Frédéric, Stefano Zapperi, and Hans J. Herrmann (2001). "Force fluctuation in a driven elastic chain". In: *Phys. Rev. B* 63 (10), p. 104104. DOI: 10.1103/PhysRevB.63.104104.

Lin, Han-Jou et al. (2010). "Free energy and critical force for adhesion clusters". In: *Phys. Rev. E* 81 (6), p. 061908. DOI: 10.1103/PhysRevE.81.061908.

Linari, Marco et al. (1998). "The Stiffness of Skeletal Muscle in Isometric Contraction and Rigor: The Fraction of Myosin Heads Bound to Actin". In: *Biophysical Journal* 74.5, pp. 2459 –2473. ISSN: 0006-3495. DOI: https://doi.org/10.1016/S0006-3495(98)77954-8.

M. Kloster, A. Hansen and P. C. Hemmer (1997). "Burst avalanches in solvable models of fibrous materials". In: *Physical Review E* 56.3, pp. 2615–2625. DOI: 10.1103/PhysRevE.56.2615.

Machta, Benjamin B., Sarah L. Veatch, and James P. Sethna (2012). "Critical Casimir Forces in Cellular Membranes". In: *Phys. Rev. Lett.* 109 (13), p. 138101. DOI: 10.1103/PhysRevLett.109.138101.

Machta, Benjamin B. et al. (2011). "Minimal Model of Plasma Membrane Heterogeneity Requires Coupling Cortical Actin to Criticality". In: *Biophysical Journal* 100.7, pp. 1668 –1677. ISSN: 0006-3495. DOI: https://doi.org/10.1016/j.bpj.2011.02.029.

Maddalena, F. et al. (2009). "Mechanics of reversible unzipping". English. In: *Continuum Mechanics and Thermodynamics* 21.4, pp. 251–268. ISSN: 0935-1175. DOI: 10.1007/s00161-009-0108-2.

Manghi, Manoel and Nicolas Destainville (2016). "Physics of base-pairing dynamics in DNA". In: *Physics Reports* 631. Physics of base-pairing dynamics in DNA, pp. 1 –41. ISSN: 0370-1573. DOI: https://doi.org/10.1016/j.physrep.2016.04.001.

Marcucci, L. and L. Truskinovsky (2010a). "Mechanics of the power stroke in myosin II". In: *Phys. Rev. E* 81 (5), p. 051915. DOI: 10.1103/PhysRevE.81.051915.

— (2010b). "Muscle contraction: A mechanical perspective". In: *The European Physical Journal E* 32.4, pp. 411–418. ISSN: 1292-895X. DOI: 10.1140/epje/i2010-10641-0.

Mezard, M., G. Parisi, and M. Virasoro (1987). *Spin Glass Theory and Beyond*. World Scientific Lecture Notes in Physics. ISBN: 9789813103917.

Mishra, R. K. et al. (2015). "On the rupture of DNA molecule". In: *The Journal of Chemical Physics* 142.17, p. 174910. DOI: 10.1063/1.4919646.

Mora, Thierry and William Bialek (2011). "Are Biological Systems Poised at Criticality?" In: *Journal of Statistical Physics* 144.2, pp. 268–302. ISSN: 1572-9613. DOI: 10.1007/s10955-011-0229-4.

Moreno, Y., J. B. Gómez, and A. F. Pacheco (2000). "Fracture and Second-Order Phase Transitions". In: *Phys. Rev. Lett.* 85 (14), pp. 2865–2868. DOI: 10.1103/PhysRevLett.85.2865.

Moretti, Paolo and Miguel A Muñoz (2013). "Griffiths phases and the stretching of criticality in brain networks". In: *Nature Communications* 4, p. 2521. DOI: 10.1038/ncomms3521.

Müller, Daniel J et al. (2009). "Force probing surfaces of living cells to molecular resolution". In: *Nature chemical biology* 5.6, p. 383.

Mungan, Muhittin and Cem Yolcu (2010). "Frenkel-Kontorova models, pinned particle configurations, and Burgers shocks". In: *Phys. Rev. B* 81 (22), p. 224116. DOI: 10.1103/PhysRevB.81.224116.

Muñoz, Miguel A (2017). "Colloquium: Criticality and dynamical scaling in living systems". In: *arXiv preprint arXiv:1712.04499*.

Newman, Mark EJ (2005). "Power laws, Pareto distributions and Zipf's law". In: *Contemporary physics* 46.5, pp. 323–351.

O'Connor, Clare M, Jill U Adams, and Jennifer Fairman (2010). "Essentials of cell biology". In: *Cambridge: NPG Education*.

Owedyk, J. and A. Kociszewski (1985). "On the Fokker-Planck equation with time-dependent drift and diffusion coefficients and its exponential solutions". In: *Zeitschrift für Physik B Condensed Matter* 59.1, pp. 69–74. ISSN: 1431-584X. DOI: 10.1007/BF01325384.

P., Cantelli F. (1933). "Sulla determinazione empirica della legge di probabilita". In: *Giorn. Ist. Ital. Attuari* 4, pp. 221–424.

Pathria, R.K. and P.D. Beale (1996). *Statistical Mechanics*. Elsevier Science.

Patinet, S. et al. (2014). "Cracks in random brittle solids:" in: *The European Physical Journal Special Topics* 223.11, pp. 2339–2351. ISSN: 1951-6401. DOI: 10.1140/epjst/e2014-02268-9.

Peirce, F. T. (1926). "Theorems on the Strength of Long and of Composite Specimens". In: *Journal of the Textile Industry* 17, pp. 355–368.

Petrov, V. A. and A. N. Orlov (1976). "Statistical kinetics of thermally activated fracture". In: *International Journal of Fracture* 12.2, pp. 231–238. ISSN: 1573-2673. DOI: 10.1007/BF00036980.

Peyrard, M. and A. R. Bishop (1989). "Statistical mechanics of a nonlinear model for DNA denaturation". In: *Phys. Rev. Lett.* 62 (23), pp. 2755–2758. DOI: 10.1103/PhysRevLett.62.2755.

Piazzesi, G et al. (Nov. 2007). "Skeletal Muscle Performance Determined by Modulation of Number of Myosin Motors Rather Than Motor Force or Stroke Size". In: *Cell* 131.4, pp. 784 –795. ISSN: 0092-8674. DOI: 10.1016/j.cell.2007.09.045.

Piazzesi, Gabriella et al. (Feb. 2002). "Mechanism of force generation by myosin heads in skeletal muscle". In: *Nature* 415.6872, pp. 659–662.

Podolsky, R. J. (Nov. 1960). "Kinetics of Muscular Contraction : the Approach to the Steady State". In: *Nature* 188, pp. 666–668. DOI: 10.1038/188666a0.

Politi, Antonio, Sergio Ciliberto, and Riccardo Scorretti (2002a). "Failure time in the fiber-bundle model with thermal noise and disorder". In: *Phys. Rev. E* 66 (2), p. 026107. DOI: 10.1103/PhysRevE.66.026107.

— (2002b). "Failure time in the fiber-bundle model with thermal noise and disorder". In: *Phys. Rev. E* 66 (2), p. 026107. DOI: 10.1103/PhysRevE.66.026107.

Polizzi, Stefano et al. (2018). "A minimal rupture cascade model for living cell plasticity". In: *New Journal of Physics* 20.5, p. 053057.

Pomeau, Yves (1992). "Brisure spontanée de cristaux bidimensionnels courbés". In: *C. R. Acac. Sci. Paris* Serie II, pp. 553–555.

Pradhan, Srutarshi, Alex Hansen, and Bikas K. Chakrabarti (2010). "Failure processes in elastic fiber bundles". In: *Reviews of Modern Physics* 82.1, pp. 499–555. DOI: 10.1103/RevModPhys.82.499.

Puglisi, G. and L. Truskinovsky (2013). "Cohesion-decohesion asymmetry in geckos". In: *Phys. Rev. E* 87 (3), p. 032714. DOI: 10.1103/PhysRevE.87.032714.

Rajan, Vinoth Sundar et al. (2017). "Unraveling the receptor-ligand interactions between bladder cancer cells and the endothelium using AFM". In: *Biophysical journal* 112.6, pp. 1246–1257.

Rayment, I et al. (1993a). "Structure of the actin-myosin complex and its implications for muscle contraction". In: *Science* 261.5117, pp. 58–65. ISSN: 0036-8075. DOI: 10.1126/science.8316858.

Rayment, I et al. (1993b). "Three-dimensional structure of myosin subfragment-1: a molecular motor". In: *Science* 261.5117, pp. 50–58. ISSN: 0036-8075. DOI: 10.1126/science.8316857.

Riedo, Elisa and Enrico Gnecco (2004). "Thermally activated effects in nanofriction". In: *Nanotechnology* 15.4, S288.

Roux, Stéphane (2000). "Thermally activated breakdown in the fiber-bundle model". In: *Phys. Rev. E* 62 (5), pp. 6164–6169. DOI: 10.1103/PhysRevE.62.6164.

S. Jayatilaka, A. de (1979). *Fracture of engineering brittle materials*. Applied Science Publishers. ISBN: 9780853348252.

Schneider, T. and E. Pytte (1977). "Random-field instability of the ferromagnetic state". In: *Phys. Rev. B* 15 (3), pp. 1519–1522. DOI: 10.1103/PhysRevB.15.1519.

Schwarz, Ulrich (2007). "Soft matters in cell adhesion: rigidity sensing on soft elastic substrates". In: *Soft Matter* 3 (3), pp. 263–266. DOI: 10.1039/B606409D.

Schwarz, Ulrich S. and Samuel A. Safran (2013). "Physics of adherent cells". In: *Rev. Mod. Phys.* 85 (3), pp. 1327–1381. DOI: 10.1103/RevModPhys.85.1327.

Scorretti, R., S. Ciliberto, and A. Guarino (2001). "Disorder enhances the effects of thermal noise in the fiber bundle model". In: *EPL (Europhysics Letters)* 55.5, p. 626.

Seifert, U. (2002). "Dynamic strength of adhesion molecules: Role of rebinding and self-consistent rates". In: *EPL (Europhysics Letters)* 58.5, p. 792.

Seifert, Udo (2000). "Rupture of Multiple Parallel Molecular Bonds under Dynamic Loading". In: *Phys. Rev. Lett.* 84 (12), pp. 2750–2753. DOI: 10.1103/PhysRevLett.84.2750.

Selinger, Robin L. Blumberg, Zhen-Gang Wang, and William M. Gelbart (1991). "Effect of temperature and small-scale defects on the strength of solids". In: *The Journal of Chemical Physics* 95.12, pp. 9128–9141. DOI: 10.1063/1.461192.

Selinger, Robin L. Blumberg et al. (1991). "Statistical-thermodynamic approach to fracture". In: *Phys. Rev. A* 43 (8), pp. 4396–4400. DOI: 10.1103/PhysRevA.43.4396.

Sens, Pierre (2013). "Rigidity sensing by stochastic sliding friction". In: *EPL (Europhysics Letters)* 104.3, p. 38003.

Shekhawat, Ashivni, Stefano Zapperi, and James P. Sethna (2013). "From Damage Percolation to Crack Nucleation Through Finite Size Criticality". In: *Phys. Rev. Lett.* 110 (18), p. 185505. DOI: 10.1103/PhysRevLett.110.185505.

Sherrington, David and Scott Kirkpatrick (1975). "Solvable Model of a Spin-Glass". In: *Phys. Rev. Lett.* 35 (26), pp. 1792–1796. DOI: 10.1103/PhysRevLett.35.1792.

Sheshka, R., P. Recho, and L. Truskinovsky (2016). "Rigidity generation by nonthermal fluctuations". In: *Phys. Rev. E* 93 (5), p. 052604. DOI: 10.1103/PhysRevE.93.052604.

Sornette, D (1989). "Elasticity and failure of a set of elements loaded in parallel". In: *Journal of Physics A: Mathematical and General* 22.6, p. L243.

Sundar Rajan, Vinoth Edal Joseph (2016). "Adhesion and transendothelial migration of cancer cells". Thèse de doctorat dirigée par Duperray, Alain Biologie du développement - Oncogenèse Grenoble Alpes 2016. PhD thesis.

Suzuki, Madoka and Shin'Ichi Ishiwata (2011). "Quasiperiodic distribution of rigor cross-bridges along a reconstituted thin filament in a skeletal myofibril". In: *Biophysical Journal* 101.11, pp. 2740–2748. ISSN: 00063495. DOI: 10.1016/j.bpj.2011.10.040.

Tortora, G.J. and B.H. Derrickson (2014). *Principles of Anatomy and Physiology, 14th Edition: 14th Edition*. Wiley Global Education. ISBN: 978-1-118-34500-9.

Touchette, Hugo (2015). "Equivalence and Nonequivalence of Ensembles: Thermodynamic, Macrostate, and Measure Levels". In: *Journal of Statistical Physics* 159.5, pp. 987–1016. DOI: 10.1007/s10955-015-1212-2.

Toussaint, Renaud and Alex Hansen (2006). "Mean-field theory of localization in a fuse model". In: *Phys. Rev. E* 73 (4), p. 046103. DOI: 10.1103/PhysRevE.73.046103.

Tregear, R T et al. (Mar. 1998). "X-ray diffraction indicates that active cross-bridges bind to actin target zones in insect flight muscle." In: *Biophysical Journal* 74.3, pp. 1439–1451.

Tregear, Richard T. et al. (2004). "Cross-Bridge Number, Position, and Angle in Target Zones of Cryofixed Isometrically Active Insect Flight Muscle". In: *Biophysical Journal* 86.5, pp. 3009 –3019. ISSN: 0006-3495. DOI: https://doi.org/10.1016/S0006-3495(04)74350-7.

Tucker, Howard G. (1959). "A Generalization of the Glivenko-Cantelli Theorem". In: *The Annals of Mathematical Statistics* 30.3, pp. 828–830. ISSN: 00034851.

Van Kampen, Nicolaas Godfried (1992). *Stochastic processes in physics and chemistry*. Vol. 1. Elsevier.

Vanossi, Andrea et al. (2013). "Colloquium: Modeling friction: From nanoscale to mesoscale". In: *Rev. Mod. Phys.* 85 (2), pp. 529–552. DOI: 10.1103/RevModPhys.85.529.

Vasseur, R. et al. (2012). "Phase diagram of ferroelastic systems in the presence of disorder: Analytical model and experimental verification". In: *Phys. Rev. B* 86 (18), p. 184103. DOI: 10.1103/PhysRevB.86.184103.

Vilfan, Andrej and Thomas Duke (2003). "Two Adaptation Processes in Auditory Hair Cells Together Can Provide an Active Amplifier". In: *Biophysical Journal* 85.1, pp. 191 –203. ISSN: 0006-3495. DOI: https://doi.org/10.1016/S0006-3495(03)74465-8.

Vilfan, I (1987). "The Random-Field Ising Model: A Free Energy Study". In: *Physica Scripta* 1987.T19B, p. 585.

Vilfan, I and R A Cowley (1985). "Static properties of the random-field Ising model". In: *Journal of Physics C: Solid State Physics* 18.26, p. 5055.

Virgilii, Alessandro, Alberto Petri, and Silvio R Salinas (2007). "A thermodynamical fibre bundle model for the fracture of disordered materials". In: *Journal of Statistical Mechanics: Theory and Experiment* 2007.04, P04009.

Vologodskii, Alexander and Maxim D. Frank-Kamenetskii (2017). "DNA melting and energetics of the double helix". In: *Physics of Life Reviews*.

Wakabayashi, K. et al. (1994). "X-ray diffraction evidence for the extensibility of actin and myosin filaments during muscle contraction". In: *Biophysical Journal* 67.6, pp. 2422 –2435. ISSN: 0006-3495. DOI: http://dx.doi.org/10.1016/S0006-3495(94)80729-5.

Wang, Yu, Xiaobing Ren, and Kazuhiro Otsuka (2006). "Shape Memory Effect and Superelasticity in a Strain Glass Alloy". In: *Phys. Rev. Lett.* 97 (22), p. 225703. DOI: 10.1103/PhysRevLett.97.225703.

Wang, Zhen-Gang et al. (1991). "Molecular-dynamics study of elasticity and failure of ideal solids". In: *Phys. Rev. B* 44 (1), pp. 378–381. DOI: 10.1103/PhysRevB.44.378.

Weibull, W. (1951). "A Statistical Distribution Function of Wide Applicability". In: *J. Appl. Mech.* 18, pp. 293–297.

Whitham, Gerald Beresford (2011). *Linear and nonlinear waves*. Vol. 42. John Wiley & Sons.

Xing, Xiu-San (1991). "Nonequilibrium statistical theory of thermally activated delayed fracture". In: *Engineering Fracture Mechanics* 38.1, pp. 1 –12. ISSN: 0013-7944. DOI: https://doi.org/10.1016/0013-7944(91)90201-B.

Yeomans, J.M. (1992). *Statistical Mechanics of Phase Transitions*. Clarendon Press. ISBN: 9780191589706.

Yeung, Tony et al. (2004). "Effects of substrate stiffness on cell morphology, cytoskeletal structure, and adhesion". In: *Cell Motility* 60.1, pp. 24–34. DOI: 10.1002/cm.20041.

Yoshioka, Naoki, Ferenc Kun, and Nobuyasu Ito (2015). "Kinetic Monte Carlo algorithm for thermally induced breakdown of fiber bundles". In: *Phys. Rev. E* 91 (3), p. 033305. DOI: 10.1103/PhysRevE.91.033305.

Zaanen, Jan (2010). "The benefit of fractal dirt". In: *Nature* 466, p. 825. DOI: 10.1038/466825a.

Zapperi, Stefano et al. (1997). "First-Order Transition in the Breakdown of Disordered Media". In: *Phys. Rev. Lett.* 78 (8), pp. 1408–1411. DOI: 10.1103/PhysRevLett.78.1408.

Part III:
Appendix

Appendix A

Order Statistics

We introduce basic concepts of order statistics that are necessary to understanding part of the derivation of the asymptotic distribution of avalanches in the equilibrium augmented FBM, the theory here presented is based on the great works of (Arnold, Balakrishnan, and Nagaraja, 1992), (Gumbel, 2004) and (David and Nagaraja, 2004). We will briefly state the principal results and theorems.

Assume that n random variables are extracted from a continuous population with cumulative density function (cdf) $P(x)$ and probability density function $p(x)$. If the random variables $X_1, \ldots, X_n$ are arranged in increasing order of magnitude and then written as

$$X_{1:n} \leq \cdots \leq X_{n:n}, \tag{A.1}$$

we call $X_{k:n}$ the kth order statistic $(k = 1, \ldots, n)$. We are mainly dealing with the case where the X_i are assumed to be statistically independent and identically distributed (iid) random variables. Sometimes the variables are written as $X_{r:n}$ to emphasize the importance of the sample size.

Distribution of a single order statistics Let $X_{1:n} \leq X_{2:n} \leq \cdots \leq X_{n:n}$ be the order statistics obtained by arranging the random sample X_i in increasing order of magnitude. Then, the event $x < X_{i:n} < x + \delta x$ is essentially same as the event:

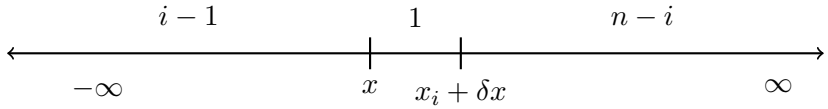

$X_r \leq x$ for $i-1$ of the X_r's, $x < X_r \leq x + \delta x$ for exactly one of the X_r's, and $X_r > x + \delta x$ for the remaining $n - i$ of the X_r's. Considering δx to be small, we can write

$$\begin{aligned} \Pr\{x < X_{i:n} \leq x + \delta x\} = \frac{n!}{(i-1)!(n-i)!}[P(x)]^{i-1}[1 - P(x + \delta x)]^{n-i} \\ \times \big[P(x + \delta x) - P(x)\big] + O((\delta x)^2), \end{aligned} \tag{A.2}$$

where $O((\delta x)^2)$, a term of order $(\delta x)^2$, is the probability corresponding to the event of having more than one X_r in the small interval $(x, x + \delta x]$. Thus, we can derive the density function of $X_{i:n}$, for $i = 1, \ldots, n$ as

$$\begin{aligned} p_{i:n} &= \lim_{\delta x \to 0} \frac{\Pr\{x < X_{i:n} \leq x + \delta x\}}{\delta x} \\ &= \frac{n!}{(i-1)!(n-i)!}[P(x)]^{i-1}[1 - P(x)]^{n-i}p(x), \quad -\infty < x < \infty \end{aligned} \tag{A.3}$$

The cumulative density function of $X_{i:n}$ may be obtained by integrating the pdf of $X_{i:n}$ in (A.3). But it can also be derived by

$$\begin{aligned} P_{i:n}(x) &= \Pr\{X_{i:n} \le x\} \\ &= \Pr\{\text{at least } i \text{ of } X_1, X_2, \ldots, X_n \text{ are at most } x\} \\ &= \Pr\{\text{exactly } r \text{of} X_1, X_2, \ldots, X_n \text{ are at most } x\} \\ &= \sum_{r=i}^{n} \binom{n}{r} [P(x)]^r [1-P(x)]^{n-r}, \quad -\infty < x < \infty. \end{aligned} \tag{A.4}$$

Joint distribution of two order statistics To derive the joint probability density function of two order statistics $X_{i:n}$ and $X_{j:n}$ $(1 \le i < j \le n)$, let us visualize the event $(x_i < X_{i:n} \le x_i + \delta x_i, x_j < X_{j:n} \le x_j + \delta x_j)$ as,

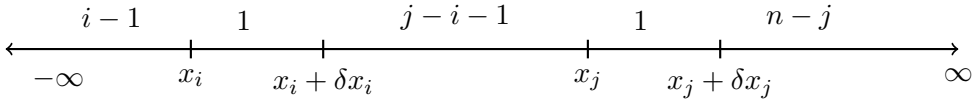

$X_r \le x_i$ for $i-1$ of the X_r's, $x_i < X_r \le x_i + \delta x_i$ for exactly one of the X_r's, $x_i + \delta x_i < X_r \le x_j$ for $j-i-1$ of the X_r's, $x_j < X_r \le x_j + \delta x_j$ for exactly one of the X_r's, and $X_r > x_j + \delta x_j$ for the remaining $n-j$ of the X_r's. Considering both δx_i and δx_j to be small, we write

$$\begin{aligned} &\Pr\{x_i < X_{i:n} \le x_i + \delta x_i, x_j < X_{j:n} \le x_j + \delta x_j\} \\ &= \frac{n!}{(i-1)!(j-i-1)!(n-j)!} [P(x_i)]^{i-1} [P(x_j) - P(x_i + \delta x_i)]^{j-i-1} \\ &\times \left[1 - P(x_j + \delta x_j)\right]^{n-j} \left[P(x_i + \delta x_i) - P(x_i)\right] \left[P(x_j + \delta x_j) - P(x_j)\right] \\ &+ O((\delta x_i)^2 \delta x_j) + O((\delta x_j)^2 \delta x_i), \end{aligned} \tag{A.5}$$

where $O((\delta x_i)^2 \delta x_j)$ and $O((\delta x_j)^2 \delta x_i)$ are high order terms corresponding to the probabilities of having more than one X_r in the interval $(x_i, x_i + \delta x_i]$ and at least one X_r in the interval $(x_j, x_j + \delta x_j]$, and of the event of having one X_r in the interval $(x_i, x_i + \delta x_i]$ and more than one X_r in the interval $(x_j, x_j + \delta x_j]$, respectively. We are able, then to derive the joint probability density function of $X_{i:n}$ and $X_{j:n}$ as

$$\begin{aligned} p_{i,j:n}(x_i, x_j) &= \lim_{\delta x_i \to 0, \delta x_j \to 0} \frac{\Pr\{x_i < X_{i:n} \le x_i + \delta x_i, x_j < X_{j:n} \le x_j + \delta x_j\}}{\delta x_i \delta x_j} \\ &= \frac{n!}{(i-1)!(j-i-1)!(n-j)!} [P(x_i)]^{i-1} [P(x_j) - P(x_i)]^{j-i-1} \\ &\times \left[1 - P(x_j)\right]^{n-j} p(x_i) p(x_j), \quad -\infty < x_i < x_j < \infty. \end{aligned} \tag{A.6}$$

Asymptotic theory of order statistics The asymptotic theory of order statistics is concerned with the distribution of $X_{k:n}$, as $n \to \infty$. When studying the asymptotic limit of order statistics one have to consider three distinct separate situation where $X_{k:n}$ is classified as one of the following:

1. *extreme order statistic* when either k or $n-k$ is fixed and the sample size $n \to \infty$,
2. *central order statistic* when $k/n \to p$ as $n \to \infty$ and $0 < p < 1$ and
3. *intermediate order statistic* when both k and $n-k$ approaches infinity, but $k/n \to 0$ or 1.

One important message about extreme order statistics is that if the limit distribution exists, it is non-normal and depends on F only through its tail behavior. For our purposes we are only concerned with the central order statistics. In contrast to extreme values, the asymptotic distribution of a central order statistic is normal under mild conditions, which is shown in the following theorem,

Theorem A.0.1 (Asymptotic distribution of a central order statistic)**.** *For $0 < \phi < 1$, let P be absolutely continuous with pdf p which is positive at $P^{-1}(\phi)$ and is continuous at that point. For $k \approx n\phi$, as $n \to \infty$,*

$$\sqrt{n}p(P^{-1}(\phi))\frac{X_{k:n} - P^{-1}(\phi)}{\sqrt{\phi(1-\phi)}} \xrightarrow{d} N(0,1) \tag{A.7}$$

where the symbol $\xrightarrow{d}$ means convergence in distribution.

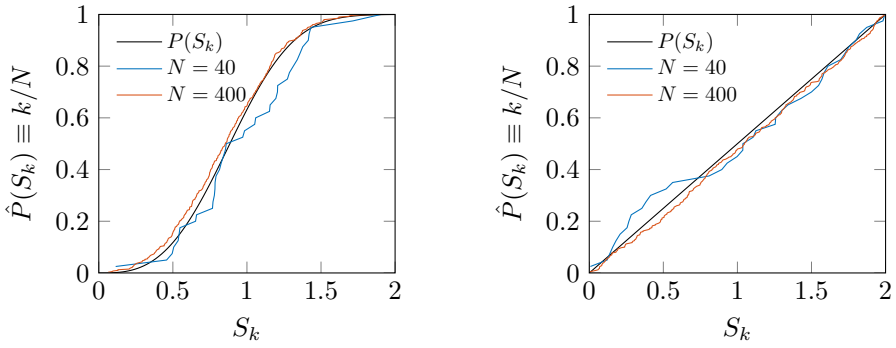

(a) Weibull **(b)** Uniform

Figure A.1: The empiric distribution function of the order statistics is plotted for different sizes of the system and different distributions.

The Fig. A.1 illustrate the above theorem. When we increase the size of the sample of the data, here the number of thresholds. The empiric distribution, $\tilde{P}(S_k) \equiv k/N$ approaches the cdf of the random variable.

Lemma A.0.2. *Let S_k be a random variable from a continuous distribution with pdf p and cdf P and $S_{k:N}$ is the order statistics of the aforementioned random variable. If $N \to \infty$ and $k/N \to \phi$, with $0 < \phi < 1$, we have*

$$S_{k:N} \to P^{-1}\left(\frac{k}{N}\right) \tag{A.8}$$

The empirical distribution function The empirical distribution function is the distribution function associated with the empirical measure of a sample.

Definition A.0.3. *Let $X_1, \ldots, X_n$ be independent and identically distributed random variables, with cumulative distribution function $P(x) = \Pr(X_1 \leq x)$. The empirical cumulative distribution function (ECDF) is defined as*

$$\hat{P}_n(x) = \frac{1}{n}\sum_{i=1}^{n} \mathbf{1}\{X_i \leq x\}, \tag{A.9}$$

where $\mathbf{1}$ is the indicator function, defined as

$$\mathbf{1}\{X_i \leq x\} = \begin{cases} 1 \text{ if } X_i \leq x, \\ 0 \text{ otherwise.} \end{cases} \tag{A.10}$$

It is easy to see that $\hat{F}_n$ is a step function with jumps of size $1/n$ at each of the n data points, and an increasing and right-continuous function taking values in the interval $[0, 1]$. Its value at any specified point of the measured variable is the fraction of observations of the sample that are less than or equal to the specified value.

The ECDF is a clear estimator of the CDF of the data and converges with probability one to the to the true CDF according to the Glivenko-Cantelli theorem (Glivenko, 1933; P., 1933; Tucker, 1959).

Theorem A.0.4 (Glivenko-Cantelli theorem)**.** *The empirical distribution converges uniformly to $P(x)$, namely*

$$\sup_{x\in\mathbb{R}} |\hat{P}_n(x) - P(x)| \xrightarrow{a.s.} 0, \tag{A.11}$$

as $n \to \infty$, where the superscript a.s. denotes convergence almost surely.

We can further predict how close the ECDF will be to the distribution function from which the empirical samples are drawn.

Theorem A.0.5 (Dvoretzky-Kiefer-Wolfowitz inequality)**.** *For any $\epsilon > 0$ and any $n > 0$*

$$\Pr\{\sup_{x\in\mathbb{R}} |\hat{P}_n(x) - P(x)| \geq \epsilon\} \leq 2e^{-2n\epsilon^2}. \tag{A.12}$$

Appendix B

Combinatorics problem

Here we state and prove the lemma used in the analytical derivation of the distribution of avalanches.

Lemma B.0.1. *The probability that by distributing h non-identical particles among n numbered boxes, box number 1 will contain no particles, box number 2 will contain at most 1 particle, and in general box number i will contain at most $i-1$ particles is,*

$$p_{h,n} = 1 - \frac{h}{d} \tag{B.1}$$

Proof. First we build a recurrence relation in n supposing we know the probability for $n-1$. If we know $p_{k,n-1}$, then when we add an extra box, number n, this box can contain any number of particles from 1 to h.

Therefore, the probability $p_{h,n}$ is the probability of having all the particles h in n and none in the $n-1$ boxes ($\Pr\{h$ particles in $n\} \times p_{0,n-1}$), plus the probability of having $h-1$ particles in n and 1 in the $n-1$ boxes ($\Pr\{h-1$ particles in $n\} \times p_{1,n-1}$), and so on. Which is translated into,

$$\begin{aligned} p_{h,n} =& p_{0,n-1} \times \Pr\{h \text{ particles in } n\} + p_{1,n-1} \times \Pr\{h-1 \text{ particles in } n\} + \dots \\ & p_{k,n-1} \times \Pr\{h-k \text{ particles in } n\} + \dots + p_{h,n-1} \times \Pr\{0 \text{ particles in } n\}. \end{aligned} \tag{B.2}$$

Since the probability of having $h-k$ particles in box number n is

$$\binom{h}{k} \left(\frac{1}{n}\right)^{h-k} \left(\frac{n-1}{n}\right)^{k}, \tag{B.3}$$

we can write the recurrence relation as,

$$p_{h,n} = \sum_{k=0}^{h} p_{k,n-1} \binom{h}{k} \left(\frac{1}{n}\right)^{h-k} \left(\frac{n-1}{n}\right)^{k}. \tag{B.4}$$

We will prove, by mathematical induction in n that

$$p_{h,n} = 1 - \frac{h}{n}. \tag{B.5}$$

Assuming that this expression holds for $p_{h,n-1}$, for any $h \leq d$, the inductive step reads,

$$\begin{aligned}
p_{h,n} &= \sum_{k=0}^{h} \left(1 - \frac{k}{n-1}\right) \binom{h}{k} \left(\frac{1}{n}\right)^{h-k} \left(\frac{n-1}{n}\right)^{k} \\
&= \sum_{k=0}^{h} \binom{h}{k} \left(\frac{1}{n}\right)^{h-k} \left(\frac{n-1}{n}\right)^{k} - \sum_{k=0}^{h} \frac{k}{n-1} \binom{h}{k} \left(\frac{1}{n}\right)^{h-k} \left(\frac{n-1}{n}\right)^{k} \\
&= 1 - \frac{h}{n} \sum_{k=1}^{h} \binom{h-1}{k-1} \left(\frac{1}{n}\right)^{h-k} \left(\frac{n-1}{n}\right)^{k-1} \\
&= 1 - \frac{h}{n} \sum_{k=0}^{h-1} \binom{h-1}{k} \left(\frac{1}{n}\right)^{h-k-1} \left(\frac{n-1}{n}\right)^{k} \\
&= 1 - \frac{h}{d}.
\end{aligned} \tag{B.6}$$

Because the equation is valid for the base case, $n = 2$, the induction is complete $\square$

Appendix C

Weibull distribution

To assign the randomness of the thresholds or the values in which the bonds dissociate, different probability distributions can be considered. In probability theory and statistics, the Weibull distribution is one of the most important continuous distribution. Named for its inventor, Waloddi Weibull, this distribution is widely used in reliability engineering and elsewhere due to its versatility and relative simplicity.

The Weibull distribution is one of the three limiting distributions in extreme statistics, also known as the third asymptotic distribution of extremes. It holds for limited distributions, bound from below and above. It is the correct distribution for the weakest element, when the distribution is bounded from below. One of its derivation for the strength of chain of materials is as follows (S. Jayatilaka, 1979).

First, regarding the characteristics of the material, it is assumed that,

1. The material is isotropic and statistically homogeneous;
2. The failure of the most critical flaw leads to total failure.

Assume that we have a chain consisting of N links and we have found, by testing, the probability of failure, $P(x)$, at any load x applied to a single link. The probability of survival of the whole chain, $1 - P_{chain}(x)$, at a load x is the probability of survival of all the links. Thus,

$$1 - P_{chain}(x) = \left[1 - P(x)\right]^N \tag{C.1}$$

Using the limit $\lim_{n\to\infty}\left(1 - \frac{x}{n}\right)^n = \exp(-x)$, we have for large N

$$1 - P_{chain}(x) = \left[1 - P(x)\right]^N = \exp\left(-NP(x)\right) \tag{C.2}$$

One have $P(x)$ as the distribution function for one single link and it is only a function of x and independent of the number of links, N. The number of links is proportional to the total volume of matter, V. If we call the probability of failure, at a given load x, of the chain $P(x)$ we may rewrite the equation above as

$$P(x) = 1 - \exp\left[-V\phi(x)\right] \tag{C.3}$$

where $V\phi(x) = NP(x)$.

Now one have to specify the function $\phi(x)$. The necessary general conditions, as stated by (Weibull, 1951), are to be a positive, nondecreasing function, vanishing at a value x_u, not necessarily equal to zero. Weibull thus assumed an empirical form for this function, given by

$$\phi(x) = \left(\frac{x - x_u}{x_0}\right)^\rho \quad \text{for } x > x_u \tag{C.4}$$

and

$$\phi(x) = 0 \quad \text{for } x \leq x_u$$

where x_u is the stress at which there is zero probability of failure and is called the threshold stress, x_0 is a normalising factor and ρ is a material parameter, sometimes referred to as the Weibull modulus or shape parameter.

With the function $\phi(x)$ being set one can now write the so called three-parameter Weibull distribution

$$P(x) = 1 - \exp\left[-V\left(\frac{x - x_u}{x_0}\right)^{\rho}\right] \quad \text{for } x > x_u \tag{C.5}$$

and

$$P(x) = 0 \quad \text{for } x \leq x_u$$

In this work it is used the two-parameter Weibull distribution, which is simply (C.5) with $x_u = 0$. Moreover, we call $l = x_0/\sqrt[\rho]{V}$, leading us to a probability density function (pdf) of the Weibull distribution as

$$p(x) = \frac{\rho}{l}\left(\frac{x}{l}\right)^{\rho-1} e^{-(x/l)^{\rho}} \tag{C.6}$$

and its correspondent cumulative distribution function as

$$P(x) = 1 - e^{-(x/l)^{\rho}}. \tag{C.7}$$

Here l is a scale parameter or the reference threshold and ρ is the Weibull slope or shape parameter. An important aspect of the Weibull distribution is how the values of the shape parameter, ρ, and the scale parameter, l, affect such distribution characteristics as the shape of the pdf curve. The Weibull distribution is widely used in reliability and life data analysis, due to its versatility, depending on the values of the parameters, the Weibull distribution can be used to model a variety of life behaviors.

A value of $\rho < 1$ indicates that the failure rate decreases over time. This happens if there is significant "infant mortality", or defective items failing early and the failure rate decreasing over time as the defective items are weeded out of the population. A value of $\rho = 1$ indicates that the failure rate is constant over time. This might suggest random external events are causing mortality, or failure. A value of $\rho > 1$ indicates that the failure rate increases with time. This happens if there is an "ageing" process, or parts that are more likely to fail as time goes on. In the field of materials science, the shape parameter ρ of a distribution of strengths is known as the Weibull modulus.

Weibull distribution can also reflect the defect of material and the effects of stress concentration, that is why it has been considered as appropriate model to describe strength of fiber material and of failure times. Thus, when it comes to distributed threshold of the fiber we shall use the Weibull distribution.

The strength or threshold of a fiber is usually determined by the stress value x it can bear and beyond which it fails. Therefore, we denote the strength (threshold) distribution of the fibers in the bundle by $p(x)$ and the corresponding cumulative distribution by $P(x) = \int_0^x p(y)dy$. Since the similarity of the modeling of fiber bundles and adhesion problem we investigate we shall use the Weibull distribution in this work.

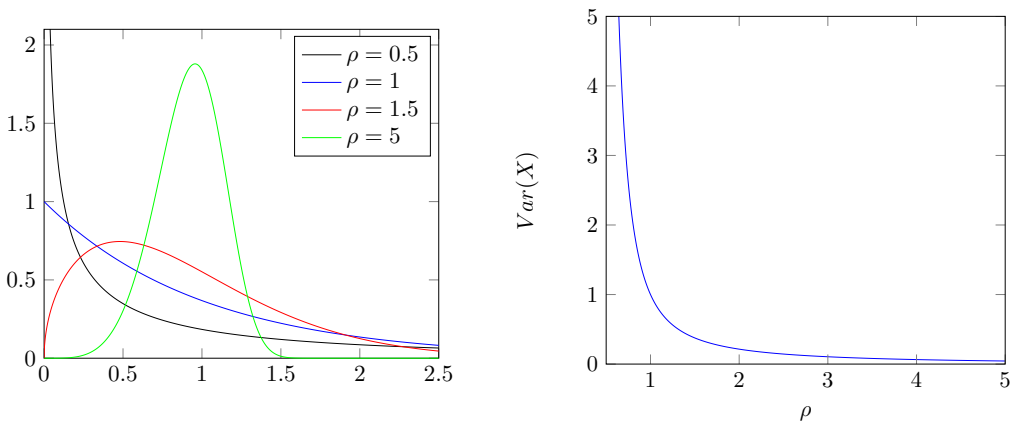

(a) **(b)**

Figure C.1: (a) The Weibull probability density function for several values of shape parameter ρ and fixed scale parameter l. (b) Variance of Weibull distribution as a function of ρ.

Appendix D

Statistics of the disorder

To better understand the role and transformations of the three random variables l_k, $\bar{x}_k$ and S_k, we illustrate in Fig. D.1 a single realization of the disorder in the thresholds for a system with 100 units. The dashed blue line in Fig. D.1a and Fig. D.1c represent the breaking thresholds l_k as extracted from two continuous probability density: Weibul and Uniform distributions, the dotted blue curve is the ordered sequence $\bar{x}_k$, the black dotted curve corresponds to S_k. Fig. D.1b and Fig. D.1d for Weibull and Uniform distribution, respectively.

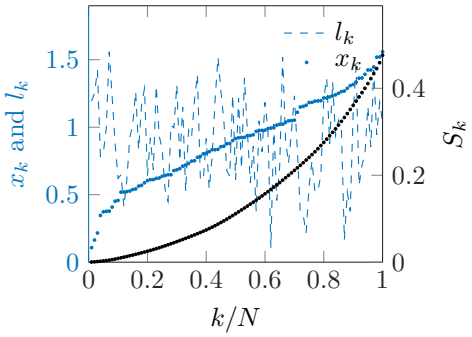

(a) Energy, $\lambda_f = 1$

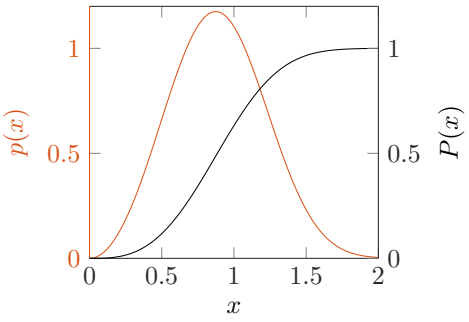

(b) $\lambda_f = 1$

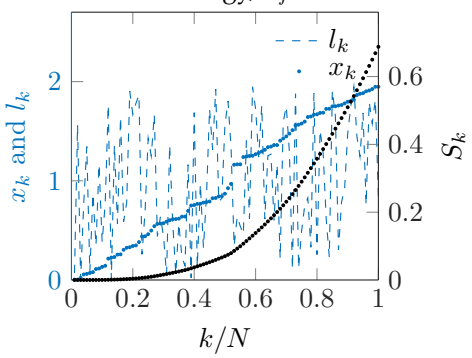

(c) Energy, $\lambda_f = 1$

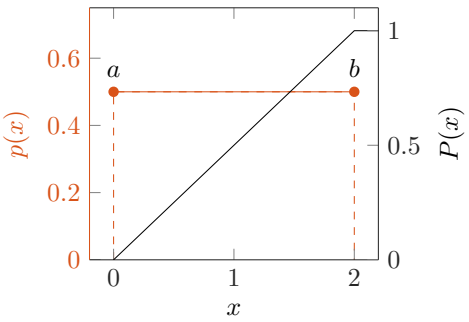

(d) $\lambda_f = 1$

Figure D.1: Statistical properties of the breaking thresholds for two different probability distributions. Weibull distribution with shape parameter $\rho = 3$ for (a) and (b) and Uniform $\mathcal{U}(0, 2)$ for (c) and (d).

Appendix E

Quality of the power law

In the study of criticality in physical systems we are faced with the occurrence of power laws, which is a signature of complex behavior. Hence, it is of great importance to be able to asses whether an observed distribution follows a power law. Unfortunately, the detection and characterization of power laws is complicated by the large fluctuations in the tails of the distribution. Following closely the works of Clauset *et al.* and Newman we use an accurate method of dicerning and quantifying power law behavior in empirical data (Clauset, Shalizi, and Newman, 2009; Newman, 2005; Baró and Vives, 2012).

Definitions A continuous power law distribution is described by a probability density $p(x)$ such that

$$p(x)dx = \Pr(x \leq X \leq x + dx) = Cx^{-\alpha}dx, \tag{E.1}$$

where X is the observed value and C is a normalization constant. This density diverges as $x \to 0$, therefore Eq. (E.1) cannot hold for all $x \geq 0$. We denote the lower bound x_{min}, so that the pdf is valid for all $x \geq x_{min}$. Then, provided that we have $\alpha > 1$ (for normalization), we can write,

$$p(x) = \frac{\alpha - 1}{x_{min}} \left(\frac{x}{x_{min}} \right)^{-\alpha}. \tag{E.2}$$

In the discrete case, the random variable x can only take a discrete set of values. We are mainly interested in the case of positive integers, so that the probability distribution is written in the form,

$$p(x) = \Pr(X = x) = Cx^{-\alpha}. \tag{E.3}$$

As in the continuous case, this distribution diverges as $x \to 0$, so we define the lower bound $x_{min} > 0$. After calculating the normalizing constant, we have that,

$$p(x) = \frac{x^{-\alpha}}{\zeta(\alpha, x_{min})}, \tag{E.4}$$

where $\zeta(\alpha, x_{min}) = \sum_{n=0}^{\infty} (n + x_{min})^{-\alpha}$ is the Hurwitz zeta function.

Estimating the parameters of the power law One way to find the scaling parameter α is by simply fit the slope of the curve on a log-log plot. However, this method is known to introduce systematic biases into the value of the exponent (Goldstein, Morris, and Yen, 2004). Instead, we use a more robust method, maximum likelihood estimation (MLE).

For the continuous case, the MLE is,

$$\hat{\alpha} = 1 + n \left[\sum_{i=1}^{n} \ln \frac{x_i}{x_{min}} \right]^{-1}, \tag{E.5}$$

where x_i, $i = 1, \ldots, n$ are the observed values of x such that $x_i \geq x_{min}$. Following the reference (Newman, 2005), we use the "hat" to denote estimates derived from data. The standard error in the calculation of $\hat{\alpha}$ can also be derived from MLE and is

$$\sigma = \frac{\hat{\alpha - 1}}{\sqrt{n}} + \mathcal{O}(1/n). \tag{E.6}$$

There is no exact closed form for the estimation of the scaling parameter in the discrete case. Nevertheless, we are able to provide an approximate expression, based on a approximation of the integers as continuous reals rounded to the nearest integer, to which the scaling parameter $\hat{\alpha}$ is

$$\hat{\alpha} \approx 1 + n \left[\sum_{i=1}^{n} \ln \frac{x_i}{x_{min} - 1/2} \right]^{-1}. \tag{E.7}$$

The estimate for the error in $\hat{\alpha}$ can be calculated by employing Eq. (E.6).

Testing the power law hypothesis After estimating the scaling parameter for the power law, we need to provide evidence to whether the power law is a plausible fit to the data. To assess the goodness of fit of the estimate we use a Kolmogorov-Smirnov (KS) test, which is based on the following test statistic

$$K = \sup_x |F^*(x) - S(x)|, \tag{E.8}$$

where $F^*(x)$ is the hypothesized cumulative distribution function and $S(x)$ is the empirical distribution function based on the sampled data.

The approach to measuring the goodness-of-fit is based on sampling many synthetic data sets from a true power law distribution, measuring how far they fluctuate from the power law form, and then compare the results with similar measurements on the empirical data. Such approach is based on a measurement of a "distance" between the distributions of the empirical data and the hypothesized model. This distance is compared with distance measurements for comparable synthetic data sets, and the p-value is defined to be the fraction of the synthetic data that are larger than the empirical distances. Hence, if p is large (close to 1), then the difference between the empirical data and the model can be attributed to statistical fluctuations, while if it is small, the model is not a plausible fit to the data. For a clear description of goodness of fit models refer to (Clauset, Shalizi, and Newman, 2009).

Appendix F

Burgers equation

The Burgers equation is the simplest equation presenting both nonlinear wave propagation and diffusive effects. The Cauchy problem for the viscid Burgers equation is,

$$\begin{cases} u_t + uu_x = \epsilon u_{xx} & (x,t) \in \mathbb{R} \times (0,\infty),\ \epsilon > 0, \\ u(x,0) = u_0(x) & x \in \mathbb{R} \end{cases} \tag{F.1}$$

where $\epsilon > 0$ is a viscosity. The *Cole-Hopf transformation* reduces the viscid Burgers problem, Eq. (F.1), to the linear heat equation through the nonlinear transformation,

$$u = -2\epsilon \frac{\psi_x}{\psi} \tag{F.2}$$

We also are able to obtain ψ as a function of u,

$$\psi(x,t) = \exp\left(-\int_0^x \frac{u(y,t))}{2\epsilon} dy\right). \tag{F.3}$$

That is important to determine the initial condition,

$$\psi(x,0) = \exp\left(-\int_0^x \frac{u(y,0))}{2\epsilon} dy\right) \tag{F.4}$$

Leading to the following Cauchy problem for the heat equation,

$$\begin{cases} \psi_t = \epsilon \psi_{xx} & (x,t) \in \mathbb{R} \times (0,\infty),\ \epsilon > 0 \\ \psi(x,0) = \psi_0(x) = e^{-\int_0^x \frac{u_0(x')}{2\epsilon} dx'},\ x \in \mathbb{R} \end{cases} \tag{F.5}$$

whose solution is given by,

$$\psi(x,t) = \frac{1}{\sqrt{4\pi\epsilon t}} \int_{-\infty}^{\infty} \exp\left(-\frac{(x-y)^2}{4\epsilon t}\right) \psi_0(y) dy \tag{F.6}$$

Inviscid Burgers equation When the diffusion term is absent, $\epsilon \to 0$, we obtain the inviscid Burgers equation

$$\begin{cases} u_t + uu_x = 0 & (x,t) \in \mathbb{R} \times (0,\infty), \\ u(x,0) = u_0(x) & x \in \mathbb{R} \end{cases} \tag{F.7}$$

Method of characteristics We define the characteristics as the curves $x(t)$ in the (x,t) plane on which $u(x,t)$ remains constant. Which is attained if the characteristic equation follows,

$$\begin{cases} \dfrac{dx(t)}{dt} = u(x(t),t) & t > 0, \\ x(0) = x_0. & x \in \mathbb{R} \end{cases} \tag{F.8}$$

To prove that the solution $u(x,t)$ is constant along the curve $x(t)$ we compute the total derivative,

$$\frac{du(x(t),t)}{dt} = \frac{\partial u}{\partial t} + \frac{\partial u}{\partial x}\frac{dx}{dt} = \frac{\partial u}{\partial t} + \frac{\partial u}{\partial x}u = 0. \tag{F.9}$$

Therefore,

$$u(x(t),t) = u(x(0),0) = u_0(x_0). \tag{F.10}$$

From Eq. (F.8), the characteristic curves are straight lines determined by the initial data,

$$x(t) = x_0 + u_0(x_0)t,\ t > 0. \tag{F.11}$$

Finally, the solution $u(x(t),t)$ is described by the implicit relation,

$$u(x,t) = u_0(x - u_0(x_0)t, t). \tag{F.12}$$

We note that all the characteristics are straight lines, but not all lines have the same slope. Thus, it is possible for characteristics to intersect and the solution becomes multivalued. The time t_b at which the characteristic intersect is called the breaking time

Breaking time Even for a smooth initial condition $u_0(x)$ the solution of the inviscid Burgers equation may become discontinuous in a finite time. This happens at the intersection of the characteristic curves, i.e. the wave breaks. To find the breaking time we consider two characteristics arising from initial conditions x_1 and $x_2 = x_1 + \Delta x$, according to Eq. (F.11), these characteristic will cross when

$$x(t) = u_0(x_1)t + x_1 = u_0(x_2)t + x_2. \tag{F.13}$$

Solving this equation for t leads to,

$$t = -\frac{x_1 - x_2}{u_0(x_1) - u_0(x_2)} = -\frac{\Delta x}{u_0(x_1) - u_0(x_1 + \Delta x)} \tag{F.14}$$

When $\Delta x \to 0$ the time in Eq. (F.14) converges to

$$t = -\frac{1}{u_0'(x_1)}. \tag{F.15}$$

The breaking time is the minimum possible value for t,

$$t_b = \min_{x \in \mathbb{R}} \left\{ -\frac{1}{u_0'(x)} \right\} \tag{F.16}$$

Appendix G

Replica trick formulation

The solution of the problem now relies in the computation of the mean of the logarithm, which cannot be done analytically. That is where the so-called Replica-Trick enters. It is based on the following identity

$$\langle \log Z \rangle = \left. \frac{\partial \langle Z^n \rangle}{\partial n} \right|_{n=0} = \lim_{n \to 0} \frac{Z^n - 1}{n} = \lim_{n \to 0} \frac{1}{n} \log \langle Z^n \rangle \tag{G.1}$$

The idea is to compute the right hand side for a finite integer n, then perform an analytical continuation to $n \to 0$. To perform this calculations we restart with the energy $E\{v_i\}$ and write the partition function

$$\mathcal{Z}^n = e^{-\beta E(v,x^1) - \cdots - \beta E(v,x^n)} = e^{-\beta \sum_a^n E(v,x^a)} \tag{G.2}$$

Here we introduced n replicas of the system, which is shown in the upper indices for x. It is important to notice that the *disorder is fixed* for all replicas. To simplify the notation we denote $Dv_i = \prod_{i=1}^N dv_i$.

$$\langle \mathcal{Z}^n \rangle = \sum_{x_i^a} \int Dv_i p(v_i) e^{-\beta \sum_a^n \sum_i^N \left[(1+x_i^a) v_i + \frac{1}{2}(y - x_i^a)^2 \right]} \tag{G.3}$$

We assume that the disorder follows a Gaussian distribution, $p(v_i) = \dfrac{1}{\sqrt{2\pi\sigma^2}} e^{-\frac{(v_i - \mu)^2}{2\sigma^2}}$. Then, we separate the disorder-dependent terms and get,

$$\langle \mathcal{Z}^n \rangle = \sum_{x_i^a} \frac{e^{\sum_i^N \sum_a^n -\frac{\beta}{2}(y - x_i^a)^2}}{(2\pi\sigma^2)^{N/2}} \int Dv_i e^{\sum_i^N \left[-\frac{(v_i - \mu)^2}{2\sigma^2} - \beta \sum_a^n (1 + x_i^a) v_i \right]}, \tag{G.4}$$

Performing the integration leads to,

$$\langle \mathcal{Z}^n \rangle = \sum_{x_i^a} e^{\sum_i^N \left[\frac{\sigma^2 \beta^2}{2} \left(\sum_a^n (1 + x_i^a) \right)^2 - \mu\beta \sum_a^n (1 + x_i^a) - \sum_a^n \frac{\beta}{2}(y - x_i^a)^2 \right]}, \tag{G.5}$$

we use the Hubbard-Stratonovich transformation to decouple the individual sites by writing,

$$e^{\frac{\sigma^2 \beta^2}{2} \left(\sum_a^n (1 + x_i^a) \right)^2} = \int \frac{ds}{\sqrt{2\pi}} e^{-\frac{1}{2}s^2 + \sigma\beta \sum_a^n (1 + x_i^a) s}, \tag{G.6}$$

leading to

$$
\begin{aligned}
\langle \mathcal{Z}^n \rangle &= \sum_{x_i^a} \int \frac{ds}{\sqrt{2\pi}} e^{\sum_i^N \left[-\frac{1}{2}s^2 + \sigma\beta \sum_a^n (1+x_i^a)s - \mu\beta \sum_a^n (1+x_i^a) - \sum_a^n \frac{\beta}{2}(y-x_i^a)^2 \right]}, \\
&= \int \frac{ds}{\sqrt{2\pi}} \sum_{x_i^a} \prod_i^N e^{-\frac{1}{2}s^2 + \sigma\beta n s - \mu\beta n - \frac{\beta}{2}y^2 n + \sum_a^n \left[\sigma\beta x_i^a s - \mu\beta x_i^a + \beta y x_i^a - \frac{\beta}{2}(x_i^a)^2 \right]}, \\
&= \prod_i^N \int \frac{ds}{\sqrt{2\pi}} e^{-\frac{1}{2}s^2 + \sigma\beta n s - \mu\beta n - \frac{\beta}{2}y^2 n} \prod_a^n \sum_{x_i^a = \{-1,0\}} e^{\sigma\beta x_i^a s - \mu\beta x_i^a + \beta y x_i^a - \frac{\beta}{2}(x_i^a)^2}, \\
&= e^{-N\beta n(y^2/2+\mu)} \left\{ \int \frac{ds}{\sqrt{2\pi}} e^{-\frac{1}{2}s^2 + \sigma\beta n s} \left[1 + e^{-\beta(\sigma s - \mu + y + \frac{1}{2})} \right]^n \right\}^N .
\end{aligned}
\tag{G.7}
$$

Now we are able to compute the free energy using $\langle \log Z \rangle = \left. \frac{\partial \langle Z^n \rangle}{\partial n} \right|_{n=0}$.

$$
\begin{aligned}
\left. \frac{\partial \langle \mathcal{Z}^n \rangle}{\partial n} \right|_{n=0} &= N\beta\left(\frac{y^2}{2} + \mu\right) \\
&\quad + N \int \frac{ds}{\sqrt{2\pi}} e^{-\frac{1}{2}s^2} \left[\log\left(1 + e^{-\beta(\sigma s - \mu + y + \frac{1}{2})} \right) + \sigma\beta s \right].
\end{aligned}
\tag{G.8}
$$

Finally, since $\mathcal{F} = -\frac{1}{\beta N} \langle \log \mathcal{Z} \rangle$, we can write

$$
\mathcal{F} = \frac{y^2}{2} + \mu - \frac{1}{\beta} \int \frac{ds}{\sqrt{2\pi}} e^{-\frac{1}{2}s^2} \left[\log\left(1 + e^{-\beta(\sigma s - \mu + y + \frac{1}{2})} \right) + \sigma\beta s \right]. \tag{G.9}
$$

If we define $-h = \sigma s - \mu$ and note that $1 + e^{-\beta(-h+y+\frac{1}{2})}$ as $e^{-\frac{\beta}{2}(-h+y+\frac{1}{2})}(e^{-\frac{\beta}{2}(-h+y+\frac{1}{2})} + e^{\frac{\beta}{2}(-h+y+\frac{1}{2})}) = e^{-\frac{\beta}{2}(-h+y+\frac{1}{2})} 2\cosh\left[\frac{\beta}{4}(-2h+2y+1)\right]$, we may rewrite the equation as

$$
\begin{aligned}
\mathcal{F} =& \frac{y^2}{2} + \mu - \frac{1}{\beta} \int \frac{dh}{\sqrt{2\pi\sigma^2}} e^{-\frac{(h-\mu)^2}{2\sigma^2}} \left[\log\left(1 + e^{-\beta(-h+y+\frac{1}{2})} \right) + \beta(h-\mu) \right] \\
=& \frac{y^2}{2} + \mu - \frac{1}{\beta} \int \frac{dh}{\sqrt{2\pi\sigma^2}} e^{-\frac{(h-\mu)^2}{2\sigma^2}} \log\left[1 + e^{-\beta(-h+y+\frac{1}{2})} \right] \\
=& \frac{y^2}{2} + \frac{y}{2} + \frac{1}{4} + \frac{\mu}{2} - \frac{1}{\beta} \int \frac{dh}{\sqrt{2\pi\sigma^2}} e^{-\frac{(h-\mu)^2}{2\sigma^2}} \log\left[2\cosh\left[\frac{\beta}{4}(-2h+2y+1) \right] \right].
\end{aligned}
\tag{G.10}
$$

From the free energy we find the tension $t = \frac{\partial \mathcal{F}}{\partial y}$,

$$
\begin{aligned}
t &= y + \int \frac{dh}{\sqrt{2\pi\sigma^2}} \frac{e^{-\frac{(h-\mu)^2}{2\sigma^2}}}{1 + e^{\beta(-h+y+\frac{1}{2})}} \\
&= y + \frac{1}{2} - \frac{1}{2} \int \frac{dh}{\sqrt{2\pi\sigma^2}} e^{-\frac{(h-\mu)^2}{2\sigma^2}} \tanh\left[\frac{\beta}{4}(1 - 2h + 2y) \right]
\end{aligned}
\tag{G.11}
$$

The stiffness K is the derivative of the tension t with respect to the elongation y

$$
K = 1 - \frac{\beta}{4} \int \frac{dh}{\sqrt{2\pi\sigma^2}} e^{-\frac{(h-\mu)^2}{2\sigma^2}} \operatorname{sech}^2\left[\frac{\beta}{4}(1 - 2h + 2y) \right] \tag{G.12}
$$

Appendix H

Convergence result

In this section we want to prove the following result

$$\lim_{k\to\infty} \frac{k}{2}\operatorname{sech}^2 kx \to \delta(x). \tag{H.1}$$

It is trivial to check that the basic properties of the delta function are fulfilled: for $x = 0$, $\lim_{k\to\infty} \frac{k}{2}\operatorname{sech}^2 kx \to \infty$, and for $x \neq 0$, $\lim_{k\to\infty} \frac{k}{2}\operatorname{sech}^2 kx \to 0$. However, this is not enough, we need to show that for a continuous and integrable function $f : \mathbb{R} \to \mathbb{R}$, we have $\int_{-\infty}^{\infty} f(x)\frac{k}{2}\operatorname{sech}^2 kxdx = f(0)$, for $k \to \infty$. To prove that we write,

$$\int_{-\infty}^{\infty} f(x)\frac{k}{2}\operatorname{sech}^2 kx\,dx = \int_{-\infty}^{\infty} \left[f(x) - f(0)\right]\frac{k}{2}\operatorname{sech}^2 kx\,dx + \int_{-\infty}^{\infty} f(0)\frac{k}{2}\operatorname{sech}^2 kx\,dx. \tag{H.2}$$

But, $\displaystyle\int_{-\infty}^{\infty} f(0)\frac{k}{2}\operatorname{sech}^2 kx\,dx = f(0)\frac{\tanh kx}{2}\Big|_{-\infty}^{\infty} = f(0)$. Thus we need to show that,

$$\lim_{k\to\infty} \int_{-\infty}^{\infty} \left[f(x) - f(0)\right]\frac{k}{2}\operatorname{sech}^2 kx\,dx = 0. \tag{H.3}$$

Let us consider a change in variables, $y = kx$, allowing us to write,

$$\lim_{k\to\infty} \int_{-\infty}^{\infty} \left[f\left(\frac{y}{k}\right) - f(0)\right]\frac{1}{2}\operatorname{sech}^2 y\,dy = 0. \tag{H.4}$$

The function $\operatorname{sech}^2 y$ is compact, and since $f(x)$ is continuous it means that we can make $f(y/k)$ as close to $f(0)$ as we want, rigorously, it means that $\forall\,\epsilon > 0$, $\exists\delta > 0$ such that, $0 < \left|\frac{y}{k}\right| < \delta \Rightarrow \left|f\left(\frac{y}{x}\right) - f(0)\right| < \epsilon$. Therefore, for any ϵ, we can find a large enough $k = y/\delta$, such that we have

$$\int_{-\infty}^{\infty} \left[f\left(\frac{y}{k}\right) - f(0)\right]\frac{1}{2}\operatorname{sech}^2 y\,dy < \epsilon\int_{-\infty}^{\infty} \frac{1}{2}\operatorname{sech}^2 y\,dy \tag{H.5}$$

Consequently, $\int_{-\infty}^{\infty} \left[f\left(\frac{y}{k}\right) - f(0)\right]\frac{1}{2}\operatorname{sech}^2 y\,dy < \epsilon$. Therefore, we have that

$$\lim_{k\to\infty} \int_{-\infty}^{\infty} f(x)\frac{k}{2}\operatorname{sech}^2 kx\,dx = f(0). \tag{H.6}$$

Allowing us to identify $\frac{k}{2}\operatorname{sech}^2 kx = \delta(x)$.

Appendix I

Mapping on Random-Field Ising Model (RFIM)

We start with the energy function Eq. (13.2) in the main text and assume that the internal variable y is eliminated using the condition $\partial E/\partial y = 0$. Then,

$$y = \frac{\lambda_f z}{1+\lambda_f} + \frac{1}{N(1+\lambda_f)} \sum_i x_i.$$

and the relaxed energy reads

$$\begin{aligned} E(x_i, z) = &-\frac{1}{2N(1+\lambda_f)} \left(\sum_i x_i \right)^2 \\ &+ \sum_i (1+x_i) v_i - \frac{\lambda_f z}{1+\lambda_f} \sum_i x_i + \sum_i \frac{x_i^2}{2} + \frac{N\lambda_f z^2}{2(1+\lambda_f)} \end{aligned}$$

Since x_i is either 0 or -1, we may write $\sum_i x_i^2 = -\sum_i x_i$ and $\left(\sum_i x_i\right)^2 = \sum_i \sum_j x_i x_j = \sum_{i,j} x_i x_j$. In terms of spin variables, $2x_i = s_i - 1$, with $s_i = \pm 1$ the relaxed energy can be written as,

$$\begin{aligned} E(s_i, z) = &-\frac{1}{8N(1+\lambda_f)} \sum_{i,j} s_i s_j \\ &- \sum_i \left(\frac{2\lambda_f z - 1}{4(1+\lambda_f)} + \frac{1}{4} - \frac{v_i}{2} \right) s_i \\ &+ \sum_i \left(\frac{\lambda_f z(1+z)}{2(1+\lambda_f)} + \frac{1}{4} + \frac{v_i}{2} - \frac{1}{8(1+\lambda_f)} \right) \\ = &-\frac{J}{2N} \sum_{i,j} s_i s_j - \sum_i h_i s_i + f(z). \end{aligned} \tag{I.1}$$

where $J = \frac{1}{4(1+\lambda_f)}$, $h_i = \frac{2\lambda_f z - 1}{4(1+\lambda_f)} + \frac{1}{4} - \frac{v_i}{2}$ and $f(z) = \sum_i \frac{\lambda_f z(1+z)}{2(1+\lambda_f)} + \frac{1}{4} + \frac{v_i}{2} - \frac{1}{8(1+\lambda_f)}$.

Appendix J

Case of uniform distribution

Let $\mathcal{U}(\mu, \sigma)$ be the uniform distribution defined in terms of mean μ and variance σ^2 the pdf is for a random variable x,

$$p(x) = \begin{cases} \dfrac{1}{2\sigma\sqrt{3}} & \text{for } -\sigma\sqrt{3}+\mu \leq x \leq \sigma\sqrt{3}+\mu \\ 0 & \text{otherwise} \end{cases} \tag{J.1}$$

and cdf

$$P(x) = \begin{cases} 0 & \text{for } x < -\sigma\sqrt{3}+\mu \\ \dfrac{1}{2}\left(\dfrac{x-\mu}{\sigma\sqrt{3}}+1\right) & \text{for } -\sigma\sqrt{3}+\mu \leq x \leq \sigma\sqrt{3}+\mu \\ 1 & \text{for } x > \sigma\sqrt{3}+\mu \end{cases} . \tag{J.2}$$

Using this probability density we are able to explicitly calculate the integral

$$\left\langle \log \tilde{\mathcal{Z}}\{v\} \right\rangle = \int_{-\sigma\sqrt{3}+\mu}^{\sigma\sqrt{3}+\mu} \frac{dv}{2\sigma\sqrt{3}} \log\left(e^{-\frac{\beta}{2}(y_0+1)^2} + e^{-\beta(y_0^2/2+v)}\right). \tag{J.3}$$

The existence of multiple solutions of y_0 is what characterizes the critical behavior. To obtain such change in the qualitative response we may tune either temperature β, the disorder σ or the external stiffness λ_f. We can also characterize the multiplicity of minima in y by studying the convexity of the free energy with respect to y.

$$\mathcal{F}(\beta, y_0, z) = \frac{\lambda_f}{2}(z-y_0)^2 - \frac{1}{\beta}\left\langle \log \tilde{\mathcal{Z}}\{v_i\}(\beta, y_0, z) \right\rangle . \tag{J.4}$$

Which is exactly,

$$\begin{aligned} \mathcal{F} = \frac{\lambda_f}{2}(z-y_0)^2 + \mu + \frac{y_0^2}{2} + \frac{\mathrm{Li}_2\left(-e^{\beta\left(-y_0+\mu+\sqrt{3}\sigma-\frac{1}{2}\right)}\right)}{2\sqrt{3}\beta^2\sigma} \\ - \frac{\mathrm{Li}_2\left(-e^{-\frac{1}{2}\beta\left(2y_0-2\mu+2\sqrt{3}\sigma+1\right)}\right)}{2\sqrt{3}\beta^2\sigma}, \end{aligned} \tag{J.5}$$

where y_0 is obtained from the following self-consistent relation

$$y_0 = \frac{\lambda_f z}{\lambda_f+1} - \frac{1}{2\sqrt{3}\sigma\beta(\lambda_f+1)} \log\left(\frac{e^{\beta\left(\mu+\sqrt{3}\sigma-y_0-\frac{1}{2}\right)}+1}{e^{-\frac{1}{2}\beta\left(-2\mu+2\sqrt{3}\sigma+2y_0+1\right)}+1}\right) \tag{J.6}$$

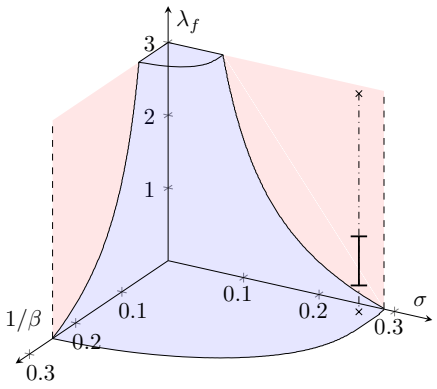

Figure J.1: Phase diagram for uniform distribution

Appendix K

Landau's phenomenological description: Soft device

We proceed similarly as the mixed device. For the definition of the order parameter in the soft device we notice that the equilibrium of the system with respect to the variable y implies,

$$y = t + \frac{1}{N}\sum_i x_i. \tag{K.1}$$

It is natural then to define the order parameter $\phi = \langle x \rangle + \frac{1}{2}$, therefore,

$$\phi = y + \frac{1}{2} - t. \tag{K.2}$$

We assume, for simplicity, $v_0 = 0$ and $t = 0$. We observe that t here plays the role of an external field, similar to an external magnetic field in ferromagnetic systems. We then introduce in Eq. (15.31) the order parameter through, $y = \phi - 1/2$ and we get,

$$\mathcal{G}(\beta,\phi) = \frac{1}{2}\left(\phi - \frac{1}{2}\right)^2 + \frac{\phi}{2} - \frac{1}{\beta}\log\left[\cosh\frac{\beta\phi}{2} + \sqrt{e^{-\beta\lambda_J} + \sinh^2\frac{\beta\phi}{2}}\right], \tag{K.3}$$

the corresponding self-consistent relation for the order parameter ϕ is,

$$\phi = \frac{\sinh\frac{\beta\phi}{2}}{2\sqrt{e^{-\beta\lambda_J} + \sinh^2\frac{\beta\phi}{2}}}. \tag{K.4}$$

Near the critical temperature we can expand the free energy for small ϕ, *i.e.* $\mathcal{G}$ is an analytical function of both the order parameter and the coupling constants.

To study the occurrence of second-order phase transitions we perform a Taylor expansion in the free-energy Eq. (15.37) around $\phi = 0$ leading to,

$$\mathcal{G}(\beta,\phi) = \frac{1}{8} - \frac{\log\left(\sqrt{e^{-\beta\lambda_J}} + 1\right)}{\beta} + \left(\frac{1}{2} - \frac{\beta}{8\sqrt{e^{-\beta\lambda_J}}}\right)\phi^2 + \frac{\beta^3\left(3e^{\beta\lambda_J} - 1\right)}{384\sqrt{e^{-\beta\lambda_J}}}\phi^4 + \mathcal{O}(\phi^5). \tag{K.5}$$

As in the mixed device, due to the symmetry of the free energy $\mathcal{G}(\beta,\phi) = \mathcal{G}(\beta,-\phi)$ the Taylor expansion around $\phi = 0$ presents only even powers of ϕ. In this expansion we must ensure that the fourth-order term is positive, otherwise the free energy would be minimized by $|\phi| \to \infty$. Hence,

$$3e^{\beta\lambda_J} - 1 > 0. \tag{K.6}$$

The order parameter that minimizes the free energy will be the one that is observed,

$$\frac{\partial \mathcal{G}}{\partial \phi} = 0 = 2\left(\frac{1}{2} - \frac{\beta}{8\sqrt{e^{-\beta\lambda_J}}}\right)\phi + \frac{\beta^3\left(3e^{\beta\lambda_J} - 1\right)}{96\sqrt{e^{-\beta\lambda_J}}}\phi^3. \tag{K.7}$$

Clearly, one of the solutions is $\phi = 0$. Furthermore, we have

$$\phi = \pm\sqrt{\frac{24\left(\beta - 4\sqrt{e^{-\beta\lambda_J}}\right)}{\beta^3\left(3e^{\beta\lambda_J} - 1\right)}}. \tag{K.8}$$

The critical inverse temperature, β_c is such that the second order term in the expansion is zero, hence

$$\frac{1}{2} - \frac{\beta_c}{8\sqrt{e^{-\beta_c\lambda_J}}} = 0, \tag{K.9}$$

for given λ_J. In the limit case were $\lambda_J \to 0$ we have $\beta_c = 4$. In general, we are able to write β_c as,

$$\beta_c = \frac{2W(4\lambda_J)}{\lambda_J} \tag{K.10}$$

where $W(x)$ is the Lambert function, implicitly defined by the functional equation $z = W(z)e^{W(z)}$. This function makes sense for $z \geq -1/e$. The typical shape of the free energy with respect to the order parameter is presented in Fig. 15.9a. For temperatures above the critical value the stable position corresponds to $\phi = 0$, while for temperatures below T_c the stable configuration corresponds to $\phi \neq 0$.

The system presents a second-order phase transition on the (β, λ_J) space up to the tricritical point (TCP), where the transition becomes first order. We now use Landau's formulation to describe first order phase transition by introducing the sixth-order term in the expansion, which must be positive, so that the system is globally stable, otherwise $\phi \to \pm\infty$ would minimize the free energy. However, now the fourth-order term is negative, otherwise were are in the previous case of second-order phase transition.

$$\begin{aligned}\mathcal{G}(\beta,\phi) = \frac{1}{8} - \frac{\log\left(\sqrt{e^{-\beta\lambda_J}} + 1\right)}{\beta} + \left(\frac{1}{2} - \frac{\beta}{8\sqrt{e^{-\beta\lambda_J}}}\right)\phi^2 \\ + \frac{\beta^3\left(3e^{\beta\lambda_J} - 1\right)}{384\sqrt{e^{-\beta\lambda_J}}}\phi^4 + \frac{\beta^5\left(30e^{\beta\lambda_J} - 45e^{2\beta\lambda_J} - 1\right)}{46080\sqrt{e^{-\beta\lambda_J}}}\phi^6 + \mathcal{O}(\phi^7).\end{aligned} \tag{K.11}$$

Again, due to the symmetry of the free energy we only have even powers of ϕ. The minimization of the free energy with respect to the order parameter yields,

$$\frac{\partial \mathcal{G}}{\partial \phi} = 2a_2\phi + 4a_4\phi^3 + 6a_6\phi^5 = 0, \tag{K.12}$$

where $a_2 = \frac{1}{2} - \frac{\beta}{8\sqrt{e^{-\beta\lambda_J}}}$, $a_4 = \frac{\beta^3\left(3e^{\beta\lambda_J}-1\right)}{384\sqrt{e^{-\beta\lambda_J}}} < 0$ and $a_6 = \frac{\beta^5\left(30e^{\beta\lambda_J}-45e^{2\beta\lambda_J}-1\right)}{46080\sqrt{e^{-\beta\lambda_J}}} > 0$ are the coefficients of the Taylor expansion of the free energy.

Out of the five solutions to the equation we have at most three that are real and stable, the stability of the solutions will depend on the temperature and on the coupling constant λ_J.

The trivial solution is $\phi = 0$ and for $\phi \neq 0$ we have a bi-quadratic equation whose real solutions are,

$$\phi = \pm\sqrt{\frac{-a_4 + \sqrt{a_4^2 - 3a_2a_6}}{3a_6}}, \tag{K.13}$$

The system presents a second order phase transition up to the tricritical point, where the transition becomes first-order, the tricritical point is found considering a vanishing fourth-order term in the expansion. Therefore, if we consider $\beta = 4e^{-\beta\lambda_J/2}$, from the second-order term and $e^{-\beta\lambda_J/2} = \sqrt{3}$ from the fourth-order we have the tricritical point TCP given by, $\beta_{TCP} = 4\sqrt{3}$ and $\lambda_J = -\log 3/4\sqrt{3}$. The first-order transition line is obtained by requiring that $\mathcal{G}(\beta, \phi = 0) = \mathcal{G}(\beta, \phi = \phi^*)$.

We can build the full phase diagram in the (λ_J, β) space separating the regions where $\phi = 0$ is the stable state from the region where $\phi \neq 0$ is stable. In our system the order parameter ϕ plays the same role as the magnetization in magnetic systems. When we set $z = z_0$ we create the symmetry around $\phi = 0$, for applied displacements $z \neq z_0$ the situation is different.

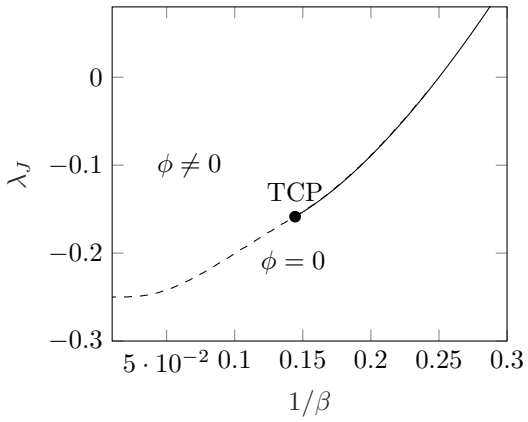

Figure K.1: Phase diagram for the system. In the canonical ensemble the transition is continuous (bold solid line) down to the tricritical point TCP, where it becomes first-order (dashed line).

université PARIS-SACLAY

ÉCOLE DOCTORALE
Sciences mécaniques et énergétiques, matériaux et géosciences (SMEMAG)

Titre: Effets collectifs dans la contraction musculaire et l'adhésion cellulaire

Mots clés: Criticalité, Adhesion cellulaire, méchanique musculaire

Résumé: Deux systèmes biologiques distincts, les muscles squelettiques et les sites d'adhésion de cellules kératocytes en mouvement, sont considérés dans un même cadre en raison de la similitude profonde de leur structure et de leur fonctionnalité. La réponse passive de l'un et de l'autre peut être modélisée à l'aide d'un grand nombre d'unités multi-stables couplées par des interactions à longue portée, et exposées à un désordre spatial fixé et un bruit thermique/mécanique. Les interactions à longue portée dans de tels systèmes conduisent à une synchronisation malgré les fluctuations temporelles et spatiales. Nous utilisons une description en champ moyen pour obtenir des résultats analytiques et élucider la remarquable dépendance du comportement mécanique de tels systèmes par rapport à l'ensemble statistique dans la limite thermodynamique. Bien que les deux systèmes biologiques considérés présentent des différences structurelles importantes, nous montrons que l'on peut identifier une structure de verre de spin sous-jacente commune, que nous exploitons pleinement dans ce travail. À la lumière de cette analogie, ces systèmes vivants semblent être proches de points critiques et, à cet égard, le désordre gelé, reflétant l'incommensurabilité stérique des unités parallèles, peut être fonctionnel. Nous utilisons l'analogie entre le détachement cellulaire et la fracture thermique de solides désordonnés pour étudier la statistique des fluctuations lors de l'adhésion cellulaire. Nous mettons en relation les résultats obtenus aux observations récentes de comportement intermittent impliqué dans le détachement cellulaire, suggérant également une proximité de points critiques. En plus de l'étude des propriétés à l'équilibre des sites d'adhésion, nous présentons également les premiers résultats sur leur comportement cinétique en présence de charges dépendantes du temps.

Title: Collective effects in muscle contraction and cellular adhesion

Keywords: Criticality, Cell adhesion, Muscle mechanics

Abstract: Two biological systems, a half-sarcomere of a skeletal muscle and an adhesive cluster of a crawling keratocyte, are considered in parallel because of the deep similarity in their structure and functionality. Their passive response can be modeled by a large number of multi-stable units coupled through long-range interactions, frustrated by quenched disorder and exposed to thermal noise. In such systems, long-range interactions lead to synchronization, defying temporal and spatial fluctuations. We use a mean-field description to obtain analytic results and elucidate the remarkable ensemble-dependence of the mechanical behavior of such systems in the thermodynamic limit. Despite important structural differences between muscle cross-bridges and adhesive binders, one can identify a common underlying spin glass structure, which we fully exploit in this work. Our study suggests that the muscle machinery is fine-tuned to operate near criticality, and we argue that in this respect the quenched disorder, reflecting here steric incommensuration, may be functional. We use the analogy between cell detachment and thermal fracture of disordered solids to study the statistics of fluctuations during cellular adhesion. We relate the obtained results to recent observations of intermittent behavior involved in cell debonding, also suggesting near-criticality. In addition to the study of the equilibrium properties of adhesive clusters, we also present the first results on their kinetic behavior in the presence of time-dependent loading.

Université Paris-Saclay
Espace Technologique / Immeuble Discovery
Route de l'Orme aux Merisiers RD 128 / 91190 Saint-Aubin, France